TANDEM MASS SPECTROMETRY OF POLYMERIC MATERIALS

Anthony Trevor Jackson

Submitted to the University of Warwick in fulfilment of the requirements for the award of the degree of Doctor of Philosophy

University of Warwick
Department of Chemistry

November 1995

Table of Contents.

List of Tables.

List of Figures.

List of Schemes.

Acknowledgements.

I am very grateful to Professor Keith Jennings and Professor James Scrivens, my academic and industrial supervisors respectively, for their support and guidance during the last three years.

I wish to acknowledge EPSRC and ICI for their financial support of this work. Furthermore, I would like to thank BMSS for their contribution towards travel expenses for conferences.

My thanks go to friends, colleagues and technical staff in the department of chemistry at University of Warwick. In particular, I would like to thank Dominique Despeyroux and Armelle Buzy for their help with some of this work. My thanks to the staff in the mass spectrometry group at ICI Wilton for their willing assistance, especially Richard Jennings, Mike Taylor, George Patterson and Hilary Yates.

My family have been a constant source of support throughout my education. I would particularly like to thank my parents, Peter and Eileen Jackson for their patient encouragement during my studies.

Declaration.

I hereby declare that this thesis is my own work and that, to the best of my knowledge and belief, it contains no material previously published or written by another person, nor material which to a substantial extent has been accepted for the award of any other degree or diploma of a university or other institute of higher learning, except where due acknowledgement is made in the text.

Papers Presented at the Following Conferences:

20th Meeting of the British Mass Spectrometry Society (BMSS), University of Kent, Canterbury, September, 1993.

42nd Meeting of the American Society for Mass Spectrometry and Allied Topics, Chicago, USA, May, 1994.

13th International Conference on Mass Spectrometry (ICMS), Budapest, Hungary, August, 1994.

43rd Meeting of the American Society for Mass Spectrometry and Allied Topics, Atlanta, USA, May, 1995.

22nd Meeting of the British Mass Spectrometry Society (BMSS), University of Manchester Institute of Science and Technology, Manchester, September, 1995.

Paper:

'The Observation of Broad Metastable Peaks in the Surface Induced Dissociation Mass Spectra of Protonated and Cationated Peptides', A. T. Jackson, D. Despeyroux and K. R. Jennings, *Int. J. Mass Spectrom. Ion Proc.*, **141**, 91 (1995).

List of Abbreviations.

a	Mathieu Stability Parameter
A	Amperes
B	Magnetic Sector Analyser
B	Magnetic Field Strength
$\mathbf{B_2}$	Magnetic Field Strength Required to Pass the Product Ion m_2^+
$\mathbf{B_1}$	Magnetic Field Strength Required to Pass the Precursor Ion m_1^+
BAT	Best Anode Temperature
Cat	Metal Cation
CCD	Charge Coupled Device
CEM	Channel Electron Multiplier
CID	Collision Induced Dissociation
CI	Chemical Ionisation
d.c.	Direct Current
Da	Daltons
DCI	Desorption Chemical Ionisation
eV	Electron Volts
e	Elementary Unit of Electronic Charge
E	Electric Sector Analyser
E	Electric Sector Field Strength
$\mathbf{E_2}$	Electric Sector Field Required to Pass the Product Ion m_2^+
E_{coll}	Extra Energy Imparted on Reacceleration in a Floated Collision Cell
E_{coll}	Collision Energy

E_{COM}	Collision Energy in the Centre of Mass Reference Frame
E_{lab}	Collision Energy in the Laboratory Reference Frame
E_1	Electric Sector Field Required to Pass the Precursor Ion m_1^+
EI	Electron Impact
ESI	Electrospray Ionisation
FAB	Fast Atom Bombardment
FD	Field Desorption
FI	Field Ionisation
FT	Fourier Transform
GC	Gas Chromatography
GPC	Gel Permeation Chromatography
h	R.f.-Only Hexapole
IAA	Indole Acrylic Acid
ICR	Ion Cyclotron Resonance
IR	Infrared Spectroscopy
LC	Liquid Chromatography
LDI	Laser Desorption/Ionisation
LSIMS	Liquid Secondary Ionisation Mass Spectrometry
m	Mass of an Ion
m_a	Mass of an atom Involved in the CID Process
m_i	Mass of a Precursor Ion
m_t	Mass of the Collision Gas
m_{pa}	Mass of Portion of a Molecule Involved in the CID Process
$M^{+\bullet}$	Molecular Ion

M_n	Number Average Molecular Weight
M_w	Weight Average Molecular Weight
m/z	Mass to Charge Ratio of an Ion
MALDI	Matrix Assisted Laser Desorption/Ionisation
MCP	Microchannel Plate
MH^+	Protonated Molecule Ion
MS	Mass Spectrometry
MS1	First Mass Spectrometer of a Tandem Instrument
MS2	Second Mass Spectrometer of a Tandem Instrument
MS/MS	Tandem Mass Spectrometry
NBA	*meta*-Nitrobenzyl Alcohol
NMR	Nuclear Magnetic Resonance Spectroscopy
PAD	Post Acceleration Detector
PEG	Polyethyleneglycol
PMMA	Polymethylmethacrylate
PP	Polypropylene
PS	Polystyrene
py	Pyrolysis
q	Rf-Only Quadrupole
q	Mathieu Stability Parameter
Q	Quadrupole Mass Analyser
Q	Internal Energy Uptake During Collision Induced Dissociation
QET	Quasi-Equilibrium Theory
Q_1	First Quadrupole Mass Analyser in a Tandem Quadrupole Instrument

Q_2	Second Quadrupole Mass Analyser in a Tandem Quadrupole Instrument
r	Radius of Curvature of an Electric Sector
R	Radius of Curvature of a Magnetic Sector
r.f.	Radio Frequency
RMM	Relative Molecular Mass
s	Distance
SAM	Self Assembled Monolayer
SIMS	Secondary Ionisation Mass Spectrometry
t	Time
TFHS	2,3,5,6-Tetrafluoro-4-hydroxystyrene
TOF	Time-of-Flight
TS	Thermospray Ionisation
U	Direct Current Voltage Applied to a Quadrupole
UV	Ultraviolet
v	Velocity of an Ion
V_{acc}	Source Acceleration Voltage
V_{cell}	Collision Cell Voltage in a Sector Tandem Instrument
V_0	Zero-to-Peak Rf-Voltage Applied to a Quadrupole
ω	Frequency Measured in Radians of the Rf-Voltage Applied to a Quadrupole
z	Number of Elementary Charges on an Ion

Abstract.

Mass spectrometry and tandem mass spectrometry (MS/MS) has been employed to analyse peptides (< 600 daltons), synthetic polymers of low molecular weight (<10,000 daltons) and a mixture of polymer additives (300-1200 daltons). Mass spectrometry experiments were performed on a four sector mass spectrometer, a tandem quadrupole mass spectrometer and a time-of-flight instrument. High and low energy collision induced dissociation (CID) spectra were obtained by means of a four sector mass spectrometer and a tandem quadrupole instrument respectively. Surface induced dissociation (SID) spectra of peptides were obtained by means of a four sector mass spectrometer with a modified collision cell in the third field free region.

Sequence data were generated by SID from protonated and cationated precursor ions of all four peptides analysed. Furthermore, broad metastable ion peaks were observed in the spectra, arising from fragmentation of precursor ions in the field free region between the electric sector and the magnetic sector of the second mass spectrometer.

Field desorption was a good ionisation technique for the generation of molecular weight information from the polymer additives used. High energy CID was found to be more applicable than low energy CID to the structural determination of polymer additives as characteristic ions were observed in the spectra. Mechanisms have been proposed for the generation of some of the fragment ions observed.

Ultraviolet-matrix assisted laser desorption/ionisation spectra of synthetic polymers of low molecular weight (< 10,000 daltons) were used to calculate molecular weight averages. Furthermore, end group information was also obtained from CID spectra of the same polymer samples.

End group and structural information was also obtained from polystyrene and a substituted polystyrene by means of FD-MS/MS.

CHAPTER 1.

INTRODUCTION.

1.1. Introduction to Mass Spectrometry.

The seminal work of J. J. Thomson [1] in 1913 on the analysis of positively charged species was followed by the development of mass spectrometry (MS) by physicists initially and later by chemists and biochemists. The mass spectrometer is most commonly employed to determine the relative molecular mass (RMM) of a sample. Furthermore, the elemental composition of the analyte may be established if the RMM is sufficiently accurate.

The mass spectrometer may be divided into four separate stages: sample introduction/ionisation, mass analysis, ion detection and data system. The most commonly used ionisation technique is still electron impact (EI), which was initially developed by Nier [2] in the 1940's, as a consequence of its high sensitivity and reproducibility. The generation of gas phase ions is a two stage process for liquid and solid samples by means of EI and chemical ionisation (CI) but may be reduced to a single step by employing desorption/ionisation techniques such as field desorption (FD), fast atom bombardment (FAB), liquid secondary ion mass spectrometry (LSIMS) and matrix assisted laser desorption/ionisation (MALDI) or spray ionisation methods such as electrospray ionisation (ESI). The introduction and ionisation of samples for mass spectrometric analysis is further developed in Chapter 2.

The type of mass spectrometer is characterised by the mass analyser. The five commonly used mass analysers are magnetic sectors, quadrupole mass filters, time-of-flight (TOF), fourier transform-ion cyclotron resonance (FT-ICR) and ion

traps. The ion detection systems that are employed in mass spectrometers are typically based on electron multipliers, with the exception of FT-ICR instruments. Chapter 3 considers the mass analysis and detection of ions in a mass spectrometer.

Mass spectrometry offers both high selectivity and sensitivity and the type of mass spectrometer employed is highly dependent on the application. Many samples, especially those which are biological by nature, are available only in picomole or femtomole quantities and require high sensitivity which is available from FT-ICR instruments. High selectivity may be accessed by using tandem mass spectrometry (MS/MS) which is introduced in Chapter 4. The four mass spectrometers used in the present work are described in Chapter 5.

1.2. Introduction to Polymer Chemistry.

1.2.(a) Polymeric Systems. Polymeric materials now play a very important role in modern life and in fact it would be difficult to imagine everyday existence without them. Many industries rely heavily on these materials. The chemical industry itself, which produces the vast quantities of synthetic polymers which are a large percentage of their output, is a very important part of Britain's economy. Polymeric materials are commonly employed in many areas including transport, clothing, building and packaging. The many forms of these products include viscous liquids, fibres, films, mouldings, composites, powders and granules.

A polymer is a large molecule which is made up of smaller units called monomers and may be linear, slightly branched or a three dimensional network. Polymers composed of two or more different monomers are termed copolymers. Polymeric materials are also classified by their mechanism of formation. The step-wise generation of a polymer by a reaction between any two molecular species is termed step polymerisation. The formation of polymers by successive reaction of monomer units possessing a reactive end group, originally produced by reaction of monomer with an initiator, is called chain polymerisation.

Chain-growth mechanisms include those of free radical polymerisation, ionic polymerisation (both cationic and anionic) and Ziegler-Natta catalysis. An example of free radical polymerisation is the generation of polystyrene (PS) whereas polypropylene (PP) may be produced by means of Ziegler-Natta catalysis [3]. Other polymers are formed by specialised mechanisms, such as poly(methylmethacrylate) (PMMA) which is commonly generated by group transfer polymerisation [3].

Many of the common synthetic polymers such as polyolefins, poly(vinyl chloride), polystyrene and rubbers have been employed for more than half a century. The increase in sophistication and efficiency of their production has given a corresponding improvement in quality and reproducibility. Furthermore, health and safety regulations result in stringent control on the statutes for polymers as with many materials. The characterisation of polymeric materials is therefore essential in establishing the required specifications. The quality tests employed are often required to characterise completely the whole material that may be a blend of polymers which often also

contains additives. The level of characterisation required is partially determined by the application for the material.

1.2.(b) Types of Polymer Additives. Several distinct components are present in a commercial polymer including unreacted catalyst, low molecular weight oligomers, intact monomer and polymer additives. Additives are added to a polymer to enable a formulation to retain its physical and chemical properties.

The many types of polymer additives include fillers, reinforcers, pigments, flame retardents, lubricants, antistatic agents, accelerators, thermal stabilisers, plasticisers, antioxidants and ultraviolet absorbers [4], some of which are considered below.

1.2.(b)(i) Antioxidants. The free radical mechanism involving molecular oxygen (O_2) for the autoxidation of polymeric materials is widely accepted [5,6], as shown in Scheme 1.1:

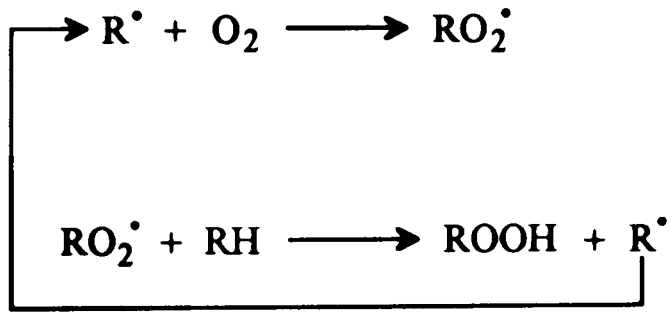

Scheme 1.1.

A Possible Path of Autoxidation of a Polymeric Material. RH is a Polymer.

where R$^{\bullet}$ represents the free radical formed by homolytic dissociation of a polymeric species, RH. The efficiency of an antioxidant is dependent on its ability to inhibit this cycle, as shown in Scheme 1.2:

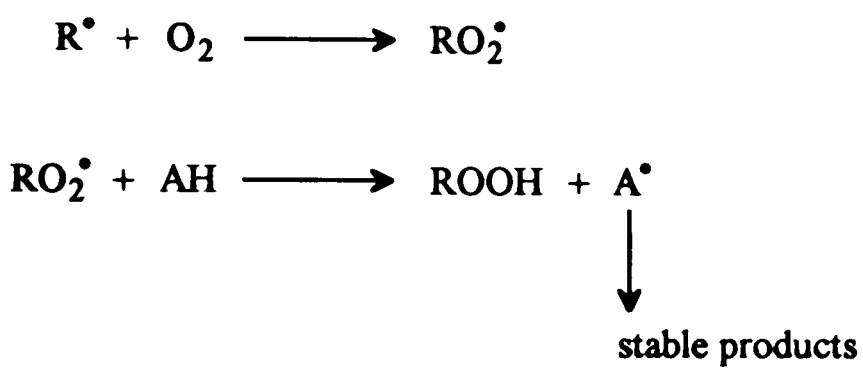

Scheme 1.2.

The Inhibition of an Autoxidation Chain Reaction by an Antioxidant. AH is an Antioxidant.

where A$^{\bullet}$ is the non-propagating free radical formed from the inhibitor molecule AH. The properties required in antioxidants include the molecule's having a labile hydrogen atom bound to a heteroatom and that the free radical, A$^{\bullet}$, decomposes to give stable products. Two species which have these qualities are hindered phenols and aromatic amines. The free radical, A$^{\bullet}$, is formed from phenols by the process shown in Scheme 1.3:

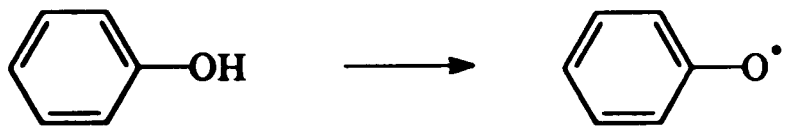

Scheme 1.3.

Formation of a Free Radical Inhibitor from Phenol.

where the lability of the active proton can be increased by adding electron-repelling groups such as *tert*-butyl substituents to the aromatic ring. The radical species (A$^{\bullet}$) generated is also resonance stabilised as shown in Scheme 1.4:

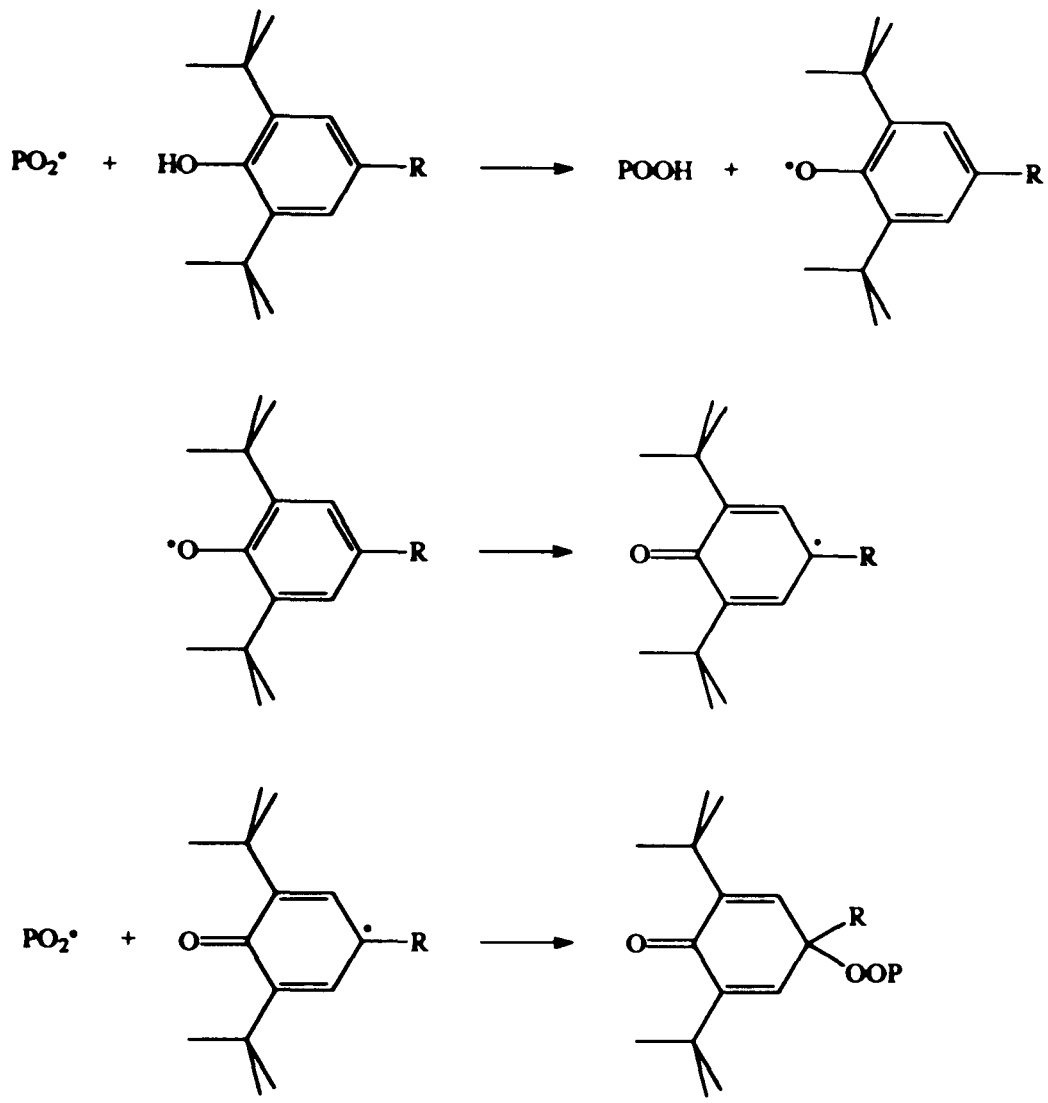

Scheme 1.4.

Stabilisation of a Polymer (POO•) by a Hindered Phenol Antioxidant.

1.2.(b)(ii) Ultraviolet Absorbers. UV-induced degradation can cause discoloration and/or a reduction of the mechanical properties of a polymer and these effects can be less pronounced when a UV-absorber is introduced. Common UV-absorbers include *ortho*-hydroxybenzophenones and *ortho*-hydroxyphenylbenzotriazoles [4] which absorb radiation in the 300-400 nm region of the electromagnetic spectrum and dissipate energy in a harmless manner *via* the material to be protected.

The decomposition of linear polymers often starts with generation of a ketone or aldehyde group, as indicated in Scheme 1.5. The products can be detected by infrared spectroscopy (IR), electron spin spectroscopy or mass spectrometry [4].

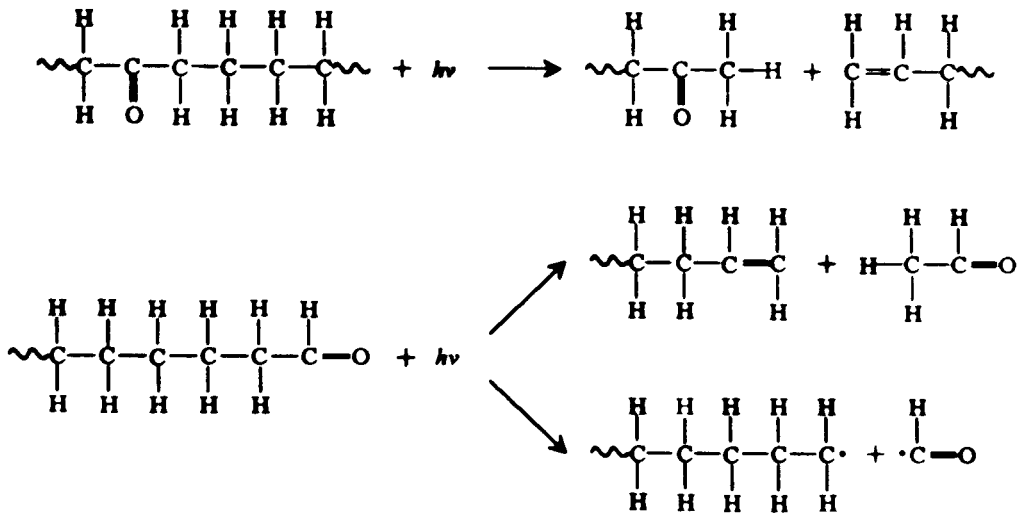

Scheme 1.5.

Equations Showing the Effect of Ultraviolet Irradiation on Linear Polymers.

The most commonly employed UV stabilisers are benzophenones and benzotriazoles which form chelates, enabling energy to be dissipated throughout the entirety of the molecule. The efficiency of the additive is related to the efficiency of the chelating H-bond. The chelation of benzotriazole is shown in Scheme 1.6.

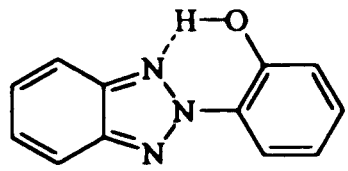

Scheme 1.6.

The Chelation of 2-(Hydroxyphenyl) Benzotriazole.

1.3. Analysis of Polymers.

1.3.(a) *Introduction*. Accurate and thorough polymer characterisation is fundamental as the understanding of relationships between the molecular and bulk properties are essential in following the performance of a polymeric material after preparation and in its working environment. The technique used for characterisation of the material depends on the level of information required.

The macroscopic properties of a polymeric material are typically determined directly by techniques such as mechanical testing, rheology [7] and thermal analysis [8]. Thermal analysis [8], scattering techniques and microscopy [9] are often used to generate information about the microscopic properties of a polymer. The performance of a polymeric material is also related to the nature of its surface. Techniques that are employed to analyse surface defects and imperfections include X-ray photoelectron spectroscopy (XPS) [10] and secondary ion mass spectrometry (SIMS) [11].

Knowledge of the average molecular weight of a polymer is very important as a variation in this mean value can affect the physical properties of the material. Two common measurements of the average molecular weight of a polymer are the number-average molecular weight, M_n, and the weight-average molecular weight, M_w [12]. The number-average molecular weight is defined as:

$$\overline{M}_n = \frac{\Sigma n_i M_i}{\Sigma n_i} \qquad \text{(Equation 1.1)}$$

where the number of molecules of molecular weight M_i is denoted n_i, the total weight of the sample is $\Sigma n_i M_i$ and the total number of molecules in the sample is Σn_i. Osmometry, end group titrimetry and spectroscopy (typically nuclear magnetic resonance (NMR) spectroscopy) are the traditional methods of measuring the number-average molecular weight of a polymer. Low molecular weight impurities can distort the values yielded by these techniques.

The weight-average molecular weight (M_w) is defined as:

$$\overline{M}_w = \frac{\Sigma M_i^2 n_i}{\Sigma M_i n_i} \qquad \text{(Equation 1.2.)}$$

and can be measured by light scattering experiments [12]. Light scattering techniques are based upon the measurement of elastically (Rayleigh) scattered light resulting from the interaction of radiation with polymer molecules and can give accurate values for M_w up to approximately 5 Megadaltons (MDa) in favourable cases. The values obtained are not absolute, however, as a constant related to the molecular shape is required in calculations for M_w. A commonly employed light scattering technique is low-angle laser light scattering (LALLS).

Viscometry is a low cost technique that generates mean molecular weight values (M_v) which typically fall between M_n and M_w. It is possible to analyse polymers of any molecular weight but the technique does not yield absolute values of the mean molecular weight.

Gel permeation chromatography (GPC), a form of size exclusion chromatography (SEC) as the constituents of the polymer are eluted from a column in order of decreasing size, is superior to the techniques previously mentioned in that the data generated can be converted to give a full mass distribution for a polymer. At present, GPC is the most commonly used technique for yielding M_n and M_w values for polymers. Advantages of GPC include the low cost of equipment and the high working molecular weight range. Polymers with average molecular weights of up to 1 MDa may be analysed by GPC and the additives present in blends may also be characterised. The main disadvantages of GPC are that the data generated are very

dependent on the molecular shape, which can be altered substantially when the end group is altered in low molecular weight polymers and also relies heavily on the calibration curve used [13]. Calibration compounds are not available for many polymers.

The determination of molecular structure of polymeric materials includes the characterisation of individual chains. Included in this are tacticity, conformational isomerism, end group information, monomer sequence distribution, chain branching and minor structural defects of polymer chains. Spectroscopic techniques excel in this area of polymer characterisation.

The chemical composition of polymers is traditionally determined by means of NMR [14,15] and infrared (IR) [16] spectroscopy. NMR is the most commonly employed technique for the determination of molecular structure of synthetic polymers. It is often used to name the type of polymer, determine the composition and conformation and also to find any irregularities such as branching and end groups [15]. The methods that are typically used are ^{1}H and ^{13}C NMR but the low sensitivity of the latter means that long acquisition times are often necessary [14]. IR is commonly employed for quality control testing and its advantages over NMR include: low instrument costs, ease of operation, the simple achievement of low measurement error and the short time-scale of analysis. IR spectra are often complicated by peaks arising from additives present in the blend but can aid polymer identification and indicate molecular structure and average copolymer composition.

One advantage that mass spectrometry has over all of these techniques is its ability to generate absolute mass data giving accurate masses and intensities of particular oligomers. This is advantageous in that it gives the potential for the determination of both accurate mass envelopes of polymers and end group information.

1.3.(b) Analysis of Polymer Additives. Most methods of analysis of organic additives require prior separation from the polymer matrix [17,18]. Liquid chromatography (LC) [19,20] and gas chromatography (GC) [21,22,23,24] are common separation techniques and may also be employed as the method of identification of the separate components when coupled to a suitable detection system. Analysis is commonly carried out by means of UV spectroscopy [21,22,23], IR spectroscopy [21,22,23,25, 26] and mass spectrometry [27].

Analysis of the components of polymer blends has become more difficult due to the increasing complexity of the mixtures. The use of less labile, higher molecular weight organic additives in polymer mixtures has reduced the applicability of some of the traditional methods of analysis for these compounds, especially that of *in situ* techniques. The relatively high mass range that is accessible by means of mass spectrometry, especially when desorption/ionisation or spray ionisation techniques are employed, may be beneficial in enabling the analysis of complex additive mixtures to be carried out.

1.4. Mass Spectrometry of Polymeric Materials.

1.4.(a) Mass Spectrometry of Polymers. Direct analysis of synthetic polymers by mass spectrometry is problematical due to the involatility and high molecular weight of many systems. Pretreatment, by chemical [28] or thermal means [29], of polymers before analysis has provided the traditional answer to this problem, thus generating ions of a suitable mass-to-charge ratio for mass spectrometry. Thermal analysis is the most common method of pretreatment. Scheme 1.7 represents the various pathways employed for the mass spectrometric analysis of polymeric formulations.

Polymers that are subjected to thermal stresses can undergo partial degradation or complete pyrolysis. Fragments induced by thermal treatment can be analysed by direct injection into a mass spectrometer [30,31,32,33,34,35,36,37,38,39], after prior separation by gas chromatography (GC-MS) [40,41,42], or they can be trapped before examination occurs [43]. Direct pyrolysis-mass spectrometry (py-MS) is advantageous in that the experimental time-scale is short allowing the detection of reactive thermal degradation products [13]. Furthermore, the mass range is increased when suitable ionisation techniques such as field ionisation (py-FI) [44,45,46,47,48,49,50,51,52,53,54,55] are utilised to analyse higher mass pyrolyzates. The degradation mechanisms of polymers undergoing thermal treatment are dependent on type [13].

The spectra generated by means of LSIMS-MS, EI-MS and CI-MS do not, in general, yield average molecular weight information of polymers as a consequence of the

Scheme 1.7.

Polymer Analysis by Means of Mass Spectrometry.

fragmentation observed and the low efficiency of ionisation of species with higher RMM values but the composition and microstructure of copolymers may be indicated by statistical analysis of the data [56,57,58,59,60,61,62,63,64]. The information obtained may also be used to complement that derived from NMR spectroscopy [64].

The direct analysis of polymer formulations by mass spectrometry has become more facile in recent years with advances in ionisation techniques. The development of MALDI [65,66] and ESI [67] has enabled the analysis of polymers with molecular weights of above 250 kDa to be accomplished.

Previously, FD was the most commonly employed ionisation technique for direct average mass measurements of polymers [68]. The mass limit of FD-MS is approximately 15 kDa since this is the upper mass limit of the mass analysers normally used in conjunction with FD. FD is most appropriate for analysis of aromatic polymers such as polystyrene (PS) [69,70] but has found applications in the analysis of many other systems such as polybutadiene [71] and polyethylene [72]. Thermal degradation is observed in some polymers, such as polyethylene glycol (PEG), above approximately 5 kDa and therefore the mass envelopes obtained can be inaccurate.

ESI has generated ions from polymers with molecular weights up to and above 5 MDa [73]. Even though ESI has routinely been employed to study biopolymers of up to and above 1 MDa, the study of synthetic polymers by this ionisation technique has been hampered by their lack of acidic or basic functional groups. Generation of multiply charged ions is therefore not facile. Furthermore, the nature of polymers, often having

a large number of different oligomers, complicates the assignment of multiply charged ions. Attention has centred on systems with an average molecular weight of less than 5000 Da [74,75,76,77,78,79] due to the limitations in mass range of the instrumentation normally employed with ESI.

Laser desorption has been used for the analysis of polymers for over a decade with variable success [80,81,82,83,84,85,86] but the advances in MALDI have generated a major increase in interest in the mass spectrometry of polymeric materials in the last three years [87,88,89,90,91,92,93,94,95,96,97,98,99,100,101] and systems such as polyglycols [87,79,97], PS [92,101], and PMMA [90,101] have been studied. Comparisons with GPC have been made and the agreement has often been found to be good [90,101], but recently it has been observed that MALDI can have limitations in the analysis of samples with high polydispersity values [99]. The discrepancies between the average molecular weights obtained by GPC and MALDI for polydisperse samples could be due to the difference in scale used for displaying the data and more importantly, the definition of the average molecular weight calculated.

There have been very few reports on the application of MS/MS for the determination of the structure of polymeric materials [102,103] as a consequence of the low ion currents that are often generated by these compounds. The developments in ionisation techniques and instrumentation over the past decade, especially in desorption/ionisation techniques and tandem mass spectrometers which are typically employed for MS/MS experiments, have generated the potential for an increase in the applicability of MS/MS for the structural characterisation of synthetic polymeric

systems. In the present work, spectra of polymers yielding average molecular mass data have been obtained by MALDI-MS. MS/MS has been employed in this work to aid end group determination and generate information on the molecular structure of intact and thermally degraded low molecular weight polymers.

1.4.(b) Mass Spectrometric Characterisation of Polymer Additives. Interest in the mass spectrometric analysis of polymer additives has increased in the last decade [19,54,104,105,106,107,108,109,110,111,112,113,114,115,116,117,118,119], especially with the developments in soft ionisation techniques such as fast atom bombardment (FAB) [108,109,110,111] and laser desorption (LD) [111,113,114,115]. These techniques are more useful for the detection of non-volatile, sometimes oligomeric, polymer additives which are now often used in polymer blends. Analysis by means of traditional mass spectrometric ionisation techniques such as EI [19, 105, 108] and CI [106,107,108] requires the analyte to be thermally labile.

Few reports have been published on the quantitative analysis of polymer additives by means of mass spectrometry [68]. Furthermore, the application of MS/MS to the structural characterisation of polymer additives is far from widespread even though intense ion currents are often generated for these organic polymer additives by many ionisation techniques. In the present work, a five component mixture of additives commonly employed in polymer blends has been analysed by mass spectrometry and tandem mass spectrometry, yielding a protocol for characterising an unknown mixture of polymer additives and a better understanding of the fragmentation pathways of these types of molecules.

1 J. J. Thomson, *Rays of Positive Electricity*, Longmans, Green and Co., London (1913).

2 A. O. Nier, *Rev. Sci. Instrum.*, **18**, 398 (1947).

3 R. J. Young and P. A. Lovell, *Introduction to Polymers*, Chapman and Hill, London (1991).

4 R. B. Seymour, *Introduction to Polymer Chemistry*, McGraw-Hill, New York (1971).

5 W. O. Lundberg (Ed.), *Autoxidation and Antioxidants, Vol. I*, Interscience, New York (1961).

6 H. F. Mark, N. C. Gaylord and N. M. Bikales (Eds.), *Encyclopedia of Polymer Science and Technology, Vol. II*, Interscience, New York (1965).

7 M. Flanagan, *Polymer Characterisation* (Eds., B. J. Hunt and M. I. James), Blackie Academic and Professional, Chapman and Hall, Glasgow, Chapter 9 (1993).

8 R. E. Whetton, *Polymer Characterisation* (Eds., B. J. Hunt and M. I. James), Blackie Academic and Professional, Chapman and Hall, Glasgow, Chapter 7 (1993).

9 A. S. Vaughan, *Polymer Characterisation* (Eds., B. J. Hunt and M. I. James), Blackie Academic and Professional, Chapman and Hall, Glasgow, Chapter 10 (1993).

10 D. Briggs and M. P. Sean (Eds.), *Practical Surface Analysis, Vol. 1*, Wiley (1990).

11 D. Briggs, A. Brown and J. C. Vickerman, *Handbook of Static SIMS*, John Wiley and Sons (1986).

12 F. Beuche, *Physical Properties of Polymers*, Wiley, New York (1962).

13 J. H. Scrivens, *Proceedings of the 13th International Conference on Mass Spectrometry*, Budapest (1994).

14 P. A. Mirau, *Polymer Characterisation* (Eds., B. J. Hunt and M. I. James), Blackie Academic and Professional, Chapman and Hall, Glasgow, Chapter 3 (1993).

15 A. Bunn, *NMR Basic Principles and Progress*, Vol. 29, Springer-Verlag, Berlin, Heidelberg (1993).

16 J. M. Chalmers and N. J. Everall, *Polymer Characterisation* (Eds., B. J. Hunt and M. I. James), Blackie Academic and Professional, Chapman and Hall, Glasgow, Chapter 4 (1993).

17 D. C. M. Squirrell, *Analyst*, **106**, 1042 (1981).

18 D. Braun and E. Bezdadea, *Angew. Makromol. Chem.*, **113**, 77 (1983).

19 A. M. Wims and S. J. Swarin, *J. Appl. Polym. Sci.*, **19**, 1243 (1975).

20 D. Munteanu, A. Isfan, C. Isfan and I. Tincul, *Chromatographia*, **23**, 7 (1987).

21 D. A. Wheeler, *Talanta*, **15**, 1315 (1968).

22 T. R. Crompton, *Chemical Analysis of Additives in Plastics, 2nd Ed.*, Pergamon Press, Oxford (1977).

23 D. O. Hummel and F. Scholl, *Atlas der Polymer- und Kuntststoffanalyse, Vol. 3, 2nd Ed.*, Carl Hanser Verlag und Verlag Chemie, Munich (1981).

24 P. A. D. T. Vimalasiri, J. K. Haken and R. P Burford, *J. Chromatogr.*, **300**, 303 (1984).

25 C. Guiochon and J. Henniker, *Br. Plast.*, **37**, 74 (1964).

26 W. C. Wake, B. K. Tidd and M. J. R. Loadman, *Analysis of Rubber and Rubber-Like Polymers, 3rd Ed.*, Applied Science Publishers, London (1983).

27 J. D. Vargo and K. L. Olson, *Anal. Chem.*, **57**, 672 (1985).

28 G. Montaudo, E. Scamporrino and D. Vitalini, *Macromolecules*, **22**, 627 (1989).

29 J. J. Boon, *Int. J. Mass Spectrom. Ion Proc.*, **118**, 755 (1992).

30 G. Montaudo, C. Puglisi, E. Scamporrino and D. Vitalini, *Macromolecules*, **19**, 870 (1986).

31 G. Montaudo, C. Puglisi, E. Scamporrino and D. Viatalini, *Macromolecules*, **19**, 2157 (1986).

32 S. Foti, P. Maravigna and G. Montaudo, *Macromolecules*, **15**, 883 (1982).

33 A. Ballistreri, D. Garozzo, M. Giuffrida, P. Maravigna and G. Montaudo, *Macromolecules*, **19**, 2693 (1986).

34 A. Ballistreri, D. Garozzo and G. Montaudo, *Macromolecules*, **17**, 1312 (1984).

35 A. Ballistreri, G. Montaudo and R. W. Lenz, *Macromolecules*, **17**, 1848 (1984).

36 G. Montaudo, C. Puglisi and F. Samperi, *Polym. Degrad. Stab.*, **31**, 291 (1991).

37 G. Montaudo, E. Scamporrino, C. Puglisi and D. Vitalini, *J. Polym. Sci. Part A: Polym. Chem.*, **25**, 475 (1987).

38 M. M. Fares, J. Hacaloglu and S. Suzer, *Eur. Polym. J.*, **30**, 845, (1994).

39 M. M. Fares, T. Yalcin, J. Hacaloglu, A. Gungor and S. Suzer, *Analyst*, **119**, 693 (1994).

40 V. G. Zaikin, R. G. Mardanov, V. I. Kleiner, B. A. Krentsel and B. N. Bobrov, *J. Anal. Appl. Pyrolysis*, **26**, 185 (1993).

41 M. M. Shapi, *Spectrosc. Int.*, **3**, 28 (1901).

42 V. P. Senthil, *J. Anal. Appl. Pyrolysis*, **21**, 163 (1991).

43 T. G. Blease, G. A. Paterson and J. H. Scrivens, *Brit. Polym. J.*, **21**, 37 (1989).

44 H.-R. Schulten, N. Simmleit and R. Muller, *Anal. Chem.*, **59**, 2903 (1987).

45 H.-R. Schulten, B. Plage, H. Ohtani and S. Tsuge, *Die Ang. Makromol. Chem.*, **155**, 1 (1987).

46 H.-R. Schulten, B. Plage, *J. Polym. Sci. Part A: Polym. Chem.*, **26**, 2381 (1988).

47 B. Plage and H.-R. Schulten, *J. Anal. Appl. Pyrolysis*, **15**, 197 (1989).

48 B. Plage and H.-R. Schulten, *Macromolecules*, **23**, 2642 (1990).

49 B. Plage and H.-R. Schulten, *Macromolecules*, **21**, 2018 (1988).

50 H. Ohtani, T. Yuyama, S. Tsuge, B. Plage and H.-R. Schulten, *Eur. Polym. J.*, **26**, 893 (1990).

51 B. Plage and H.-R. Schulten, *Die Ang. Makromol. Chem.*, **184**, 133 (1991).

52 B. Plage, H.-R. Schulten, H. Ringsdorf and A. Schuster, *Makromol. Chem.*, **192**, 1567 (1991).

53 B. Plage and H.-R. Schulten, *J. Anal. Appl. Pyrolysis*, **19**, 285 (1991).

54 R. P. Lattimer, *J. Anal. Appl. Pyrolysis*, **26**, 65 (1993).

55 R. P. Lattimer, *J. Anal. Appl. Pyrolysis*, **31**, 203 (1995).

56 G. Montaudo, *Rapid Commmun. Mass Spectrom.*, **5**, 95 (1991).

57 M. S. Montaudo and G. Montaudo, *Macromolecules*, **25**, 4264 (1992).

58 G. Montaudo, M. S. Montaudo, E. Scamporrino and D. Vitalini, *Macromolecules*, **25**, 5099 (1992).

59 M. S. Montaudo and G. Montaudo, *Makromol. Chem.-Macromol. Symp.*, **65**, 269 (1993).

60 G. Montaudo, M. S. Montaudo, E. Scamporrino and D. Vitalini, *Makromol. Chem.-Macromol. Chem. Phys.*, **194**, 993 (1993).

61 M. S. Montaudo, *Macromolecules*, **26**, 2451 (1993).

62 M. S. Montaudo, *Makromol. Chem.-Theo. Simul.*, **2**, 735 (1993).

63 G. Montaudo, M. S. Montaudo, *J. Macromol. Sci.-Pure Appl. Chem.*, **A31**, 1053 (1994).

64 G. Montaudo, M. S. Montaudo, C. Puglisi and F. Samperi, *Macromol. Chem. Phys.*, **196**, 499 (1995).

65 M. Karas, U. Bahr and F. Hillenkamp, *Int. J. Mass Spectrom. Ion Proc.*, **78**, 53 (1987).

66 K. Tanaka, H. Waki, Y. Ido, S. Akita, Y. Yoshida and T. Yoshida, *Rapid Commun. Mass Spectrom.*, **2**, 151 (1988).

67 J. B. Fenn, M. Mann, C. K. Wong and C. M. Whitehouse, *Science*, **246**, 64 (1989).

68 R. P. Lattimer and H.-R. Schulten, *Mass Spectrom. Rev.*, **3**, 231 (1984).

69 T. Matsuo, H. Matsuda and I. Katakuse, *Anal. Chem.*, **51**, 1329 (1979).

70 K. Rollins, J. H. Scrivens, M. J. Taylor and H. Major, *Rapid Commun. Mass Spectrom.*, **4**, 355 (1990).

71 A. G. Craig, P. G. Cullis and P. J. Derrick, *Int. J. Mass Spectrom. Ion Phys.*, **38**, 297 (1981).

72 R. P. Lattimer and H.-R. Schulten, *Int. J. Mass Spectrom. Ion Phys.*, **52**, 105 (1983).

73 T. Nohmi and J. B. Fenn, *J. Am. Chem. Soc.*, **114**, 3241 (1992).

74 C. N. McEwen, B. S. Larsen and W. J. Simonsick, *Proceedings of 42nd ASMS Conference on Mass Spectrometry and Allied Topics*, May 29-June 3, Chicago, Illinois, 317 (1994).

75 S. Corless, L. W. Tetler, V. Parr and D. Wood, *Proceedings of 42nd ASMS Conference on Mass Spectrometry and Allied Topics*, May 29-June 3, Chicago, Illinois, 515 (1994).

76 C. B. Jacoby, D. A. Weil and R. L. Cerny, *Proceedings of 42nd ASMS Conference on Mass Spectrometry and Allied Topics*, May 29-June 3, Chicago, Illinois, 516 (1994).

77 L.-S. Sheng, B. E. Winger and J. E. Campana, *Proceedings of 42nd ASMS Conference on Mass Spectrometry and Allied Topics*, May 29-June 3, Chicago, Illinois, 517 (1994).

78 R. B. Cody and J. W. Finch, *Proceedings of 42nd ASMS Conference on Mass Spectrometry and Allied Topics*, May 29-June 3, Chicago, Illinois, 522 (1994).

79 J. E. Campana, L.-S. Sheng, S. L. Shew and B. E. Winger, *Trac/Trends Anal. Chem.*, **13**, 239 (1994).

80 R. J. Cotter, J. P. Honowich, J. K. Olthoff and R. P. Lattimer, *Macromolecules*, **19**, 2996 (1986).

81 C. F. Ijames and C. L. Wilkins, *J. Am. Chem. Soc.*, **110**, 2687 (1988).

82 L. M. Nuwaysir and C. L. Wilkins, *Anal. Chem.*, **60**, 279 (1988).

83 L. M. Nuwaysir, C. L. Wilkins and W. J. Simonsick, Jr., *J. Am. Chem. Soc.*, **112**, 66 (1990).

84 J. D. Hogan and D. A. Laude, Jr., *Anal. Chem.*, **64**, 763 (1992).

85 C. F. Lienes and R. M. O'Malley, *Rapid Commun. Mass Spectrom.*, **6**, 564 (1992).

86 M. S. Kahr and C. L. Wilkins, *J. Am. Soc. Mass Spectrom.*, **4**, 453 (1993).

87 U. Bahr, A. Deppe, M. Karas, F. Hillenkamp and U. Giessmann, *Anal. Chem.*, **64**, 2866 (1992).

88 P. O. Danis, D. E. Karr, F. Meyer, A. Halle and C. H. Watson, *Org. Mass Spectrom.*, **27**, 843 (1992).

89 J. A. Castro, C. Köster and C. L. Wilkins, *Rapid Commun. Mass Spectrom.*, **6**, 239 (1992).

90 P. O. Danis and D. E. Karr, *Org. Mass Spectrom.*, **28**, 923 (1993).

91 G. Montaudo, M. S. Montaudo, C.Puglisi and F. Samperi, *Rapid Commun. Mass Spectrom.*, **8**, 981 (1994).

92 G. Montaudo, M. S. Montaudo, C.Puglisi and F. Samperi, *Rapid Commun. Mass Spectrom.*, **8**, 1011 (1994).

93 G. Montaudo, M. S. Montaudo, C.Puglisi and F. Samperi, *Anal. Chem.*, **66**, 4366 (1994).

94 M. Eggert and R. Freitag, *J. Polym. Sci. Part A: Polym. Chem.*, **32**, 803 (1994).

95 R. Freitag, T. Baltes and M. Eggert, *J. Polym. Sci. Part A: Polym. Chem.*, **32**, 3019 (1994).

96 L.-S. Sheng, J. E. Corey, S. L. Shew, B. E. Winger and J. E. Campana, *Rapid Commun. Mass Spectrom.*, **8**, 498 (1994).

97 M. Dey, J. A. Castoro and C. L. Wilkins, *Anal. Chem.*, **67**, 1575 (1995).

98 P. O. Danis, D. E. Karr, W. J. Simonsick and D. T. Wu, *Macromolecules*, **28**, 1229 (1995).

99 M. Montaudo, *Rapid Commun. Mass Spectrom.*, **9**, 453 (1995).

100 H. Pasch and K. Rode, *J. Chromatog.*, **699**, 21 (1995).

101 P. Lloyd, K. G. Suddaby, J. E. Varney, E. Scrivener, P. J. Derrick and D. Haddleton, *Eur. Mass Spectrom.*, **1**, 293 (1995).

102 A. G. Craig and P. J. Derrick, *Aust. J. Chem.*, **39**, 1421 (1986).

103 R. P. Lattimer, *J. Am. Soc. Mass Spectrom.*, **5**, 1072 (1994).

104 R. P. Lattimer and R. E. Harris, *Mass Spectrom. Rev.*, **4**, 369 (1985).

105 J. Lehotay, J. Danecek, O. Líska, J. Lesko and E. Brandsteterová, *J. Appl. Poly. Science*, **25**, 1943 (1980).

106 P. Rudewicz and B. Munson, *Anal. Chem.*, **58**, 358 (1986).

107 R. P. Lattimer, R. E. Harris, C. K. Rhee and H.-R. Schulten, *Anal. Chem.*, **58**, 3188 (1986).

108 T. L. Riley, T. J. Prater, J. L. Gerlock, J. E. deVries and D.. Schuetzle, *Anal. Chem.*, **56**, 2145 (1984).

109 R. P. Lattimer, R. E. Harris, D. B. Ross and H. E. Diem, *Rubber Chem. Technol.*, **57**, 1013 (1984).

110 C. L. Johlman, C. L. Wilkins, J. D. Hogan, T. L. Donovan, D. A. Laude, Jr. and M.-J. Youssefi, *Anal. Chem.*, **62**, 1167 (1990).

111 J. O. Lay and B. J. Miller, *Anal. Chem.*, **59**, 1323A (1987).

112 A. T. Hsu and A. G. Marshall, *Anal. Chem.*, **60**, 932 (1988).

113 B. Asamato, J. R. Young and R. J. Citerin, *Anal. Chem.*, **62**, 61 (1990).

114 J. E. Hunt, K. R. Lykke and M. J. Pellin in *Methods and Mechanisms for Producing Ions from Large Molecules* (K. G. Standing, Ed.), Plenum Press, New York (1991).

115 M. P. Mawn, R. W. Linton, S. R. Bryan, B. Hagenhoff, U. Jürgens and A. Benninghoven, *J. Vac. Sci. Technol.*, **A9**, 1307 (1991).

116 M. P. Mawn, A. M. Belu, R. W. Linton and A. Benninghoven, *Proceedings of 40th Annual Conference on Mass Spectrometry and Allied Topics*, Washington, DC, ASMS, 295 (1992).

117 R. P. Lattimer, *Rubber Chem. Technol.*, **61**, 658 (1988).

118 R. P. Lattimer, H. Muenster and H. Budzikiewicz, *Rubber Chem. Technol.*, **63**, 298 (1990).

119 S. W. Chen and G. R. Her, *Appl. Spectrosc.*, **47**, 844 (1993).

CHAPTER 2.

SAMPLE INTRODUCTION AND IONISATION TECHNIQUES.

2.1. Introduction.

This chapter introduces some of the methods of sample introduction and ionisation commonly employed in modern mass spectrometers. Particular emphasis will be given to those ionisation techniques used in these experiments.

The ionisation technique employed depends to a certain extent on the method of introduction of the analyte into the mass spectrometer. Volatile samples may be introduced as a solid or liquid on a variable temperature probe, a heatable septum inlet or as effluent from a gas chromatograph (GC). Introduction of thermally labile, involatile samples is typically by means of a direct insertion probe or as the outflow of a liquid chromatograph (LC).

2.2. Electron Impact.

The electron impact (EI) source, developed by Nier [1] after its conception by Dempster in 1921 [2], is still the most commonly used in mass spectrometry. The sample is introduced into the source as a vapour at reduced pressure ($< 10^{-4}$ Torr) and ionised by a beam of high energy electrons. A schematic of a typical EI ion source is shown in Figure 2.1.

The filament, when electrically heated, emits electrons which are accelerated towards the source, normally by a voltage of 70 V. At this voltage small variations do not greatly affect the total and relative ion abundances, as indicated in Figure 2.2, a typical

plot of ion current *versus* electron energy. Some electrons pass through a small slit into the ionisation region and most interact with the sample vapour, those remaining hitting the trap electrode (Figure 2.1). The electron beam is constrained to a tight, helical path by a small magnetic field which is generated by the source magnet and a constant electron current is maintained by a feedback circuit between the filament power supply and trap electrode. A repeller electrode aids the ejection of ions from the source, partially assisted by the field penetration arising from the accelerating voltage.

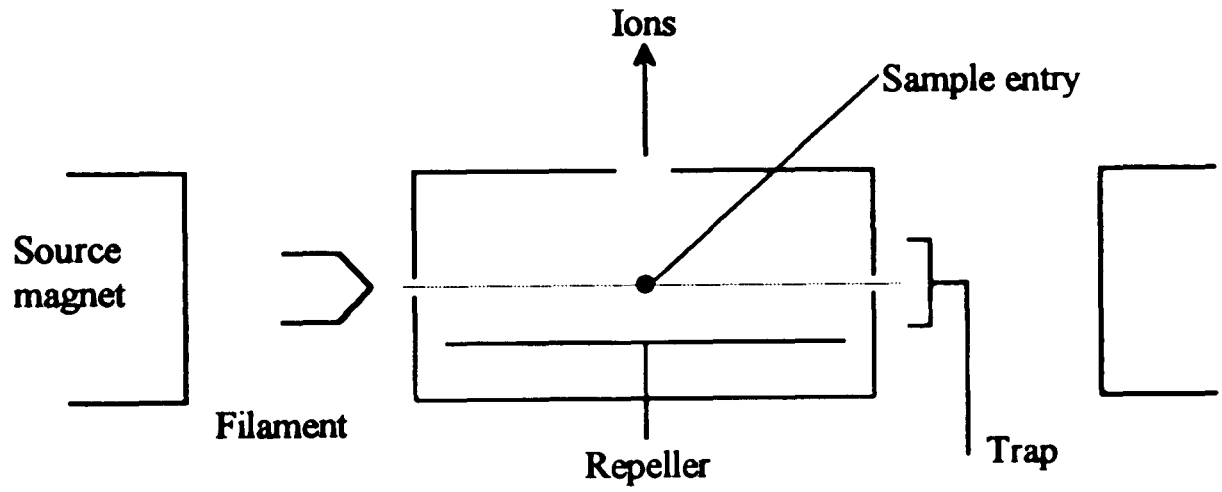

Figure 2.1.
Schematic Diagram of an Electron Impact Source.

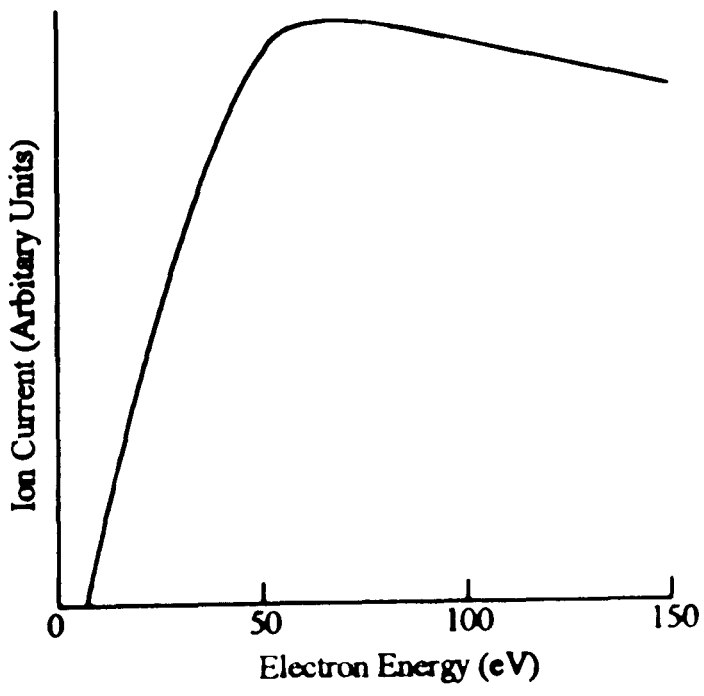

Figure 2.2.
Plot of Ion Current Versus Electron Energy.

The EI source is heated to reduce contamination by sample molecules that may lower the sensitivity and shorten the lifetime of the filament. The source chamber is continuously pumped so as to minimise the re-entry of analyte into the ionisation region and to reduce the occurrence of ion-molecule reactions. The high compatability of GC with EI ionisation is partially due to the short half-life of molecules in the source, a consequence of the maintenance of low pressure conditions.

The two main processes that occur when an electron interacts with a sample molecule are ionisation and dissociative ionisation, as indicated by Equation 2.1.

$$M + e \rightarrow M^{+\bullet} + 2e \rightarrow A^{+} + B^{\bullet} \rightarrow C^{+} + D \qquad \text{(Equation 2.1.)}$$

The energy required to remove an electron from the highest occupied molecular orbital of an organic molecule is approximately 7-11 eV and the EI ionisation process results in the transfer of several electronvolts to the analyte. The molecular ion formed is typically the radical cation, $M^{+\bullet}$, which may dissociate by the loss of radicals ($B^{\bullet}$) and/or neutrals (D) to give fragment ions (C^{+}, D^{+}) in accordance with the even electron rule. Further discussion on the dissociation of ions is given in Chapter 4.

2.3. Chemical Ionisation.

The molecular ion is not observed in the EI spectra of some organic molecules if the dissociation pathways to generate fragment ions are very facile and therefore the relative molecular mass (RMM) cannot be determined. Chemical ionisation (CI) [3], which is a 'soft' ionisation technique in that it generates predominantly protonated

molecule (MH^+) ions with little fragmentation observed, was developed primarily to overcome this problem. Ions characteristic of the analyte are generated by means of ion-molecule reactions with reagent ions in a high pressure source (at approximately 1 Torr). The reagent ions are formed by EI ionisation, typically with electrons having an energy of 150 eV, and by subsequent ion-molecule reactions. These ions are only slightly reactive with the neutral reagent gas molecules but interact readily with the sample which is at a low partial pressure in proportion to the reagent gas (approximately 1:1000).

The most common type of reaction that occurs in CI is protonation of the sample by means of an ion-molecule reaction with the reagent ion to generate an even electron species, typically MH^+. Equation 2.2 is a representation of this process, where BH^+ is the reagent ion and M is the analyte molecule. The proton affinity of the sample must be higher than that of the conjugate base of the reagent ion for the transfer of a proton to occur. Some selected proton affinities of reagent gases are given in Table 2.1.

$$BH^+ + M \rightarrow MH^+ + B \qquad \text{(Equation 2.2)}$$

Conjugate base (B)	Reagent ion	Proton affinity (B) (kJ mol^{-1})
CH_4	CH_5^+	551
$(CH_3)_2CCH_2$‡	$(CH_3)_3C^+$‡	824
NH_3	NH_4^+	854

Table 2.1.

Proton Affinities of Selected CI Reagent Gases.
(‡ The Reagent Ion of *Iso*-butane.)

Association reactions may occur when the proton affinity of the sample is similar to or less than that of the reagent ion and this process is demonstrated by Equation 2.3. This type of reaction commonly occurs in ammonia CI when the proton transfer reaction of Equation 2.2 is endothermic and a $[M+NH_4]^+$ adduct is often formed. Other categories of ion-molecule reactions that can occur under CI conditions are charge exchange, electrophilic addition and anion abstraction.

$$BH^+ + M \rightarrow MBH^+ \qquad \text{(Equation 2.3)}$$

CI experiments are often performed in combined EI/CI sources which can be modified depending on the mode of operation. The high pressure requirement of a CI source means that the dimensions of the source exit slits are much smaller than for EI applications.

2.4. Field Ionisation/Field Desorption.

Ionisation by means of EI and CI requires the analyte to be introduced in the gaseous phase. Thermally labile, involatile samples were not suitable for mass spectrometric analysis before the development of field desorption (FD) by Beckey in 1969 [4] from field ionisation (FI) [5,6]. The analyte is ionised by intense local electric fields in the FD/FI source. These two techniques differ in the method of sample introduction: the sample is deposited and desorbed from an emitter in the FD experiment whereas the sample is introduced as a vapour in FI, typically from a solids probe.

A schematic of the FD/FI source of the ZAB-T four sector mass spectrometer (VG Organic, Manchester, UK) is shown in Figure 2.3. The emitter is typically a tungsten wire of 13 μm diameter which has been treated with pyrolysed benzonitrile to generate carbonaceous dendrites on the surface [7]. Increasing the length and the sharpness of the dendrites generates higher local electric fields at the tips of the microneedles, typically 10^7-10^8 V cm^{-1} compared to the 10^6 V cm^{-1} obtained from untreated wires [8]. The emitter current is carefully increased by electrical heating to generate the ions which are accelerated towards the counter electrode by an electrical potential of typically 13 kV. The quality of the spectra obtained by FD-MS is partially governed by the temperature of the emitter and the rate of the increase in temperature. An emitter current is reached, as the temperature is gradually increased, where intense molecular ion signals are observed with little fragmentation and is termed the best anode temperature (BAT) [9]. The signals generated below the BAT are often weak and unstable. Fast and controlled thermal degradation of complex materials such as synthetic polymers occurs at emitter currents considerably above the BAT.

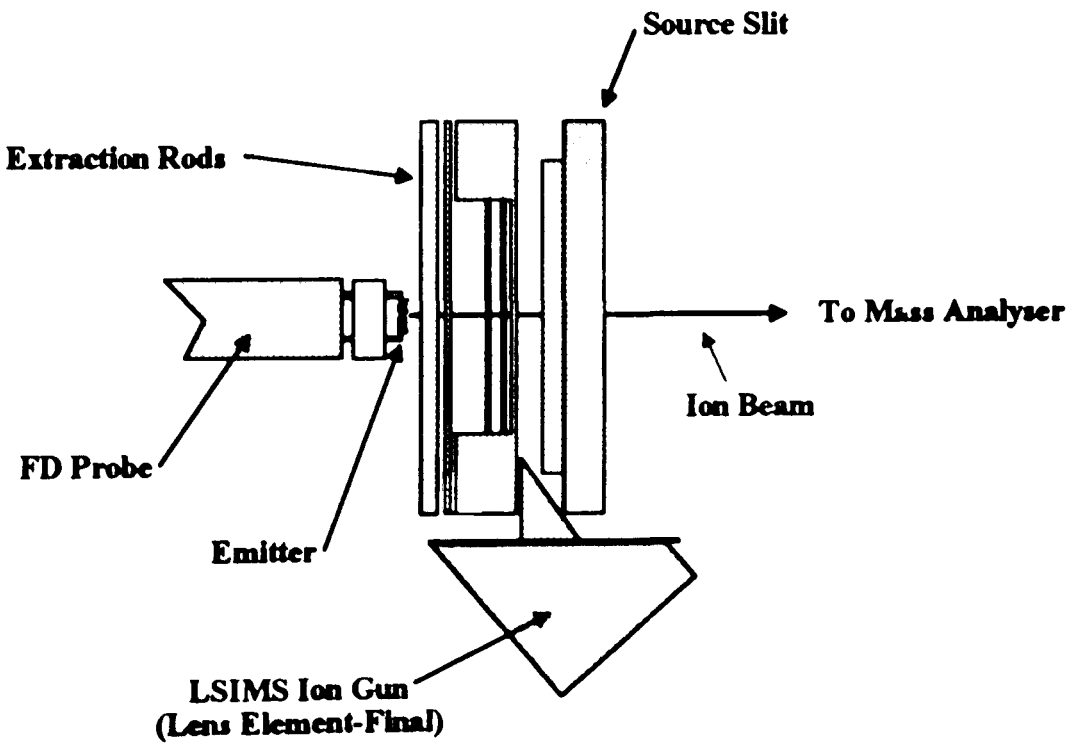

Figure 2.3.

Schematic of the FD Source of the ZAB-T.

The three commonly attributed mechanisms of ionisation in FD are field ionisation [10,11,12], desolvation [13]/ion evaporation [14] and thermal ionisation. The mechanism of ionisation depends on the analyte and the conditions. These processes are summarised in Table 2.2.

Analyte	Molecular Ion Generated	Mechanism of Formation
M, Neutral molecule	$M^{+\bullet}$	FI
	MH^+	FI Desolvation/Ion Evaporation
	$[M+Cat]^+$	Desolvation/Ion Evaporation
Salt (organic or inorganic)	$[C^+A^-]^{+\bullet}$	FI
	C^+; $[C_{n+1}A_n]^+$	Desolvation/Ion Evaporation Thermal Ionisation

Table 2.2.

Ion Formation Mechanisms in FD.

In the field ionisation mechanism the FD sample, which is predominantly located between the microneedles of the emitter, must undergo gas-phase transport by a "hopping motion" (polar, non-volatile molecules) [15] or surface diffusion (volatile compounds) [16] to the tips of the dendrites prior to ionisation by an electron tunneling mechanism. Ionisation is presumed to occur at the tips of the microneedles as approximately 10^7 V cm^{-1} is required for electron tunneling to be initiated. Less sample heating is normally required in the FD experiment compared to FI as the gas-phase transport distance is much shorter in the former and therefore ionisation occurs close to the evaporation zone. Only a small percentage of the sample impinges on the tips of the microneedles with the latter. The field ionisation mechanism is prevalent for non-electrolytic analytes and molecular radical cations ($M^{+\bullet}$) are normally generated. Some basic organic molecules generate protonated molecular ions (MH^+)

[17] and doubly charged ions are occasionally formed from aromatic compounds. Post-ionisation, generating multiply charged ions, may occur as the ions are accelerated from the surface of the emitter by means of further electron tunneling [18,19].

The field induced extraction of ions is proposed to be the most important mechanism for the desorption of thermally unstable, non-volatile molecules to generate MH^+ or $[M+Cat]^+$ species, where Cat is an alkali metal cation [13]. The MH^+ and $[M+Cat]^+$ ions are preformed on the emitter, from salt layers for the generation of alkali metal ion adducts, and may be desorbed at low electric fields (10^6 V cm^{-1}) and high emitter temperatures. These ions may therefore be desorbed from the valleys between the microneedles, which are in relatively low electric field regions compared to the tips, and also from untreated (bare wire) emitters. The first step in the mechanism is the charging of the surface by solvated ions. Stress in the charged layer induced by the electrical potential causes instabilities at the surface and can lead to the emission of charged droplets and clusters. Field enhancing projections may develop and solvent evaporation generates a glassy state from which the electrical potential is strong enough to extract the preformed MH^+ or $[M+Cat]^+$ ions.

The field assisted ion evaporation model is divided into two distinct steps: the accumulation of excess charge at the surface of the analyte and the evaporation of ions from the condensed phase as a consequence of the molecule-molecule or ion-molecule interactions being overcome by the intense local electrical potential [14]. The ions have also been proposed to be desorbed from the tips of field-induced protuberances

as the ion-molecule and molecule-molecule interactions weaken with increasing length of such projections [20].

The desorption of ions by means of a purely thermal process occurs at much higher emitter currents than other mechanisms of field desorption and is restricted to a limited range of materials such as metals and complex salts.

FD-MS found many applications in the biological field before the development of FAB and is currently employed in the analysis of synthetic polymers [21] and complex lubricants [22]. FI is often used to analyse pyrolyzates of polymers [23,24], coal [25] and soil samples [26].

2.5. Fast Atom Bombardment and Liquid Secondary Ion Mass Spectrometry.

Fast atom bombardment (FAB) [27] and liquid secondary ion mass spectrometry (LSIMS) [28] employ a high energy (kiloelectronvolts) primary particle beam to desorb and ionise the analyte which is suspended in a liquid matrix. The FAB technique was developed by Barber et al. [27] from static secondary ion mass spectrometry (static SIMS) [29]. A beam of fast neutral atoms, often xenon or argon, are used in the FAB technique [27] whereas the target is bombarded by a primary ion beam, typically caesium ions (Cs^+), in the LSIMS experiment [28]. Improved sensitivity and ultimate maximum mass are obtained by employing LSIMS over FAB [28] due to the improved collimation and the increased momentum of the caesium ion

beam. A background gas pressure from the fast atom gun can also cause contamination problems and a reduction in operating pressure in the FAB source.

The matrix, typically a viscous liquid such as glycerol or thioglycerol, provides a continuous renewal of the surface giving prolonged intense ion signals. This is not the case in static SIMS where the secondary ion intensity reduces considerably over a short period of time due to surface damage. One drawback of the high matrix concentrations used in the LSIMS and FAB techniques is the appearance of peaks at every mass number due to clusters and fragments of the matrix, sometimes refered to as 'chemical noise'. This phenomenon may be reduced by employing a technique termed continuous-flow FAB (CF-FAB) [30] where the sample is continually pumped to the probe tip in a solution containing only a small proportion of matrix. This technique also reduces the surface effects that are often prevalent in LSIMS and gives improved detection limits.

The mechanism of ion formation in FAB and LSIMS is not completely understood. Impact of the primary particle beam generates a collision cascade which includes ions, radicals and excited neutral species [31] by vibrational excitation [32,33]. The ions observed in the mass spectrum are presumed to be generated predominantly by reactions occuring in the selvedge [34], a high density region just above the bulk matrix and sample [35,36]. These reactions include those between ions and electrons generated in the collision cascade, and preformed ions with desorbed matrix and analyte molecules. These reactions have been compared to those occuring in CI [37].

Figure 2.4 is a schematic diagram of the LSIMS source of the ZAB-T. Caesium ions are evaporated from a heated caesium salt, normally caesium alumina silicate, and accelerated by a gun voltage of 35 kV with an ion current of approximately 1 μA. Collimation of the primary ion beam is enhanced by focus lenses 1 and 2 whose voltages reduce the gun voltage to 90-100 % and 66-89 % respectively of the original value. Secondary ions generated are accelerated from the probe tip by the electrical potential difference (normally 8 kV) between the probe and the source extraction plates.

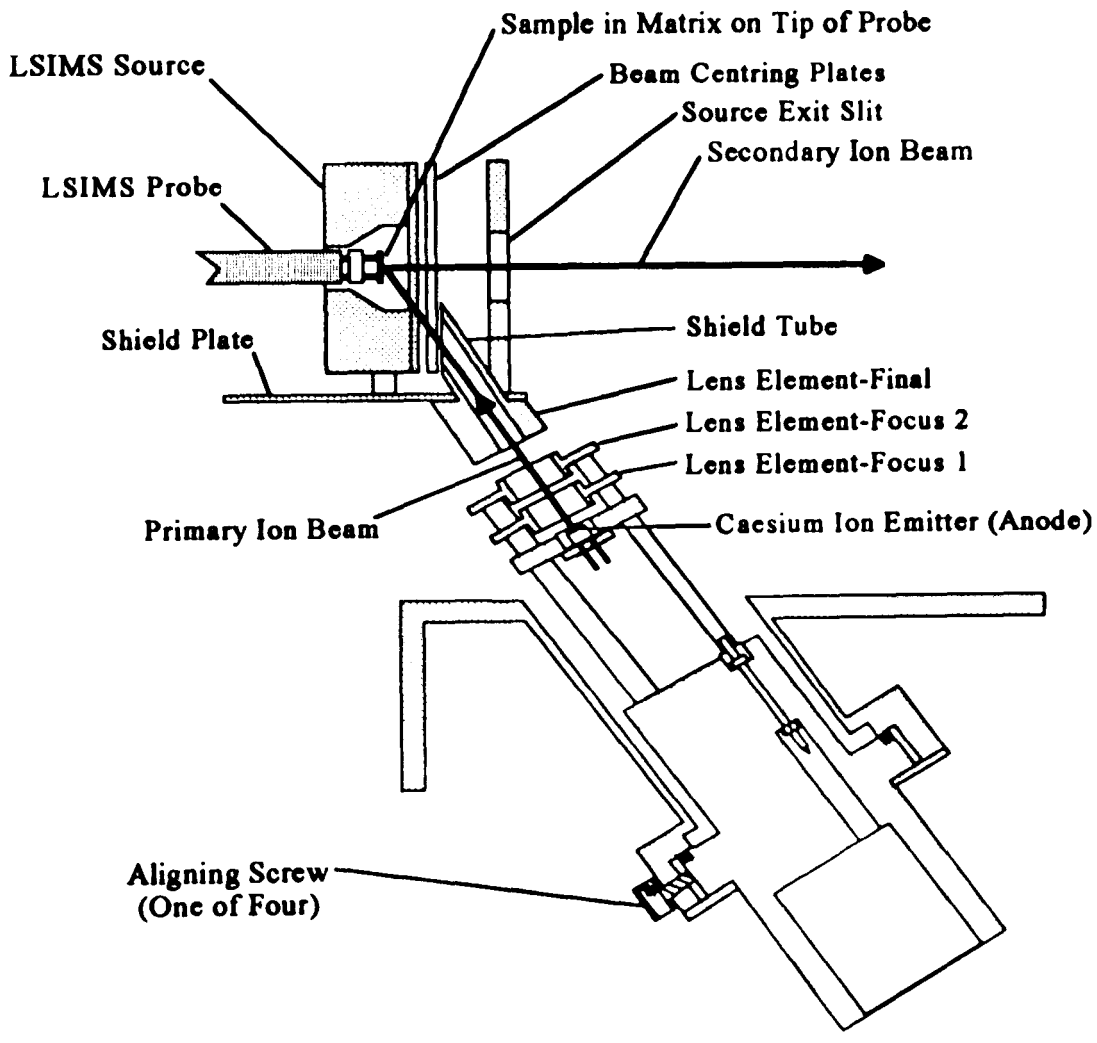

Figure 2.4.
Schematic of the LSIMS Source of the ZAB-T.

The design of the LSIMS source of the Concept II HH four sector mass spectrometer (Kratos Analytical, Manchester, UK) is shown schematically in Figure 2.5. Cs^+ ions are initially accelerated from the caesium pellet by a 5 kV potential and the potential

difference between the ion gun and the probe is normally 7 kV for an accelerating voltage of 8 kV. The typical impact energy of Cs^+ ions on the probe tip is therefore 12 keV with a primary ion current of approximately 1 μA.

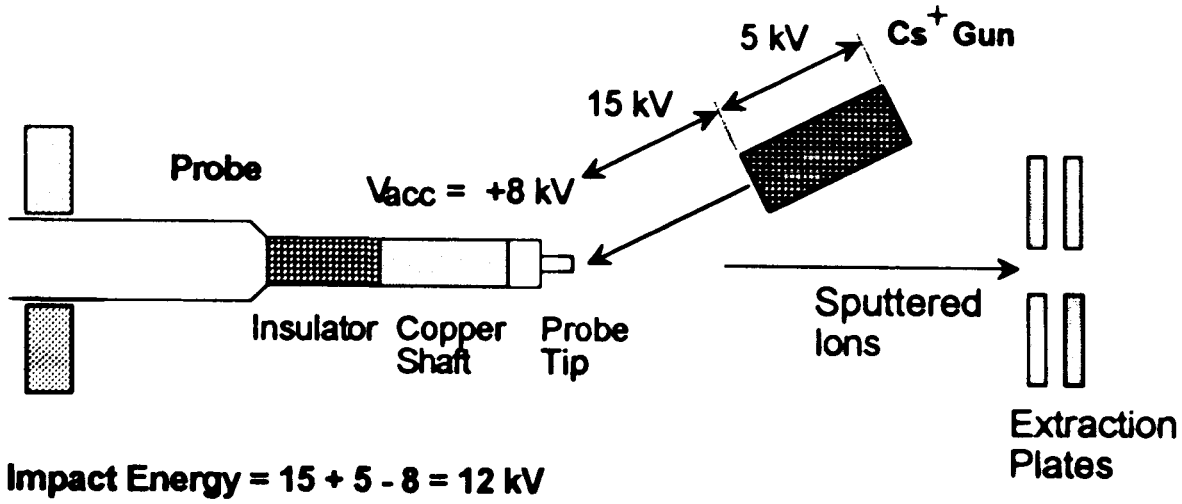

Figure 2.5.

Schematic of the LSIMS Source of the Concept.

2.6. Spray Methods.

A mist of small, charged droplets generated from a solution containing the analyte which break down to form the ions observed in the mass spectrum forms the experimental basis of spray ionisation techniques, of which the two most commonly employed are electrospray (ESI) [38,39] and thermospray (TS) [40]. ESI and TS differ in the method employed for the desorption of droplets from the bulk solution containing the analyte. The solute is thermally desorbed with TS and gas phase ions are generated by a high electric field with ESI.

2.6.(i) Electrospray. A schematic of the electrospray source of the Quattro II tandem quadrupole mass spectrometer (VG Organic, Manchester, UK) is Figure 2.6. The source is approximately at atmospheric pressure and close to ambient temperature in

the ESI experiment. The sample is either the elute of a liquid chromatograph or is injected into the mobile phase which is pumped through the capillary at a rate of typically 1-20 μL min^{-1}. An electrical potential of 2-5 kV is held between the stainless steel spraying capillary and the counter electrode (the Multiple Axial Sampling (MAS™) filter or high voltage lens in Figure 2.6) which are separated by a few millimetres. The liquid emerging from the capillary forms a cone shape, termed a Taylor cone [41], and the charged droplets resulting from ion separation [42], containing both analyte ions and solvent, are ejected from the tip of this cone [43,44]. A bath gas, typically nitrogen, is present to initiate desolvation by maintaining the temperature of the droplets [45]. Furthermore, the bath gas also reduces corona discharge in the source region which can occur at elevated electrical potentials. The addition of a high-velocity coaxial nebulising gas such as nitrogen aids desolvation and this technique is termed ionspray [46].

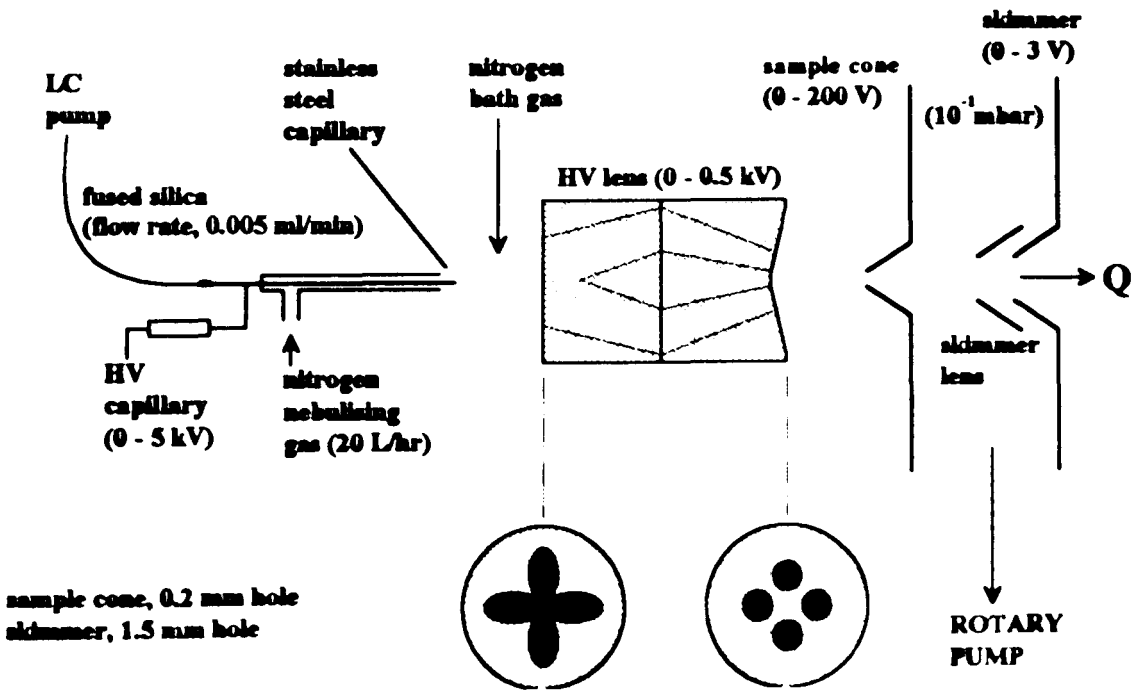

Figure 2.6.

Schematic of the Electrospray Source of the Quattro II.

The desolvated ions migrate towards the cone through the high voltage lens, whose functions include the removal of involatile material which could cause blockages to the cone and is heated to aid further desolvation (Figure 2.6). This filter also serves to focus the ions through the cone aperture (0.2 mm) into the first vacuum stage (approximately 10^{-1} mbar). The sample cone is held at 0-200 V and the value of the potential can effect the distribution of multiple charging [47] and fragmentation [48] observed in the mass spectrum. The dissociation observed at higher values of potential on the cone can result in spectra that are similar to conventional CID spectra [49] and this phenomenon is often referred to as skimmer CID. A percentage of the resulting ion beam passes through the skimmer assembly, consisting of the skimmer lens (typically offset from the skimmer cone by 5 V) and skimmer cone (0-3 V), into the mass analyser (approximately 4×10^{-4} mbar). The skimmer assembly aids the diffusion of solvent molecules away from the mass analyser.

Many theories have been proposed to explain the desolvation of the charged droplets in ESI [38,50,51,52] but the actual mechanism is still not clear. It is unambiguous that ions are initially generated in the liquid phase in ESI, contrasting with the gas-phase ion-molecule reactions that often occur in TS ionisation [53]. Two popular mechanisms are those originally proposed by Dole et al. [38] and promoted by Röllgen [50], often called the charge residue model (CRM) or single ion in droplet theory (SIDT) [54], and a model described by Iribane and Thomson which is commonly termed the atmospheric pressure ion evaporation model (IEM) [51].

The IEM involves the formation of a droplet containing many solute ions. Solvent evaporation increases the coulomb repulsion in the droplet until the forces resulting from the charge are greater than that of surface tension and a 'coulomb explosion' occurs [51]. This is proposed to occur with droplet sizes in the μm range, that is close to the Rayleigh limit [55].

Röllgen has proposed that the gas-phase ions result from the desolvation of very small droplets (nm's) [56] at the Rayleigh limit [55]. The CRM proposes that droplets are generated that contain only one analyte ion and solvent evaporation from the droplet due to instabilities at the surface leads to the formation of a gas phase ion [38,50].

The model described by Fenn et al. is a development of the IEM and attempts to explain the observation of the series of multiply charged ions from large molecules such as proteins and high average molecular weight PEG [52]. The number of charges on a desorbing ion is proposed to be partially determined by the charges on the droplet surface rather than as an analyte adduct. As the droplet size is decreased by solvent evaporation so the net charges available to a desorbing analyte ion is increased and therefore a distribution of charge states is observed as a consequence of the variance in the volume of the droplet from which the ion is desorbed. The charge distribution is also related to the conformation of the analyte, the competition between electrostatic repulsion and bonding energy, the droplet evaporation time, the surface concentration of the species and its desorption free energy [52].

The multiply charged ions that are often observed in the ESI spectra of samples with R.M.M. greater than 1000 Da has enabled the analysis of large biomolecules to be performed. The observed envelope of molecular ions with different charge states often conveniently falls in the mass range of a quadrupole mass spectrometer (up to 4000 Da) and FT-ICR instruments. Proteins with molecular weights above 100 kDa [57] and PEG of 5 MDa [58] have been analysed by means of ESI-MS.

2.7. Laser Desorption/Ionisation.

2.7.(i) Introduction to Laser Techniques. The ionisation of small inorganic [59,60] and organic [60] molecules by means of a laser was first reported by Vastola et al. towards the end of the 1960's. The laser desorption/ionisation (LDI) technique involves the desorption and ionisation of the sample from a metal substrate by means of an infrared (IR) or ultraviolet (UV) laser [61,62]. The desorption process is presumed to occur via direct optical absorption by the sample [63] or heat conduction from the substrate [64] and ionisation of the gas-phase analyte by ion-molecule reactions similar to those of FAB ionisation [37]. The ions observed in IR-LDI spectra are formed predominantly by cationisation of the analyte whereas protonated molecular ions are more readily generated by means of UV-LDI [65]. Interest in the separation of the desorption and ionisation steps arose due to the lack of reproducibility of LDI experiments and the number of gas-phase neutrals generated by desorption which is typically approximately 10^3 times higher than that of the number of ions formed [66,67]. This technique employs separate lasers for the desorption and ionisation and is often termed L^2TOF when used in conjunction with a time-of-flight

(TOF) mass analyser. The ion yields are low due to the losses that arise in the transport process from the desorption region to the point of ionisation [68].

2.7.(ii) Matrix Assisted Laser Desorption/Ionisation. It was observed that the ion yield from LDI was dramatically increased with strongly absorbing analytes [69,70] and as the desorption of these samples requires a much lower photon flux, the process of energy absorption by the substrate is prevented. These observations led to the development of UV-matrix assisted laser desorption/ionisation (UV-MALDI) [71,72], a technique in which the analyte is dissolved in a matrix which is strongly absorbing at the wavelength of the laser employed [73]. The matrix acts as an intermediate in the transfer of energy of the photons from the laser beam to the sample [69,71] and is presumed to separate the analyte molecules in the lattice, therefore limiting aggregation [74].

The original experiments of Tanaka et al. [72] and Hillenkamp and coworkers [71] were quite different. The former used an ultra-fine metal powder (cobalt of approximately 30 nm diameter) dissolved in glycerol as a matrix [72] whereas the sample was suspended in nicotinic acid in the technique of the latter [71]. Most MALDI experiments have since concentrated on the method adopted by Hillenkamp et al. which employs a organic molecule of low molecular weight as the matrix [73]. Most matrices commonly used in MALDI experiments are solids [71,75,76,77] with the exception of *meta*-nitro benzyl alcohol (NBA) [78] which is a viscous liquid. Very little is known about the required properties of a matrix for it to be suitable for MALDI except that it must have a high molar absorption coefficient at the wavelength

of the laser [79]. Most matrices have an aromatic ring and/or carboxylic acid group but this is not an essential property for an intermediate in energy transfer to the analyte [75].

A thermal spike model has been proposed for the desorption process operating in MALDI which involves the sublimation of matrix and analyte by local heating [80,81,82]. The lack of fragmentation observed in the analyte may be due to the the poor vibrational coupling, the weak bonds of the sample to the matrix causing a 'bottleneck' which therefore reduces energy transfer. The 'photochemical' model [83,84] proposes that protonated matrix molecules, generated by laser irradiation, act as proton donors to form analyte ions by gas-phase reactions. The proton transfer and cationisation of analytes observed in MALDI has been proposed to be via a CI type process [37]. The charging of the analyte molecules in the gas-phase is known to be a very inefficient process as much higher proportions of neutrals are formed.

MALDI spectra are often dominated by intense peaks at low mass which arise from intact molecular ions, fragments, clusters and adduct ions of the matrix employed. This phenomenon may be reduced by using lower laser powers approaching that of the threshold for analyte ion production and by employing certain matrices from which less intense peaks are generated [85,86,87]. These low mass ions may also be deflected away from the mass analyser by a technique known as matrix suppression prior to mass analysis.

Proton attachment is favoured for proteins and cationisation is often observed for synthetic polymers. Multiple charging and clustering is often observed in the spectra of high mass proteins and polymers. Satellite peaks from adducts of the analyte with the matrix are also commonly seen in spectra of large biopolymers but very little fragmentation is observed from large molecules except that of some small functional groups from certain species [88,89]. Fragmentations occuring after acceleration in a time-of-flight (TOF) instrument, termed post-source decay (PSD), may be observed as a tail on the molecular ion peak due to the loss of translational energy on dissociation [90,91]. PSD has been proposed to occur via monomolecular and/or bimolecular (by collisions with gas atoms and molecules) pathways and the amount of fragmentation has been found to be dependent on the matrix employed [92].

Spectra may be obtained from a sample deposition as small as 50 femtomoles [93], with as low as 10^{-17} mole of analyte being consumed in one laser shot [94]. Molecular ions of proteins [95] with molecular weights of above 200 kDa have been observed in MALDI spectra. The reproducibility of the MALDI technique is highly dependent on crystallisation characteristics, especially the size and homogeneity of the crystals [96]. Many sample preparation techniques have been proposed to generate reproducible results, including quick drying of the matrix [97] and/or use of a comatrix [98].

The resolution of the peaks observed in the UV-MALDI spectra is degraded by the distribution of velocities of the analyte desorbed from the target spot. The average velocity of analyte species emerging from the target has been estimated as approximately 800 m s^{-1} [99]. Furthermore, the variance in distance between the point

of desorption and acceleration also aids peak broadening. The latter effect may be reduced by the acceleration of ions by multiple steps in a device termed an ion 'buncher'.

There are no restrictions on the laser wavelength that may be employed in MALDI experiments if suitable matrices are available. Neodynium doped/yttrium aluminium garnet (Nd/YAG) lasers operating at wavelengths of 335 nm [100] and 266 nm [101], a nitrogen (N_2) laser at 337 nm [100] and a XeCl excimer laser at 308 nm [102] have all been successfully used with appropriate matrices. In addition, the technique of IR-MALDI with a carbon dioxide (CO_2) laser of wavelength 2.94 μm or 10.6 μm has been employed with a glycerol matrix to give results comparable to that of UV-MALDI [103]. The ability to control the laser flux is very important as the analyte signal has a non-linear correlation with power [75,86] and the required beam intensity is sample dependent.

Figure 2.7 is a schematic of the UV-MALDI source of the TOFSPEC time-of-flight mass spectrometer, which employs a N_2 laser operating at 337 nm to desorb the analyte.

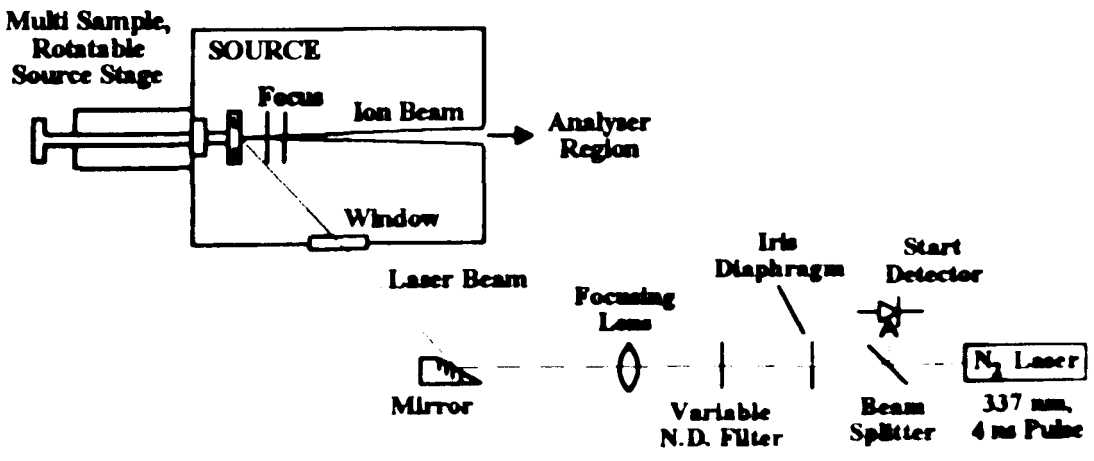

Figure 5.7,

Schematic of the UV-MALDI Source of the TOFSPEC.

1 A. O. Nier, *Rev. Sci. Instrum.*, **18**, 398 (1947).

2 A. J. Dempster, *Phys. Rev.*, **18**, 415 (1921).

3 M. S. B. Munson and F. H. Field, *J. Am. Chem. Soc.*, **88**, 2621 (1966).

4 H. D. Beckey, *Int. J. Mass Spectrom. Ion Phys.*, **2**, 500 (1969).

5 E. W. Müller, *Phys. Rev.*, **102**, 618 (1956).

6 R. Gomer, *J. Chem. Phys.*, **31**, 341 (1959).

7 H. D. Beckey, E. Hilt, A. Maas, M. D. Migahed and E. Ochterbeck, *Int. J. Mass Spectrom. Ion Phys.*, **3**, 161 (1969).

8 L. Prokai, *Field Desorption Mass Spectrometry*, Marcel-Dekker, New York (1990).

9 H. U. Winkler and H. D. Beckey, *Org. Mass Spectrom.*, **6**, 655 (1972).

10 M. G. Ingram and R. Gomer, *J. Chem. Phys.*, **22**, 1279 (1954).

11 M. G. Ingram and R. Gomer, *Z. Naturforsch.*, **10a**, 863 (1955).

12 E. W. Müller and K. Bahadur, *Phys. Rev.*, **102**, 624 (1956).

13 F. W. Röllgen in *Ion Formation from Organic Solids* (A. Benninghoven, Ed.), Springer-Verlag, Heidelberg (1983).

14 P. J. Derrick, *Fresnius' Z. Anal. Chem.*, **324**, 486 (1986).

15 J. F. Holland, B. Soltman and C. C. Sweeley, *Biomed. Mass Spectrom.*, **3**, 340 (1976).

16 F. Okuyama and G. H. Shen, *Int. J. Mass Spectrom. Ion Proc.*, **39**, 327 (1981).

17 F. W. Röllgen and K. H. Ott, *Int. J. Mass Spectrom. Ion Phys.*, **32**, 363 (1980).

18 F. W. Röllgen and H. D. Beckey, *Surface Sci.*, **23**, 69 (1970).

19 D. R. Kingham, *Surface Sci.*, **116**, 273 (1982).

20 S. C. Davis, V. Natoli, G. M. Neumann and P. J. Derrick, *Int. J. Mass Spectrom. Ion Proc.*, **78**, 17 (1987).

21 J. H. Scrivens, *Proceedings of the 13th International Conference on Mass Spectrometry*, Budapest (1994).

22 J. H. Scrivens, H. T. Yates, A. Bunn, P. Tayler, M. Beckett, M.Taylor and R. C. K. Jennings, *Proceedings of the 43rd ASMS Conference on Mass Spectrometry and Allied Topics*, May 22-26, Atlanta, Georgia (1995).

23 B. Plage and H.-R. Schulten, *J. Anal. Appl. Pyrolysis*, **19**, 285 (1991).

24 R. P. Lattimer, *J. Anal. Appl. Pyrolysis*, **31**, 203 (1995).

25 A. A. Herod, B. J. Stokes and H.-R. Schulten, *Fuel*, **72**, 31 (1993).

26 C. Sorge, R. Müller, P. Leinweber and H.-R. Schulten, *Fresnius' Z. Anal. Chem.*, **346**, 697 (1993).

27 (a) M. Barber, R. S. Bordoli, R. D. Sedgwick and A. N. Tyler, *J. Chem. Soc., Chem. Commun.*, 7, 325 (1981).

(b) M. Barber, R. S. Bordoli, R. D. Sedgwick and A. N. Tyler, *Nature*, **293**, 270 (1981).

28 W. Arberth, K. M. Straub and A. L. Burlingame, *Anal. Chem.*, **54**, 2029 (1982).

29 A. Benninghoven, D. Jaspers and W. Sichtermann, *Appl. Phys.*, **11**, 35 (1976).

30 R. M. Caprioli, T. Fan and J. S. Cottrell, *Anal. Chem.*, **58**, 2949 (1986).

31 J. Sunner, *Org. Mass Spectrom.*, **28**, 805 (1993).

32 C. J. McNeal, *Anal. Chem.*, **54**, 43A (1982).

33 C. Fenslau and R. J. Cotter, *Chem. Rev.*, **87**, 501 (1987).

34 F. Honda, G. M. Lancaster, Y. Fukuda and J. W. Rabalais, *J. Chem. Phys.*, **69**, 4931 (1978).

35 R. J. Day, S. E. Unger and R. G. Cooks, *Anal. Chem.*, **52**, 557 (1980).

36 G. H. Lancaster, F. Honda, Y. Fukuda and J. W. Rabalais, *J. Am. Chem. Soc.*, **101**, 1951 (1979).

37 J. A. Sunner, R. Kulatunga and P. Kebarle, *Anal. Chem.*, **58**, 1312 (1986).

38 M. Dole, L. L. Mack and R. L. Hines, *J. Chem. Phys.*, **49**, 2240 (1968).

39 M. Yamashita and J. B. Fenn, *J. Phys. Chem.*, **88**, 4451 (1984).

40 C. R. Blakley, M. J. McAdams and M. L. Vestal, *J. Chromatogr.*, **158**, 261 (1978).

41 G. I. Taylor, *Proc. R. Soc. London A.*, **A280**, 383 (1964).

42 M. G. Ikonomou, A. T. Blades and P. Kerbarle, *Anal. Chem.*, **62**, 957 (1990).

43 R. J. Pfeifer and C. D. Hendricks, *AIAA J.*, **6**, 496 (1968).

44 D. P. H. Smith, *IEEE Trans. Ind. Appl.*, **IA-22**, 527 (1986).

45 M. G. Ikonomou, A. T. Blades and P. Kerbarle, *Anal. Chem.*, **63**, 1989 (1991).

46 P. B. Bruins, T. R. Covey and J. Henion, *Anal. Chem.*, **59**, 2642 (1987).

47 D. S. Ashton, C. R. Beddell, D. J. Cooper, B. N. Green and R. W. A. Oliver, *Org. Mass Spectrom.*, **28**, 721 (1993).

48 R. D. Smith, J. A. Loo, C. J. Baringa, C. G. Edmonds and H. R. Udseth, *J. Am. Soc. Mass Spectrom.*, **1**, 53 (1990).

49 R. D. Smith, J. A. Loo, C. G. Edmonds, C. J. Baringa and H. R. Udseth, *Anal. Chem.*, **62**, 882 (1990).

50 F. W. Röllgen, E. Bramer-Weger and L. Buetfering, *J. Phys. Colloq. (Paris)*, **48-C6**, 253 (1987).

51 (a) J. V. Iribarne and B. A. Thomson, *J. Chem. Phys.*, **64**, 2287 (1976).

(b) B. A. Thomson and J. V. Iribarne, *J. Chem. Phys.*, **71**, 4451 (1979).

(c) B. A. Thomson, J. V. Iribarne and P. J. Dziedzic, *Anal. Chem.*, **54**, 2219 (1982).

52 (a) S. F. Wong, C. K. Meng and J. B. Fenn, *J. Phys. Chem.*, **92**, 546 (1988).

(b) J. B. Fenn, *J. Am. Soc. Mass Spectrom.*, **4**, 524 (1993).

53 T. R. Covey, A. P. Bruins and J. D. Henion, *Org. Mass Spectrom.*, **23**, 178 (1988).

54 P. Kebarle and L. Tang, *Anal. Chem.*, **65**, 972A (1993).

55 Lord Rayleigh, *Philos. Mag.*, **14**, 31 (1882).

56 G. Schmelzeisen-Redecker, L. Bütfering and F. W. Röllgen, *Int. J. Mass Spectrom. Ion Proc.*, **90**, 139 (1989).

57 J. A. Loo, H. R. Udseth and R. D. Smith, *Anal. Biochem.*, **179**, 404 (1989).

58 T. Nohmi and J. B. Fenn, *J. Am. Chem. Soc.*, **114**, 3241 (1992).

59 F. J. Vastola and A. J. Pirone, *Adv. Mass Spectrom.*, **4**, 107 (1968).

60 F. J. Vastola, R. O. Mumma and A. J. Pirone, *Org. Mass Spectrom.*, **3**, 101 (1970).

61 R. J. Conzemius and J. M. Capellen, *Int. J. Mass Spectrom. Ion Phys.*, **34**, 197 (1980).

62 R. J. Cotter, *Anal. Chem.*, **56**, 485A (1984).

63 F. Hillenkamp, *Adv. Mass Spectrom.*, **11A**, 354 (1989).

64 R. N. Zare, J. H. Hahn and R. Zanobi, *Bull. Chem. Soc. Jpn.*, **61**, 87 (1988).

65 R. Stoll, and F. W. Röllgen, *Z. Naturforsch.*, **37A**, 9 (1982).

66 J. Grotemeyer and E. W. Schlag, *Org. Mass Spectrom.*, **23**, 388 (1988).

67 B. Spengler, M. Karas, U. Bahr and F. Hillenkamp, *Ber. Bunsen-Ges, Phys. Chem.*, **93**, 396 (1989).

68 F. Engelke. J. H. Hahn, W. Henke and R. N. Zare, *Anal. Chem.*, **59**, 909 (1987).

69 M. Karas, D. Buchmann and F. Hillenkamp, *Anal. Chem.*, **57**, 2935 (1985).

70 F. Hillenkamp, M. Karas, D. Holtkamp and P. Klusener, *Int. J. Mass Spectrom. Ion Proc.*, **69**, 265 (1986).

71 M. Karas, D. Bachmann, U. Bahr and F. Hillenkamp, *Int. J. Mass Spectrom. Ion Proc.*, **87**, 53 (1987).

72 K. Tanaka, H. Waki, Y. Ido, S. Akita, Y. Yoshida and T. Yoshida, *Rapid Commun. Mass Spectrom.*, **2**, 151 (1988).

73 F. Hillenkamp, M. Karas, R. C. Beavis and B. T. Chait, *Anal. Chem.*, **63**, 1193A (1991).

74 M. Karas, U. Bahr and F. Hillenkamp, *Int. J. Mass Spectrom. Ion Proc.*, **92**, 231 (1989).

75 R. C. Beavis and B. T. Chait, *Rapid Commun. Mass Spectrom.*, **3**, 233 (1989).

76 R. C. Beavis and B. T. Chait, *Rapid Commun. Mass Spectrom.*, **3**, 432 (1989).

77 R. L. Hettkich and M. V. Buchmann, *J. Am. Soc. Mass Spectrom.*, **2**, 22 (1991).

78 S. Zhao, K. V. Somayajula, A. G. Sharkey and D. M. Hercules, *Anal. Chem.*, **63**, 450 (1991).

79 R. C. Beavis, *Org. Mass Spectrom.*, **27**, 653 (1992).

80 A. Vertes, R. Gijbels and R. D. Levine, *Rapid Commun. Mass Spectrom.*, **4**, 228 (1990).

81 A. Vertes and R. D. Levine, *Chem. Phys. Lett.*, **171**, 284 (1990).

82 A. Vertes and R. D. Levine, *Scanning Microscopy*, **5**, 317 (1991).

83 H. Ehring, M. Karas and F. Hillenkamp, *Org. Mass Spectrom.*, **27**, 472 (1992).

84 G. R. Kinsel, L. M. Preston and D. H. Russell, *Biol. Mass Spectrom.*, **23**, 205 (1994).

85 K. Strupat, M. Karas and F. Hillenkamp, *Int. J. Mass Spectrom. Ion Proc.*, **111**, 89 (1991).

86 T.-W. D. Chan, A. W. Colburn and P. J. Derrick, *Org. Mass Spectrom.*, **26**, 342 (1991).

87 T.-W. D. Chan, A. W. Colburn and P. J. Derrick, *Org. Mass Spectrom.*, **27**, 188 (1992).

88 J. A. Hill, R. S. Annan and K. Biemann, *Rapid Commun. Mass Spectrom.*, **5**, 395 (1991).

89 M. Karas, U. Bahr and U. Giessmann, *Mass Spectrom. Rev.*, **10**, 335 (1991).

90 B. Spengler, D. Kirsch and R. Kaufmann, *Rapid Commun. Mass Spectrom.*, **5**, 198 (1991).

91 B. Spengler, D. Kirsch, R. Kaufmann and E. Jaeger, *Rapid Commun. Mass Spectrom.*, **6**, 105 (1992).

92 M. Karas, U. Bahr, K. Strupat, F. Hillenkamp, A Tsarbopoulos and N. Pramanik, *Anal. Chem.*, **67**, 675 (1995).

93 M. Karas, A. Ingendoh, U. Bahr and F. Hillenkamp, *Biomed. Environ. Mass Spectrom.*, **18**, 841 (1989).

94 K. Strupat, M. Karas and F. Hillenkamp, *Int. J. Mass Spectrom. Ion Proc.*, **111**, 89 (1991).

95 M. Karas, U. Bahr, A. Ingendoh and F. Hillenkamp, *Angew. Chem., Int. Ed. Engl.*, **10**, 359 (1989).

96 P.-C. Liao and J. Allison, *J. Mass Spectrom.*, **30**, 763 (1995).

97 O. Vorm, P. Roepstorff and M. Mann, *Anal. Chem.*, **66**, 3281 (1994).

98 A. I. Guses, W. R. Wilkinson, A. Proctor and D. M. Hercules, *Anal. Chem.*, **67**, 1034 (1995).

99 T.-W. D. Chan, I. Thomas, A. W. Colburn and P. J. Derrick, *Chem. Phys. Lett.*, **222**, 579 (1994).

100 R. C. Beavis and B. T. Chait, *Rapid Commun. Mass Spectrom.*, **3**, 436 (1989).

101 M. Karas and F. Hillenkamp, *Anal. Chem.*, **60**, 2299 (1988).

102 W. Ens, Y. Mao, F. Mayer and K. G. Standing, *Rapid Commun. Mass Spectrom.*, **3**, 117 (1991).

103 A. Overburg, M. Karas, U. Bahr, R. Kaufmann and F. Hillenkamp, *Rapid Commun. Mass Spectrom.*, **5**, 128 (1991).

CHAPTER 3.

MASS ANALYSERS AND ION DETECTION.

3.1. Introduction to Mass Analysers.

A mass spectrum is a plot of the relative abundance of ions, passed by the mass analyser to the detector, against their m/z ratios. The techniques of mass analysis and ion detection that are commonly employed in mass spectrometry are introduced in this chapter with particular attention given to the systems that have been used in the present work. Table 3.1 lists the mass analysers that are commonly employed and their typical maximum mass-to-charge ratio (m/z) and resolving power. The resolving power is defined as the value of $m/\Delta m$ required to separate two peaks of mass m and $m+\Delta m$.

Type of Analyser	Maximum Mass-to-Charge (m/z) Ratio	Typical Maximum Resolving Power
Magnetic Sector	15,000	150,000
Quadrupole	4,000	4,000
Ion Trap	70,000	5,000
Time-of-Flight	500,000	5,000
Fourier Transform Ion Cyclotron Resonance	30,000	1,000,000

Table 3.1.

The Typical Maximum Mass-to-Charge Ratio and Resolving Power of Selected Mass Analysers.

The translational energy of singly charged ions (m_1) accelerated by V_{acc} is given by Equation 3.1:

$$eV_{acc} = \frac{m_1 v_1^2}{2} = \frac{(m_1 v_1)^2}{2m_1} \qquad \text{(Equation 3.1)}$$

where e is the electronic charge and v_1 is the velocity of m_1^+. Ions accelerated by V_{acc} all therefore have the same energy, $V_{acc}e$. Furthermore, from Equation 3.1, the

velocity is inversely proportional to the square root of the mass of the ion. Momentum increases with the square root of the mass:

$$m_1 v_1 = (2V_{acc} e m_1)^{\frac{1}{2}} \qquad \text{(Equation 3.2)}$$

As a consequence, separation by velocity or momentum is also separation by mass. Momentum separation is the operating principle of magnetic sectors while time-of-flight (TOF) analysers use the velocity distribution to separate ions by their m/z ratios. Quadrupoles employ direct current (d.c.) and radio frequency (r.f.) voltages in two dimensions to separate ions directly according to the m/z value and the same principle in three dimensions is employed for ion trap instruments. Fourier transform ion cyclotron resonance (FTICR) mass spectrometers generate frequencies that are directly related to the m/z ratios.

The choice of mass analyser for an application depends on a number of interrelated factors such as: (i) Mass range; (ii) resolving power; (iii) accuracy of mass measurement; (iv) ion transmission and dynamic range; (v) scanning speed and (vi) the ease of interfacing the analyser to other equipment such as, for example, a GC column.

3.2. Sector Mass Analysers.

3.2.(i) Electric Sector. The electric sector separates ions according to energy and focuses diverging ion beams which possess the same energy [1]. Two parallel cylindrical plates of average radius r make up a conventional electric sector across

which an electric potential, E, is applied. A schematic diagram of an electric sector is given in Figure 3.1. The electric sector is first order direction focusing as all ions exiting the source with a small angular divergence ($2\alpha_E$) are brought to focus at the exit slit and follow a path of radius r on average:

$$Ee = \frac{m_1 v_1^2}{r} = \frac{2V_{acc}e}{r} \qquad \text{(Equation 3.3)}$$

where

$$r = \frac{2V_{acc}}{E} \qquad \text{(Equation 3.4)}$$

The electric sector is energy dispersing in that ions generated at point O in the ion source (Figure 3.1) which possess different energies (E_0 and E_1) follow alternative paths and are brought to focus at separate points on the focal plane (F_0 and F_1). Most ion sources generate charged species with a significant energy spread which is reduced by the electric sector with a concurrent loss of the ion abundance. Furthermore, if the energy of the ions formed in the source is the same, there is no mass separation of ions by an electric sector.

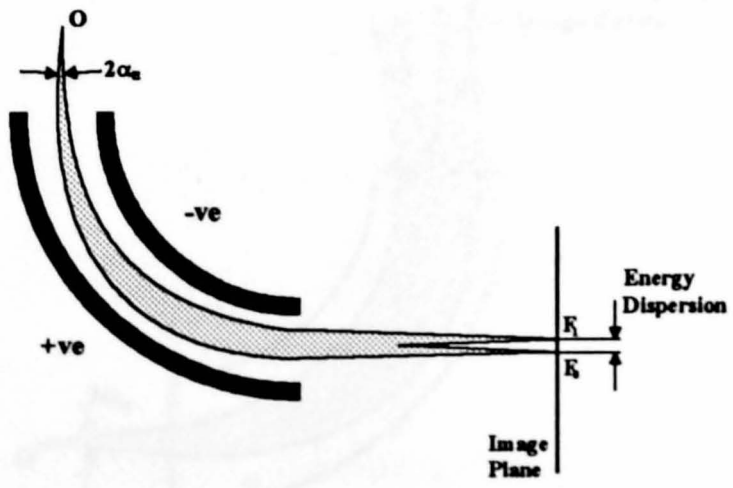

Figure 3.1.

Principle of Operation of an Electric Sector. O, Object Point for Source of Ions with Focus Points F_0 and F_1 for Ions with Energies E_0 and E_1 Respectively.

3.2.(ii) Magnetic Sector. Ions of mass m_1 entering a magnetic field follow a path of radius R which is perpendicular to the field where R is given by:

$$R = \frac{m_1 v_1}{B_1 e} \quad \text{or} \quad m_1 v_1 = R B_1 e \qquad \text{(Equation 3.5)}$$

Ions are therefore separated by momentum when the magnetic field is scanned if R is fixed. The ions passing through an exit slit are detected to generate the mass spectrum [1]. Furthermore, at fixed B, ions travelling through different radii may be collected on a photographic plate or an array detector (Section 3.4.(vi)). The standard expressions for separation of ions by a magnetic sector are given below in Equations 3.6-3.8.

$$m_1 e = \frac{R^2 B_1^2}{2V_{acc}} \qquad \text{(Equation 3.6)}$$

$$= K B_1^2 \qquad \text{(at fixed } V_{acc}\text{)} \qquad \text{(Equation 3.7)}$$

$$= \frac{K'}{V_{acc}} \qquad \text{(at fixed B)} \qquad \text{(Equation 3.8)}$$

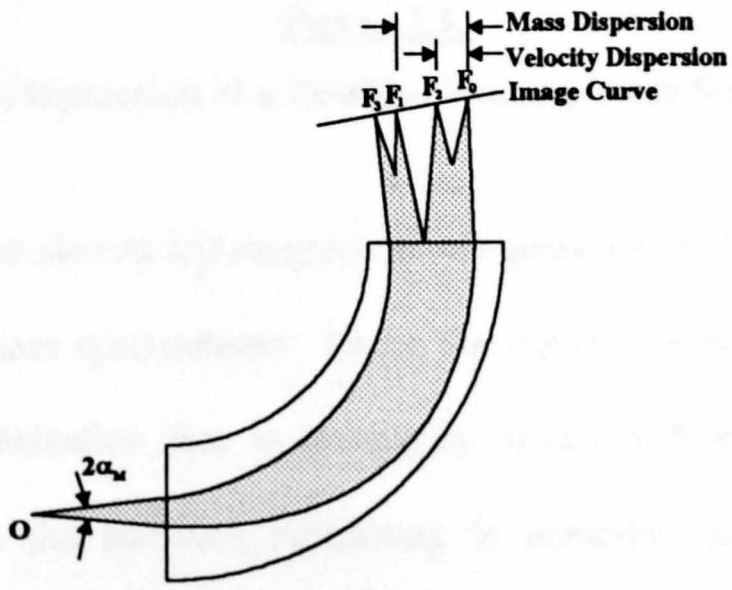

Figure 3.2.

Principle of Operation of a Magnetic Sector.
O, Points Source for Ions with Angular Spread of $2\alpha_M$.

Scanning linearly in B will therefore separate ions proportional to $m^{1/2}$ if V_{acc} is held constant [2]. A schematic diagram of a magnetic sector is shown in Figure 3.2. Ions generated at point O are separated by mass and velocity, brought to focus at points F_0, F_1 and F_0, F_2 respectively.

3.2.(iii) Principle of Double Focusing. An appropriate combination of an electric sector and a magnetic sector enables velocity and direction focusing simultaneously and generates double focusing conditions. A schematic of a double focusing mass spectrometer is Figure 3.3. The cross over point of the velocity and direction focusing curves generates double focusing at point I_0.

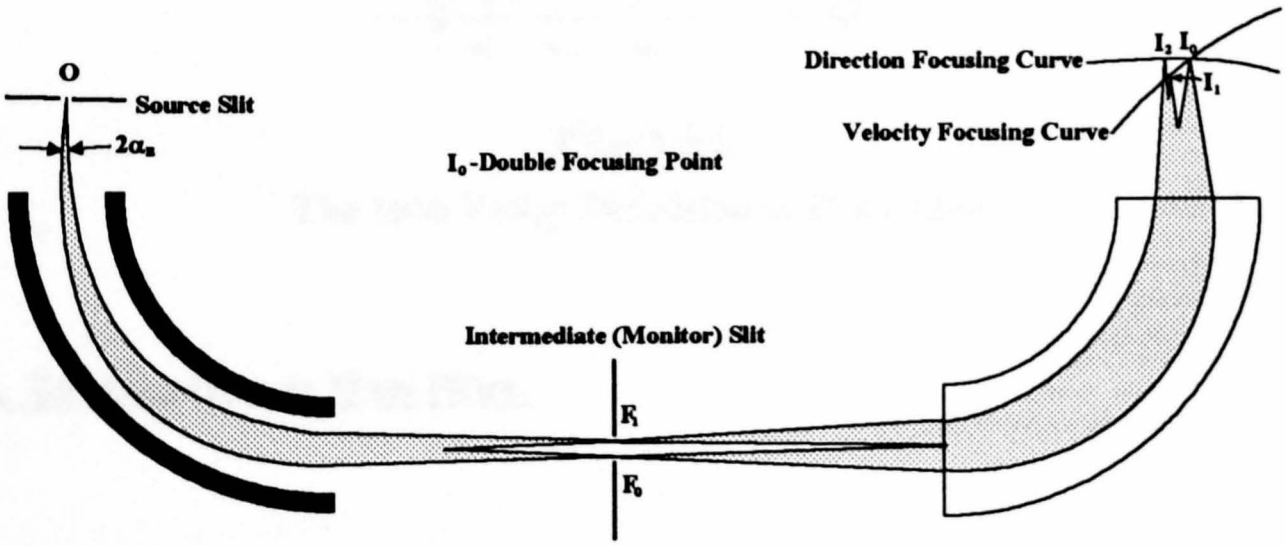

Figure 3.3.

Principle of Operation of a Double-Focusing Mass Spectrometer.

The orientation of the electric and magnetic sector gives rise to differing geometries of a double focusing mass spectrometer. Fixing the electric sector before the magnetic sector gives a combination that is commonly named a forward geometry (EB) instrument whereas the converse positioning is normally referred to as reverse geometry (BE). The performance of double focusing instruments is predominantly determined by factors such field inhomogeneities and fringing fields [3,4,5].

(iv) Resolution in Sector Mass Analysers. The resolving power of sector mass spectrometers is usually defined as the value of $m/\Delta m$ for which the height of the valley between the peaks at m and $m+\Delta m$, which are of equal intensity, is 10% of the height of the peaks. This is schematically represented in Figure 3.4. Modern sector mass spectrometers have a typical maximum resolving power of between 100,000 and 150,000 using this definition.

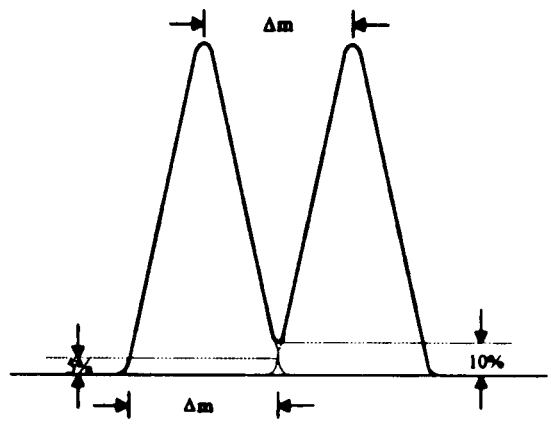

Figure 3.4.
The 10% Valley Definition of Resolution.

3.3. The Quadrupole Mass Filter.

Quadrupole mass filters are dynamic mass analysers. Quadrupolar fields induce restoring forces which are greater as the ions deviate from the central axis of the device whereas static mass analysers such as magnetic sectors generate constant forces on the charged species [6]. A quadrupole mass analyser is preferentially constructed from four equally spaced parallel rods of hyperbolic cross section. These analysers are typically made of four cylindrical rods, however, as these are more easily machined [7]. The opposite pairs of rods are connected electrically and a d.c. voltage U and r.f. voltage $V_0\cos(\omega t)$ are applied (Figure 3.5). The instability of certain ions in a

quadrupole field enables mass separation to be achieved. The potential applied to the ion is the agent responsible for this mass separation [6].

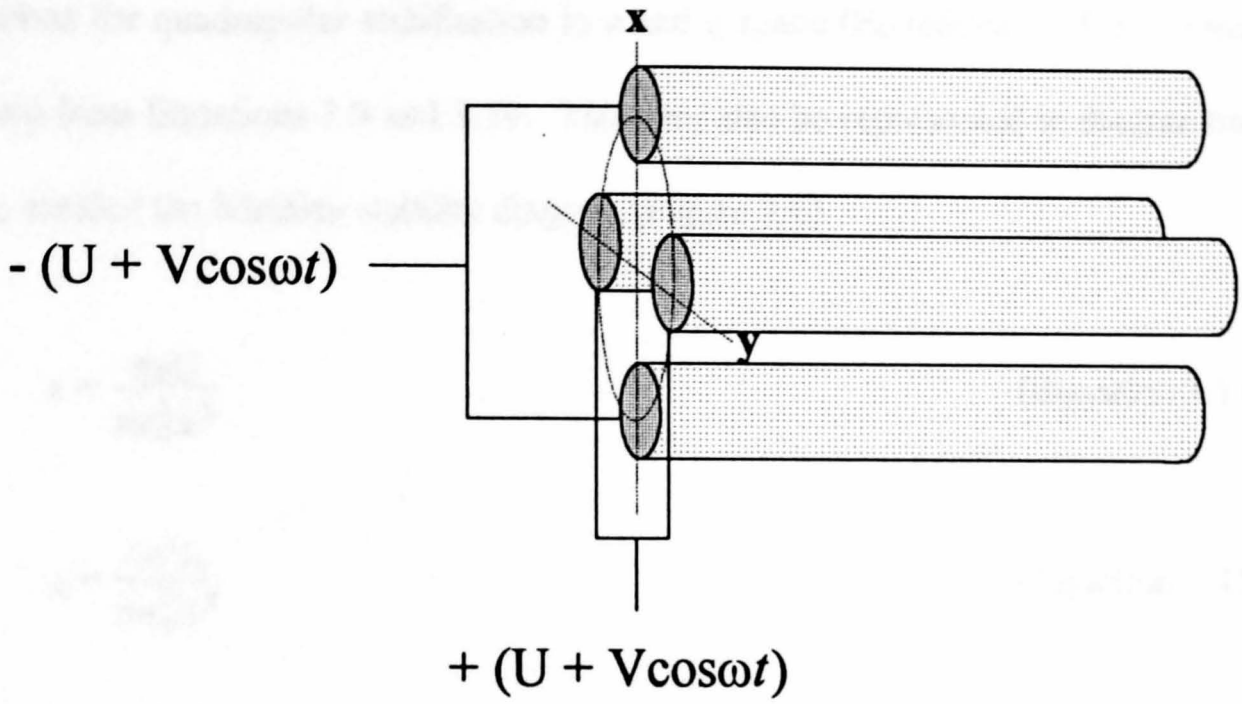

Figure 3.5.

Schematic of a Quadrupole Mass Filter Showing Electrical Potentials Applied to Four Parallel Rods of Circular Cross Section.

A mathematical representation for the path of ions in quadrupolar fields was given with solutions to a second-order linear differential equation by E. Mathieu in 1868 [8]. These equations of motion (Equation 3.9 and 3.10) give the positions of an ion in x, y space, perpendicular to the direction of motion of the ions in the z-direction.

$$\frac{d^2x}{d\left(\frac{\omega t}{2}\right)^2} + \left[a + 2q\cos 2\left(\frac{\omega t}{2}\right)\right]x = 0 \qquad \text{(Equation 3.9)}$$

$$\frac{d^2y}{d\left(\frac{\omega t}{2}\right)^2} + \left[a + 2q\cos 2\left(\frac{\omega t}{2}\right)\right]y = 0 \qquad \text{(Equation 3.10)}$$

In Equations 3.9 and 3.10, x and y are the distances from the centre of the field and a and q represent stable solutions to the Mathieu equation. The commonly quoted equations for quadrupolar stabilisation in a and q space (Equations 3.11-3.13) may be derived from Equations 3.9 and 3.10. This may also be represented in diagrammatical form, entitled the Mathieu stability diagram (Figure 3.6).

$$a = \frac{8eU}{mr_0^2\omega^2} \qquad \text{(Equation 3.11)}$$

$$q = \frac{4eV_0}{mr_0^2\omega^2} \qquad \text{(Equation 3.12)}$$

$$\frac{a}{q} = \frac{2U}{V_0} \qquad \text{(Equation 3.13)}$$

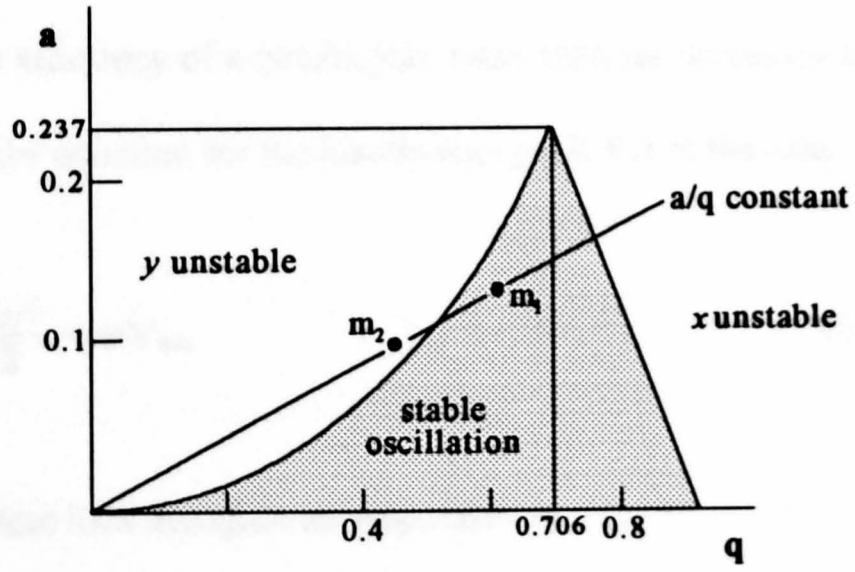

Figure 3.6.

Two Dimensional Representation of the Mathieu Stability Diagram For a Quadrupole Mass Filter.

Furthermore, as m is directly proportional to U and V_0 when the frequency is constant, scanning at a constant ratio of the latter two quantities will stabilise ions of different masses in turn and the mass spectrum may be obtained. This may be represented by

stability diagrams in U,V space as shown in Figure 3.7. Higher mass ions ($m_3 > m_2 > m_1$) are transmitted at higher values of U and V, a and q remaining constant.

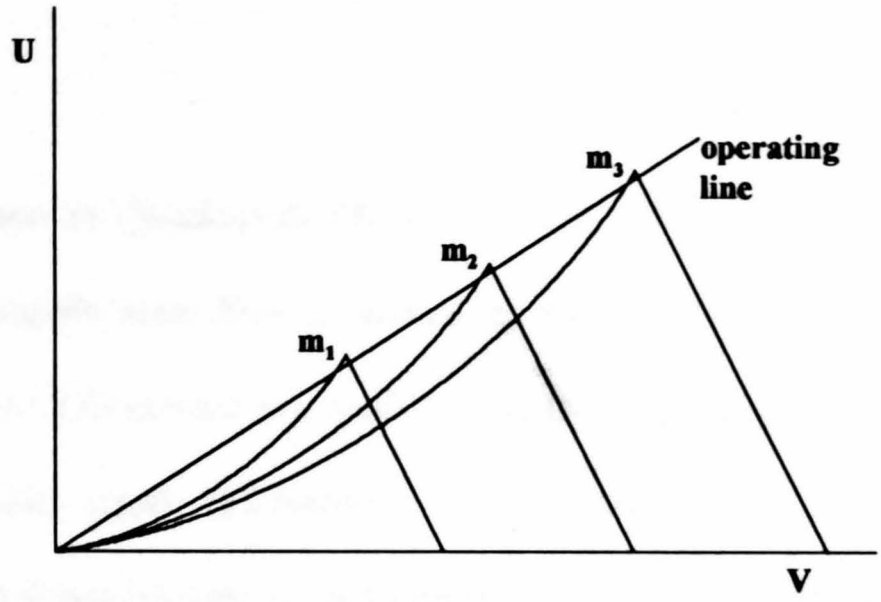

Figure 3.7.

Stability Diagrams Transformed to (U,V) Space ($m_3 > m_2 > m_1$).

The transmission efficiency of a quadrupole mass analyser decreases as the mass of the ion rises. From the equation for the kinetic energy (K.E.) of the ions:

$$\text{K.E.} = \frac{mv^2}{2} = zeV_{acc} \qquad \text{(Equation 3.14)}$$

the velocity of these ions therefore corresponds to:

$$v = \left(\frac{2zeV_{acc}}{m}\right)^{\frac{1}{2}} \qquad \text{(Equation 3.15)}$$

Furthermore, from Equation 3.15, the velocity of ions decreases as the mass increases. A lower velocity means that higher mass ions spend a longer time in fringing fields and their transmission through the analyser is reduced [9,10,11]. Short pre- and post-filters, generating r.f.-only quadrupolar fields, are often employed to define the

ion beam more closely and hence lower mass discrimination [12]. The largest modern quadrupole mass analysers have a maximum mass-to-charge ratio of approximately 4000.

3.3.(i) Resolution in Quadrupole Mass Analysers. The resolution of ions passed through a quadrupole mass filter is defined by the area in which the scan line (a/q constant in Figure 3.6) crosses the stability diagram [13]. As the line approaches the top of the stability region (increased U), the resolution is increased and the ion transmission conditions become more stringent. Conversely, as the line approaches the q axis, the resolution is reduced, more ions are passed through the analyser and the sensitivity is increased.

Resolution increases as the mass rises and there is a simultaneous fall in sensitivity which is linked to the number of cycles of ions through the quadrupole. A high mass ion undergoes more cycles as it has a lower velocity and the resolution is therefore increased. Normally, the mass analyser gives unit mass resolution up to the upper mass limit of operation.

3.4. Time-of-flight Mass Analysers.

The principle of operation of a time-of-flight (TOF) mass analyser is fairly self explanatory from the name of the mass separation device. Ions of different velocities are separated by their flight time through the analyser. The time taken (t) for ions of velocity v to travel along a flight tube of distance s is given by:

$$t = \frac{s}{v} \qquad \text{(Equation 3.16.)}$$

where the velocity of the ions having mass m after acceleration by the electrical potential V_{acc} is given by Equation 3.15. Combining Equations 3.15 and 3.16 gives the expression below:

$$t = s\left(\frac{m}{2zeV_{acc}}\right)^{\frac{1}{2}} \qquad \text{(Equation 3.17)}$$

Furthermore, as s and V_{acc} are constant for a given experiment, the time-of-flight can be represented as:

$$t = a\,(m/z)^{\frac{1}{2}} \qquad \text{(Equation 3.18)}$$

where a is a constant of proportionality. Thus ions of low mass will reach the detector first. The ratio of flight times (t_1/t_2), for ions of masses m_1 and m_2 and velocities v_1 and v_2 respectively, through the analyser can be represented as:

$$\frac{t_1}{t_2} = \frac{v_2}{v_1} = \left(\frac{m_1}{m_2}\right)^{\frac{1}{2}} \qquad \text{(Equation 3.19)}$$

A mass spectrum may therefore be generated by measuring the flight time of ions from the source to the detector [14,15,16].

The advantages of TOF analysers are their low cost, high transmission due to the absence of beam defining slits, the temporal separation of ions which does not deflect

any ions from the detector and high mass range [17]. The main disadvantage is the difficulty in obtaining high mass resolution.

3.4.(i) Resolution in Time-of-flight Mass Analysers. The maximum resolution obtainable of ions analysed in a linear TOF instrument is limited by differing points of ionisation, the kinetic energy spread of ions and space charge coulombic effects [18]. The resolution may be increased by the addition of a reflectron [19,20] or by orthogonal acceleration of the ions prior to mass analysis [21,22]. A schematic diagram of a reflectron-TOF instrument is shown below in Figure 3.8.

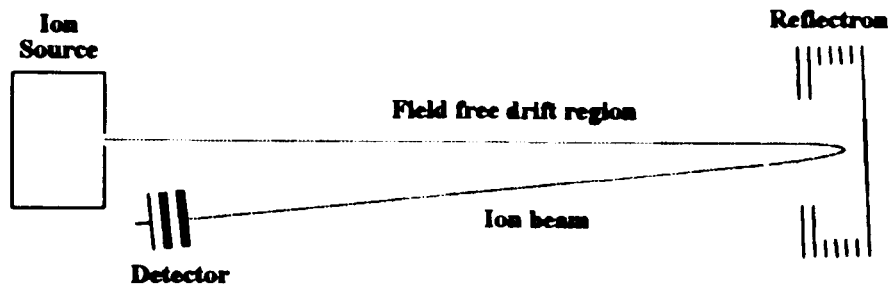

Figure 3.8.

Schematic of a Reflectron-TOF Instrument.

A reflectron is an electrostatic lens which is positioned at the end of the flight tube of the TOF mass analyser. This device decreases the time window at which ions of the same m/z ratio, but differing translational energies, reach the detector. Ions with higher translational energy penetrate the reflectron more deeply than those of lower energy and hence follow slightly different paths to the detector. As a consequence the translational energy discrimination is reduced and the resolution is enhanced. Furthermore, ions resulting from metastable decomposition, which can reduce the obtained mass resolution in linear mode, are not passed to the detector in reflectron mode.

3.5. Ion Detection.

3.5.(i) Introduction. The ion detectors that are commonly employed with mass spectrometers can be divided into two categories, that of direct measurement of the charge arriving at the detector and those that rely on multipliers to function. Direct measurement detectors such as the Faraday cup are capable of quantitative readings of intensity for isotope analysis but have limited applications and will not be described further here. Employment of multiplier detectors, which rely on electron multiplication to amplify the ion signal, is desirable for most modes of use due to the capabilities for single-ion detection and rapid scanning. Multiplier detectors are not capable of accurate measurements of ion intensity as the gain of the system is partially dependent on the structure of the ion impinging on the first dynode or plate.

3.5. (ii) Electron Multipliers. Discrete dynode electron multipliers consist of a series of approximately twenty copper/beryllium or aluminium plates which are connected by a series of resistors and give a maximum gain of typically 10^8 which allows single-ion detection. An ion striking the first dynode causes the emission of secondary electrons which are accelerated to the next electrode by a negative potential of up to -5 kV applied across the whole of the electron multiplier unit. Field emission may be observed as high noise intensity at elevated voltage values, normally above a value of 200 V between each dynode. Each electron generates more secondary electrons on impact with the next dynode in the series and this process is repeated until the final plate is reached which is connected to a variable amplifier, typically held at ground potential. The amplified signal is transferred to the data system for storage. The most

common type of electron multiplier is the Venetian blind which is employed in post acceleration detectors (PAD). Electron multipliers have limited lifetimes due to the reduction of maximum gain by sample contamination and the effects of high charge on the final dynodes.

Channel electron multipliers (CEM) are made of a continuous dynode of lead doped glass which generates high secondary electron emission intensities whilst remaining electrically resistive [23]. The two electrodes at either end of the CEM have an electrical potential applied across them which maintains a uniform voltage across the device. Figure 3.9 shows a cut-off cross section schematic of a straight CEM.

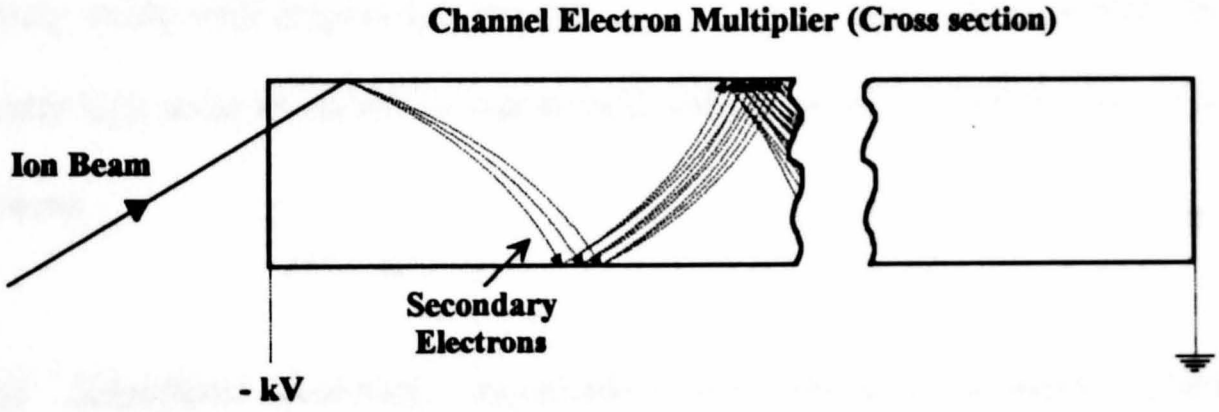

Figure 3.9.

Cross sectional Representation of a Channel Electron Multiplier.

An ion striking the inner surface of the CEM promotes the emission of secondary electrons. These electrons are accelerated by the field and collide with the opposite side of the wall, generating further electron multiplication. The output electron charge is measured by a separate plate at the end of the tube. The maximum operating gain, a function of the length-to-width ratio of the tube, is approximately 10^5 due to the negative ion feedback at higher values which may generate spurious noise. Multiple

small (approximately 10 μm diameter) CEM devices are fixed in parallel to generate microchannel plate (MCP) detectors [24,25]. MCP detectors, often consisting of two plates arranged in chevron to reduce ion feedback, are commonly employed in TOF instruments and array detection [26].

3.5.(iii) Photomultipliers. Photomultiplier detectors are identical to electron multiplier detectors except that they are enclosed by a sealed glass vacuum envelope and have a photocathode as the first electrode which is coated on the inner surface of the glass. Secondary electrons are generated and accelerated towards an electron multiplier by the photocathode when photons impinge upon it. The photomultiplier is extremely stable with respect to time due to the high vacuum characteristics but has inherently high noise levels which may be reduced by use of a scintillator as the source of photons.

3.5.(iv) Scintillator Detectors. Accelerated ions striking a scintillator, typically a phosphor screen with a sputter coating of aluminium (which forms a conducting surface), generating photons which are detected by a photomultiplier forms the basis of operation of the Daly detector [27], a scintillator detector. A similar device is employed for the detection of positive and negative ions in the Quattro II mass spectrometer (Figure 3.10).

Ions are accelerated on to an aluminium coated stainless steel conversion dynode by an electrical potential of 5 kV and the secondary electrons generated are drawn to the phosphor screen which is at 6 kV above ground potential in positive ion mode. The

photons produced by electrons impinging on the screen are detected by the photomultiplier. The applied potentials to the dynode and phosphor screen in negative ion mode are -5 kV and 3 kV respectively which gives approximately 3-5 times lower efficiency of detection than for positive ions.

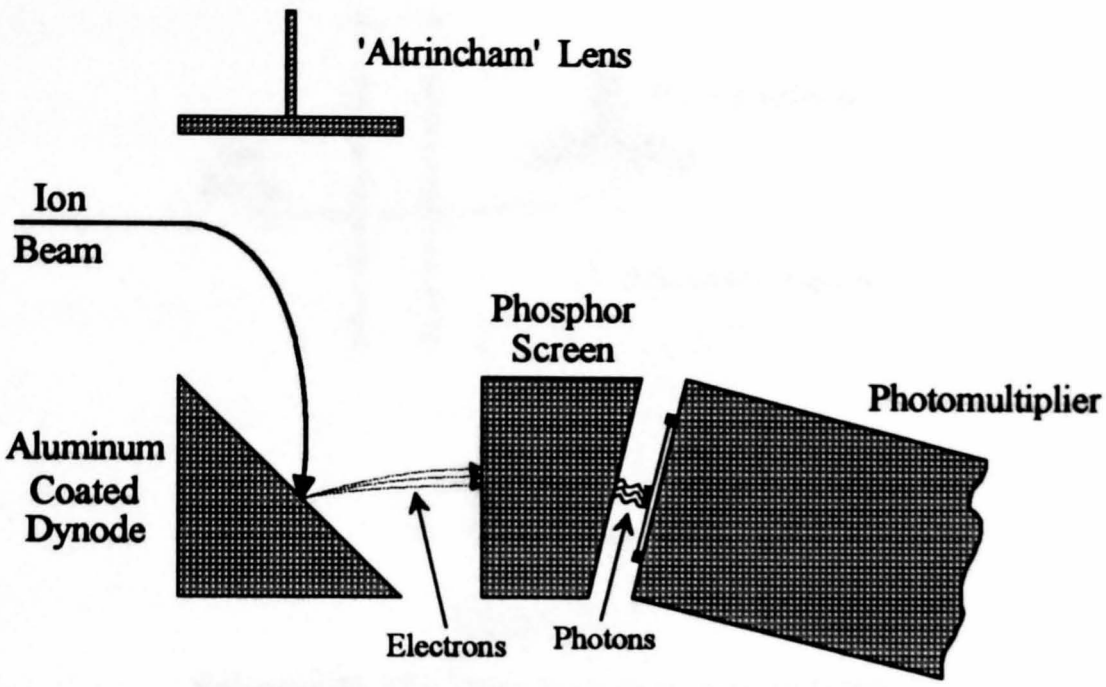

Figure 3.10.

Schematic of the Scintillator Detector (MS1) of the Quattro II.

3.5.(v) Post Acceleration Detectors. The secondary ion yield when an ion impinges upon a dynode is proportional to the velocity rather than energy of the ion and therefore the detection efficiency of high mass charged species is significantly reduced if the accelerating potential is held constant. The detection of high molecular weight charged species is improved if a PAD is employed. This device (Figure 3.11) consists of an off-axis target (PAD electrode) which is held at high electrical potential (-8 to -30 kV) and a discrete dynode electron multiplier.

Ions focused through the ion exit slit of the mass analyser are accelerated onto the PAD electrode and the secondary electrons hastened towards the electron multiplier.

The addition of a curved PAD electrode enhances the focusing of electrons onto the electron multiplier. In negative ion mode (on sector instruments), ions may be decelerated onto the PAD electrode and still generate secondary electrons but the detection efficiency is reduced.

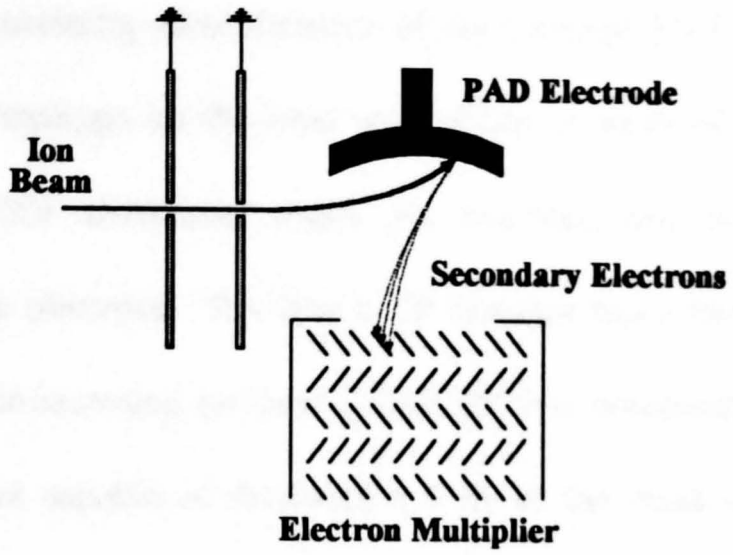

Figure 3.11.

Schematic of a Post Acceleration Detector.

3.5.(vi) Array Detectors. The most efficient detector would be capable of recording the intensities of all the ions instantaneously. Although this is not possible in most sector instruments due to the configuration and scanning characteristics, an array detector may be employed to detect large proportions of the mass range at one instant in time [28]. The detection limits have been found to improve by a factor of approximately 100 when the final point detector of a four sector mass spectrometer is replaced by an array detector [29]. Product ion spectra of peptides have been obtained in the femtomole range by means of a four sector mass spectrometer fitted with an array detector [30]. The most common array detectors combine MCP detectors with photodiode or charge-coupled device (CCD) technology to record ion intensity values. The advantage of the CCD array detector is the fast response time which enables the

mass spectrometer to be scanned as for the collection of data on a point detector [31]. A photodiode array detector is scanned across the mass range of interest in a stepwise manner and the resulting information is 'stitched' by the data system.

A schematic of the scanning array detector of the Concept [32] is Figure 3.12. The incoming ion beam impinges on the inner wall of one or more of the CEM devices of the first of two MCP detectors, which are touching and arranged in chevron, generating secondary electrons. The first MCP detector has a fixed focal plane at 30° to the direction of the incoming ion beam. Each MCP is constructed of 1048 channels and together they are capable of detecting ± 2 % of the mass range simultaneously with an approximate gain of 10^7 when the maximum electrical potential of 1.2 kV is applied across them. Secondary electrons exiting the second MCP are accelerated by a voltage of 3 kV onto the phosphor screen, generating photons which are transmitted by means of fibre optic cables to the CCD array which is external to the vacuum. The CCD array converts photons to charge and consists of 1152 pixels which are each capable of accumulating the charge resulting from 10^4-10^5 ions before saturation [33]. A Peltier device is employed to cool the CCD to -20 °C, thereby reducing dark current. Each pixel of the CCD array is approximately 25 μm wide and 2.5 mm long and takes a few microseconds to read, by measuring the charge required to neutralise that accumulated by the device over 10-40 ms. These data are transferred to the data system and are treated as those from a point detector. A resolution of between 500 and 3000 (10% valley definition) is accessible depending on the conditions.

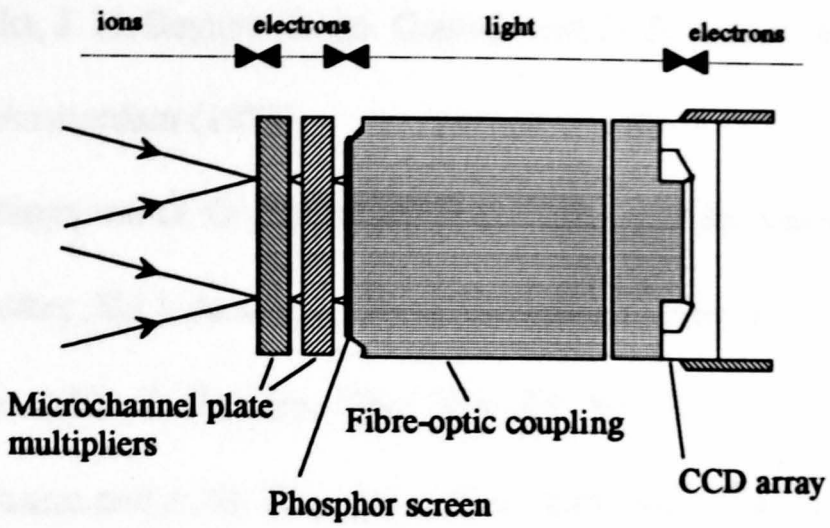

Figure 3.12.

Schematic of the Scanning Array Detector of the Concept.

The array detector of the ZAB-T is essentially the same as that shown in Figure 3.12 except that the CCD is replaced by a photodiode array [34]. The MCP detectors are comprised of over 3000 channels and have a length of 76 mm in the dispersive plane. They can detect a ratio of 1.225:1 of the mass range simultaneously when at a 30° angle to the ion beam and the collision cell is floated at a value of 4 kV. At the maximum angle of 90°, under the same conditions, the array is capable of encapsulating a ratio of 1.4:1 of the mass range instantaneously but the resolution is highly degraded. Electrical potentials of 1.75 kV and 4 kV are held between the MCP detectors and on the phosphor screen respectively. The photons emitted by the phosphor are converted to charge by two 1024 channel photodiode arrays that are stitched together. The data system removes the image of the seam of the arrays from the data arriving at the computer.

1 R.G. Cooks, J. H. Beynon, R. M. Caprioli and G. R. Lester, *Metastable Ions*, Elsevier, Amsterdam (1973).

2 K. R. Jennings and G. G. Dolnikowski in *Methods in Enzymology, Vol. 193* (J. A. McCloskey, Ed.), Academic Press, San Diego, Chapter 2 (1990).

3 A. O. Nier and T. R. Roberts, *Phys. Rev.*, **81**, 507 (1951).

4 W. H. Johnson and A. O. Nier, *Phys. Rev.*, **105**, 1014 (1957).

5 H. Hintenberger and L. A. Konig, *Adv. Mass Spectrom.*, **1**, 16 (1959).

6 R. E. March and R. J. Hughes, *Quadrupole Storage Mass Spectrometry*, Wiley, New York, Chapter 2 (1989).

7 D. R. Denison, *J. Vac. Sci. Technol.*, **8**, 266 (1971).

8 E. Mathieu, *J. Math. Pures Appl.*, **13**, 137 (1868).

9 P. H. Dawson and N. R. Whetton, *Adv. Electron. Electron Phys.*, **27**, 58 (1969).

10 P. H. Dawson, *Int. J. Mass Spectrom. Ion Phys.*, **17**, 423 (1969).

11 P. H. Dawson, *Int. J. Mass Spectrom. Ion Phys.*, **6**, 33 (1971).

12 N. M. Brubaker, *Adv. Mass Spectrom.*, **4**, 293 (1968).

13 J. E. Campana, *Int. J. Mass Spectrom. Ion Phys.*, **33**, 101 (1980).

14 W. E. Stephens, *Phys. Rev.*, **69**, 691 (1946).

15 A. E. Cameron and D. F. Eggers, Jr., *Rev. Sci. Instrum.*, **19**, 605 (1948).

16 W. C. Wiley and I. H. McLaren, *Rev. Sci. Instrum.*, **26**, 1150 (1955).

17 C. Brunée, *Int. J. Mass Spectrom. Ion Proc.*, **76**, 1 (1987)

18 G. Sanzone, *Rev. Sci. Instrum.*, **41**, 741 (1970).

19 B. A. Mamyrin, V. I. Karataev, D. V. Snmikk and V. A. Zagulin, *Sov. Phys. JETP*, **37**, 45 (1973).

20 W. Gohl, R. Kutscher, H. J. Laue and H. Wollnik, *Int. J. Mass Spectrom. Ion Phys.*, **48**, 411 (1983).

21 J. H. J. Dawson and M. Guilhaus, *Rapid Commun. Mass Spectrom.*, **3**, 155 (1989).

22 J. Coles and M. Guilhaus, *Trac/Trends Anal. Chem.*, **12**, 203 (1993).

23 E. A. Kurz, *Amer. Labor.*, March (1989).

24 C. E. Griffin, H. G. Boettger and D. D. Norris, *Int. J. Mass Spectrom. Ion Phys.*, **15**, 437 (1974).

25 H. H. Tuithof, A. J. H. Boerboom and H. L. C. Meuzelaar, *Int. J. Mass Spectrom. Ion Phys.*, **17**, 299 (1975).

26 J. S. Cottrell and S. Evans, *Anal. Chem.*, **59**, 1990 (1987).

27 N. R. Daly, *Rev. Sci. Instrum.*, **34**, 1116 (1963).

28 S. Evans in *Methods in Enzymology, Vol. 193* (J. A. McCloskey, Ed.), Academic Press, San Diego, Chapter 3 (1990).

29 J. A. Hill, S. A. Martin, J. E. Biller and K. Biemann, *Biomed. Environ. Mass Spectrom.*, **17**, 147 (1988)

30 P. T. M. Kenny and R. Orlando, *Anal. Chem.*, **64**, 957 (1992).

31 A. D., Hofmann, P. A. Ryan, P. Ireland, P. J. Derrick, P. J. Morgan and R. Self in *Proceedings of Kyoto '92 International Conference on Biological Mass Spectrometry* (T. Matsuo, Ed.), San-ei Publishing, Kyoto, 280 (1992).

32 A. D., Hofmann, P. A. Ryan and C. Moore, *Proceedings of the 40th ASMS Conference on Mass Spectrometry and Allied Topics*, May 31-June 5, Washington, DC, 519 (1992).

33 S. Evans, R. Buchanan, A. D. Hofmann, F. A. Mellon, K. R. Price, S. Hall., F. C. Walls, A. L. Burlingame, S. Chen and P. J. Derrick, *Org. Mass Spectrom.*, **28**, 289 (1993).

34 M. L. Gross in *Methods in Enzymology, Vol. 193* (J. A. McCloskey, Ed.), Academic Press, San Diego, Chapter 6 (1990).

CHAPTER 4.

TANDEM MASS SPECTROMETRY.

4.1. Introduction to Collisional Activation.

The determination of molecular structure by mass spectrometry requires that structurally informative fragments of the molecular ion are generated. The dissociation of the molecular ion may be induced during ionisation or by another means of excitation. Structural analyses of low molecular weight samples may be performed by means of EI-MS as fragment ions are typically formed in the source as a consequence of the high amounts of internal energy transferred to the sample in the ionisation process. As the mass and/or involatility of the analyte increases, however, EI is often an unsuitable ionisation technique and desorption methods must be used to generate gas phase ions. Furthermore, desorption ionisation techniques generate predominantly molecular ions or cationated molecule ions with little fragmentation and therefore structurally informative data are often not obtained. Fragmentation may be effected by means of collisional activation of an ion with inert gas atoms such as helium, argon or xenon, resulting in collision induced dissociation (CID), sometimes called collisionally activated decomposition (CAD) [1,2].

The yield of dissociation products from collisionally activated ions is controlled by the probability of unimolecular decomposition of the excited precursor ion. The rules of these reactions are usually explained in terms of the quasi-equilibrium theory (QET) which postulates that the internal excitation energy is distributed randomly over all the vibrational modes of the ion [3,4,5,6,7]. The rate of dissociation of a precursor ion is therefore related to the probability of particular vibrational modes acquiring enough energy for bond cleavage. The ions observed in the mass spectrum consequently arise

from a series of competing and consecutive unimolecular decomposition reactions originating from the molecular ion. The rate of each reaction is dependent on the internal energy of the system. Furthermore, as there are 3N-6 vibrational modes in a molecule of a given species made up of N atoms, the number of modes usually increases as the molecular weight (RMM) gets larger. The average energy per mode should therefore decrease as the RMM increases and hence lower fragmentation yields from the precursor ion are possible. Direct bond cleavages are predominantly processes of high critical energy which have high frequency factors whereas molecular rearrangement reactions require less energy but have low frequency factors.

Factors that influence the distribution of fragment ions include acquired internal energy, reaction time, method of energy uptake, scattering of ions after collision and angle of ion collection [4,8,9,10]. The method of activation controls the internal energy uptake of the ion. These activation pathways are normally divided into two categories: those of high and low energy collisions. High energy collisions are usually defined as those occurring in the kiloelectron volt range [1,2,8,9,10,11,12,13] whereas low energy collisions occur in the region of 0-200 eV [10,12,13,14,15,16,17]. Both of these collision ranges have been utilised in the present work: high energy collisions on a four sector mass spectrometer and low energy collisions on both a four sector and a tandem quadrupole instrument (See Chapter 5).

CID is considered to be a two step process that occurs over well separated time scales [9,10,18]. The first step is excitation of the precursor ion (m_1^*) by collisional activation which has a time scale in the region of 10^{-15}-10^{-13} s. Fast moving polyatomic

ions involved in inelastic collisions with neutral gas atoms lose a portion of their translational energy. A small percentage of the lost translational energy is converted to internal energy of the precursor ion. This is followed by rapid randomisation of the excitation energy throughout all the degrees of freedom of the ground electronic state of the molecule, if the initial excitation is *via* vibrational modes. The energetically excited precursor ion $m_1^{+\bullet}$ then undergoes unimolecular dissociation to yield a fragment ion m_2^+ and normally a neutral molecule m_3 if the precursor ion is a protonated species. This process is shown below in Equation 4.1. A radical $m_3^{\bullet}$ and fragment ion m_2^+ are predominantly generated when m_1^+ is a radical cation. Further losses of neutrals are possible from m_2^+ to generate fragment ions of lower mass in both cases.

$$m_1^+ \xrightarrow{CA} m_1^{+\bullet} \longrightarrow m_2^+ + m_3 \qquad \text{(Equation 4.1)}$$

Tandem mass spectrometry (MS/MS) is employed as a term to describe a technique in which two mass spectrometers are combined in tandem. In this process, ions generated in the source are selected by the first mass spectrometer (MS1) and passed into the collision region where collisional activation is typically induced by collision with an inert gas. The fragments generated are passed by the second mass spectrometer (MS2) to the detector to generate the mass spectrum. Furthermore, MS/MS experiments may be performed by means of FT-ICR and ion trap instruments in a single mass analyser.

4.2. High Energy Collision Induced Dissociation.

4.2.(i) Instrumentation. High energy collisional activation is only attainable over a large mass range (up to approximately 3500 Da) on magnetic sector and some hybrid instruments. These instruments include two sector (BE and EB), three sector (typically EBE or BEE) and four sector mass spectrometers (EBEB and BEBE). The most favourable configuration for high energy MS/MS is that of two double-focusing sector mass spectrometers in tandem. The two mass spectrometers are separated by a field free region in which a collision cell is located. Precursor ions are selected by the first mass spectrometer (MS1) and the product ions generated in the collision cell are passed by the second mass spectrometer (MS2) to the detector. High resolving power of both precursor and product ions is accessible as a consequence of the double focusing properties of the four sector instrument. Four sector mass spectrometers in which high energy experiments are performed become increasingly superior in performance over tandem quadrupole and hybrid instruments for analysing compounds with a mass-to-charge (m/z) ratio of above 1000. This is due to comparatively better ion transmission and product ion yield obtained in four sector instruments at higher mass.

4.2.(ii) Mechanism of High Energy CID. The interaction time of the precursor ion with the target (10^{-15} s) is an order of magnitude faster than the fastest molecular vibrations (10^{-14} s) and is closer to the Bohr period of an electron which is in the valence orbital of a polyatomic ion. The adiabatic criterion of Massey and Burhop asserts that the duration of collisional interactions should be comparable to that of

excitation [19]. Consequently, the collisions of ions at high energies are expected to result from electronic excitation. The electronic excitation energy is rapidly converted to vibrational energy prior to randomisation. Furthermore, as the mass of the precursor ion increases, the interaction time with the collision gas is also increased if the translational energy of the system is constant and thus the excitation mechanism of CID is more likely to be *via* vibrational modes.

The broad distribution of internal energies that are deposited into the molecular ion by high energy collisional activation is presumed to indicate a change of excitation mechanism from vibrational to electronic excitation [20]. A smooth distribution of internal energies is observed with a maximum at low energy (1-3 eV) and also a high energy 'tail' of low intensity up to approximately 15 eV [21,22,23].

4.2.(iii) Collision Gas Effects. Helium has commonly been employed as the collision gas as the scattering of lighter fragment ions is minimised and the main excitation process is believed to be electronic [24,25,26]. Argon was proved to be more efficient, however, as the collision gas for the activation of molecular ions from biopolymers with RMM above 1000 Da [27,28,29,30]. Argon also enhances the production of fragment ions resulting from high energy decomposition pathways, often called charge remote fragmentations [31,32]. It is therefore presumed that vibrational excitation plays a more important role for precursor ions of higher RMM.

The maximum amount of kinetic energy available for conversion to internal excitation energy of the precursor ion, the centre-of-mass kinetic energy E_{COM}, is given by Equation 4.2.

$$E_{COM} = \frac{m_t E_{lab}}{m_t + m_i} \qquad \text{(Equation 4.2)}$$

where E_{lab} is the kinetic energy of the precursor ion in the lab frame and m_t and m_i are the masses of the target gas and the precursor ion respectively. The value of E_{COM} will therefore increase with E_{lab} or m_t and is approximately inversely proportional to the mass of the precursor ion.

The increase in E_{COM} is close to linearity with the value of m_t when E_{lab} and m_i are constant and $m_i < m_t$ which suggests that heavier collision gases are preferable if scattering is not a factor. The impulsive collision theory (ICT) [33] suggests that the value of the average internal energy uptake Q may be calculated from Equation 4.3.

$$Q = E_{COM} \frac{2m_a m_t}{(m_a + m_t)^2} \qquad \text{(Equation 4.3)}$$

where m_a is the average mass of the atoms in the precursor ion. The value of Q is therefore greater when argon is replaced by helium for a given E_{COM}. The amount of E_{COM} increases by approximately an order of magnitude for an ion of greater than 1000 Da when argon is used instead of helium, however, so that the value of Q is increased by a factor of approximately 5.

A collision gas pressure that reduces the precursor ion transmission to 20-30% is typically employed in high energy CID as this usually gives rise to optimum fragment ion yields [34]. This value for the attenuation of the ion beam corresponds to multiple collision conditions [35,36].

4.2.(iv) Linked Scans. The translational energy of a fragment ion m_2^+ generated from m_1^+ in the field free region of a sector mass spectrometer, in an earthed collision cell, is given by Equation 4.4:

$$\text{Energy} = \left(\frac{m_2}{m_1}\right) V_{acc} e \qquad \text{(Equation 4.4)}$$

The linked scan typically employed to pass an ion beam resulting from these dissociations occurring in the first or third field free region of a two or four sector mass spectrometer respectively is therefore

$$\frac{B_1}{B_2} = \frac{E_1}{E_2} = \text{constant} \quad \text{or} \quad \frac{B}{E} = \text{constant} \qquad \text{(Equation 4.5)}$$

and is commonly termed the **B/E** linked scan. All product ions generated from a selected precursor are transmitted when **B** and **E** are scanned such that the **B/E** ratio is constant. The apparent yield of low mass fragment ions is low when the **B/E** linked scan is employed. This is due to the low transmission efficiency through sector analysers at kinetic energies lower than the optimum values. The velocity of these ions is also low which causes a reduction in the efficiency of detection. Furthermore,

scattering of fragment ions becomes more important when collision gases of higher RMM are employed.

The extra energy of the lower mass fragment ions obtained from floating the collision cell at a value of V_{cell} above ground potential gives a greater detection efficiency and reduces the losses due to scattering in the collision cell which is especially important when target gases such as argon are employed [37]. The reduction in collision energy is more than compensated for by the increase in the average number of collisions and hence the larger value of E_{COM} [29,32,39]. The energy of fragment ions m_2, resulting from fragmentations in a collision cell floated at V_{cell} above ground potential after reaccelleration by V_{cell} is given by

$$\text{Energy of ions } m_2 = E_{coll}\,(m_2/m_1) + E_{cell} \qquad \text{(Equation 4.6)}$$

where E_{cell} is the extra energy imparted to the fragment ions on reaccelleration. A linked scan of constant B/E can no longer be used when the collision cell is floated above ground potential to collect the ions resulting from decomposition in the collision cell. If B_1 and B_2 are the magnetic fields which transmits the precursor m_1, which has full kinetic energy eV_{acc} and momentum $(2m_1eV_{acc})^{1/2}$, and the product ion m_2 respectively, the ratio of B_2/B_1 may therefore be expressed as

$$\left(\frac{B_2}{B_1}\right) = \left[\left(\frac{m_2}{m_1}\right)^2 + \left(\frac{m_2}{m_1}\right)\left(\frac{V_{cell}}{V_{acc}}\right)\left\{1-\left(\frac{m_2}{m_1}\right)\right\}\right]^{\frac{1}{2}} \qquad \text{(Equation 4.7)}$$

where V_{acc} is the full accelerating voltage [38]. The electric sector field strengths required to transmit m_1 and m_2 are E_1 and E_2 respectively when the collision cell is floated at potential at V_{cell} and their relationship is

$$\left(\frac{E_2}{E_1}\right) = \left(\frac{m_2}{m_1}\right)\left[1 - (V_{cell}/V_{acc})\right] + \left(\frac{V_{cell}}{V_{acc}}\right) \qquad \text{(Equation 4.8)}$$

Eliminating (m_1/m_2) from Equations 4.7 and 4.8 generates the linked scan law for a mass spectrometer with a collision cell floated at V_{cell} above ground potential [40,39]:

$$\left(\frac{B_1}{B_2}\right)^2 = \left(\frac{E_2}{E_1}\right)\left[\frac{(E_2/E_1) - (V_{cell}/V_{acc})}{1 - (V_{cell}/V_{acc})}\right] \qquad \text{(Equation 4.9)}$$

Furthermore, if the collision cell is held at earth potential ($V_{cell} = 0$), Equation 4.9 reduces to B/E = constant.

Precursor ion scans may be implemented on a two sector mass spectrometer by employing a B^2/E linked scan to give a precursor ion resolution of a few hundred at best [40] at kiloelectronvolt collision energies. The obtainable precursor ion resolution may theoretically be increased by utilising a four sector mass spectrometer. There are two possible approaches of employing MS1 and MS2 from these instruments for precursor ion scans.

The first method demands both magnets to be scanned simultaneously in opposite directions. This approach is problematical due to the difficulty in controlling the relationship of the magnetic field strengths. The second method requires MS2 to have

a wide energy acceptance and utilises a floated collision cell and has been implemented successfully on a four sector mass spectrometer [41]. This approach is discussed further in Section 5.3.

4.3. Low Energy Collision Induced Dissociation.

4.3.(i) Instrumentation. Low energy CID is typically performed on tandem quadrupole of Q*q*Q, Q*h*Q or Q*o*Q geometry (where *q*, *h* and *o* are radio-frequency (r.f.) only quadrupole, hexapole and octapole collision cells respectively) and hybrid instruments of BE*q*Q or EB*q*Q geometry.

In a tandem quadrupole instrument the first quadrupole, Q_1, selects precursor ions from the source and the third quadrupole, Q_2, passes product ions generated in the collision cell. The collision cell is a multipole (*q*, *h*, *o*), operated with no d.c. voltage applied which gives the non-mass selective ion containment required for low energy collision processes. The small r.f. voltage employed generates the high transmission conditions of the collision cell. Both mass analysers may be operated by normal quadrupole mass spectrometric techniques due to the inherent separation of ions by m/z ratio. These instruments normally offer collision regimes in the order of 0-200 eV and a maximum mass range of approximately m/z 4000.

Tandem quadrupole mass spectrometers offer unit mass resolution for precursors and product ions. One advantage of tandem quadrupole instruments over four sector instruments is the simple modification of the MS/MS experiment. Precursor ion and

constant neutral loss scans are more facile on a tandem quadrupole instrument under computer control with unit mass resolution for both precursor and product ions. In the precursor ion scanning experiment, Q_1 is scanned to pass all precursor ions that generate the product ion in the collision cell. The product ion is passed by a set value of Q_2. The constant neutral loss scan requires both Q_1 and Q_2 to be scanned, passing ions of masses that differ by a constant value simultaneously.

Radiofrequency-only multipoles are employed as collision cells in tandem quadrupole and hybrid instruments due to their strong focusing capabilities for precursor ions and fragment ions generated by collision induced dissociations whilst in transit through the reaction region. Early designs of tandem quadrupole instruments typically employed r.f.-only quadrupole collision cells but recently have more commonly been replaced by hexapoles and octapoles used in r.f.-only mode [42,43].

Hexapole collision cells are made of six uniformly spaced rods which confine most masses to a region close to the centre of the axis when used in r.f.-only mode whereas ions follow a more complicated path in a r.f.-only quadrupole collision cell [44]. As a consequence, the tuning is comparatively simple for r.f.-only hexapole collision cells. Hexapoles operated in r.f.-only mode are more suitable for MS/MS experiments in tandem quadrupole instruments than quadrupoles as the low mass fragments that have unstable trajectories in r.f.-only quadrupoles are passed by a hexapole [46]. This is especially true at low collision energies and/or for precursor ions of high m/z ratio [46].

4.3.(ii) Mechanism of Low Energy CID. The residence time of ions in a r.f.-only multipole collision cell is typically at least an order of magnitude longer than in the reaction region of a sector instrument. Furthermore, the interaction time of an ion with a gas atom or molecule is longer than the period of an electronic internal mode and therefore collisional activation is unlikely to occur by electronic excitation. The duration of these interactions is, however, comparable to the inverse of the frequency of vibrations. As a consequence, vibrational excitation is presumed to occur as a result of momentum transfer collisions between the target gas and atoms of the projectile ion [45]. The maximum internal excitation energy E_{COM} available under low energy conditions is

$$E_{COM} = \frac{E_{lab} m_t}{\left[m_i + m_t \left(m_i / m_{ip} \right) \right]} \qquad \text{(Equation 4.10)}$$

where m_{ip} is the impact portion of the projectile ion m_i [46]. The efficiency of collisional activation is dramatically reduced for singly charged ions of mass m_i of greater than 1000 Da [47]. The maximum internal energy deposited by collisional activation is low but is a high efficiency process. Charge remote fragmentations are not normally observed unless the collision energy is very high (> 200 eV) [48] due to the narrower range of internal energies deposited by low energy collisional activation [25].

4.3.(iii) Collision Gas Effects. The choice of collision gas is important for low energy collisional activation as a consequence of the vibrational excitation mechanism. Furthermore, the value of E_{COM} is increased when heavier collision gases such as argon

and xenon are employed [49,50]. Higher collision gas pressures therefore give more efficient collisional activation as a consequence of the increased probability of multiple collisions [13].

4.4. Surface Induced Dissociation.

An alternative to the excitation and fragmentation of selected molecular ions by means of collision with inert gases is that of surface activation. This technique was pioneered by Cooks and coworkers [51,52,53] and is termed surface induced dissociation (SID). A variety of different processes can occur in ion-surface reactions including adduct formation, charge exchange, chemical sputtering and neutralisation of the projectile ion [54]. These processes are summarised in Table 4.1.

Collision type	Description	Representation
Elastic scattering	Reflection	$m_1^+ \xrightarrow{SA} m_1^+$
Inelastic scattering	Surface-induced dissociation	$m_1^+ \xrightarrow{SA} m_1^+$
Reactive scattering	Charge exchange	$m_1^{2+} \xrightarrow{SA} m_1^+$
Reactive scattering	Charge inversion	$m_1^+ \xrightarrow{SA} m_1^-$ or $m_1^- \xrightarrow{SA} m_1^+$
Reactive scattering	Ion-surface reaction	$m_1^+ \xrightarrow{SA} m_1^+$
Reactive scattering	Chemical sputtering	$m_1^+ \xrightarrow{SA} A^+ + m_1$

Table 4.1.

Types of Polyatomic Ion-Surface Collisions.
SA Represents Surface (S) Covered by Adsorbate (A).

The result when polyatomic ions collide with surfaces is dependent on the collision energy [55]. The principal processes for different collision regimes and their applications are presented in Table 4.2. The reactions of interest for the present work

fall in the 5-1000 eV region and these scattering events are those shown in Table 4.1 [55].

Collision Energy (eV)	Process	Use
< 5	Chemical reactions	Surface modification
5-1000	Elastic, inelastic and reactive scattering	Ion and surface characterisation
1000-50,000	Nuclear sputtering	Surface analysis
>50,000	Electronic sputtering	Surface and thin film analysis

Table 4.2.

Phenomena Observed in Polyatomic Ion-Surface Collisions.

Operation of this technique typically requires an instrument to be modified if it is normally employed for CID experiments. A metal target is placed at a focal point in the ion beam after MS1 and the fragments m_2^+ resulting from activation of precursors m_1^+ on collision with the surface (Equation 4.3) are passed by MS2.

$$m_1^+ \xrightarrow{SA} m_1^{+*} \longrightarrow m_2^+ + m_3 \qquad \text{(Equation 4.3)}$$

Ion-surface inelastic collisions have been implemented on several types of mass spectrometer including tandem quadrupole [55,56], time-of-flight [57,58], ion trap [59], Fourier transform-ion cyclotron resonance [60,61] hybrid sector-quadrupole [62,63] and tandem sector instruments [64,65,66]. Many of these instruments have required customisation of the mass analysers to enable SID experiments to be satisfactorily performed. In-line devices must be used for the routine application of SID in 'beam' instruments such as four sector mass spectrometers.

Whereas CID results in the deposition of a broad range of internal energies, including a high energy "tail", SID spectra are normally interpreted as arising from the deposition of a relatively narrow range of energies [67], the average value of which may be varied [68].

The ion excitation mechanism operating in SID depends on the nature of the surface and the collision energy [70]. Electronic excitation is prominent at low collision energies but vibrational activation becomes increasingly important as the collision energy rises. Vibrational excitation is the predominant process on collision with fluorinated surfaces whereas electronic excitation is possible with hydrogenated or deuterated surfaces, especially at low collision energies [70].

Recent work on SID has centred on the use of self-assembled monolayer (SAM) surfaces [69,70] as they are well characterised and easy to produce. Collisions involving SAM surfaces can lead to the deposition of larger internal energies in the precursor ion than is possible by interactions with metal surfaces [71]. More recently, Cooks et al. have used a liquid perfluoropolyether (PFPE) surface for SID experiments to give superior results to SAM surfaces for ion-surface collisions [72]. Employing the liquid surface may present problems in instruments of low pumping power, however, as PFPE has a high vapour pressure.

1 K. R. Jennings, *Int. J. Mass Spectrom. Ion Phys.*, **1**, 227 (1968).

2 W. F. Haddon and F. W. McLafferty, *J. Am. Chem. Soc.*, **90**, 4745 (1968).

3 P. J. Todd and F. W. McLafferty in *Tandem Mass Spectrometry*, (F. W. McLafferty, Ed.), Wiley, New York, chapter 7 (1983).

4 K. Levson, *Fundamental Aspects of Organic Mass Spectrometry*, Verlag Chemie, Weinheim, New York (1978).

5 A. G. Brenton, R. P. Morgan and J. H. Beynon, *Annu. Rev. Phys. Chem.*, **30**, 51 (1979).

6 H. M. Rosenstock, M. B. Wallenstein, A. Wahrhaftig and H. Ehring, *Proc. Natl. Acad. Sci. USA*, **38**, 667 (1952).

7 R. A. Marcus and O. K. Rice, *J. Phys. Colloid Chem.*, **55**, 894 (1951).

8 F. W. McLafferty in *Tandem Mass Spectrometry*, (F. W. McLafferty, Ed.), Wiley, New York, chapter 1 (1983).

9 R. G. Cooks, *Collision Spectroscopy*, Plenum, New York (1978).

10 K. Levson and H. Schwarz, *Mass Spectrom. Rev.*, **2**, 77 (1983).

11 F. W. McLafferty, P. F. Bente III, R. Kornfield, S. C. Tsai and I. Howe, *J. Am. Chem. Soc.*, **95**, 2120 (1973).

12 D. Despeyroux and K. R. Jennings in *Biological Mass Spectrometry. Present and Future* (T. Matsuo, R. M. Caprioli, M. L. Gross and Y. Seyama, Eds.), Wiley and Sons, Chicester, England (1994).

13 R. N. Hayes and M. L. Gross in *Methods in Enzymology, Vol. 193: Mass Spectrometry* (J. A. McLoskey, Ed.), Academic Press, San Diego, chapter 10 (1990).

14 F. Kaplan, *J. Am. Chem. Soc.*, **90**, 4483 (1968).

15 R. A. Yost and C. K. Enke, *Anal. Chem.*, **51**, 1251A (1979).

16 P. H. Dawson, J. B. French, J. A. Buckley, D. J. Douglas and D. Simmons, *Org. Mass Spectrom.*, **17**, 205 (1982).

17 Z. Herman, J. H. Futrell and B. Friedrich, *Int. J. Mass Spectrom. Ion Proc.*, **58**, 181 (1984).

18 D. J. Douglas, *J. Phys. Chem.*, **86**, 185 (1982).

19 H. S. W. Massey and E. H. S. Burhop, *Electronic and Ionic Impact Phenomena*, Oxford University Press, Oxford (1952).

20 S. A. McLuckey, C. E. D. Ouwerkerk, A. J. H. Boerboom and P. G. Kistemaker, *Int. J. Mass Spectrom. Ion Proc.*, **59**, 85 (1984).

21 V. H. Wysocki, H. I. Kenttämaa and R. G. Cooks, *Int. J. Mass Spectrom. Ion Proc.*, **75**, 181 (1987).

22 M. S. Kim and F. W. McLafferty, *J. Am. Chem. Soc.*, **100**, 3279 (1978).

23 H. I. Kenttämaa and R. G. Cooks, *J. Am. Chem. Soc.*, **107**, 1881 (1985).

24 K. Bienmann and H. A. Scoble, *Science*, **237**, 992 (1987).

25 S. A. Carr, B. N. Green, M. E. Hemling, R. Roberts, J. Anderegg and R. Vickers, *Proceedings of the 35th Annual ASMS Conference on Mass Spectrometry and Allied Topics*, Denver, Colorado, 830 (1987).

26 A. E. Ashcroft, R. A. C. Buchanan, G. J. Elliot, S. Evans, D. J. Milton, B. Wright and F. C. Walls, *Proceedings of the 36th Annual ASMS Conference on Mass Spectrometry and Allied Topics*, San Francisco, California, 1156 (1988).

27 J. Bordas-Nagy, D. Despeyroux and K. R. Jennings, *J. Am. Soc. Mass Spectrom.*, **3**, 502 (1992).

28 J. Lemoine, B. Fornet, D. Despeyroux, K. R. Jennings, R. Rosenberg and E. De Hoffmann, *J. Am. Soc. Mass Spectrom.*, **4**, 197 (1993).

29 M. H. Florencio, D. Despeyroux and K. R. Jennings, *Org. Mass Spectrom.*, **29**, 483 (1994).

30 R. S. Bordoli and R. H. Bateman, *Int. J. Mass Spectrom. Ion Proc.*, **122**, 243 (1992).

31 J. Adams, *Mass Spectrom. Rev.*, **9**, 141 (1990).

32 M. L. Gross, *Int. J. Mass Spectrom. Ion Proc.*, **118/119**, 137 (1992).

33 C. D. Bradley, J. M. Curtis, P. J. Derrick and B. Wright, *Anal. Chem.*, **64**, 2628 (1992).

34 J. L. Holmes, *Org. Mass Spectrom.*, **20**, 169 (1985).

35 J. A. Laramee, P. Cameron and R. G. Cooks, *J. Am. Chem. Soc.*, **103**, 12 (1981).

36 C. E. D. Ouwerkerk, S. A. McLuckey, P. G. Kistemaker and A. J. H. Boerboom, *Int. J. Mass Spectrom. Ion Proc.*, **56**, 11 (1984).

37 J. Bordas-Nagy, D. Despeyroux, K. R. Jennings and S. J. Gaskell, *Org. Mass Spectrom.*, **27**, 406 (1992).

38 R. K. Boyd, *Int. J. Mass Spectrom. Ion Proc.*, **75**, 243 (1987).

39 R. K. Boyd, D. J. Harvan and J. R. Hass, *Int. J. Mass Spectrom. Ion Proc.*, **65**, 273 (1985).

40 V. H. Wysocki and M. M. Ross, *Int. J. Mass Spectrom. Ion Proc.*, **104**, 179 (1991).

41 J. H. Scrivens, K. Rollins, R. C. K. Jennings, R. S. Bordoli and R. H. Bateman, *Rapid Commun. Mass Spectrom.*, **6**, 272 (1993).

42 J. E. P. Syka and I. Szabo, *Proceedings of the 36th Annual ASMS Conference on Mass Spectrometry and Allied Topics*, San Francisco, California, 1328 (1988).

43 J. J. Monaghan and B. Wright, *Proceedings of the 36th Annual ASMS Conference on Mass Spectrometry and Allied Topics*, San Francisco, California, 819 (1988).

44 C. Hagg and I. Szabo, *Int. J. Mass Spectrom. Ion Proc.*, **73**, 295 (1986).

45 D. J. Douglas, *J. Phys. Chem.*, **86**, 185 (1982).

46 R. K. Boyd, E. E. Kingston, A. G. Brenton and J. H. Beynon, *Proc. R. Soc. London*, **A392**, 89 (1984).

47 D. F. Hunt, Y. R. Yates III, J. Schabanowitz, S. Winston, and R. C. Hauer, *Proc. Natl. Acad. Sci. USA*, **83**, 13 (1986).

48 A. J. Alexander, P. Thibault, R. K. Boyd, J. M. Curtis and R. L. Rinehart, *Int. J. Mass Spectrom. Ion Proc.*, **98**, 107 (1990).

49 J. A. Nystrom, M. M. Bursey and J. R. Hass, *Int. J. Mass Spectrom. Ion Proc.*, **55**, 263 (1983/1984).

50 M. M. Bursey, J. A. Nystrom and J. R. Hass, *Anal. Chim. Acta.*, **159**, 265 (1984).

51 R. G. Cooks, T. Ast and J. H. Beynon, *Int. J. Mass Spectrom. Ion Phys.*, **16** 348 (1975).

52 R. G. Cooks, D. T. Terwilliger, T. Ast, J. H. Beynon and T. Keough, *J. Am. Chem. Soc.*, **97**, 1583 (1975).

53 Md. A. Mabud, M. J. Dekrey and R. G. Cooks, *Int. J. Mass Spectrom. Ion Phys.*, **67**, 285 (1985).

54 R. G. Cooks, T. Ast, and Md. A. Mabud, *Int. J. Mass Spectrom. Ion Proc.*, **100**, 209 (1990).

55 V. H. Wysocki, J.-M. Ding, J. L. Jones, J. H. Callahan and F. L. King, *J. Am. Soc. Mass Spectrom.*, **3**, 27 (1992).

56 S. Le Meillour, R. Cole, F. Clairet, F. Founier, J.-C. Tabet, T. Blasco, C. Beaugrand and G. Devant, *Adv. Mass Spectrom.*, **11A**, 236 (1989).

57 G. Li, A. Duhr and H. Wollnik, *J. Am. Soc. Mass Spectrom.*, **3**, 487 (1992).

58 E. R. Williams, G. C. Jones, Jr., L. Fang, R. N. Zare, B. J. Garrison and D. W. Brenner, *J. Am. Chem. Soc.*, **114**, 3207 (1992).

59 S. A. Lammert and R. G. Cooks, *J. Am. Soc. Mass Spectrom.*, **2**, 487 (1991).

60 E. R. Williams, K. D. Henry, F. W. McLafferty, J. Shabonitz and D. F. Hunt, *J. Am. Soc. Mass Spectrom.*, **1**, 413 (1990).

61 C. F. Ijames and C. L. Wilkins, *Anal. Chem.*, **62**, 1295 (1990).

62 M. J. Dekrey, Md. A. Mabud, R. G. Cooks and J. E. P. Syka, *Int. J. Mass Spectrom. Ion Proc.*, **67**, 295 (1985).

63 D. E. Riederer, Jr., S. A. Miller, T. Ast and R. G. Cooks, *J. Am. Soc. Mass Spectrom.*, **4**, 938 (1993).

64 A. D. Wright, D. Despeyroux, K. R. Jennings, S. Evans and A. Riddoch, *Org. Mass Spectrom.*, **27**, 525 (1992).

65 R. A. Chorush, I. Vidalsky and F. W. McLafferty, *Org. Mass Spectrom.*, **28**, 1016 (1993).

66 K. L. Schey, D. A. Durkin and K. R. Thornburg, *J. Am. Soc. Mass Spectrom.*, **6**, 257 (1995).

67 M. J. Dekrey, H. I. Kenttämaa, V. H. Wysocki and R. G. Cooks, *Org. Mass Spectrom.*, **21**, 193 (1986).

68 M. Vincenti and R. G. Cooks, *Org. Mass Spectrom.*, **23**, 317 (1988).

69 V. H. Wysocki, J. L. Jones and J.-M. Ding, *J. Am. Chem. Soc.*, **113**, 8970 (1991).

70 B. E. Winger, R. K. Julian Jr., R. G. Cooks and C. E. D. Chidsey, *J. Am. Chem. Soc.*, **113**, 8967 (1991).

71 M. R. Morris, D. E. Riederer, Jr., B. E. Winger, R. G. Cooks, T. Ast and C. E. D. Chidsey, *Int. J. Mass Spectrom. Ion Proc.*, **122**, 181 (1992).

72 T. Pradeep, S. A. Miller and R. G. Cooks, *J. Am. Soc. Mass Spectrom.*, **4**, 769 (1993).

CHAPTER 5.

INSTRUMENTATION.

5.1. Introduction.

The four instruments employed in the present work are described below. Two four sector tandem mass spectrometers were applied to the study of fragmentations effected by SID and high energy CID. SID experiments at low collision energies (lab frame) were performed on the Concept II HH instrument. The ZAB-T was employed for high energy mass spectrometry and tandem mass spectrometry. Low energy MS/MS spectra were obtained from ions generated by electrospray ionisation (ESI) by means of the Quattro II tandem quadrupole instrument. The TOFSPEC was used to analyse ions formed by means of matrix-assisted laser desorption/ionisation (MALDI).

5.2. The Kratos Concept II HH Four Sector Tandem Mass Spectrometer.

All SID experiments were carried out in a Concept II HH four sector tandem mass spectrometer (Figure 5.1) of forward geometry ($E_1B_1E_2B_2$) operating at an accelerating voltage of 8 kV. The upper mass limit of both the first and second mass spectrometers (MS1 and MS2 respectively) at this accelerating potential is 10,000 Da with a maximum resolving power of 100,000 for MS1 and >10,000 for MS2 (earthed collision cell) when a linked scan at constant B/E and the final point detector (PAD4) are employed in MS/MS mode. MS1 and MS2 are modified Nier-Johnson geometry double-focusing instruments consisting of 90° electric sectors of radius 381 mm and 60° inhomogeneous field magnetic sectors of radius 686 mm.

All samples were ionised by means of LSIMS ionisation, with a Kratos caesium ion gun (Figure 2.5) operated at 15 kV and a gun current of 1 mA. Mass selection of precursor ions was performed using MS1. Optimum transmission of the precursor ions was obtained by carefully adjusting the voltages on the focusing and deflecting electrodes of the collision cell (called the "Flexicell") situated in the third field-free region between MS1 and MS2 (Figure 5.2). The collision cell voltage was set to 7800 V with respect to earth potential to give a precursor ion beam translational energy of 200 eV. The indicated pressure in the collision region was approximately $1x10^{-7}$ Torr

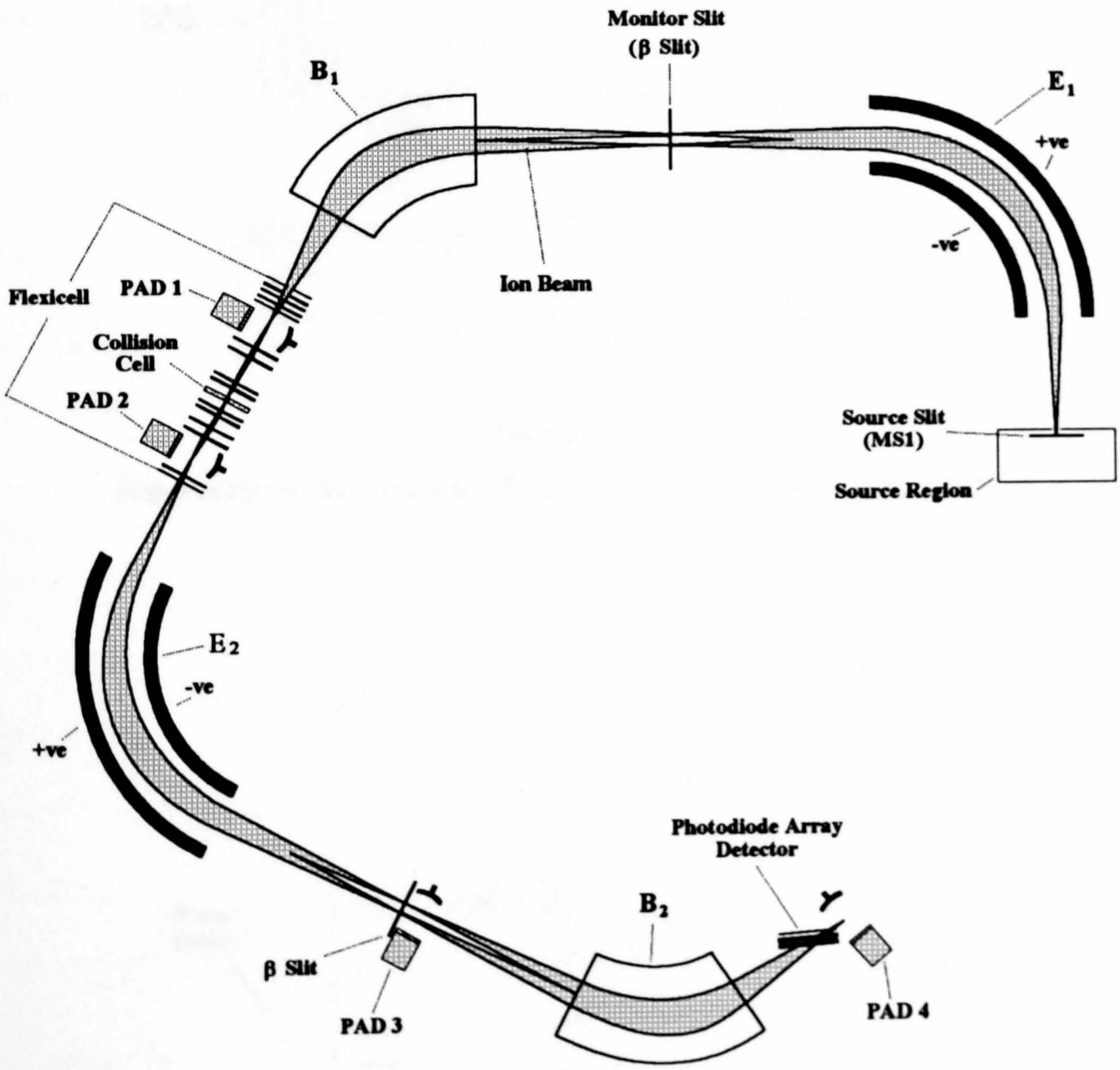

Figure 5.1.

Schematic of the Kratos Concept II HH Four Sector Mass Spectrometer.

in each of these experiments. The collision cell also has a series of lenses after the collision region so that scattered ions can be re-focused into the electrostatic analyser of MS2.

In order to carry out SID experiments the gas collision cell in the third field-free region, which forms the central section of the "Flexicell", was removed and replaced by

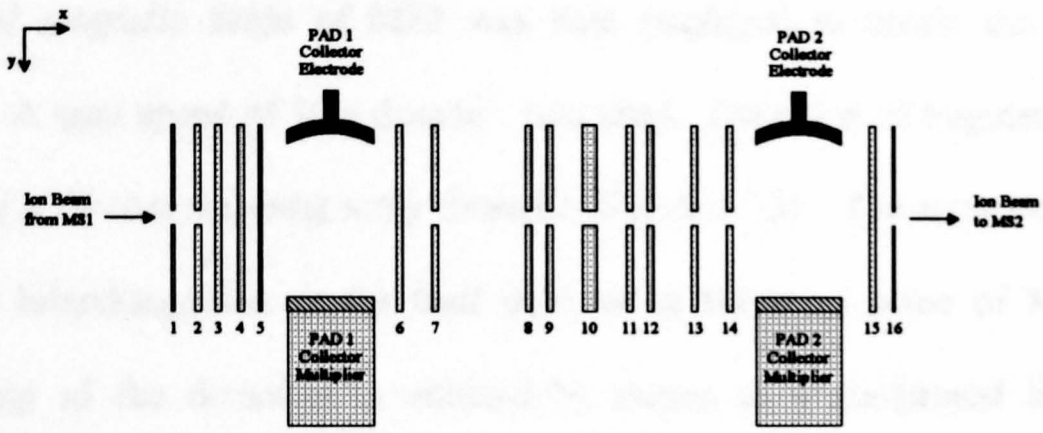

Collector (Resolving) Slit of MS1	1	Earthed Slit	5	Cell Guard	9	Y Focus 4	13
Y Deflection 1	2	Z Deflection 2	6	Collision Cell	10	Y Deflection 4	14
Z Deflection 1	3	Y Focus 1	7	Cell Guard	11	Z Deflection 3	15
Z Focus 1	4	Y Deflection 2 Y Focus 2	8	Y Deflection 3 Y Focus 3	12	Source (Resolving) Slit of MS2	16

Figure 5.2.

Schematic of the Collision Region ("Flexicell") of the Concept.

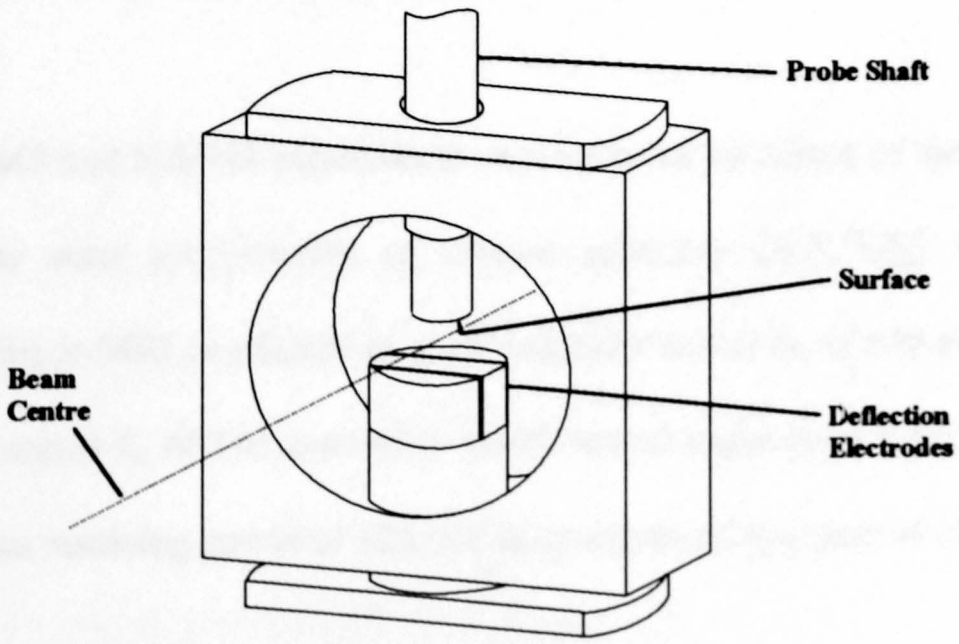

Figure 5.3.

The Collision Cell Modified for SID.

a specially-designed SID unit (Figure 5.3) [1]. This includes a group of three stainless steel electrodes to the first of which a voltage of 8-14 V was applied so that it deflects the precursor ion beam on to a polished stainless steel surface. The third electrode carried a similar voltage to deflect the various fragment ions formed in the SID process into the second electric sector. The second electrode acts as a guard electrode and therefore was at the potential of the "Flexicell". A linked scan (Equation 4.9) of the electric and magnetic fields of MS2 was then employed to obtain the SID mass spectrum. A scan speed of 10 s decade^{-1} was used. Detection of fragment ions was effected by a 25 mm scanning array detector (Figure 3.12). The array detector and PAD4 are interchangeable as the final detector in the focal plane of MS2. The repositioning of the detectors is effected by means of a mechanical linear drive operating on a sliding seal. The acquisition and processing of mass spectra was accomplished by a MACH 3 data system (Kratos Analytical, Manchester, U.K.) and 15-18 individual scans were summed to obtain the spectra.

5.3. The ZAB-T Four Sector Tandem Mass Spectrometer.

High energy MS and MS/MS experiments were effected by means of the ZAB-T four sector tandem mass spectrometer of reverse geometry ($B_1E_1B_2E_2$) (Figure 5.4). Double-focusing in MS1 is effected by a 35° magnetic sector B_1 of 660 mm radius and a 81° electric sector E_1 of 380 mm radius which has an upper mass limit of 15,000 Da and a maximum resolving power of 125,000 at an accelerating potential of 8 kV.

MS2 (B_2E_2) is a Mattauch-Herzog reverse geometry focal plane instrument. It may be employed as the second stage in MS/MS experiments or as a standalone instrument to analyse ions generated in the second source (Source 2). The second magnetic sector B_2 has the same specifications as B_1 and hence a maximum operating mass limit of 15,000 Da at an accelerating potential of 8 kV. The second electrostatic analyser (E_2) is of novel inhomogeneous design (Figure 5.5) which, by varying the voltages applied,

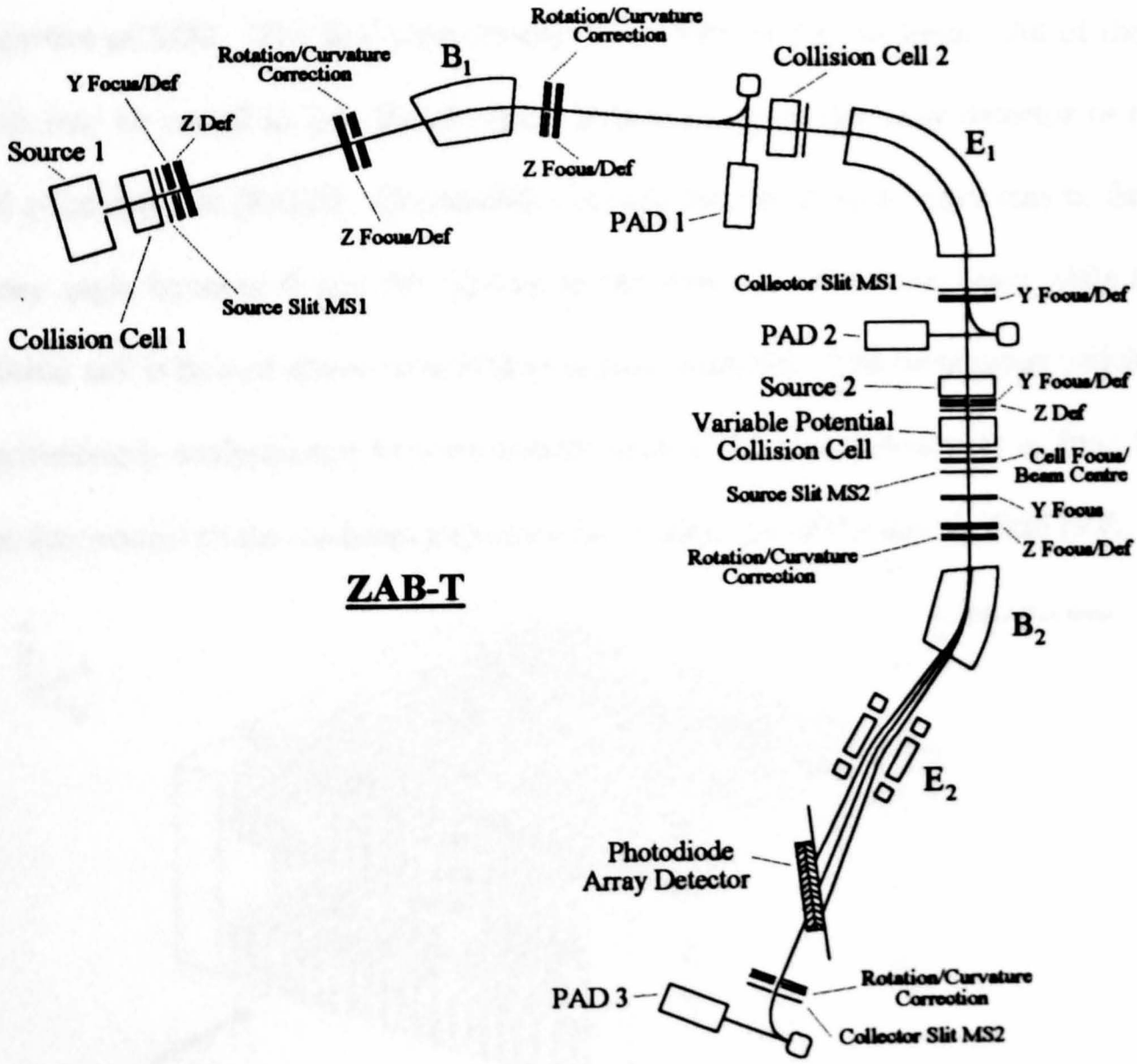

Figure 5.4.

Schematic of the ZAB-T Four Sector Mass Spectrometer.

can change the focal point, focal-plane angle and focal-plane flatness of MS2 [2]. The electric field **E** of this electric sector is described by the quadratic equation below (Equation 5.1) [3].

$$\mathbf{E} = \mathbf{E}_0 + \mathbf{E}_1 y + \mathbf{E}_2 y^2 + \mathbf{E}_3 y^3 \qquad \text{(Equation 5.1)}$$

The normal field of an electric sector is represented by $\mathbf{E}_0$. The focal length is controlled by the $\mathbf{E}_1 y$ term and the value of $\mathbf{E}_2 y^2$ determines the double focusing properties of MS2. The $\mathbf{E}_3 y^3$ term retains the flatness of the ion beam. All of these terms may be varied so that the ion beam is focused on to the array detector or the final point detector (PAD3). The flexibility is such that the array detector may be fixed at any angle between 0 and 90° relative to the direction of the ion beam while the collision cell is floated above or is held at ground potential. The mass range which is simultaneously analysed may be narrowed by rotating the array detector away from the direction normal to the ion beam trajectory and adjustment of the electric field of $\mathbf{E}_2$.

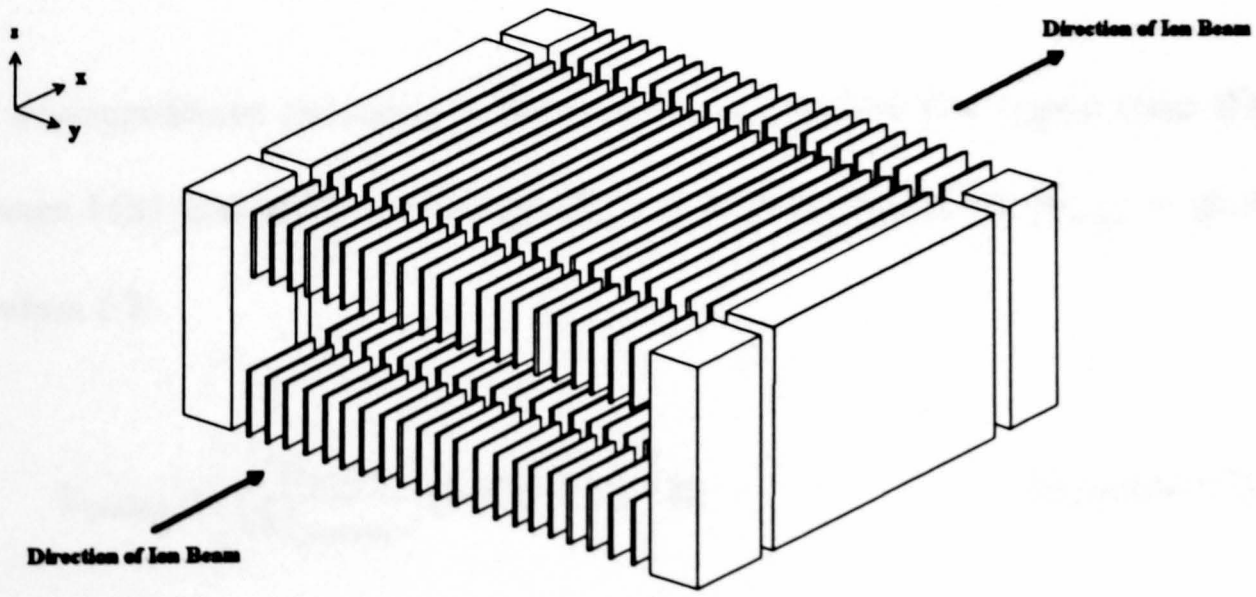

Figure 5.5.

Three-Dimensional Representation of the Inhomogeneous Electric Sector.

In the present work, ions generated in the source were accelerated by a voltage of 8 kV. Mass spectra were acquired on the point detector (PAD2) in the third field-free region of the instrument. Precursor ions for product ion scanning experiments were selected at greater than unit mass resolution (10% valley definition) by means of MS1 (B_1E_1). The ion beam was attenuated by 80 % with argon at 4 keV collision energy in an electrically floated collision cell. The fragment ions formed were re-accelerated by an energy of 4 keV and passed to the detector by a stepped linked scan (Equation 4.9) of MS2. The 75 mm photodiode array detector in the fifth field-free region of the instrument was set at an angle of 30° to the incoming ion beam to give a mass ratio of 1.225:1. Acquisition of 3-10 scans under control of the OPUS data system (VG Organic, Manchester, U.K.) was used to produce the fragment ion spectra.

The wide energy acceptance of MS2 on the ZAB-T instrument was employed to implement precursor ion scanning with the electrically floated collision cell and a collision energy of 2 keV [2].

For decompositions occurring in the collision cell in field free region three (FFR3) between MS1 and MS2, the energy ($E_{product}$) of the product ion $M_{product}$ is given by Equation 5.2:

$$E_{product} = \left[\left(\frac{M_{product}}{M_{precursor}} \right) (1-V_R) + V_R \right] E_0 \qquad \text{(Equation 5.2)}$$

Where $M_{precursor}$ is the mass of the precursor ion, V_R is the ratio of the electrical potential on the gas cell to the accelerating potential (V_{cell}/V_{acc}) and E_0 is the energy of

the precursor ion before collision. An accelerating potential of 8 kV and a cell voltage of 6 kV gives a value of 0.75 for V_R. Furthermore, the energy of the product ion is therefore:

$$8\ kV \geq E_{product} \leq 6\ kV \qquad \text{(Equation 5.3)}$$

This can be represented as a ratio:

$$1.33 \geq E_{product} \leq 1.0 \qquad \text{(Equation 5.4)}$$

The full energy transmission of MS2 is 1.34:1, therefore all M^+ ions generated from precursors M_1^+, M_2^+, M_3^+ and M_4^+ (Scheme 5.1) in the collision cell will be transmitted through MS2 to the final point detector (PAD3).

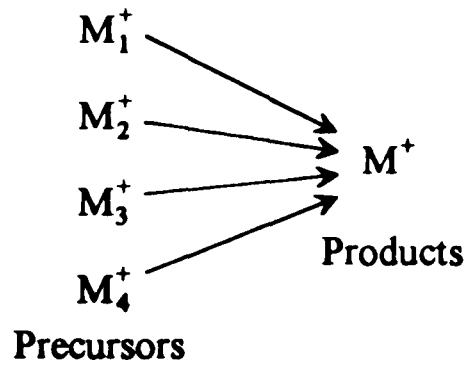

Scheme 5.1.
A Schematic Representation of Precursor Ion Scanning.

The full energy (8 keV) product ion, which is generated when the precursor ion is the same mass and does not fragment in the collision cell, traverses the outer radius of the magnet and the inner radius of the electric sector. Product ions of progressively lower energy pass through the magnet nearer to the inner radius and the outer radius of the electric sector. This is represented schematically in Figure 5.6.

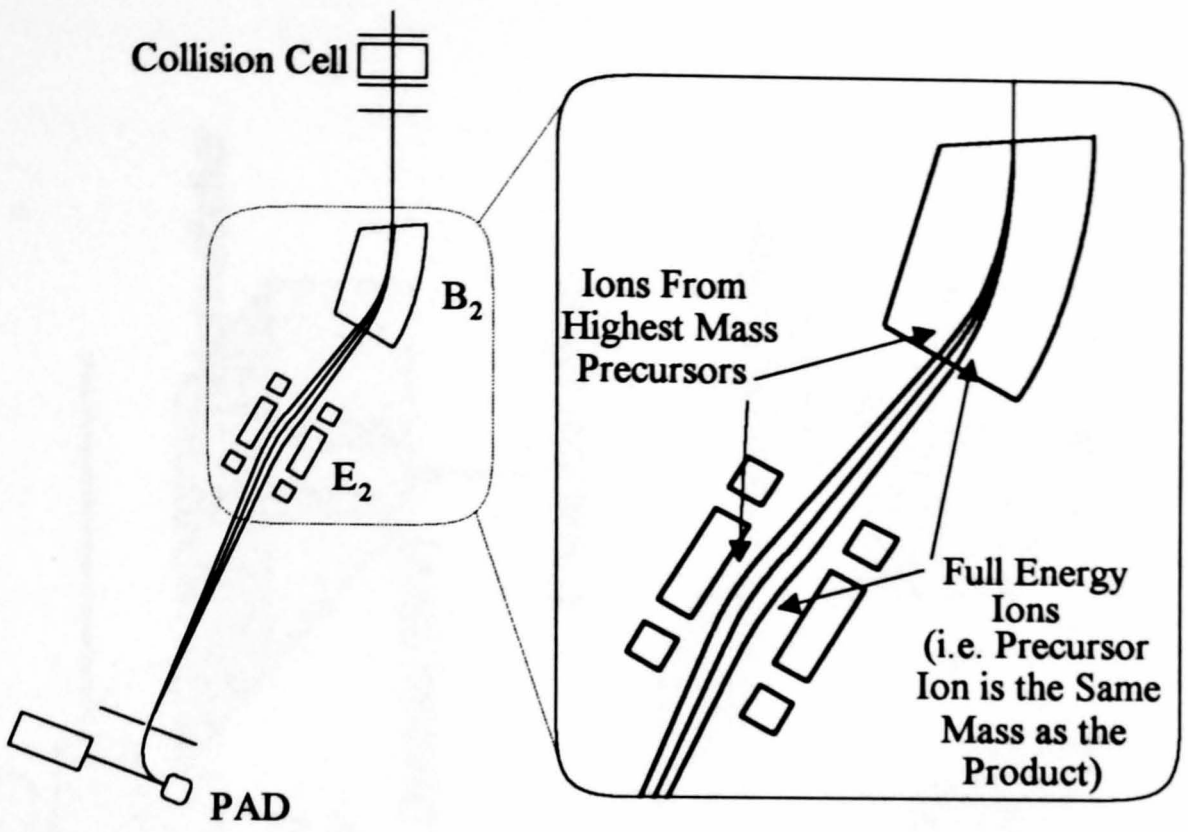

Figure 5.6.

Schematic Representation of the Ion Beam Path (MS2) when Implementing Precursor Ion Scanning on the ZAB-T Instrument.

The instrument is therefore configured such that the MS1 mass spectrum is obtained if PAD 2 is employed. Furthermore, the precursor ion spectrum is acquired if the deflection potential of PAD2 is switched off and PAD3 is used to detect the product ions resulting from dissociation in the collision cell.

5.4. The VG Quattro II Tandem Quadrupole Mass Spectrometer.

The Quattro II tandem quadrupole mass spectrometer of $Q_1 h Q_2$ geometry (Figure 5.7) is equipped with two high performance, research grade quadrupole mass analysers (Q_1 and Q_2) and a r.f.-only hexapole collision cell *h*. Precise alignment of Q_1 and Q_2 in ceramic cradles ensures the production of hyperbolic fields. Ions entering the analyser region are focused into Q_1 by the hexapole entrance filter which also serves to reduce

Figure 5.7.

Three-Dimensional Representation of the Quattro II Tandem Quadrupole Mass Spectrometer.

contamination of Q_1 and Q_2. MS1 and MS2 are equipped with pre- and post-filters which serve to direct the ion beam through the fringing fields of Q_1 and Q_2. The pre-filters also protect the quadrupole rods of Q_1 and Q_2 from contamination.

Ions, generated in the ESI source (Figure 2.6) and mass analysed by Q_1, were detected by the first scintillator detector (Figure 3.10) to obtain the MS1 mass spectrum. CID experiments may alternatively be performed if no voltage is applied to the 'Altrincham' lens, which serves to deflect ions on to the dynode of the first detector. Ions were passed into ***h*** by means of Q_1 and the fragment ions resulting from CID in ***h*** were mass analysed by Q_2 and detected by the second scintillator detector. The collision gas employed for CID experiments was argon at a pressure gauge reading of approximately 1.5×10^{-4} mbar.

5.5. The VG TOFSPEC Linear/Reflectron Time-of-Flight Mass Spectrometer.

MALDI spectra were obtained by means of a TOFSPEC (VG Organic, Manchester, U.K.) time-of-flight mass spectrometer (Figure 5.8) operated in linear or reflectron mode with an acceleration potential of 25 kV. A hybrid detector coupled to the OPUS data system was used to detect the ions generated by MALDI in linear mode. A nitrogen (N_2) laser operated at a wavelength of 337 nm was employed to generate ions by means of MALDI (Figure 2.7). A fine and coarse energy filter effect focusing and adjustment of the laser beam flux respectively on to the target spot under control of the OPUS data system. Directional focusing of the laser beam was adjusted by means

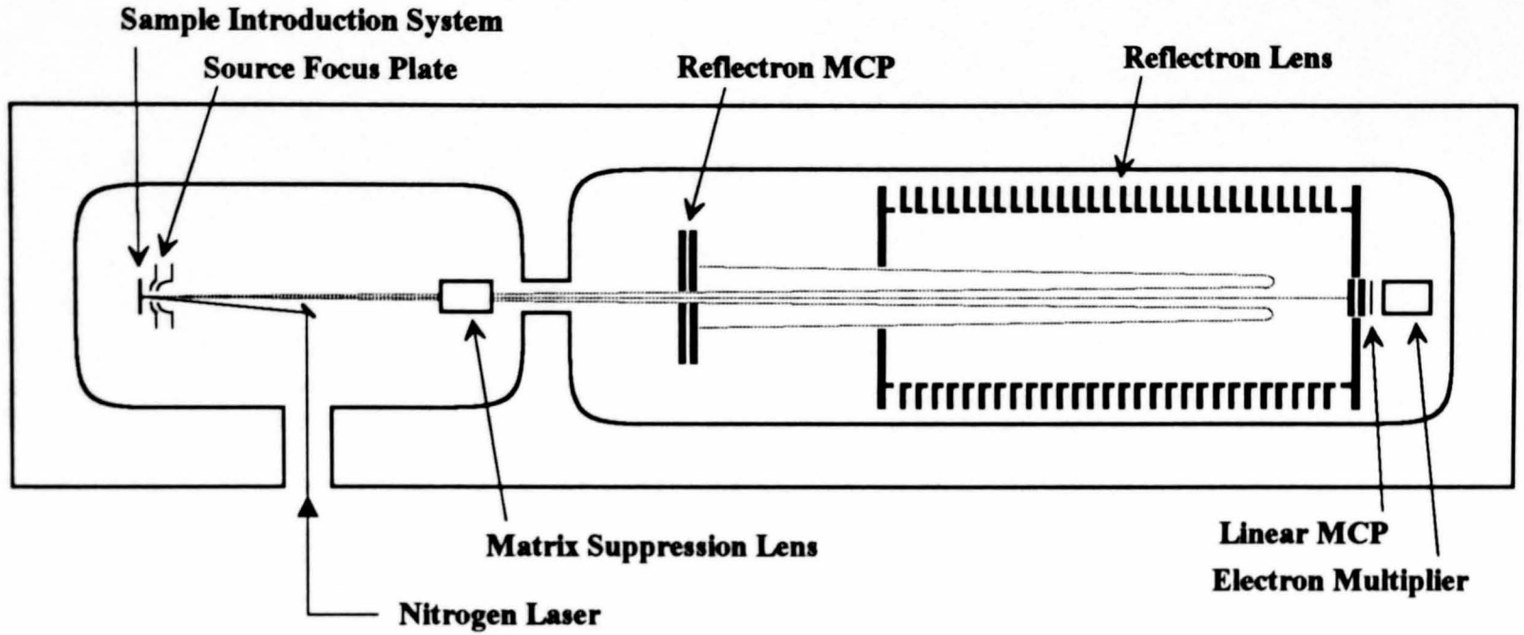

Figure 5.8.

Schematic of the TOFSPEC MALDI-TOF Mass Spectrometer.

of the OPUS data system to obtain the optimum signal for a selected sample. The sample disc allows the analysis of fifteen different samples without removal from the vacuum system of the mass spectrometer.

1 D. Despeyroux, A. D. Wright, K. R. Jennings, S. Evans and A. Riddoch, *Int. J. Mass Spectrom. Ion Proc.*, **122**, 133 (1992).

2 J. H. Scrivens, K. Rollins, R. C. K. Jennings, R. S. Bordoli and R. H. Bateman, *Rapid Commun. Mass Spectrom.*, **6**, 272 (1992).

3 M. L. Gross in *Methods in Enzymology, Vol. 193* (J. A. McCloskey, Ed.), Academic Press, San Diego, Chapter 6 (1990).

CHAPTER 6.

THE OBSERVATION OF BROAD METASTABLE PEAKS IN THE SURFACE INDUCED DISSOCIATION MASS SPECTRA OF PROTONATED AND CATIONATED PEPTIDES.

6.1. Introduction.

A project on the SID of protonated and cationated peptides was undertaken as preliminary work, leading to the technique being used to analyse materials of high RMM (> 2000 Da). The four peptides used were leucine enkephalin, leucine enkephalin amide, methionine enkephalin and methionine enkephalin amide. The structures of these four peptides are shown in Figures 6.1 and 6.2 and their sequence and RMM are presented in Table 6.1. The amide analogues of the enkephalins differ only by the nature of the C-terminus in that the hydroxy group (-OH) is replaced by an amine ($-NH_2$). All peptides were obtained from Sigma Chemical Corporation and used without further purification.

Peptide	Amino Acid Sequence	Monoisotopic Mass (Da)
Leucine enkephalin	Tyr-Gly-Gly-Phe-Leu (YGGFL)	555.3
Leucine enkephalin amide	Tyr-Gly-Gly-Phe-Leu-NH_2 (YGGFL-NH_2)	554.3
Methionine enkephalin	Tyr-Gly-Gly-Phe-Met (YGGFM)	573.2
Methionine enkephalin amide	Tyr-Gly-Gly-Phe-Met-NH_2 (YGGFM-NH_2)	572.2

Table 6.1.

The Sequence and Monoisotopic Mass of the Four Enkephalins Studied.

The enkephalins, leucine enkephalin and methionine enkephalin, are pentapeptides that are natural ligands for opiate receptors [1] and were first sequenced by Hughes et al. in 1975. They are generated in the brain by a protein, proenkephalin A [2].

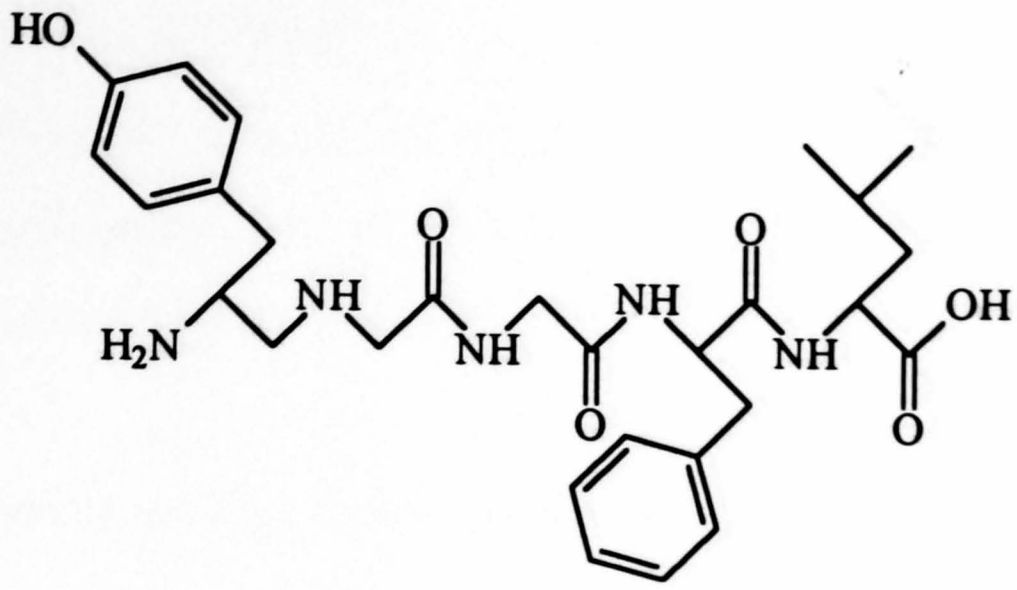

Leucine Enkephalin

YGGFL

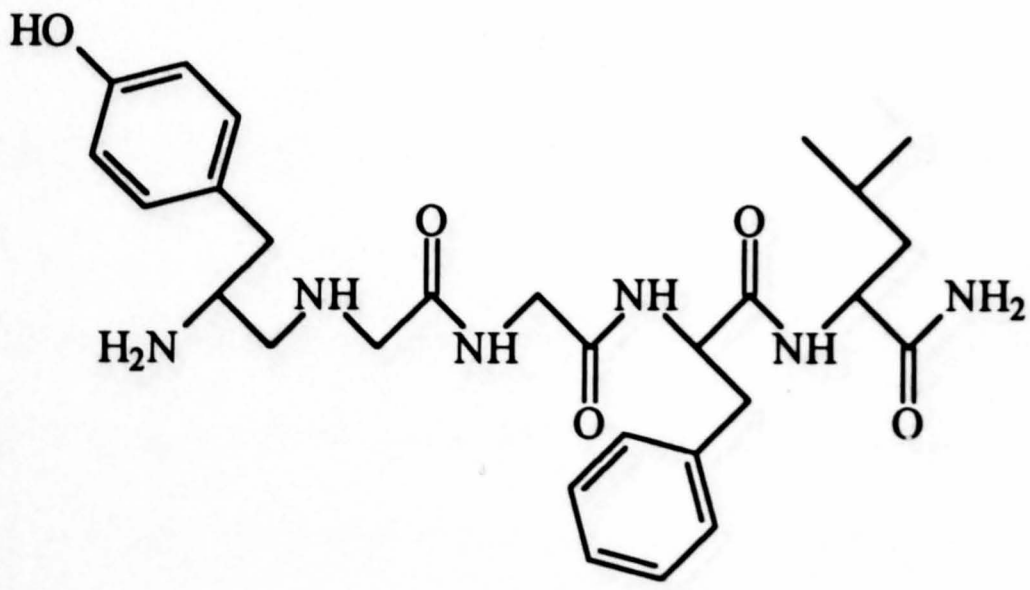

Leucine Enkephalin Amide

YGGFLNH_2

Figure 6.1.

The Structure of Leucine Enkephalin and Leucine Enkephalin Amide.

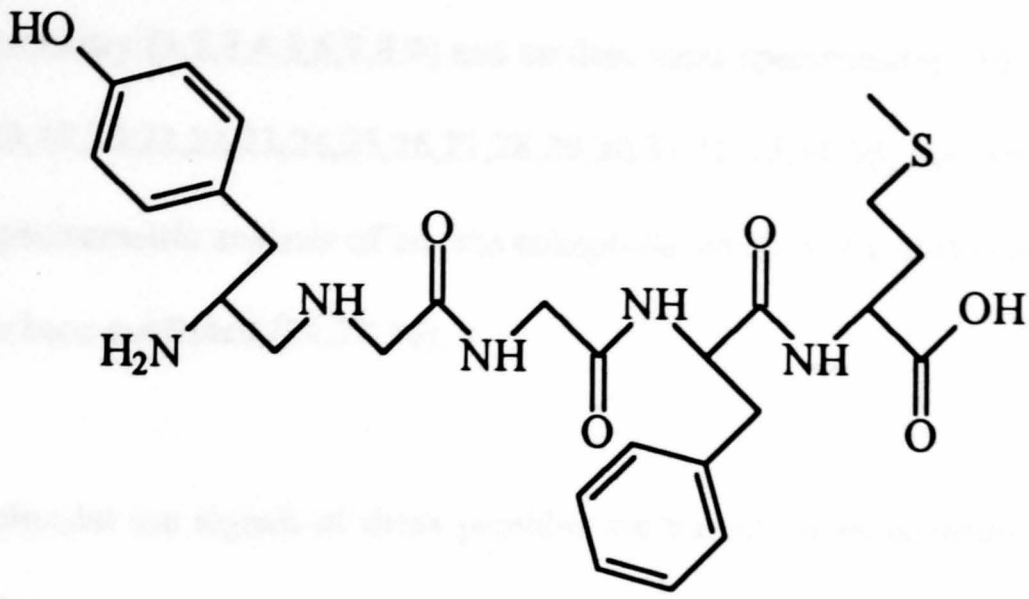

Methionine Enkephalin

YGGFM

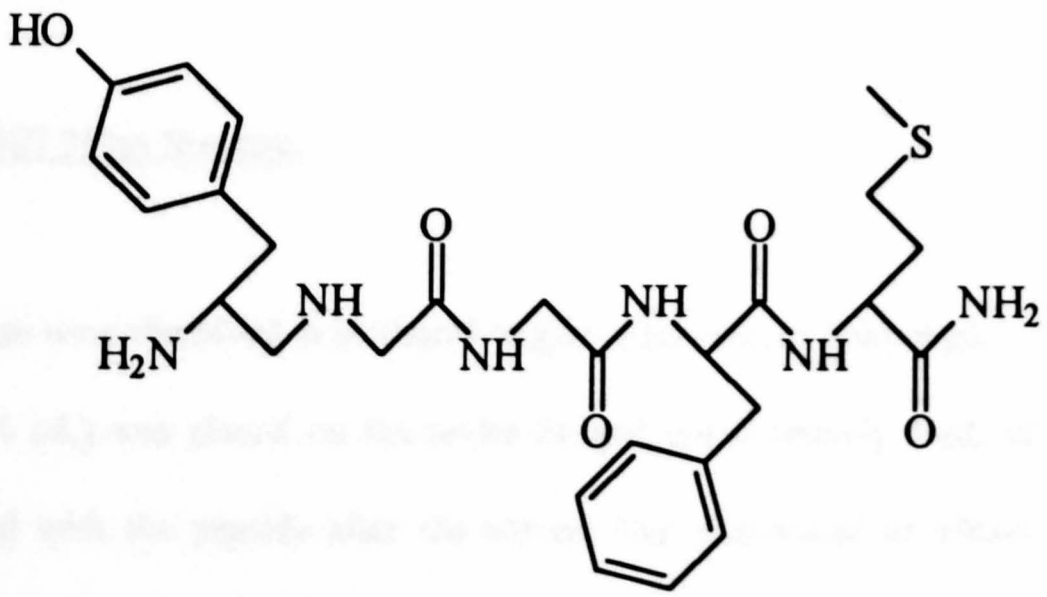

Methionine Enkephalin Amide

YGGFMNH_2

Figure 6.2.

The Structure of Methionine Enkephalin and Methionine Enkephalin Amide.

Leucine enkephalin and methionine enkephalin have been well studied by means of mass spectrometry [1,2,3,4,5,6,7,8,9] and tandem mass spectrometry [10,11,12,13,14, 15,16,17,18,19,20,21,22,23,24,25,26,27,28,29,30,31,32,33,34,35] but few papers on the mass spectrometric analysis of leucine enkephalin amide and methionine enkephalin amide have been published [24,27,36].

Intense molecular ion signals of these peptides are known to be generated by LSIMS [37] and hence these peptides were ideal for preliminary investigations into the suitability of SID as a technique for inducing decomposition of heavier materials. SID spectra from leucine enkephalin that give sequence information have been reported [23]. The first SID spectra of protonated leucine enkephalin amide, methionine enkephalin and methionine enkephalin amide are reported here. The spectra obtained from protonated precursors are also compared to those from cationated species.

6.2. LSIMS Mass Spectra.

All peptides were dissolved in methanol to give a solution of 5 nmol μL^{-1}. The peptide solution (1 μL) was placed on the probe tip and approximately 1 μL of matrix was then mixed with the peptide after the solvent had evaporated to obtain ions of the protonated sample molecule. In order to obtain SID mass spectra of cationated peptides, 1 μL of cation acetate (0.5 M in MeOH) was first deposited on the probe tip and the solvent removed by gentle heating. The peptide solution was then placed on the probe tip and the solvent again removed by moderate heating. Approximately 1 μL of matrix was then mixed with the peptide. The matrices used for each compound are

shown in Table 6.1. The only criterion of matrix selection in these experiments was the intensity of the ion of interest at the point detector preceding the collision cell, in the third field free region (PAD1). Abundant ion signals of higher mass adducts such as $[M+2Cat-H]^+$, where Cat is either Na^+ or Li^+ from sodium and lithium salts respectively, were observed when certain matrices were employed with the analyte and cation salt. The abundance of protonated peptide ions (MH^+) detected at PAD1 was much higher (when no alkali metal salt was added) than that of the respective cationated species ($[M+Cat]^+$) generated with addition of $LiCOOCH_3$ or $NaCOOCH_3$.

Peptide	Matrix
Leucine enkephalin MH^+	Glycerol
Leucine enkephalin $[M+Li]^+$	"Magic bullet" +TFA
Leucine enkephalin $[M+Na]^+$	Thioglycerol
Leucine enkephalin amide MH^+	Glycerol
Methionine enkephalin MH^+	Thioglycerol +TFA
Methionine enkephalin $[M+Li]^+$	Thioglycerol +TFA
Methionine enkephalin amide MH^+	Thioglycerol +TFA

Table 6.2.

Matrix Selection for SID Spectra.

6.3. SID Spectra of Protonated and Cationated Peptides.

6.3.(i) Leucine Enkephalin. The SID mass spectra of leucine enkephalin, MH^+ m/z 556.4, $[M+Li]^+$ m/z 562.3 and $[M+Na]^+$ m/z 578.3, are shown in Figures 6.3, 6.4 and 6.5 respectively. The collision energy (E_{coll}) was 200 eV in all SID experiments. The

differences of signal-to-noise ratios observed in SID spectra are in part due to the abundance of precursor ions before collision (see Section 6.2). The fragment ions of protonated leucine enkephalin (Figure 6.3) have a much higher absolute signal-to-noise ratio than those from lithiated or sodiated precursors (Figures 6.4 and 6.5).

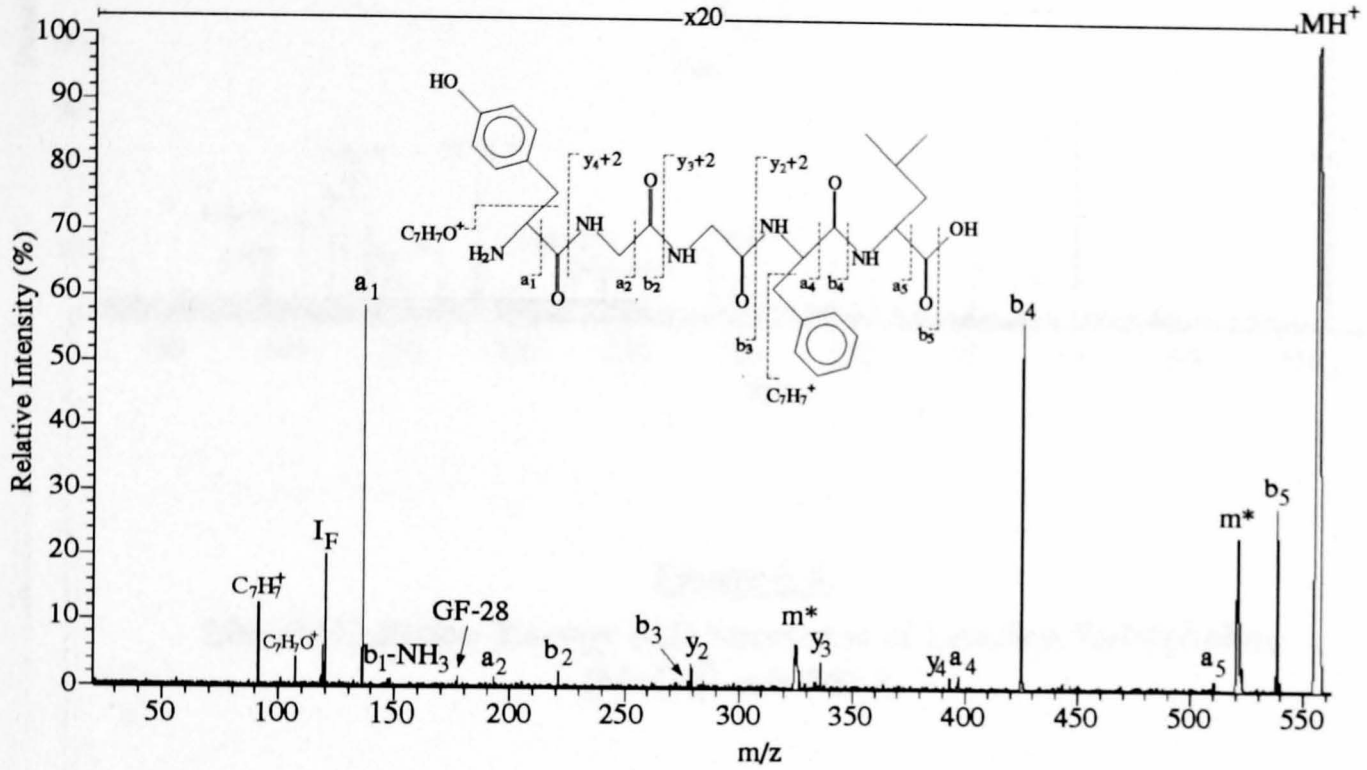

Figure 6.3.

200 eV Collision Energy SID Spectrum of Leucine Enkephalin, MH^+ m/z 556.3.

Leucine Enkephalin (MH^+)			
Mass of Fragment Ion (Da)	**Assignment**	**Mass of Fragment Ion (Da)**	**Assignment**
556	MH^+	278	b_3
538	b_5	221	b_2
510	a_5	193	a_2
425	b_4	177	FG-28
397	a_4	136	a_1
393	y_4+2	120	F-28
336	y_3+2	107	$[C_7H_7O]^+$
279	y_2+2	91	$[C_7H_7]^+$

Table 6.3.

Masses and Assignments of Fragment Ions Observed in the SID Spectrum of Leucine Enkephalin (MH^+).

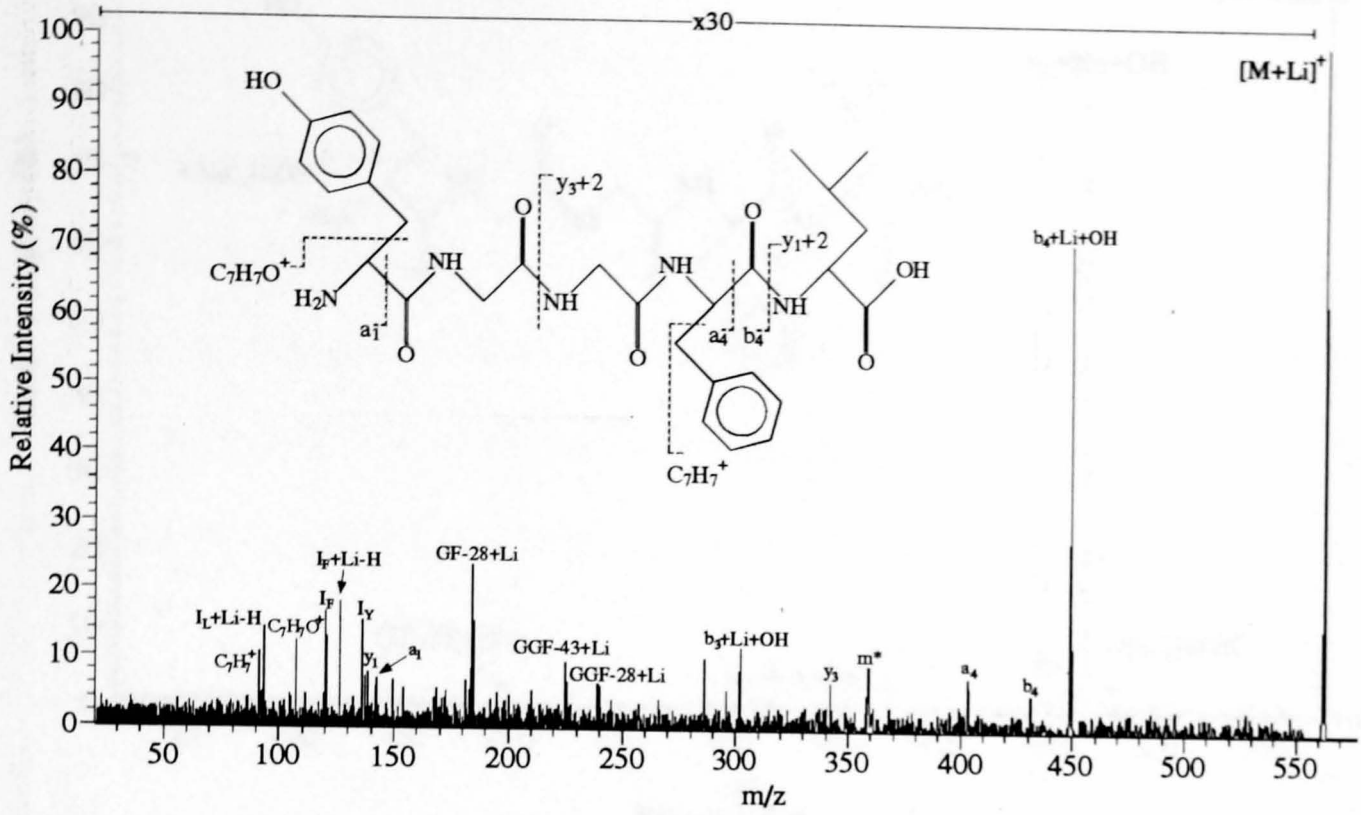

Figure 6.4.

200 eV Collision Energy SID Spectrum of Leucine Enkephalin, $[M+Li]^+$ m/z 562.3.

Leucine Enkephalin ($[M+Li]^+$)			
Mass of Fragment Ion (Da)	**Assignment**	**Mass of Fragment Ion (Da)**	**Assignment**
562	$[M+Li]^+$	225	GGF-43+Li
449	b_4+Li+OH	184	GF-28+Li
431	b_4+Li-H	136	a_1
403	a_4+Li-H	126	F-28+Li-H
342	y_3+Li+H	120	F-28
302	b_3+Li+OH	107	$[C_7H_7O]^+$
240	GGF-28+Li	91	$[C_7H_7]^+$

Table 6.4.

Masses and Assignments of Fragment Ions Observed in the SID Spectrum of Leucine Enkephalin ($[M+Li]^+$).

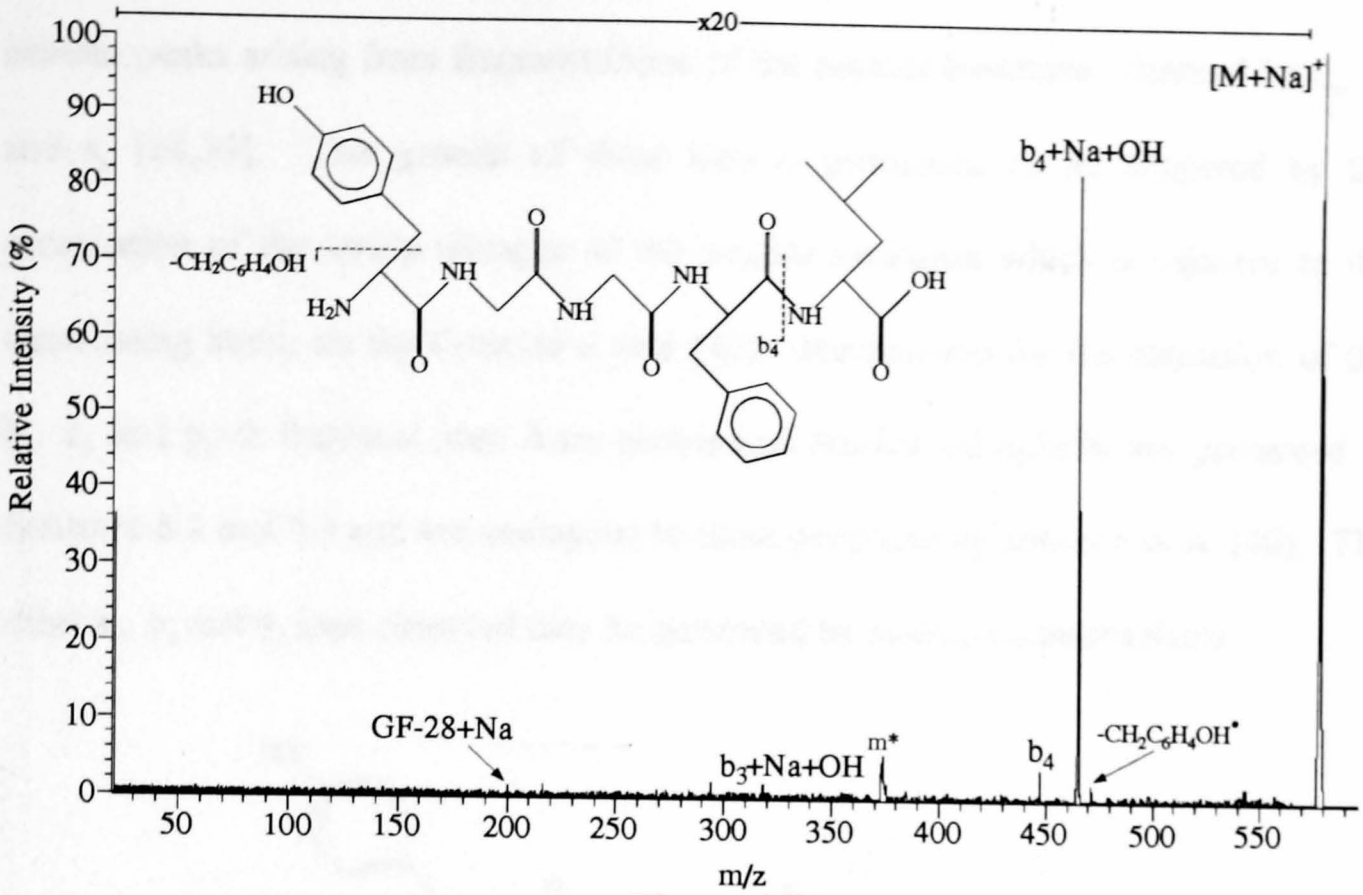

Figure 6.5.

200 eV Collision Energy SID Spectrum of Leucine Enkephalin, $[M+Na]^+$ m/z 578.3.

Leucine Enkephalin ($[M+Na]^+$)			
Mass of Fragment Ion (Da)	**Assignment**	**Mass of Fragment Ion (Da)**	**Assignment**
578	$[M+Na]^+$	447	b_4+Na-H
471	$-CH_2C_6H_4OH$	318	b_3+Na+OH
465	b_4+Na+OH	200	GF-28+Na

Table 6.5.

Masses and Assignments of Fragment Ions Observed in the SID Spectrum of Leucine Enkephalin ($[M+Na]^+$).

The proposed fragmentation pathways for the decomposition of precursor ions from leucine enkephalin are also shown in Figures 5.3, 5.4 and 5.5. The masses of the fragment ions seen and their assignments are recorded in Tables 5.3, 5.4 and 5.5. The nomenclature used is that of Biemann [38] which was adapted from that proposed by Roepstorff and Fohlman [39]. All MS/MS spectra recorded in these experiments

contain peaks arising from fragmentations of the peptide backbone, denoted by b_n, y_n and a_n [38,39]. The genesis of these ions is postulated to be triggered by the protonation of the amide nitrogen of the peptide backbone which is adjacent to the dissociating bond, on the C-terminal side [40]. Mechanisms for the formation of the b_4, a_4 and y_2+2 fragment ions from protonated leucine enkephalin are presented in Schemes 6.1 and 6.2 and are analogous to those proposed by Johnson et al. [40]. The other a_n, b_n and y_n ions observed may be generated by analogous mechanisms.

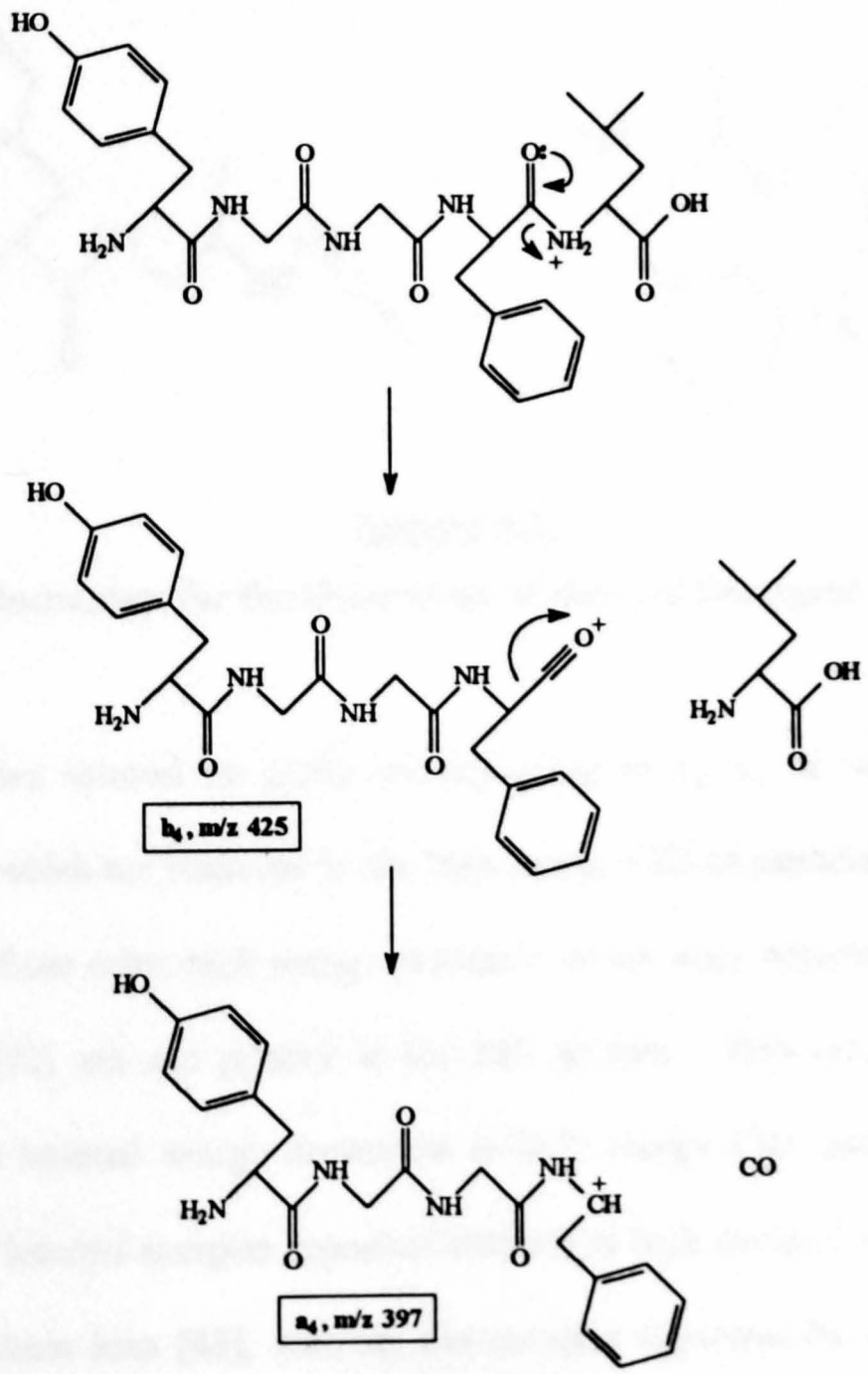

Scheme 6.1.

Mechanisms for the Generation of the b_4 and a_4 Fragment Ions.

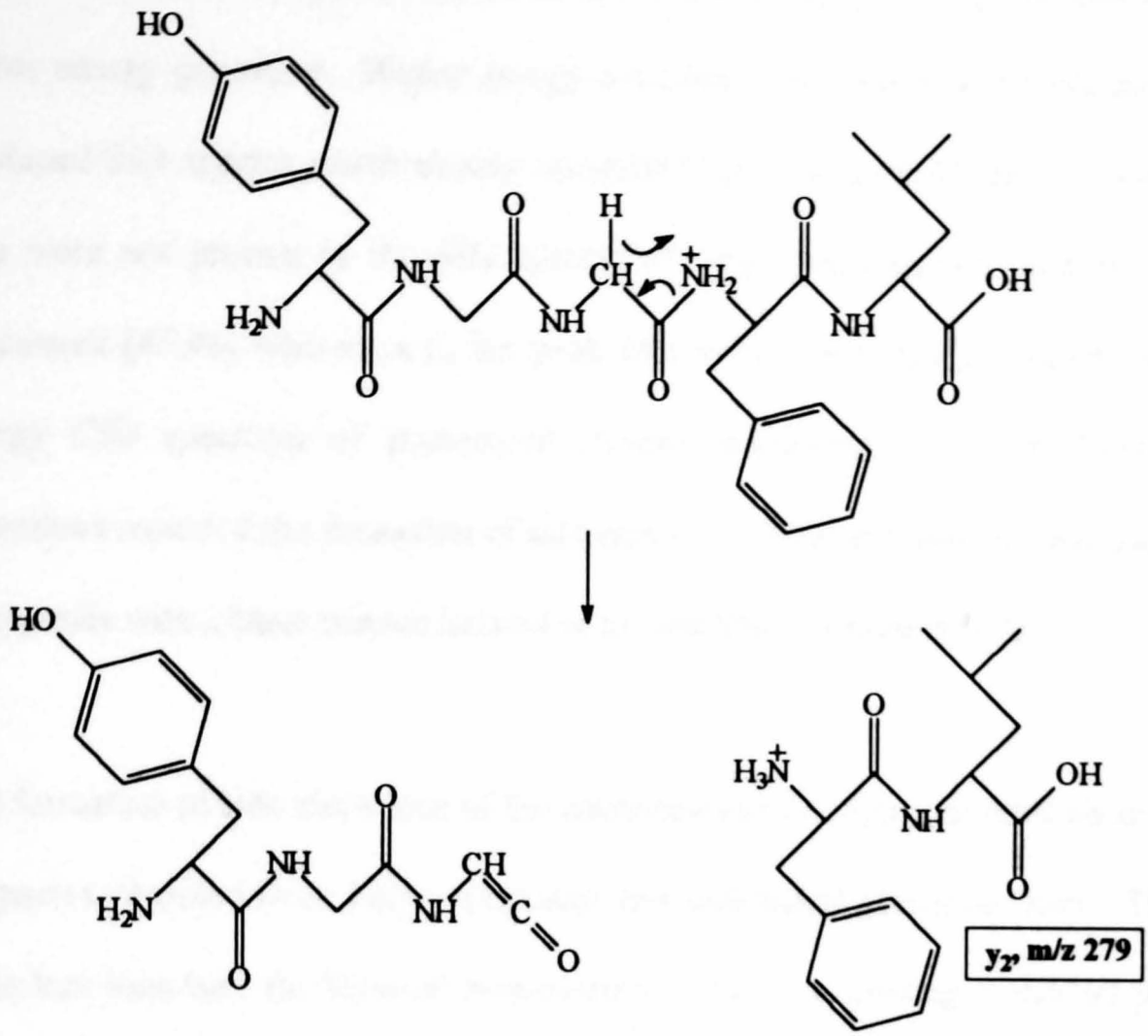

Scheme 6.2.

Mechanism for the Generation of the y_2+2 Fragment Ion.

The SID spectra showed no peaks corresponding to d_n, v_n, or w_n side chain loss fragment ions which are observed in the high energy CID of peptides [41]. Fragment ions resulting from other high energy processes which were observed in high energy CID spectra [42] are not present in the SID spectra. This can be explained by comparing the internal energy deposition in high energy CID and SID. The high energy 'tail' of internal energies deposited inherent in high energy CID can lead to the formation of these ions [43], whereas the energies deposited by SID are not high enough in the experiments reported here. Increasing the angle at which the precursor ions hit the surface should give a greater average deposition of internal energy to the

ion and so increase the possibility of the formation of d_n, v_n and w_n ions that arise from higher energy processes. Higher energy deposition was achieved by this method and produced SID spectra which closely resembled high energy CID spectra [44]. These ions were not present in the SID spectra of other peptides recorded on the same instrument [45,46] whereas a d_5 ion peak of very low intensity is present in the high energy CID spectrum of protonated leucine enkephalin [37]. McCormack and coworkers reported the formation of side chain loss fragment ions (w_n ions) in the SID of peptides with a basic residue located at or near the C-terminus [47].

The formation of side chain ions of the phenylalanine and tyrosine residues is observed in spectra obtained from both protonated and cationated precursor ions. These side chain loss ions take the form of even-electron cations, appearing at m/z 91 $[C_7H_7]^+$, a tropylium ion, and m/z 107, $[C_7H_7O]^+$, from phenylalanine and tyrosine respectively. Proposed mechanisms of formation of these two fragment ions are shown in Schemes 6.3 and 6.4. Both mechanisms involve 1,2-hydrogen rearrangement to generate a neutral peptide (YGGGL and GGGFL respectively). The ion can also be considered to have a seven-membered ring structure, a tropylium ion, as shown in Figure 6.6. These ions are presumed to be generated by a lower energy route than that of ions formed by the loss of a side-chain since the latter are not observed in the spectra. A peak at m/z 91 was reported by Tabet et al. in the SID spectrum from a protonated leucine enkephalin precursor ion and was presumed to occur via a high energy process [31].

The fragment ions observed in the SID mass spectra of the cationised adduct generally retain the cation. Fragment ions formed where the metal is lost include F, an

immonium ion from the phenylalanine residue, and a_1, in which the peptide backbone is cleaved at the tyrosine residue (RH)C-C(O) bond. The spectrum of $[M+Li]^+$ (Figure 6.3) also contains peaks due to rearrangements in the peptide such as the $[b_4+Li+OH]^+$ peak which is the dominant fragment ion peak. A mechanism for this process (Scheme 6.5) has been proposed by Renner and Spiteller involving initial interactions between lithium, bound to the C-terminus, and the carbonyl oxygen of the phenylalanine residue [48]. These spectra are similar to CID spectra obtained on the same instrument at a collision energy of 4 keV, differing predominantly in the intensity of the fragment ions [37].

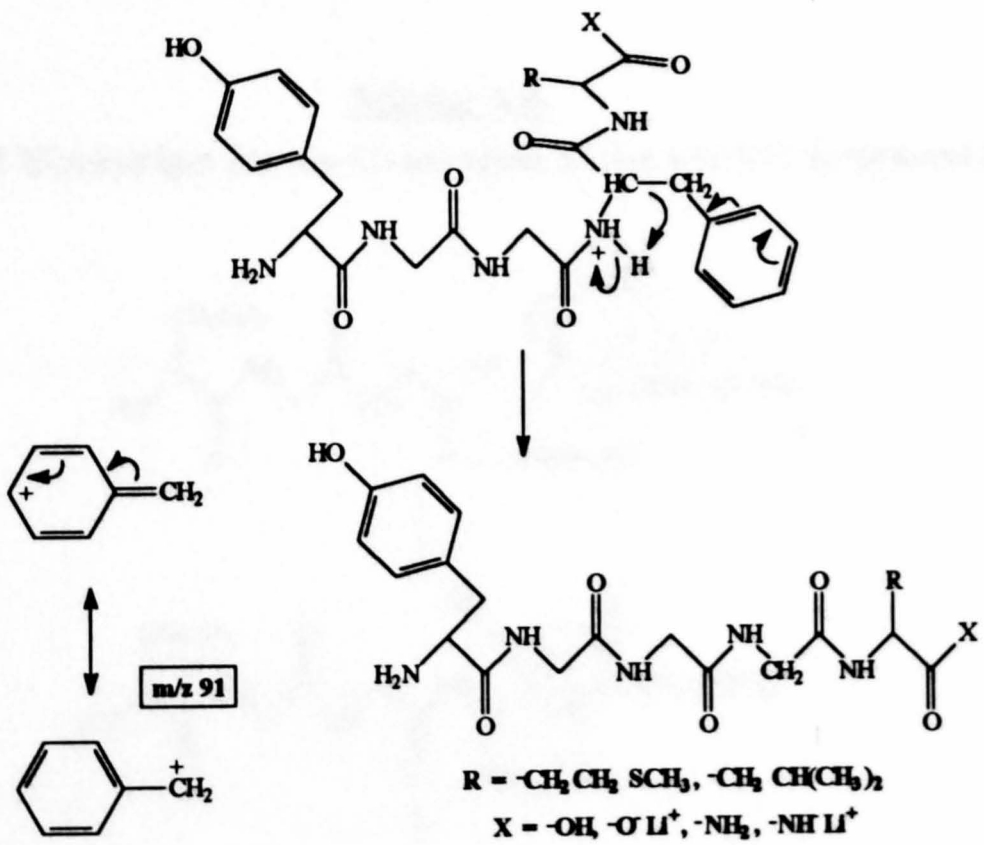

Scheme 6.3.

Proposed Mechanism for the Generation of the m/z 91 Fragment Ion.

Figure 6.6.

Another Representation of the Structure of the m/z 91 Fragment Ion, a Tropylium Ion ($C_7H_7^+$).

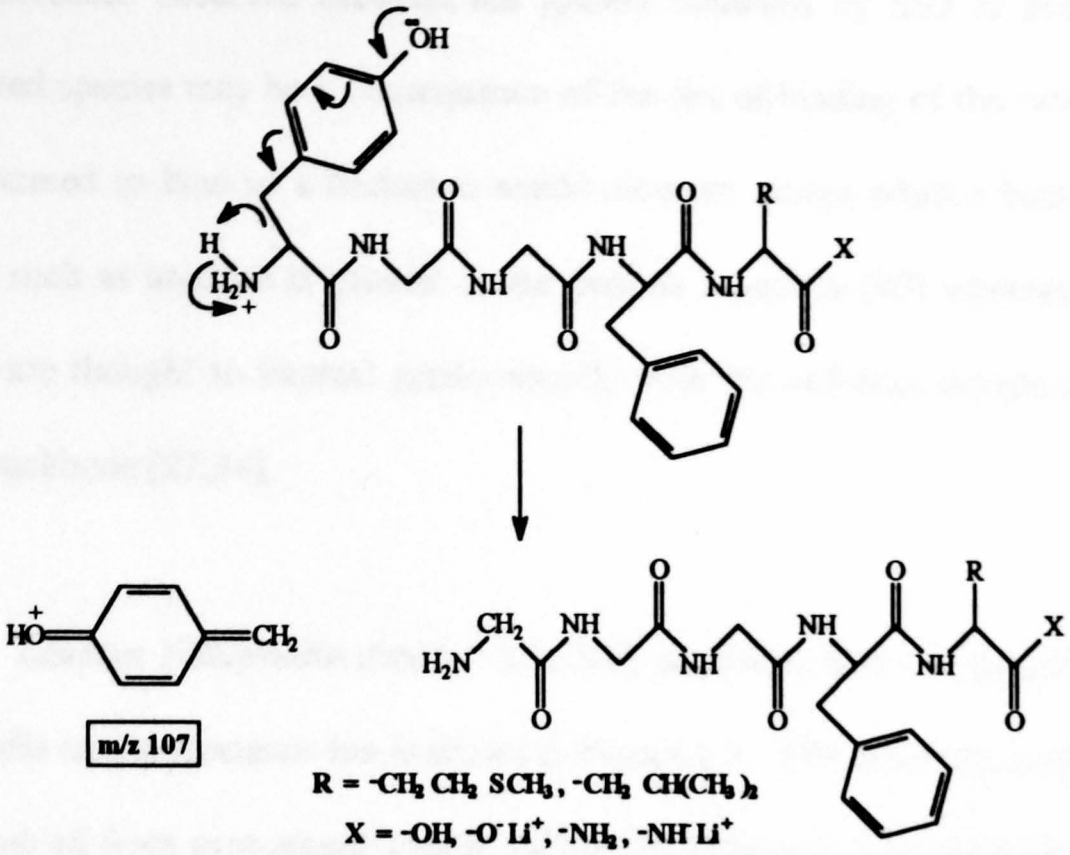

Scheme 6.4.

Proposed Mechanism for the Generation of the m/z 107 Fragment Ion.

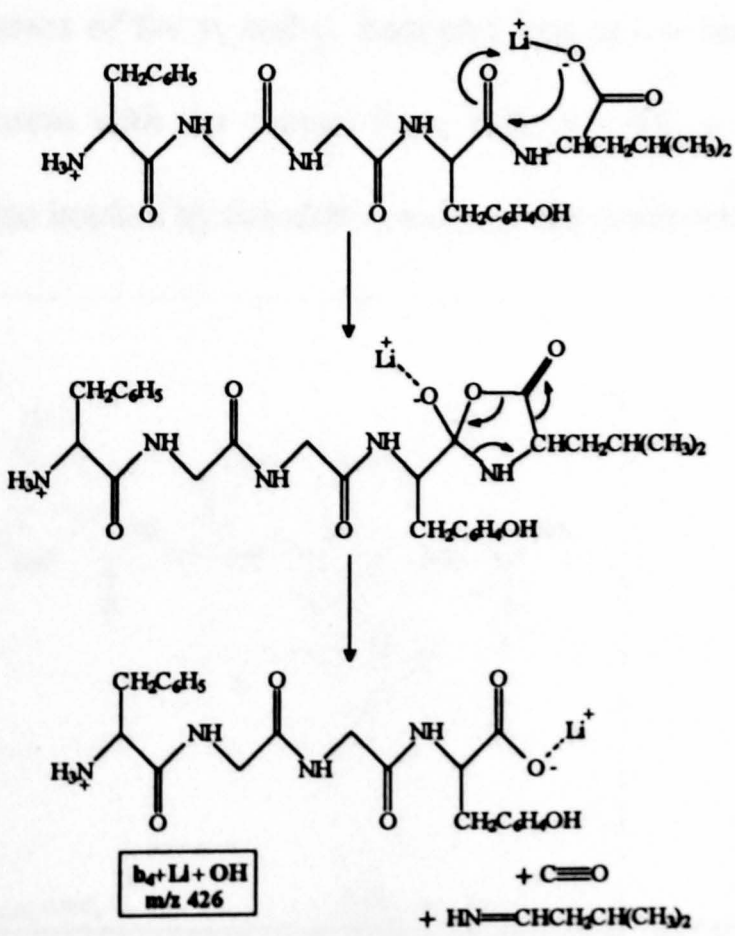

Scheme 6.5.

Mechanism of Generating the b_4+Li+OH Fragment Ion.

The differences observed between the spectra observed by SID of protonated and cationated species may be a consequence of the site of binding of the cation. Protons are presumed to bind to a backbone amide nitrogen except when a basic amino acid residue such as arginine is present in the peptide sequence [40] whereas alkali metal cations are thought to interact predominantly with the carbonyl oxygen atoms of the amide backbone [27,34].

6.3.(ii) Leucine Enkephalin Amide. The SID spectrum from the protonated leucine enkephalin amide precursor ion is shown in Figure 6.7. The spectrum is very similar to that obtained from protonated leucine enkephalin (Figure 6.3) in the high mass region of the spectrum (>m/z 250). The intensity of the low mass ions (<m/z 250) is very weak in Figure 6.7. This is possibly due to differences in the tuning of MS2. The shift of 1 Da in the masses of the y_3 and y_2 fragment ions in the leucine enkephalin amide spectrum is consistent with the change from -OH to -NH_2 at the C-terminus of the peptide. This is also implied by the shift in mass of the precursor ion by 1 Da.

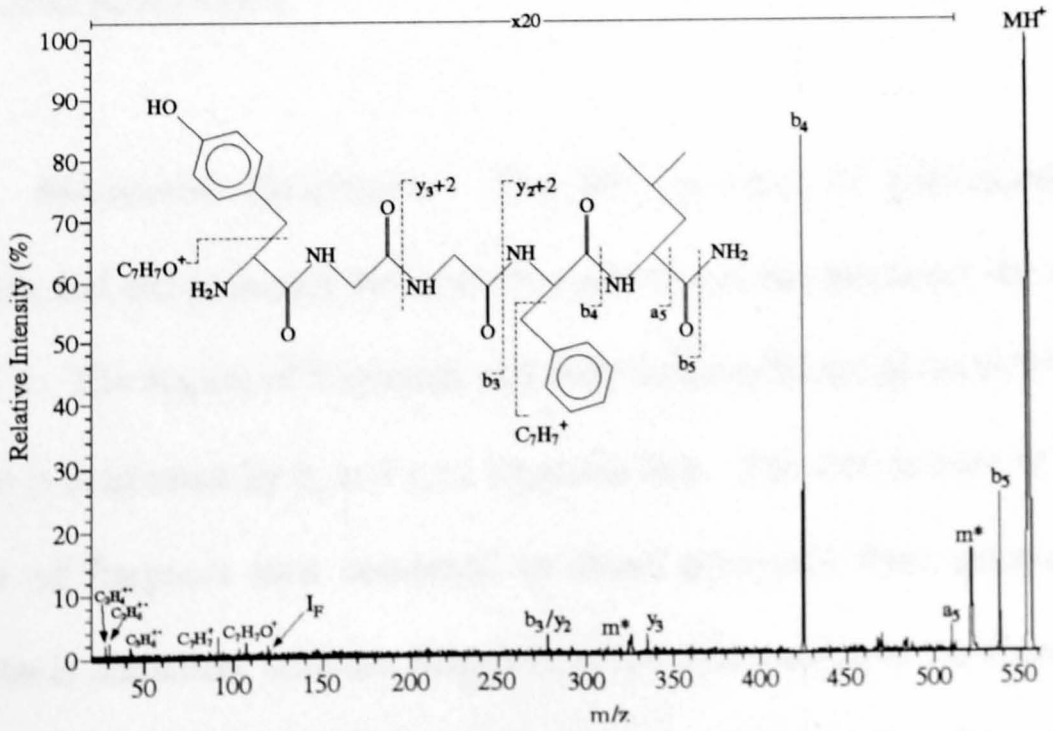

Figure 6.7.

200 eV Collision Energy SID Spectrum of Leucine Enkephalin Amide, MH^+ m/z 555.3.

Leucine Enkephalin Amide (MH^+)			
Mass of Fragment Ion (Da)	**Assignment**	**Mass of Fragment Ion (Da)**	**Assignment**
555	MH^+	107	$[C_7H_7)]^+$
538	b_5	91	$[C_7H_7]^+$
510	a_5	42	$[C_3H_6]^+$
425	b_4	30	$[C_2H_6]^+$
335	y_3+2	28	$[C_2H_4]^+$
278	y_2+2		

Table 6.6.

Masses and Assignments of Fragment Ions Observed in the SID Spectrum of Leucine Enkephalin Amide (MH^+).

Three peaks at low mass (m/z 28, 30 and 42) appear in the SID mass spectrum of leucine enkephalin amide which are not observed for the other peptides. These peaks are possibly generated by sputtering of hydrocarbons from the stainless steel surface on collision which is a charge transfer reaction (see Table 4.1). Chemical sputtering of small molecules from the collision surface has often been observed in SID experiments [49]. The origin of these hydrocarbons is probably pump oil which has coated the stainless steel surface [49].

6.3.(iii) Methionine Enkephalin. The SID spectrum of protonated methionine enkephalin and the proposed dissociation pathways of the precursor ion are shown in Figure 6.8. The masses of fragments and their assignment are given in Table 6.5. The spectrum is dominated by b_n and y_n+2 fragment ions. The shift in mass of 18 Da of the y_n series of fragment ions compared to those generated from protonated leucine enkephalin is consistent with the change in amino acid residue at the C-terminus as the RMM of leucine and methionine differs by 18 Da. An immonium ion generated from methionine (I_m) also indicates that this residue is present.

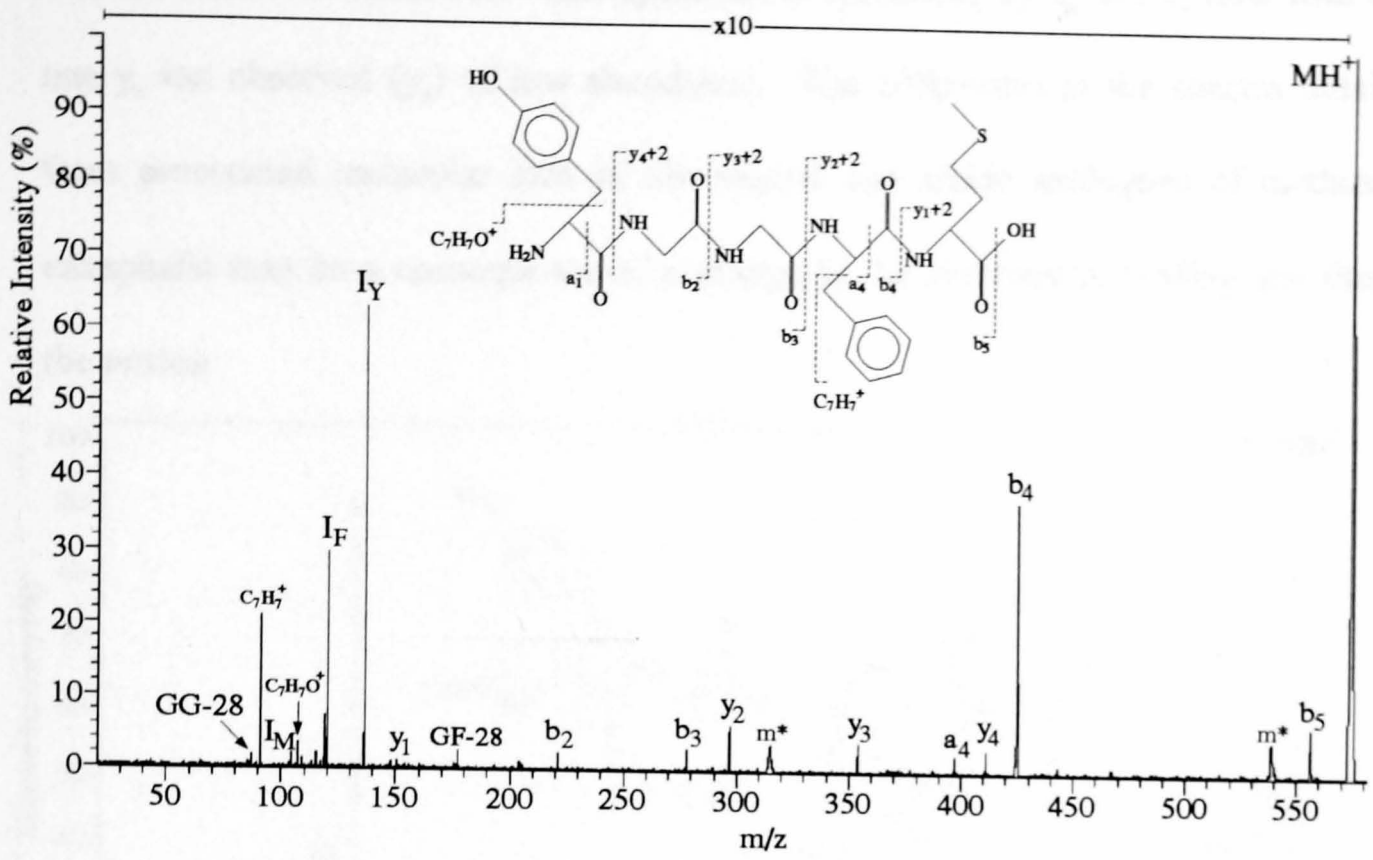

Figure 6.8.

200 eV Collision Energy SID Spectrum of Methionine Enkephalin, MH^+ m/z 574.3.

Methionine Enkephalin (MH^+)			
Mass of Fragment Ion (Da)	**Assignment**	**Mass of Fragment Ion (Da)**	**Assignment**
574	MH^+	221	b_2
556	b_5	177	FG
425	b_4	150	y_1+2
411	y_4+2	136	a_1
397	a_4	120	F-28
354	y_3+2	107	$[C_7H_7]^+$
297	y_2+2	104	M-28
278	b_3	91	$[C_7H_7]^+$

Table 6.7.

Masses and Assignments of Fragment Ions Observed in the SID Spectrum of Methionine Enkephalin (MH^+).

6.3.(iv) Methionine Enkephalin Amide. The SID mass spectrum of methionine enkephalin amide is shown in Figure 6.9. The masses and assignment of the fragment

ions are shown in Table 6.8. This spectrum is dominated by a_n and b_n ions with only one y_n ion observed (y_1) of low abundance. The differences in the spectra obtained from protonated molecular ions of the neutral and amide analogues of methionine enkephalin may be a consequence of a change in the preferential binding site/sites of the proton.

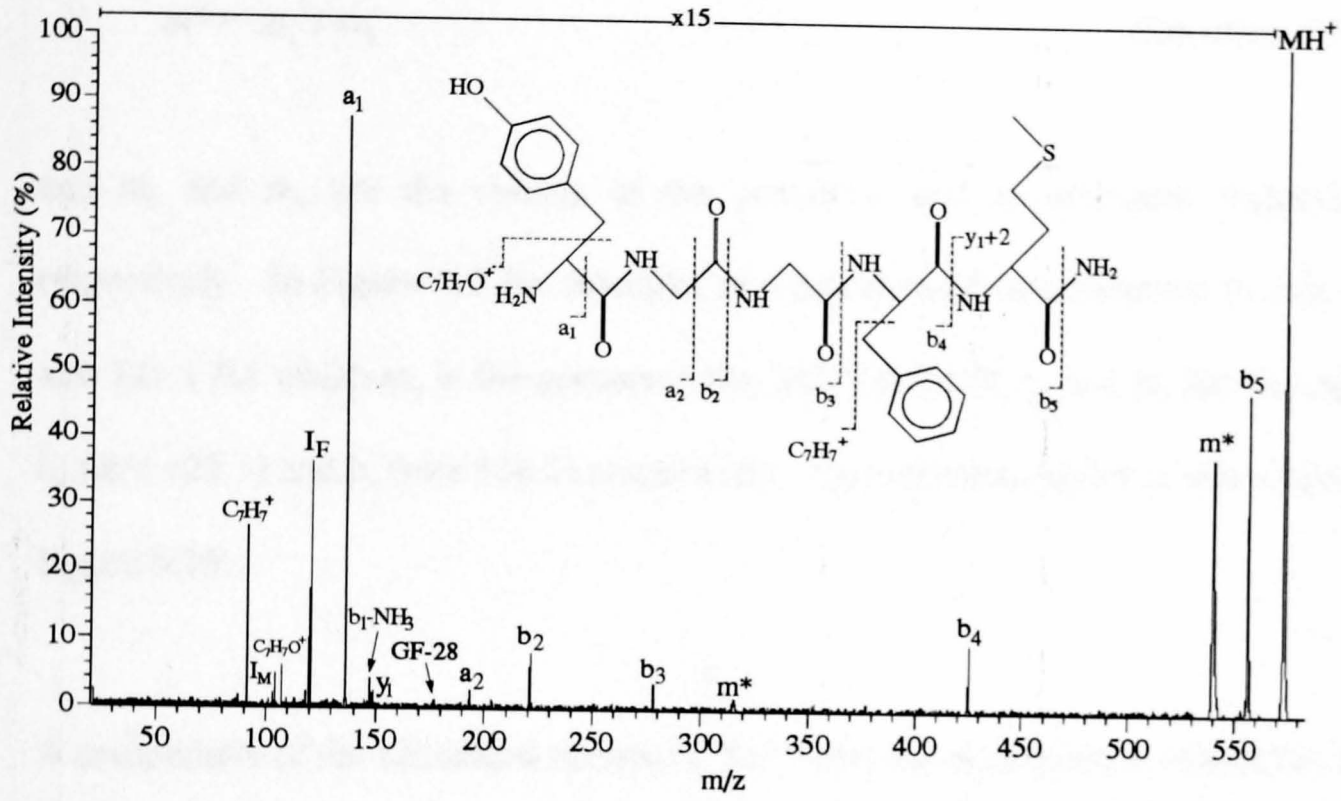

Figure 6.9.

200 eV Collision Energy SID Spectrum of Methionine Enkephalin Amide, MH^+ m/z 573.3.

Methionine Enkephalin Amide (MH^+)			
Mass of Fragment Ion (Da)	**Assignment**	**Mass of Fragment Ion (Da)**	**Assignment**
573	MH^+	147	b_1-NH_3
556	b_5	136	a_1
425	b_4	120	F-28
278	b_3	107	$[C_7H_7)]^+$
221	b_2	104	M-28
193	a_2	91	$[C_7H_7]^+$
177	FG	87	GG-28
149	y_1+2		

Table 6.8.

Masses and Assignments of Fragment Ions Observed in the SID Spectrum of Methionine Enkephalin Amide (MH^+).

6.4. The Observation of Broad Metastable Peaks in SID Spectra.

In all SID mass spectra recorded in these experiments some broad peaks were observed at an apparent mass-to-charge ratio of m* where

$$m^* = m_2^2 / m_1 \qquad \text{(Equation 6.1)}$$

and m_1 and m_2 are the masses of the precursor and an abundant fragment ion respectively. In Figure 6.3 for example, two broad peaks are observed at m/z 521.0 and 325.1 for which m_1 is the precursor ion, MH^+, m/z 556.4, and m_2 has the mass of b_4 (m/z 425.1) and b_5 (m/z 538.3) respectively. An expanded region of this spectrum is Figure 6.10.

A comparison of the calculated masses of "m*" with the experimental results for all the protonated and cationated peptides studied is shown in Table 6.9. The experimental

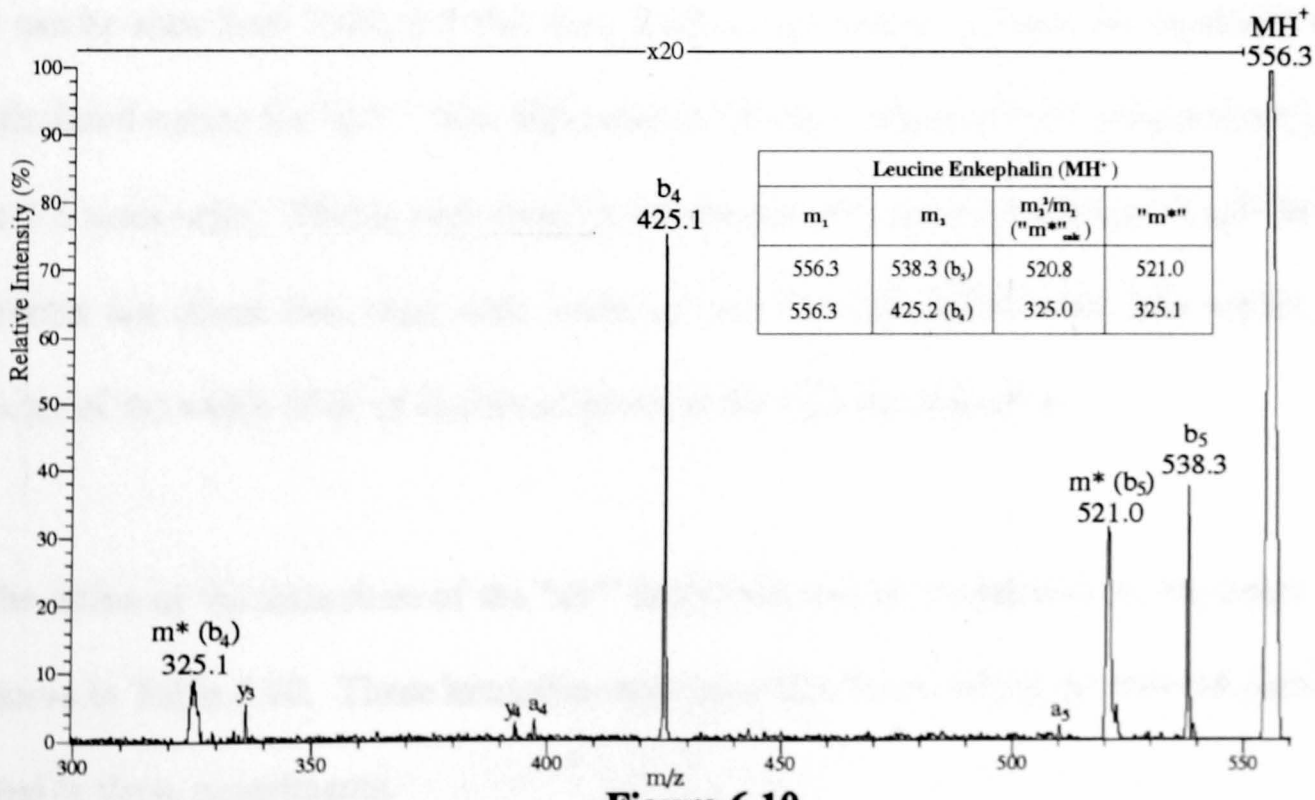

Figure 6.10.

Expanded Region (m/z 300-560) of the 200 eV Collision Energy SID Spectrum of Leucine Enkephalin, MH^+ m/z 556.3.

values for m_1 and m_2 were used to find the values of "m*"$_{calc}$ (shown as m_2^2/m_1 values in Table 6.9) so that they could be compared with the measured values for "m*" (shown as "m*" in Table 6.9).

Peptide	m_1	m_2	m_2^2/m_1	"m*"
Leucine enkephalin MH^+	556.3 556.3	538.3 425.2	520.8 325.0	521.0 325.1
Leucine enkephalin $[M+Li]^+$	562.3	449.2	358.9	359.0
Leucine enkephalin $[M+Na]^+$	578.3	465.2	374.2	373.7
Leucine enkephalinamide MH^+	555.3 555.3	538.3 425.2	521.8 325.6	521.7 325.6
Methionine enkephalin MH^+	574.2 574.2	556.2 425.2	538.8 314.8	538.7 315.0
Methionine enkephalin $[M+Li]^+$	580.2	449.2	347.8	347.5
Methionine enkephalinamide MH^+	573.2 573.2	556.2 425.2	539.7 315.4	539.8 315.3

Table 6.9.

Comparing Calculated and Experimental Values of "m*".

It can be seen from Table 6.9 that there is good agreement between the measured and calculated values for "m*". The difference in the two values of "m*" ranges from zero to 0.5 mass units. This is well within experimental error as the actual ion peaks in the spectra are about two mass units wide, so that the calculated value falls within the range of the width of all of the broad peaks in the SID mass spectra.

The ratios of the intensities of the "m*" ion peaks to their respective m_2 ion peaks are shown in Table 6.10. These intensities are compared for all of the protonated peptides used in these experiments.

Peptide	"m*"	"m*": m_2 Intensity Ratios	"m*"	"m*": m_2 Intensity Ratios
Leucine enkephalin MH^+	325.1	0.12	521	0.84
Leucine enkephalinamide MH^+	325.6	0.04	521.7	0.67
Methionine enkephalin MH^+	315	0.2	538.7	0.8
Methionine enkephalinamide MH^+	315.3	0.1	539.8	0.7

Table 6.10.

Comparing "m*": m_2 Intensity Ratios for Protonated Peptides.

The intensity ratio $I(m^*)/I(m_2)$ falls as m_2/m_1 falls in the SID mass spectrum of a given sample. The intensity ratios of the higher mass "m*" ion peaks are from four to approximately seventeen times larger than for their lower mass counterparts. The intensity ratios are all shown to two decimal places as the precision of these figures is approximately ±0.02.

These broader "m*" ion peaks in the SID mass spectra can be explained by considering the scan law for MS2 of the four sector mass spectrometer (see Equation 4.9). A plot of the magnetic sector field strength against the electric sector field strength to show how the scan law varies when the collision cell is floated at different values above earth potential is given in Figure 6.11 [50]. It can be seen that as the cell voltage is increased so that the collision energy approaches zero, the scan law curve departs increasingly from the constant B/E scan law and approaches the normal B-scan at fixed E, especially when the mass of the neutral fragment lost is relatively low. This can be seen even more clearly in Figure 6.12 which shows schematically the scan law curves

for the normal B-scan at fixed E and for the Kratos Concept II HH used in these experiments with the cell voltage of 7800 V. The energy band pass of the electric sector and the overlap region of the two scans where the broad peaks can be observed are also shown schematically.

The broader peaks in the mass spectrum arise from the decomposition of m_1^+ in the field-free region between the electric sector and the magnetic sector of MS2. The scan law for the four sector is close to the normal B-scan at masses near to the precursor ion mass. As the energy band pass of the electric sector of MS2 is roughly ±3%, this could allow precursor ions with the correct energy for metastable decomposition to be transmitted to the field-free region when the magnet current is appropriate for the transmission of these ions. The ions dissociate between E_2 and B_2 to give the ions responsible for the broad peaks in the SID spectra (see Figure 6.12).

Support for this explanation can be found in the shapes of these broader peaks, their intensities and their positions in the mass spectrum. These peaks have the shape typical of metastable ion peaks which are formed in the field-free region between the electric sector and the magnetic sector of a forward geometry mass spectrometer, arising from decomposition of m_1^+ ions in this region of the instrument. The broader peaks are in fact due to fragment ions of mass m_2, but they appear at an apparent lower mass because they have a lower energy. If the fragment ions are formed in the collision cell, they are re-accelerated as m_2^+ ions and so appear at m_2^+ on the mass scale. If m_1^+ ions are re-accelerated and fragment in the field-free region before the

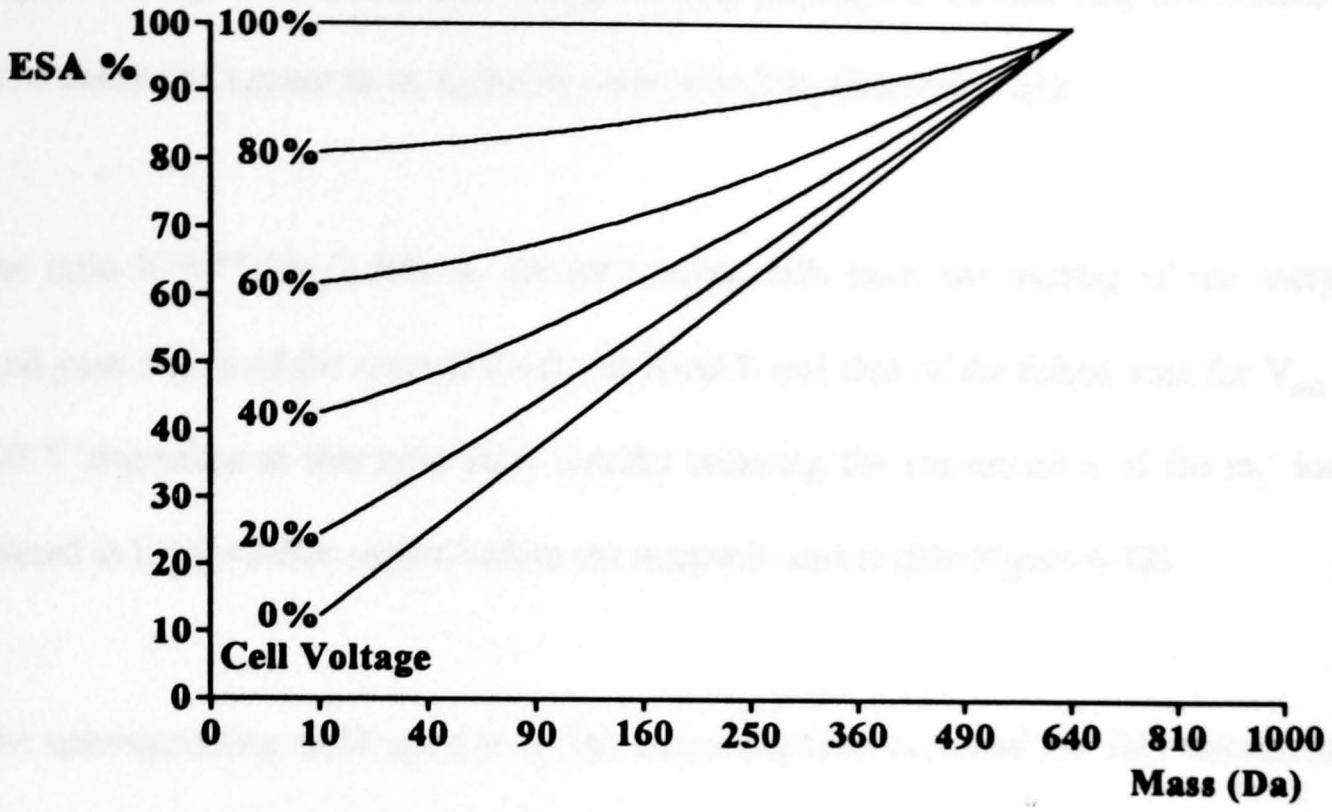

Figure 6.11.

Graph of ESA Potential Against Apparent Mass at Collision Cell Voltages of 0, 20, 40, 60, 80, and 100% of the Accelerating Voltage.

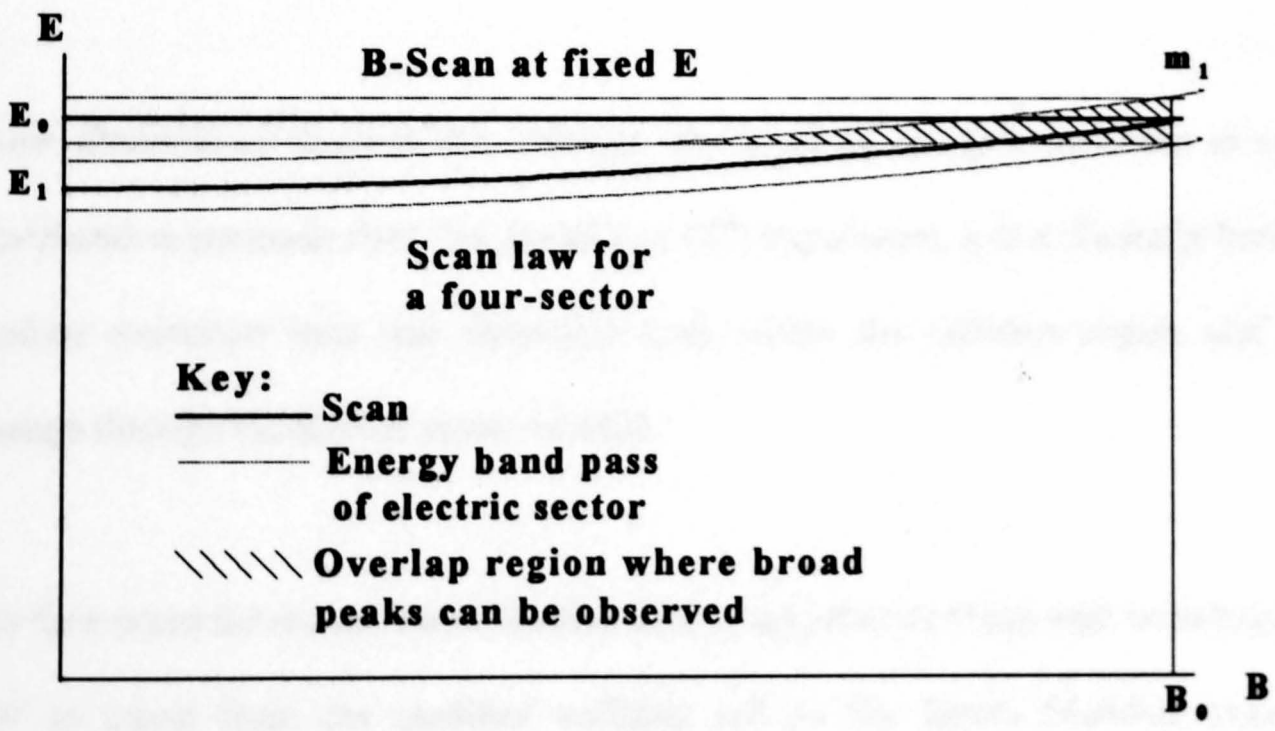

Figure 6.12.

Plot Showing Schematically the Relationship Between Two Scans of the Magnetic Field B and the Electric Sector Field E. The Energy Band Pass of the Electric Sector and the Overlap Region of the Two Scans where Broad Peaks can be Observed are also Shown Schematically for a Collision Cell Voltage of Approximately 7800 V.

magnetic analyser of MS2, their energy is only $(m_2/m_1)Ve$, so that they are deflected more easily and appear at an apparent mass of m_2^2/m_1 (Equation 6.1).

The ratio I("m*")/(m_2^+) falls as the ratio m_2/m_1 falls since the overlap of the energy band pass region of the normal **B**-scan at fixed **E** and that of the linked scan for V_{coll} = 200 V decreases as this ratio falls, thereby reducing the transmission of the m_2^+ ions formed in the field-free region before the magnetic sector (See Figure 6.12).

The corresponding CID spectra of the same peptides recorded on this instrument, fitted with the usual gas collision cell, did not contain any of these broad metastable ion peaks [37]. The cell was floated at 4 kV above earth potential for the CID studies so the scan law did not allow the fragment ions formed in the field free region between E_2 and B_2 to be transmitted through the magnetic sector (See Figure 6.11).

These observations suggest that although the range of energies deposited in a SID experiment is narrower than that found in a CID experiment, it is sufficiently broad to produce precursor ions that dissociate both within the collision region and after passage through the electric sector of MS2.

The time taken for undissociated leucine enkephalin precursor ions with an energy of 8 keV to travel from the modified collision cell to the fourth field-free region is approximately 20 μs. Precursor ions fragmenting between E_2 and B_2 must therefore have an average rate constant for fragmentation of approximately 5×10^4 s^{-1}. The rate constant of precursor ions dissociating in the collision region is approximately 10^6 s^{-1}.

The range of energies associated with ions after collision at a low angle to the surface must therefore be greater than those observed in other SID experiments where the angle of collision is larger.

6.5. Summary.

Sequence information has been generated for all four peptides analysed. The data obtained enable one to differentiate between all four peptides which differ only by the C-terminal amino acid residue or acid. Fragment ion distributions indicate that the internal energy deposited by SID in these experiments is low in comparison to high energy CID. This may be due to the low incident angles of collision employed in the SID experiments. Increasing the collision angle, with lower collision energies (E_{coll}) has been shown to increase the deposition of internal energy in SID experiments employing a similar in-line collision device on a four sector tandem mass spectrometer [43]. The SID dissociation efficiencies are low relative to that observed by high energy CID due to neutralisation of the ion beam on collision with the surface. These efficiencies may also be improved on increasing the collision angle as neutralisation is decreased.

All SID mass spectra obtained in this instrument in which a linked scan of the sectors of MS2 is used with a collision cell voltage close to that of the accelerating voltage would be expected to show metastable ion peaks arising from fragmentation of m_1 ions in the field-free region between the electric sector and magnetic sector of MS2. Furthermore, all MS/MS experiments performed on forward geometry four sector

instruments where the energy band pass is approximately ±3% or larger would be expected to give rise to spectra including broad metastable ion peaks when E_{coll} is close to that of V_{acc}.

It is expected that the intensities of these broad peaks will increase in spectra obtained with a lower collision energy (higher collision cell potential) as the overlap region of the two scans increases (See Figure 6.12). Conversely, increasing the value of E_{coll} is predicted to give decreasing intensities of these broad metastable ion peaks as the area common to the two scans decreases. The intensity of the broad peaks is also expected to increase when the ratio of m_2/m_1 increases, that is when the value gets closer to unity. This happens when m_1 gets larger but m_1-m_2 is constant or when m_1 remains constant and m_1-m_2 decreases. Evidence for these statements may be found in the high energy CID spectra of peptides in a collision cell floated at 4 kV above ground potential (E_{coll} = 4 keV) with a RMM of approximately 1000 Da [42]. Broad peaks are observed for the small losses from the precursor ion as the value of m_2/m_1 is relatively high.

1 J. Hughes, T. W. Smith, H. W. Kosterlitz, L. A. Fothergill, B. A. Morgan and H. R. Morris, *Anal. Biochem.*, **258**, 577 (1975).

2 C. Dass and D. Desiderio, *Anal. Biochem.*, **163**, 52 (1987).

3 D. M. Desiderio, S. Yamada, J. Z. Sabbatini and F. Tanzer, *Biomed. Mass Spectrom.*, **8**, 10 (1981).

4 D. M. Desiderio and S. Yamada, *Biomed. Mass Spectrom.*, **10**, 358 (1983).

5 D. M. Desiderio and M. Kai, *Biomed. Mass Spectrom.*, **10**, 471 (1983).

6 J. J. Kusmierz, C. Dass, J. T. Robertson, D. M. Desiderio, *Int. J. Mass Spectrom. Ion Proc.*, **111**, 247 (1991).

7 C. Dass, J. J. Kusmierz, D. M. Desiderio, S. A. Jarvis and B. N. Green, *J. Am. Soc. Mass Spectrom.*, **2**, 149 (1991).

8 D. M. Chambers, D. E. Goeringer, S. A. McCluckey and G. L. Glish, *Anal. Chem.*, **65**, 14 (1993).

9 S. Guan and A. G. Marshall, *Rapid Commun. Mass Spectrom.*, 7, 857 (1993).

10 D. M. Desiderio, J. Z. Sabbatini, *Biomed. Mass Spectrom.*, **8**, 565 (1981).

11 D. M. Desiderio, I. Katakuse and M. Kai, *Biomed. Mass Spectrom.*, **10**, 426 (1983).

12 I. Katakuse and D. M. Desiderio, *Int. J. Mass Spectrom. Ion Proc.*, **54**, 1 (1983).

13 L. C. E. Taylor, D. Hazelby and C. J. Wakefield, *Int. J. Mass Spectrom. Ion Phys.*, **46**, 407 (1983).

14 G. M. Neumann and P. J. Derrick, *Org. Mass Spectrom.*, **19**, 165 (1984).

15 R. L. Cerny and M. L. Gross, *Proceedings of the 35th Conference on Mass Spectrometry and Allied Topics*, May 24-29, Denver, Colorado, 82 (1987).

16 C. Guenat, J. Dino, Jr. and K. B. Tomer, *Proceedings of the 35th Conference on Mass Spectrometry and Allied Topics*, May 24-29, Denver, Colorado, 554 (1987).

17 L. M. Mallis and D. H. Russell, *Int. J. Mass Spectrom. Ion Proc.*, **78**, 147 (1987).

18 X. Tang, W. Ens, K. G. Standing and J. B. Westmore, *Anal. Chem.*, **60**, 1791 (1988).

19 A. J. Alexander and R. K. Boyd, *Int. J. Mass Spectrom. Ion Proc.*, **90**, 211 (1989).

20 R. P. Grese, R. L. Cerny and M. L. Gross, *J. Am. Chem. Soc.*, **111**, 2835 (1989).

21 L. M. Teesch and J. Adams, *Proceedings of the 37th Conference on Mass Spectrometry and Allied Topics*, May 21-26, Miami Beach, Florida, 907 (1989).

22 W. Arberth, *Anal. Chem.*, **62**, 609 (1990).

23 M. E. Bier, J. C. Schwartz, K. L. Schey and R. G. Cooks, *Int. J. Mass Spectrom. Ion Proc.*, **103**, 1 (1990).

24 L. M. Teesch and J. Adams, *J. Am. Chem. Soc.*, **112**, 4110 (1990).

25 K. D. Ballard and S. J. Gaskell, *Int. J. Mass Spectrom. Ion Proc.*, **111**, 173 (1991).

26 M. F. Bean, S. A. Carr, G. C. Thorne, M. H. Reilly and S. J. Gaskell, *Anal. Chem.*, **63**, 1473 (1991).

27 L. M. Teesch and J. Adams, *J. Am. Chem. Soc.*, **113**, 812 (1991).

28 L. M. Teesch and J. Adams, *Proceedings of the 39th Conference on Mass Spectrometry and Allied Topics*, May 19-24, Nashville, Tennessee, 128 (1991).

29 A. L. McCormack, V. H. Wysocki and A. R. Dongré, *Proceedings of the 40th Conference on Mass Spectrometry and Allied Topics*, May 31-June 5, Washington, DC, 815 (1992).

30 J. L. Jones, V. H. Wysocki and A. L. McCormack, *Proceedings of the 40th Conference on Mass Spectrometry and Allied Topics*, May 31-June 5, Washington, DC, 817 (1992).

31 R. B. Cole, S. LeMeillour and J.-C. Tabet, *Anal. Chem.*, **64**, 365 (1992).

32 J. L. Jones, A. R. Dongré, Á. Somogyi and V. H. Wysocki, *Proceedings of the 41st Conference on Mass Spectrometry and Allied Topics*, May 31-June 4, San Francisco, California, 1019 (1993).

33 A. L. McCormack, Á. Somogyi, A. R. Dongré and V. H. Wysocki, *Anal. Chem.*, **65**, 2859 (1993).

34 H. Zhao, A. Reiter, L. M. Teesch and J. Adams, *J. Am. Chem. Soc.*, **115**, 2854 (1993).

35 A. T. Jackson, D. Despeyroux and K. R. Jennings, *Int. J. Mass Spectrom. Ion Proc.*, **141**, 91 (1995).

36 A. M. Starrett and G. C. Didonato, *Rapid Commun. Mass Spectrom.*, 7, 12 (1993).

37 S. G. Summerfield, V. C. M. Dale, D. Despeyroux and K. R. Jennings, submitted for publication.

38 P. Roepstorff and J. Fohlman, *Biomed. Mass Spectrom.*, **11**, 601 (1984).

39 K. Biemann, *Biomed. Environ. Mass Spectrom.*,**16**, 99 (1988).

40 R. S. Johnson, S. A. Martin and K. Biemann, *Int. J. Mass Spectrom. Ion Proc.*, **86**, 137 (1988).

41 R. K. Boyd, D. J. Harvan and J. R. Hass, *Int. J. Mass Spectrom. Ion Proc.*, **65**, 273 (1985).

42 S. G. Summerfield, V. C. M. Dale, D. Despeyroux and K. R. Jennings, *Eur. Mass Spectrom.*, **1**, 183 (1995).

43 K. L. Schey, D. A. Durkin and K. R. Thornburg, *J. Am. Soc. Mass Spectrom.*, **6**, 257 (1995).

44 S. A. Martin, R. S. Johnson, C. E. Costello and K. Biemann in *The Analysis of Peptides and Proteins by Mass Spectrometry* (C. J. McNeal, Ed.), Wiley, New York (1988).

45 A. D. Wright, D. Despeyroux, K. R. Jennings, S. Evans and A. Riddoch, *Org. Mass Spectrom.*, **27**, 525 (1992).

46 D. Despeyroux, A. D. Wright, K. R. Jennings, S. Evans and A. Riddoch, *Int. J. Mass Spectrom. Ion Proc.*, **122**, 133 (1992).

47 A. L. McCormack, Á. Somogyi, A. R. Dongré and V. H. Wysocki, *Anal. Chem.*, **65**, 2859 (1993).

48 D. Renner and G. Spiteller, *Biomed. Mass Spectrom.*, **15**, 75 (1988).

49 T. Ast, Md. A. Mabud and R. G. Cooks, *Int. J. Mass Spectrom. Ion Proc.*, **82**, 131 (1988).

50 A. P. Bruins, K. R. Jennings and S. Evans, *Int. J. Mass Spectrom. Ion Phys.*, **26**, 395 (1978).

CHAPTER 7.

HIGH ENERGY MASS SPECTROMETRY AND TANDEM MASS SPECTROMETRY OF A FIVE COMPONENT MIXTURE OF POLYMER ADDITIVES.

7.1. Introduction.

Interest in the mass spectrometric analysis of polymer additives has increased in the last decade [1,2,3,4,5,6,7,8,9,10,11,12,13,14,15,16,17], especially with the developments in soft ionisation techniques such as fast atom bombardment (FAB) [6,7,8,9,10,11,12,13] and laser desorption (LD) [9,13,14,15]. These techniques are more suitable for the ionisation of non-volatile polymer additives which are now often used in polymer blends. Analysis by traditional mass spectrometric ionisation techniques such as electron impact (EI) and chemical ionisation (CI) require the analyte to be volatile [18].

There have been very few reports on the structural determination of polymer additives by means of tandem mass spectrometry (MS/MS). Lattimer et al. performed MS/MS experiments on additives in rubber compounds [19,20] and polypropylene [12]. A recent report by Chen et al. described desorption chemical ionisation (DCI)/low energy MS/MS as a technique for the detection of polymer additives in polyethylene [21].

A five-component mixture of polymer additives of RMM 300-1200 Da was analysed by means of mass spectrometry and a comparison was made of results obtained using various ionisation techniques. The separate components were also analysed by means of mass spectrometry. The ionisation techniques employed were EI, CI, LSIMS, FD and UV-MALDI. The CID spectra of molecular ions generated by EI, CI, LSIMS and FD were then obtained by means of tandem mass spectrometry.

The structures of the additives used in this study are shown in Figure 7.1 and their chemical names given in Table 7.1. The Irganox class of compounds (Irganox 1076, 3114 and 1010 were used in these experiments) and Hostanox 03 are incorporated as antioxidants in polymer blends and Tinuvin 327 is used as a UV stabiliser.

Trade Name	Molecular Formula	Monoisotopic Weight (Da)	Chemical Name
Tinuvin 327	$C_{20}H_{24}ON_3Cl$	357.16	2-(2-hydroxy-3,5-di-*tert*-butylphenyl)-2H-5-chlorobenzotriazole
Irganox 1076	$C_{35}H_{62}O_3$	530.47	*n*-octadecyl-β-(3,5-di-*tert*-butyl-4-hydroxyphenyl) propionate
Irganox 3114	$C_{48}H_{69}O_6N_3$	783.52	1,3,5-*tris* (3,5-di-*tert*-butyl-4-hydroxybenzyl) isocyanurate
Hostanox 03	$C_{50}H_{66}O_8$	794.48	ethylene glycol *bis* [(3,3-*bis* (3^1-*tert*-butyl-4^1-hydroxyphenyl)) butyrate]
Irganox 1010	$C_{73}H_{108}O_{12}$	1176.78	pentaerythrityl *tetrakis* [3-(3,5-di-*tert*-butyl-4-hydroxyphenyl) propionate]

Table 7.1.

Chemical Formulae, Monoisotopic Weights and Chemical Names of the Five Polymer Additives Studied.

This mixture of five additives was chosen because of the differences in their volatility and chemical reactivity. The combination is also representative of mixtures of additives employed in polymers such as polypropylene and polyethylene.

There have been very few reports in the literature of the effects of the differing internal energy of molecular ions generated by various ionisation techniques and thus, the variances in the collision induced dissociation (CID) spectra generated from these ions. Derrick et al. reported that the internal energy of protonated molecule ions of valinomycin (MH^+) formed by CI, FAB and electrospray ionisation did not significantly affect the fragment ion spectra obtained by CID [22,23]. It was suggested that the

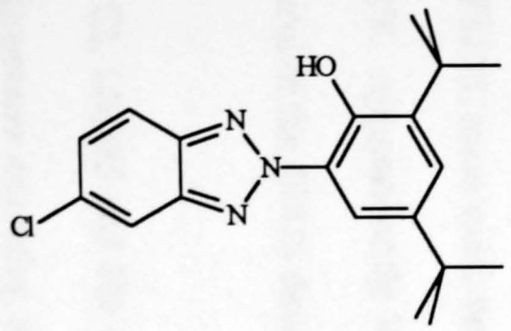

TINUVIN 327

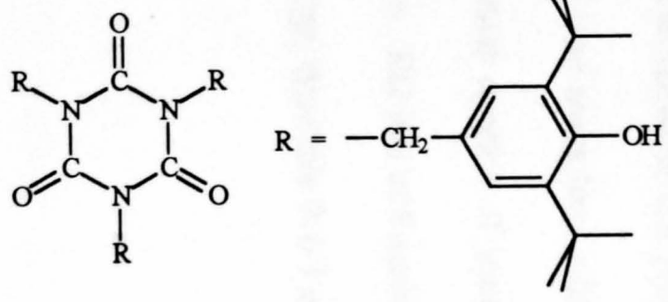

IRGANOX 3114

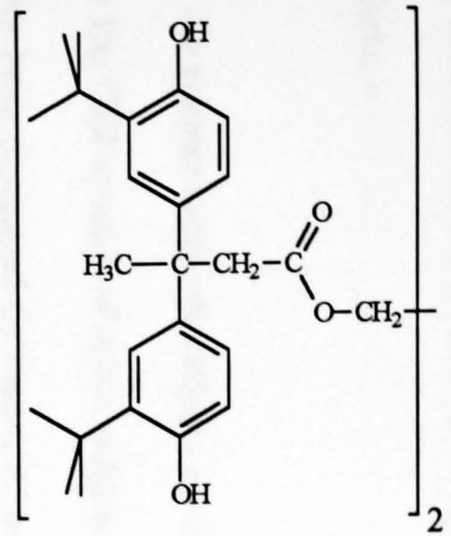

HOSTANOX 03

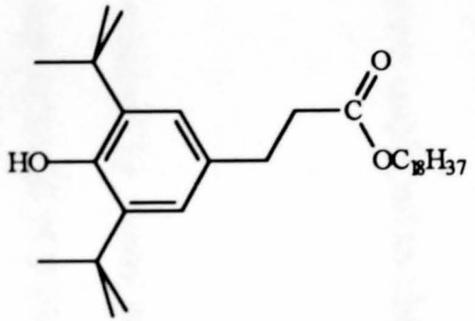

IRGANOX 1076

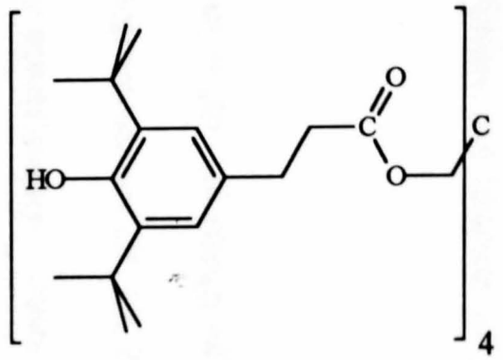

IRGANOX 1010

Figure 7.1.

Structures of the Five Organic Polymer Additives.

EI-MS/MS and FD-MS/MS spectra of valinomycin ($M^{+\cdot}$) differed as a consequence of the structure of the precursor ion prior to collision, not because of internal energy effects.

In the present work, the effects of the differences in internal energy of molecular ions on the CID spectra of some polymer additives generated by EI, CI, LSIMS and FD have been compared by means of tandem mass spectrometry. These four ionisation techniques generate ions of varying internal energy, which give rise to spectra that can normally be rationalised in terms of the precursor ion internal energy. EI-MS spectra are often dominated by low mass ions with the molecular ion giving a low intensity peak. In contrast, the mass spectra of samples generated by FD generally consist of only molecular ion peaks. FD is a soft ionisation technique which generates molecular ions of low internal energy, typically 0.1-1 eV [24].

7.2. Experimental.

7.2.(i) Mass spectrometry. UV-MALDI spectra were obtained by means of the TOFSPEC mass spectrometer operated in linear mode with an accelerating potential of 25 kV. Approximately 50 laser shots were employed to obtain the mass spectra under control of the OPUS data system.

EI, CI, LSIMS and FD spectra were acquired by means of the ZAB-T tandem mass spectrometer operating at an accelerating potential of 8 kV. Precursor ions for CID experiments were selected at greater than unit mass resolution by MS1. The ion beam

was attenuated by 80 % with argon in the mid-point collision cell at 4 keV collision energy. Acquisition of 5-20 scans under control of the OPUS data system was used to produce the fragment ion spectra.

7.2.(ii) Sample Preparation. All samples were obtained from Ciba-Geigy and dissolved in tri-chloromethane ($CHCl_3$) without further purification before analysis. The matrix employed for LSIMS-MS experiments was *meta*-nitro-benzyl alcohol (NBA) unless stated. For UV-MALDI spectra of cationated species, silver trifluoroacetate solution (10 mg $mL^{-1}/CHCl_3$) was added to the matrix solution (10 mg $mL^{-1}/CHCl_3$) and the sample solution (10 mg $mL^{-1}/CHCl_3$) in a 1:10:1 ratio.

7.3. High Energy Mass spectrometry of Polymer Additives.

7.3.(i) EI, CI, LSIMS and FD Ionisation of Single Components. With the exception of CI (discussed later), the various ionisation techniques produced $M^{+\bullet}$ ions from the five polymer additives but the LSIMS ionisation of Tinuvin 327 also produced the MH^+ ion. The LSIMS-MS and EI-MS spectra of four of the polymer additives are shown in Appendix A. Figures 7.2 and 7.3 are the LSIMS-MS and EI-MS spectra, respectively, of Irganox 1076.

Radical cation peaks are the molecule ion species typically observed in EI-MS spectra (Figure 7.3) and are often seen in FD-MS spectra. The $M^{+\bullet}$ ions observed in the present work by means of FD-MS are probably generated by field ionisation processes. Protonated molecule ion peaks are generally seen, however, in LSIMS-MS spectra.

Abundant molecular ion peaks have been observed in the LSIMS-MS and FAB-MS spectra of several, mostly non-polar [25,26,27,28,29,30,31,32,33,34,35,36], compounds.

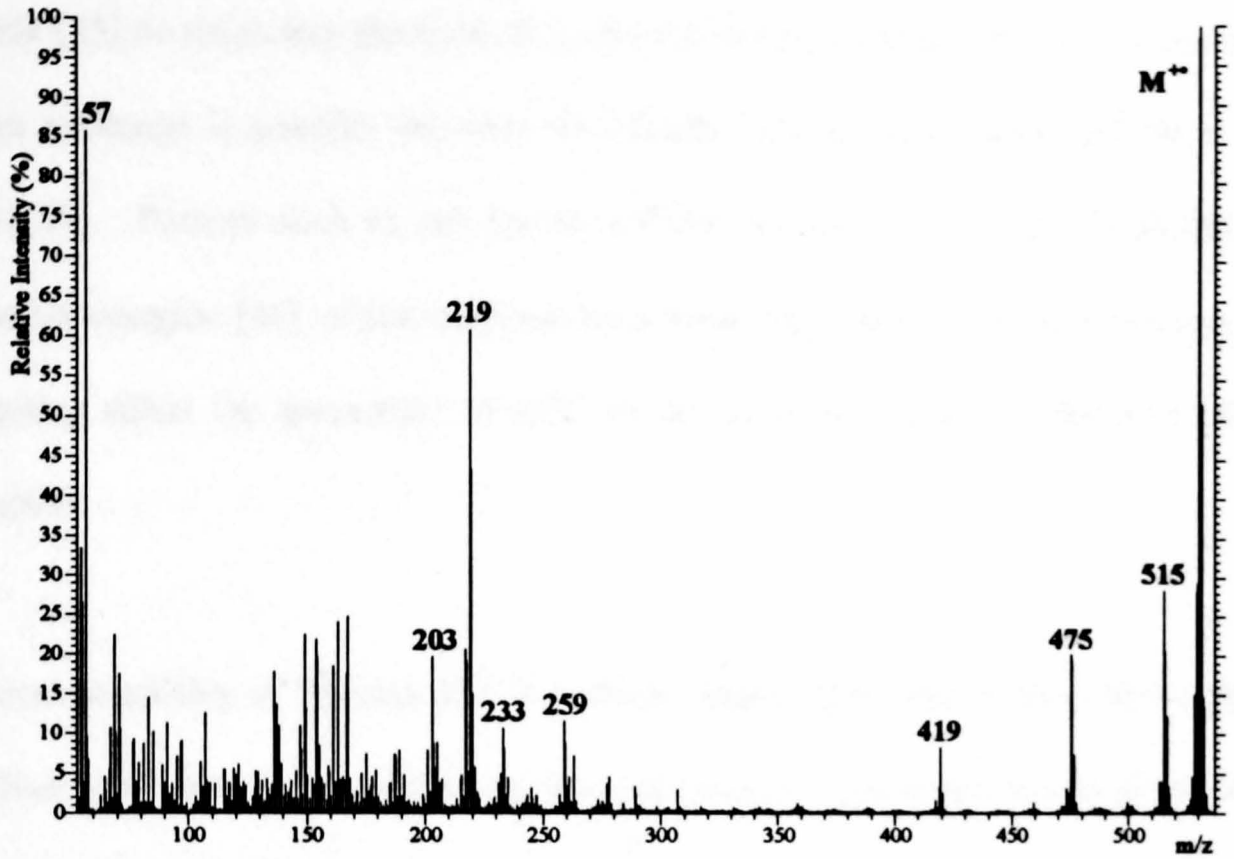

Figure 7.2.

LSIMS-MS Spectrum of Irganox 1076.

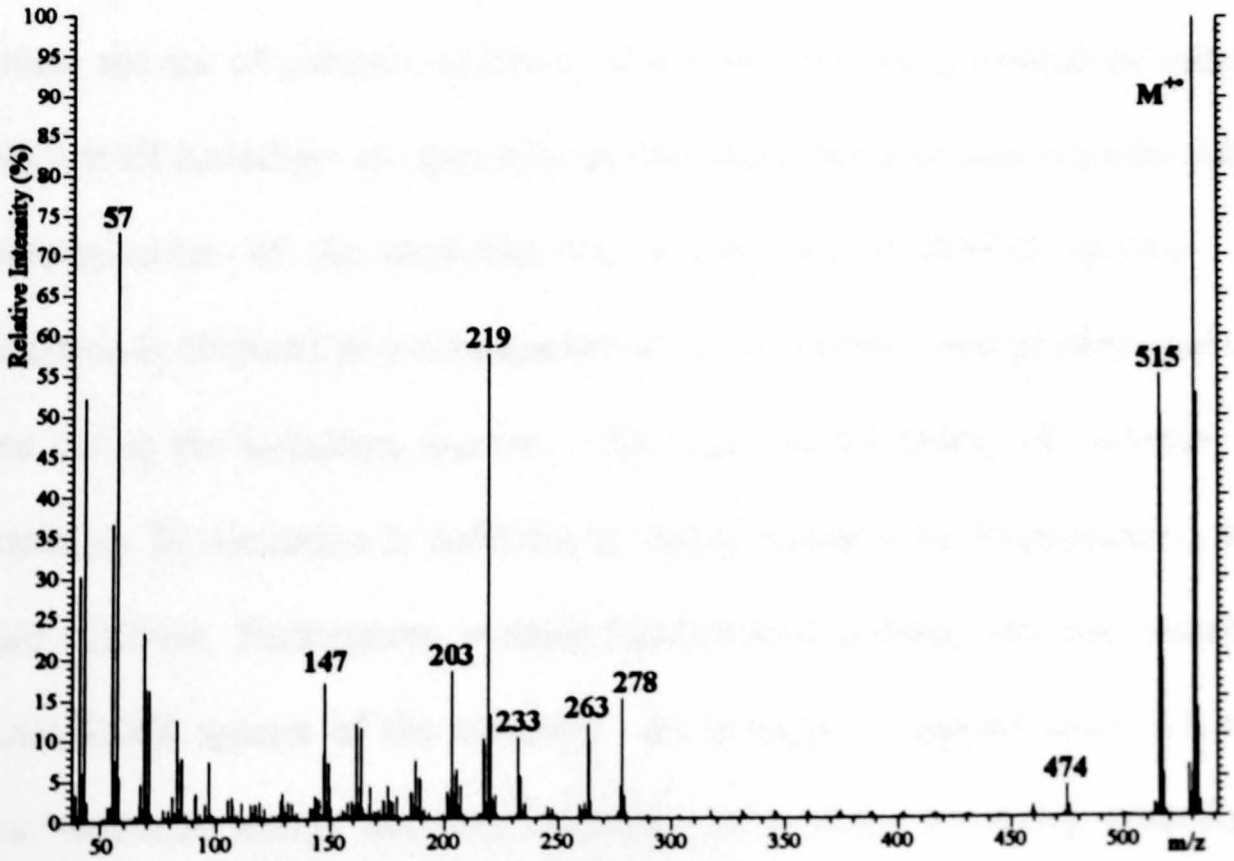

Figure 7.3.

EI-MS Spectrum of Irganox 1076.

Various processes have been suggested for the generation of these $M^{+\bullet}$ ions by means of LSIMS ionisation, including electron impact ionisation as a consequence of interaction between the analyte and high energy electrons generated in the collision cascade [25] or secondary electrons from the sputtering process [34,37]. Furthermore, charge exchange is possible between the initially formed matrix ions and the sample [28,35,36]. Factors such as the proton affinity, ionisation energies [38,39,40] and oxidation energies [41] of the analytes have been suggested to be very important in promoting either the generation of MH^+ or $M^{+\bullet}$ ions by means of FAB and LSIMS ionisation.

The proton affinity of Tinuvin 327 is probably higher than that of the other polymer additives as a consequence of the basicity of the triazole ring which would allow one to rationalise the observation of the mixture of $M^{+\bullet}$ and MH^+ in the LSIMS-MS spectra.

The mass spectra of polymer additives, where the ions are generated by means of LSIMS and EI ionisation, are generally dominated by fragment ions whereas virtually no decomposition of the molecular ion is observed in FD-MS spectra. This phenomenon is observed as a consequence of the low internal energy deposited in the analyte during the ionisation process. The high internal energy of molecular ions generated by EI ionisation is sufficient to induce consecutive fragmentation of the polymer additives. Furthermore, multiple fragmentation pathways are also observed in the LSIMS-MS spectra of the additives. An average of approximately 1-2 eV of internal excitation energy has been calculated to be imparted during ionisation by LSIMS [42,43,44].

The degree of fragmentation observed in the LSIMS-MS spectra of these polymer additives indicates that these compounds have low energy thresholds to dissociation. Lattimer et al. proposed that the dissociation of molecular species observed in FAB-MS spectra of polymer additives aided structural confirmation [11]. One disadvantage of the degree of fragmentation that is observed in LSIMS-MS spectra is that it could hinder the determination of the molecular weight of some compounds when analysing a complex mixture.

The fragmentation pathways observed in the spectra are discussed further in section 7.4. Furthermore, the distributions of fragment ions seen in the LSIMS-MS and EI-MS spectra are compared to those observed in the CID spectra of the same compounds.

The CI-MS spectra of Irganox 1076 are shown in Figure 7.4 when the reagent gas was (a) ammonia; (b) *iso*-butane and (c) methane. Abundant $[M+NH_4]^+$ ions were generated by means of CI with ammonia as the reagent gas for Irganox 1076, Irganox 3114 and Hostanox 03. Two possible general mechanisms of generation for this complex have been proposed [45] and are shown below in Equations 7.1 and 7.2:

$$M + [NH_4]^+ \longrightarrow [M \cdots H \cdots NH_3]^{+\bullet} \xrightarrow{NH_3} [M + NH_4]^+ \quad \text{(Equation 7.1)}$$

$$M + [NH_4]^+ \longrightarrow MH^+ + NH_3 \quad \text{(Equation 7.2)}$$

$$MH^+ + NH_3 \xrightarrow{NH_3} [M + NH_4]^+$$

The $[M+NH_4]^+$ ions observed in the ammonia CI-MS spectra of polymer additives are probably generated by the electrophilic attachment reaction shown in Equation 7.1. The reaction shown in Equation 7.2 is unlikely to occur as no protonated molecule ions (MH^+) are seen in most of the ammonia-CI-MS spectra of polymer additives. The electrophilic attachment process is common when the proton affinity of the analyte is less than that of ammonia (854 kJ mol^{-1} [46]). Adducts of ammonium ions with the analyte were not observed in the ammonia-CI-MS spectrum of phenol which indicates that the NH_4^+ does not form stable hydrogen bonds to this compound [45]. The site of the attachment of NH_4^+ is therefore most likely to be a carbonyl oxygen for the polymer additives used in the present work.

Predominantly protonated molecule (MH^+) ions were generated over $M^{+\bullet}$ for Tinuvin 327 by means of ammonia-CI. Intense ion peaks were observed 18 Da lower than $[M+NH_4]^+$ on the mass scale in the spectra of Irganox 1076 and Irganox 3114. These ions have the mass of the radical cation $M^{+\bullet}$ and could be formed by charge exchange with $NH_3^{+\bullet}$ [47] or low energy electron impact ionisation [45]. Molecular ions were observed at high abundance in the ammonia-CI mass spectra of dihydroxybenzenes [48], phenol and anisole [45]. The generation of the $M^{+\bullet}$ ions was proposed to be favoured as a consequence of the lower ionisation energies of the analytes in comparison to that of ammonia [47]. Another possibility is that these ions are generated by loss of H_2O from $[M+NH_4]^+$. This reaction is often observed by means of CI-MS for compounds containing hydroxyl groups. This would seem unlikely to be the case for the polymer additives analysed in the present work as the peak which corresponds to $[M + NH_4 - H_2O]^+$ is observed at lower relative intensity in the mass

spectrum of Hostanox 03 which has four hydroxyl groups whereas there is only one hydroxyl substituent in Irganox 1076. Furthermore, MS/MS spectra from the precursor ions at a mass-to-charge ratio corresponding to $M^{+\bullet}$ are very similar to those generated by means of EI-MS/MS, LSIMS-MS/MS and FD-MS/MS (Figure 7.21). This suggests that the molecular ion, $M^{+\bullet}$, is also formed by means of ammonia-CI. Furthermore, accurate mass experiments could aid the determination of the empirical formula.

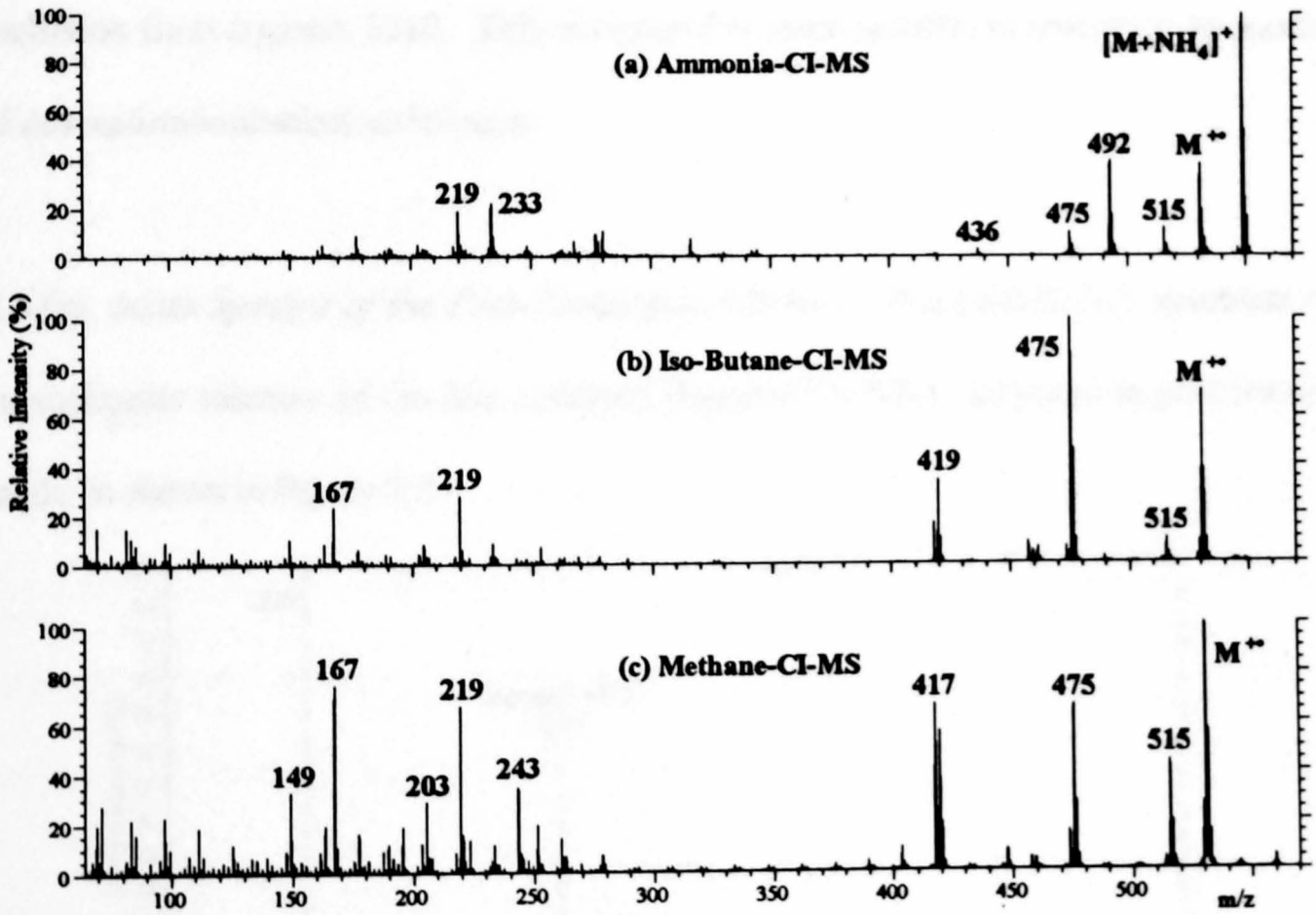

Figure 7.4.

CI-MS Spectra of Irganox 1076.
Reagent Gas: (a) Ammonia; (b) *Iso*-butane and (c) Methane.

Chemical ionisation employing *iso*-butane (*iso*-C_4H_{10}) as the reagent gas generates no protonated species for Irganox 1076, Irganox 3114 and Hostanox 03. There are peaks of low intensity, however, corresponding to the radical cation $M^{+\bullet}$. Furthermore, the

same $M^{+\cdot}$ species is seen in the CI-MS spectra of these additives when methane is employed as the reagent gas. These species are probably generated only by charge exchange with the ionised reagent gas or by low energy electron impact ionisation.

Irganox 1010 required a higher source temperature (300 °C) for analysis by means of EI-MS and CI-MS than the other additives studied due its involatility. Additives with a higher RMM (>1000 Da) are not always suited to analysis by means of EI-MS and CI-MS for this reason [18]. Low intensity molecular ion currents are generated by EI ionisation from Irganox 1010. This compound is more suitable to ionisation by means of desorption/ionisation techniques.

7.3.(ii) Mass Spectra of the Five-Component Mixture. The LSIMS-MS spectrum of an equimolar mixture of the five additives dissolved in NBA, acquired in positive ion mode, is shown in Figure 7.5.

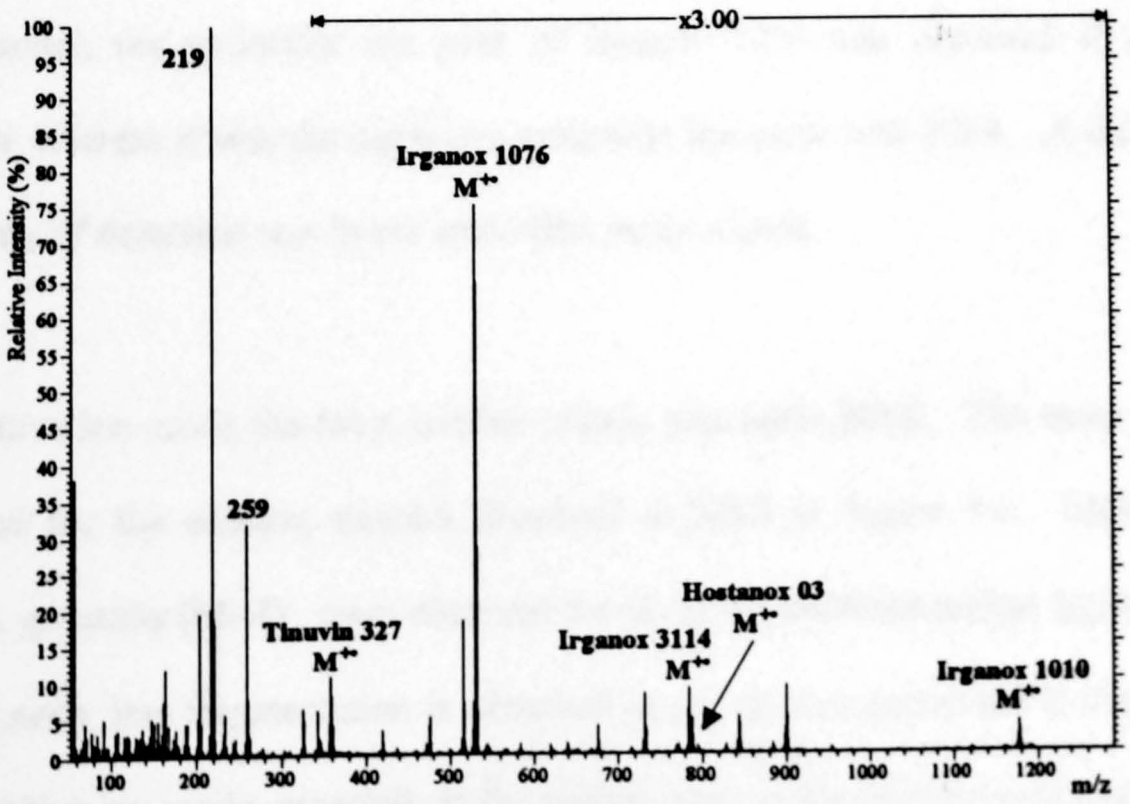

Figure 7.5.

LSIMS-MS Spectrum of the Equimolar Mixture of Polymer Additives. Positive Ion Mode.

A high signal-to-noise ratio was observed with 1 nmol of each additive in the five component mixture. Furthermore, all of the molecular ion and/or protonated molecule ion species were observed in the LSIMS mass spectrum when only 1 pmol of each additive in an equimolar mixture was placed on the probe tip. The most intense molecular ion signals are seen for Irganox 1076 and Irganox 3114 when the matrix is NBA. Relatively low intensity signals are observed for Tinuvin 327 which can be partially explained by the generation of a mixture of $M^{+\bullet}$ and MH^{+} from this compound.

The choice of matrix was very important for these experiments. The relative intensities seen in the spectra of the molecular ions of the additives changed when the matrix was an equal mixture *v/v* of glycerol and *bis*-di-hydroxyethyl-di-sulfide. This is probably a consequence of the different surface activities of the samples when the matrix is changed. The most intense molecular ion peak observed with this matrix was from Tinuvin 327, for which the lowest abundance molecular ion was observed with NBA. Furthermore, the molecular ion peak of Irganox 1076 was observed at very low intensity whereas it was the dominant molecular ion peak with NBA. A far superior sensitivity of detection was found with NBA as the matrix.

In negative ion mode the most suitable matrix was again NBA. The mass spectrum observed for the additive mixture dissolved in NBA is Figure 7.6. Molecule ion species, generally $[M-H]^{-}$, were observed for all of the additives except Irganox 3114. Furthermore, less fragmentation is observed in the spectra generated in negative ion than positive ion mode, especially in the region close to the deprotonated molecule ion peak of Hostanox 03. The overall signal-to-noise ratio was much lower than in

positive ion mode with the same matrix. Much less abundant ion signals for the additives and generally radical anions ($M^{-\cdot}$) were observed when triethanolamine was employed as the matrix in negative ion mode.

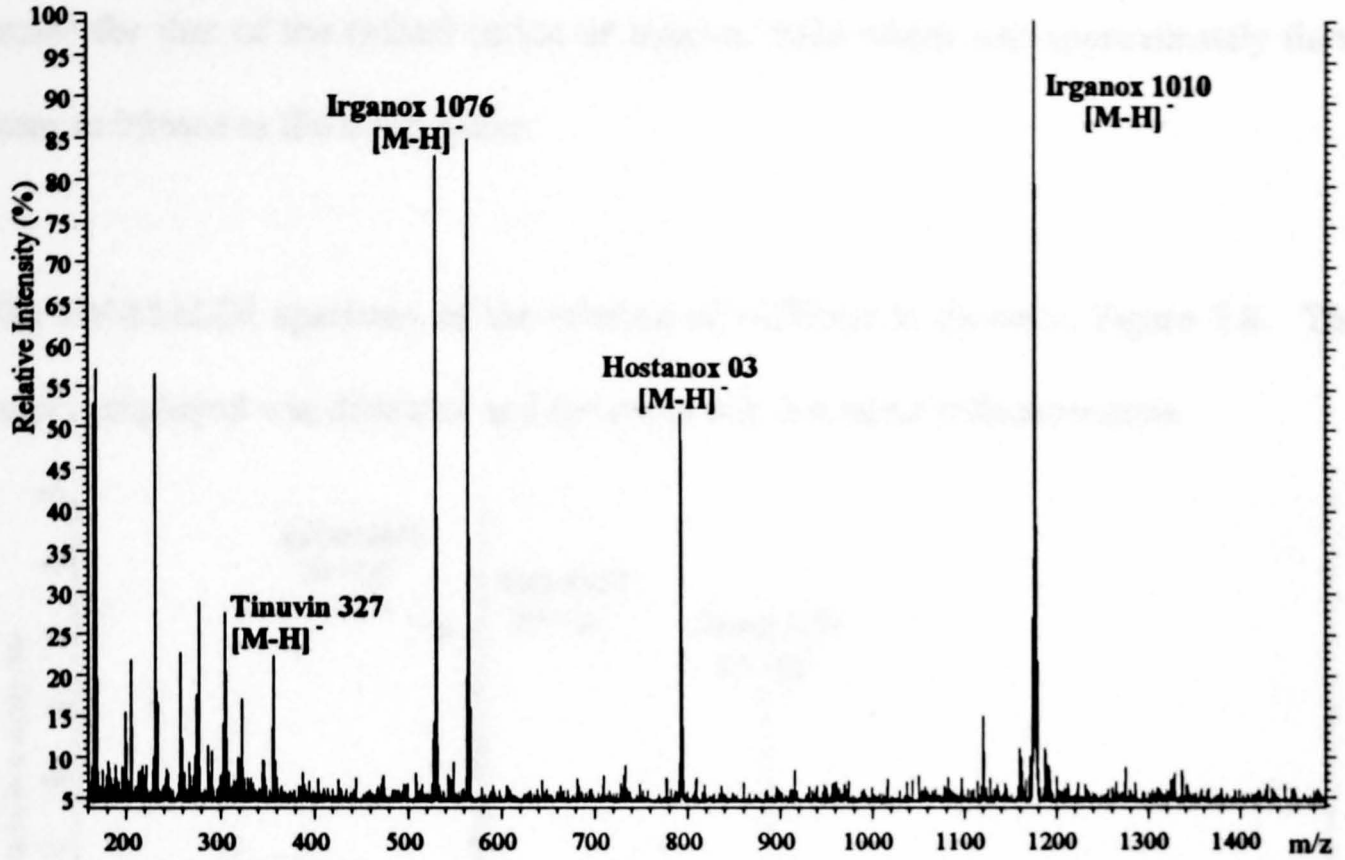

Figure 7.6.

LSIMS-MS Spectrum of the Equimolar Mixture of Polymer Additives. Negative Ion Mode.

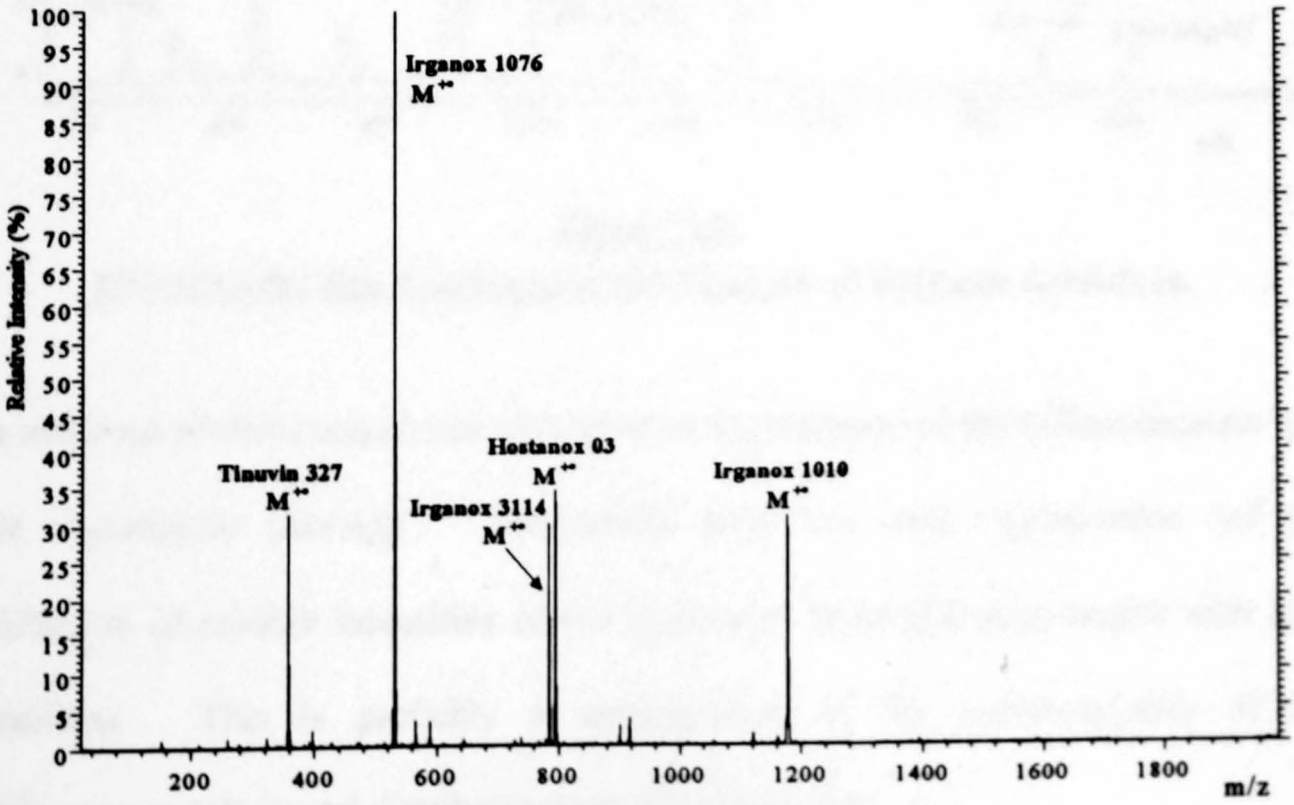

Figure 7.7.

FD-MS Spectrum of the Equimolar Mixture of Polymer Additives.

Predominantly molecular radical cations ($M^{+\bullet}$) were seen in the FD-MS spectrum of the mixture of additives (Figure 7.7). There is little fragmentation observed as FD is a very 'soft' ionisation technique. The molecular ion peaks were all of similar intensity except for that of the radical cation of Irganox 1076 which was approximately three times as intense as the other peaks.

The UV-MALDI spectrum of the mixture of additives is shown in Figure 7.8. The matrix employed was dithranol and the metal salt was silver trifluoroacetate.

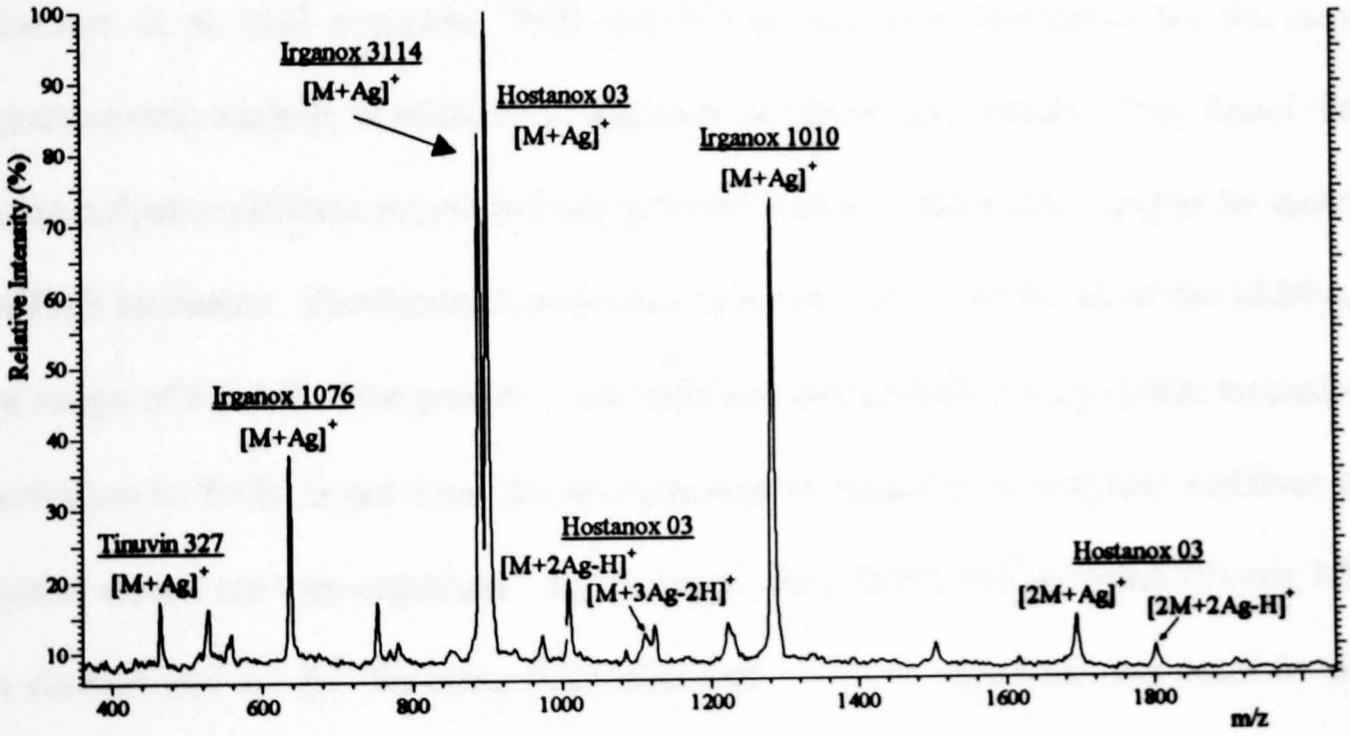

Figure 7.8.

UV-MALDI-MS Spectrum of the Mixture of Polymer Additives.

The additives all form complexes with silver in the presence of the trifluoroacetate salt, most importantly $[M+Ag]^+$. The results were not very reproducible and the distribution of relative intensities of the cationated molecular ions varied with each acquisition. This is probably a consequence of the inhomogeneity of the matrix-sample-salt crystal distributions on the sample spot.

Various adducts of Hostanox 03 with silver were observed in the UV-MALDI spectra (see Figure 7.8). These include $[M+Ag]^+$, $[M+2Ag-H]^+$, $[2M+Ag]^+$ and $[2M+2Ag-H]^+$. These types of complexes are often found in the FAB mass spectra of peptides [49] and fatty acids [50] when salts of alkali metals are added to the matrix. Assignment of ions in the lower mass range (<m/z 400) is made more problematical by the observation of various adduct ions from the matrix (dithranol) and silver. Furthermore, other unassignable peaks are often seen in the UV-MALDI spectra.

Lattimer et al. [11] compared FAB and FD as ionisation techniques for the mass spectrometric analysis of mixtures of additives in rubber compounds. They found that some polymer additives suppressed the generation of ions from other species by means of FAB ionisation. Furthermore, molecular ions were observed for all of the additives by means of FD-MS. The present work indicates that LSIMS, a very similar ionisation technique to FAB, is not ideal for the quantitative detection of polymer additives as matrix effects are very important. Furthermore, the LSIMS-MS spectrum (Figure 7.5) is complicated by the fragment ions observed. This is especially important in the molecular ion regions of Irganox 3114 and Hostanox 03 in Figure 7.5 as a consequence of the series of fragment ions of Irganox 1010 that were observed. Matrix effects are prominent in MALDI experiments and this, added to the lack of reproducibility and complication of the various adducts of some additives with silver, indicates that this ionisation technique is also unsuitable for quantitative analyses of mixtures of these types of compounds. FD is a far superior ionisation technique for quantitative analysis as there are no matrix effects which might suppress the generation of ions from certain additives.

7.4. High Energy CID of Polymer Additives.

7.4.(i)(a) Irganox compounds. All of the Irganox compounds studied had a di-*tert*-butyl substituted alkyl phenol base structure, as shown in Figure 7.9.

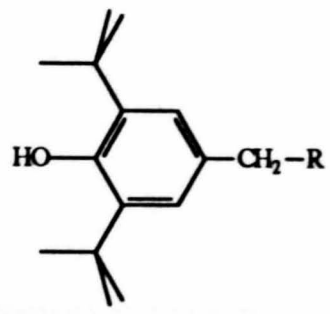

Figure 7.9.

The Base Structure of the Irganox Compounds Analysed in these Experiments.

The CID spectra of Irganox 1076 and Irganox 1010 are shown in Figures 7.10 and 7.11 respectively.

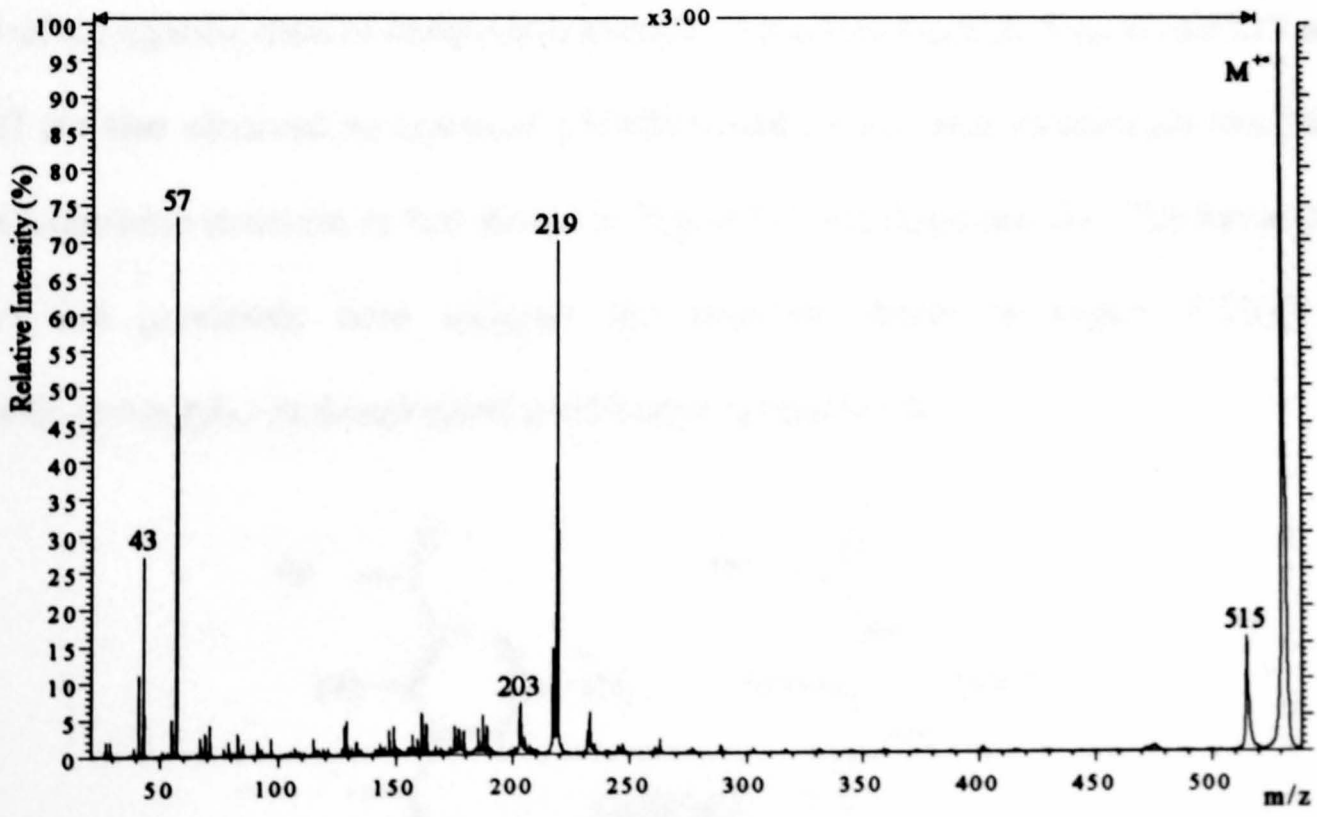

Figure 7.10.

LSIMS-MS/MS Spectrum of Irganox 1076, $M^{+\bullet}$ m/z 530, from an Equimolar Mixture of Polymer Additives.

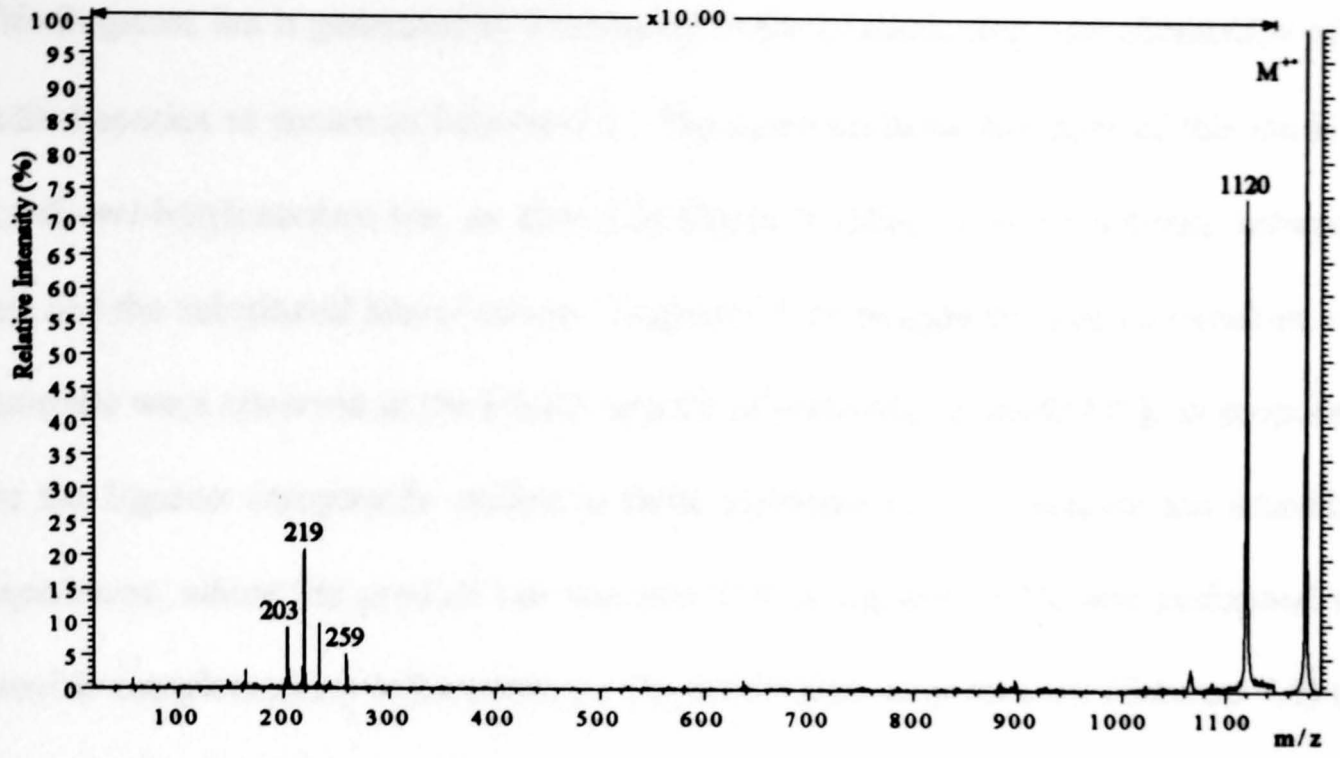

Figure 7.11.

LSIMS-MS/MS Spectrum of Irganox 1010, $M^{+\bullet}$ m/z 1177, from an Equimolar Mixture of Polymer Additives.

These spectra differ greatly from the low energy CID spectra obtained by Chen et al. [21]. Intense fragment ion peaks at m/z 203 and m/z 219 appear in the CID spectra of all of the Irganox class of compounds studied. Abundant fragment ions at m/z 219 and 203 are also observed by means of LSIMS-MS/MS from other compounds that have the same base structure as that shown in Figure 7.9 (see Appendix B). The ion at m/z 219 has previously been assigned the structure shown in Figure 7.12(a), a 2,4-di-*tert*-butyl-3-hydroxyl substituted benzyl cation [5,12].

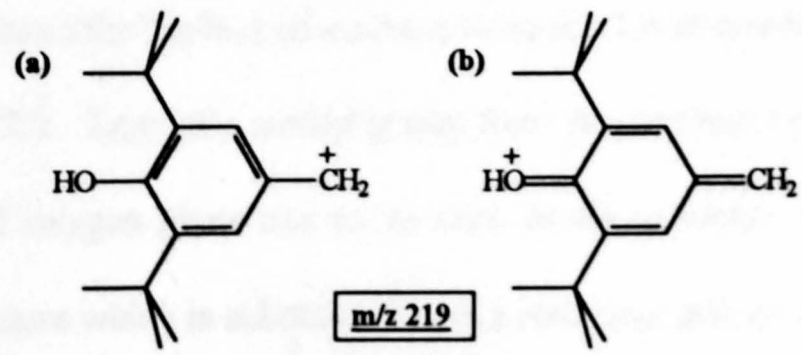

Figure 7.12.

Proposed Structures for the m/z 219 Fragment Ion Observed in Mass Spectra of Irganox Compounds.

This fragment ion is generated by cleavage β to the aromatic ring with elimination of a radical species as shown in Scheme 7.1. The more probable structure of this ion is a 2,4-di-*tert*-butyloxonium ion, as shown in Figure 7.12(b), or an equilibrium between this and the substituted benzyl cation. Fragment ions thought to have an oxonium ion structure were observed in the EI-MS spectra of *para*-alkyl phenols [51], as proposed for the Irganox compounds studied in these experiments. A precursor ion scanning experiment, where the product ion was m/z 219 of Irganox 1076, was performed to provide complementary information on the mechanism of generation (Scheme 7.1) of the fragment ion. The resulting spectrum is shown in Figure 7.13 and the data are consistent with the proposed mechanism.

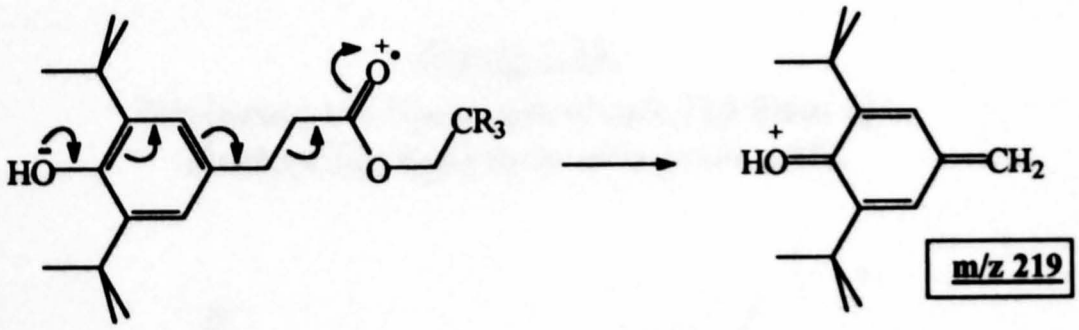

Scheme 7.1.

Proposed Mechanism for the Generation of m/z 219 from Irganox Compounds.

The fragment ion at m/z 203 is proposed to be formed by loss of methane from the m/z 219 ion. A mechanism for the loss of methane from the 2,4-di-*tert*-butyloxonium ion is shown in Scheme 7.2. Loss of a methyl group from the *tert*-butyl group and a proton from the hydroxyl oxygen gives rise to an enol structure which can rearrange to a phenol based structure which is substituted with a *tert*-butyl and an *iso*-propene group. The fragment ion is stabilised by the generation of an oxonium ion, as proposed for the

m/z 219 fragment ion. A precursor ion scan of m/z 203 from Irganox 1076 is shown in Figure 7.14 and the data are consistent with the mechanism in Scheme 7.2.

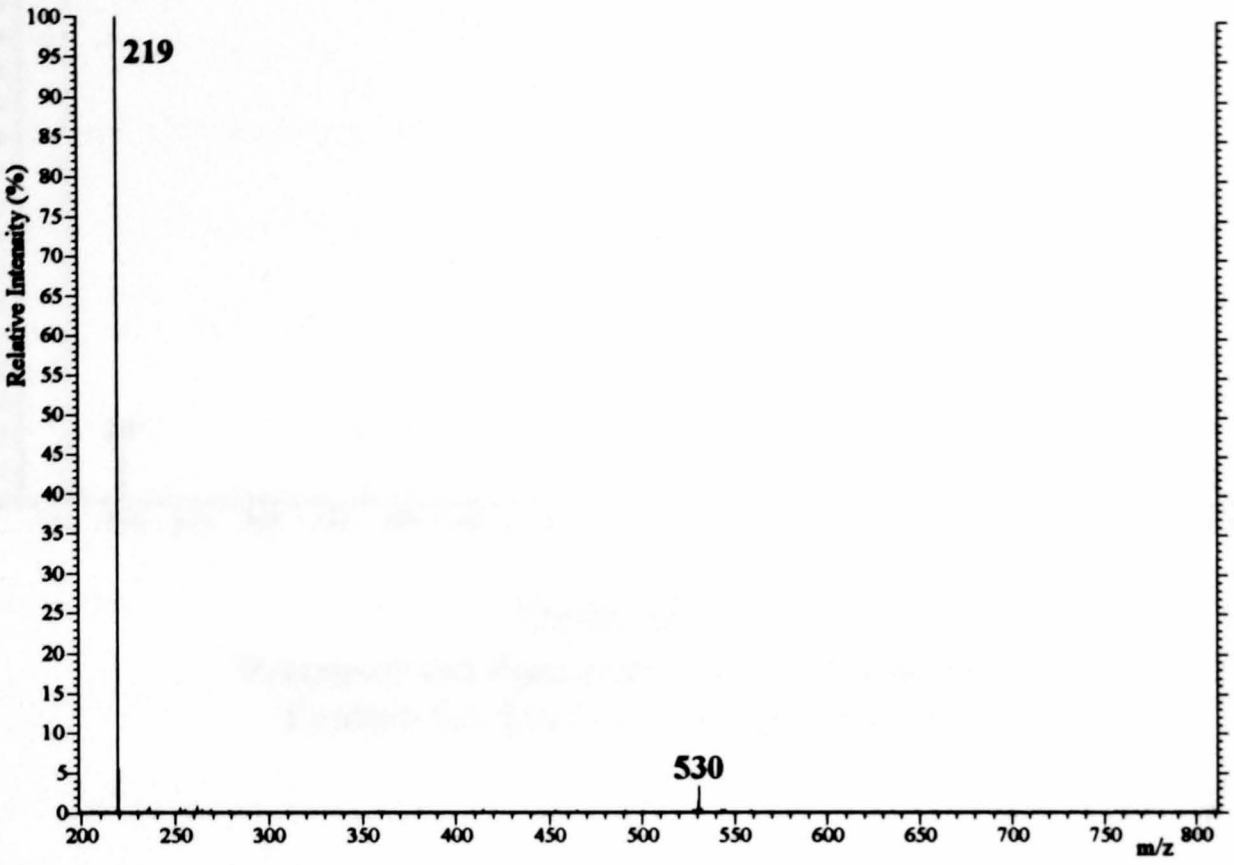

Figure 7.13.
Precursor Ion Spectrum of m/z 219 from the Product Ion Spectrum of Irganox 1076.

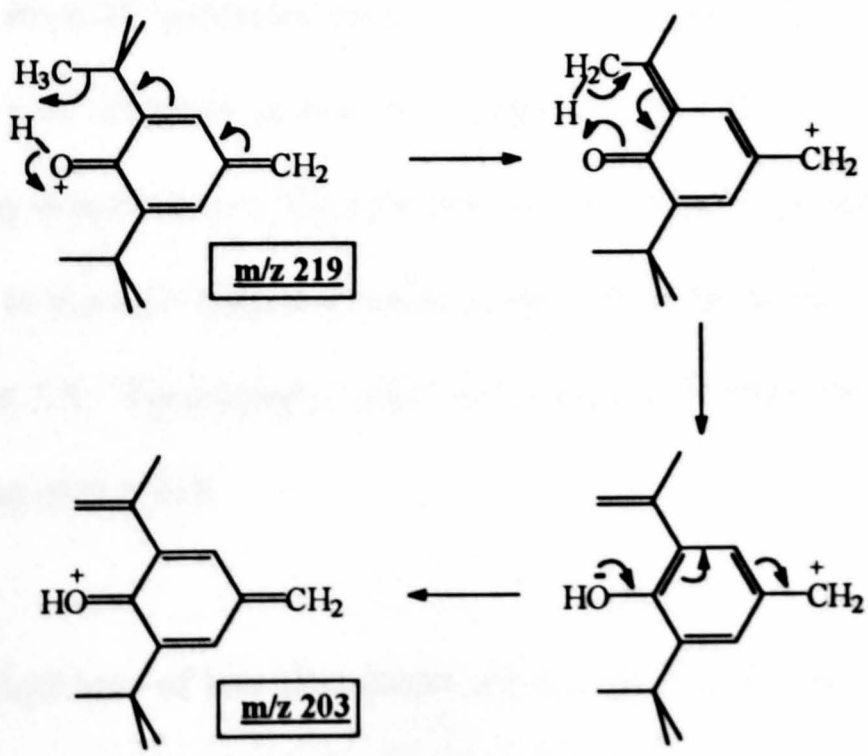

Scheme 7.2.
Proposed Mechanism for the Generation of m/z 203 from Irganox Compounds.

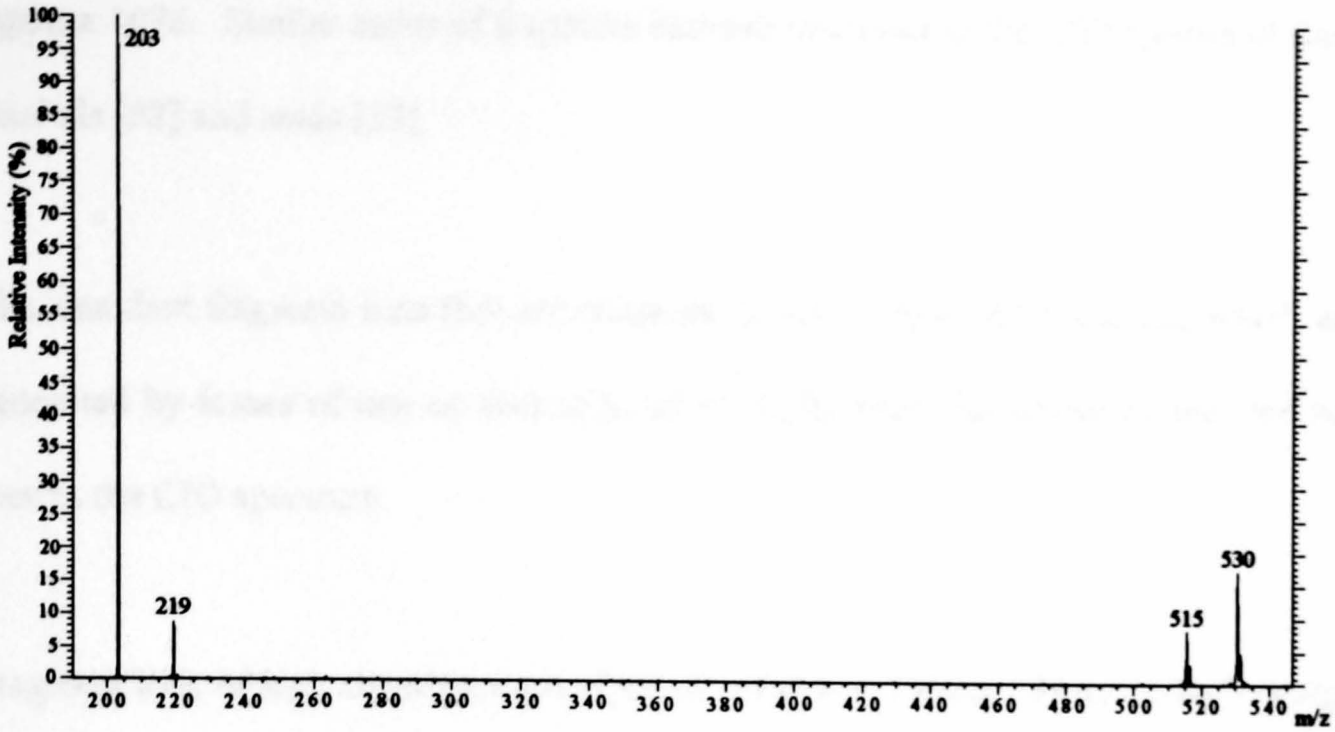

Figure 7.14.

Precursor Ion Spectrum of m/z 203 from the Product Ion Spectrum of Irganox 1076.

Other abundant ions at m/z 515, 57 and 43 are observed in the CID spectrum of Irganox 1076 (Figure 7.10). The m/z 515 ion is probably generated by loss of a methyl radical ($CH_3^{\bullet}$) from the precursor ion. Loss of the whole ($C_4H_9^+$) or part ($C_3H_7^+$) of a *tert*-butyl group from $M^{+\bullet}$ generates the m/z 57 and 43 fragment ions respectively. The other fragment ions observed at low m/z ratios (< m/z 200) are probably formed predominantly by dissociation of the m/z 219 ion. Fragment ions are observed at the same m/z ratios in the CID spectra of compounds with a similar base structure to that shown in Figure 7.9. Furthermore, ions of the same m/z ratio are observed in the MS/MS spectrum of m/z 219.

A series of product ions of low abundance, differing by 14 Da, which is observed in Figure 7.10 is probably generated by losses of part of the hydrocarbon chain from

Irganox 1076. Similar series of fragment ions are observed in the CID spectra of fatty alcohols [52] and acids [53].

The abundant fragment ions that are observed in the LSIMS-MS spectrum, which are generated by losses of one or two units of *iso*-C_4H_8 from the precursor ion, are not seen in the CID spectrum.

Fragment ions of high abundance are observed at m/z 1119 and 259 in the high energy CID spectrum of Irganox 1010. The m/z 1119 product ion is formed by loss of a *tert*-butyl group as a radical species ($C_4H_9^{\bullet}$) from $M^{+\bullet}$. Cleavage α to the carbonyl group and loss of hydrogen is proposed to generate the fragment ion which is observed at m/z 259. This ion could have the highly conjugated and therefore very stable structure that is shown in Scheme 7.3, which partially explains the intensity of the peak in the CID spectrum. This ion is observed only at very low abundance, however, in the CID spectrum of Irganox 1076.

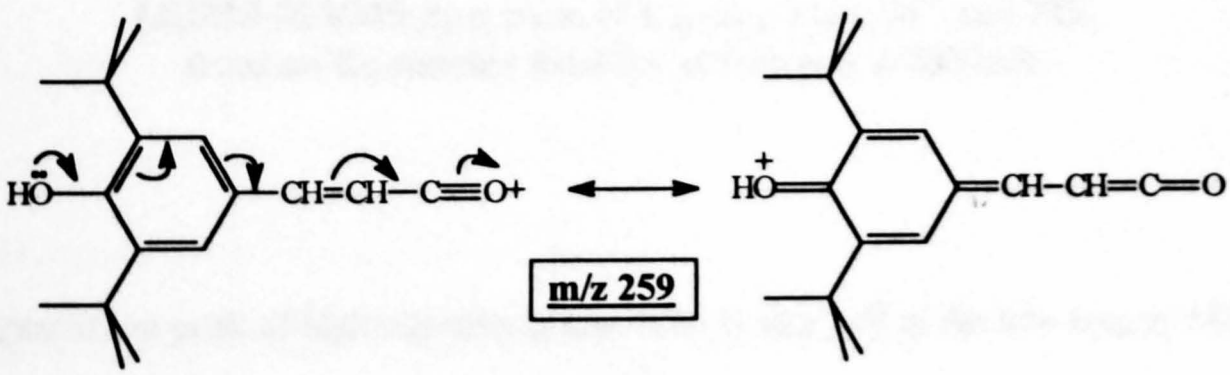

Scheme 7.3.

The Proposed Structure of the m/z 259 Fragment Ion.

Peaks arising from consecutive losses of *iso*-C_4H_8 from the precursor ion are only observed at low intensities in the high energy CID spectrum of Irganox 1010. These

rearrangement processes are very prominent in the low energy CID spectra of the same compound [21] (Chapter 8) and also in the LSIMS-MS and EI-MS spectra.

7.4.(i)(b) Irganox 3114. Fragment ions at m/z 203 and m/z 219 are observed in all high energy fragment ion spectra of Irganox 3114 (Figure 7.15).

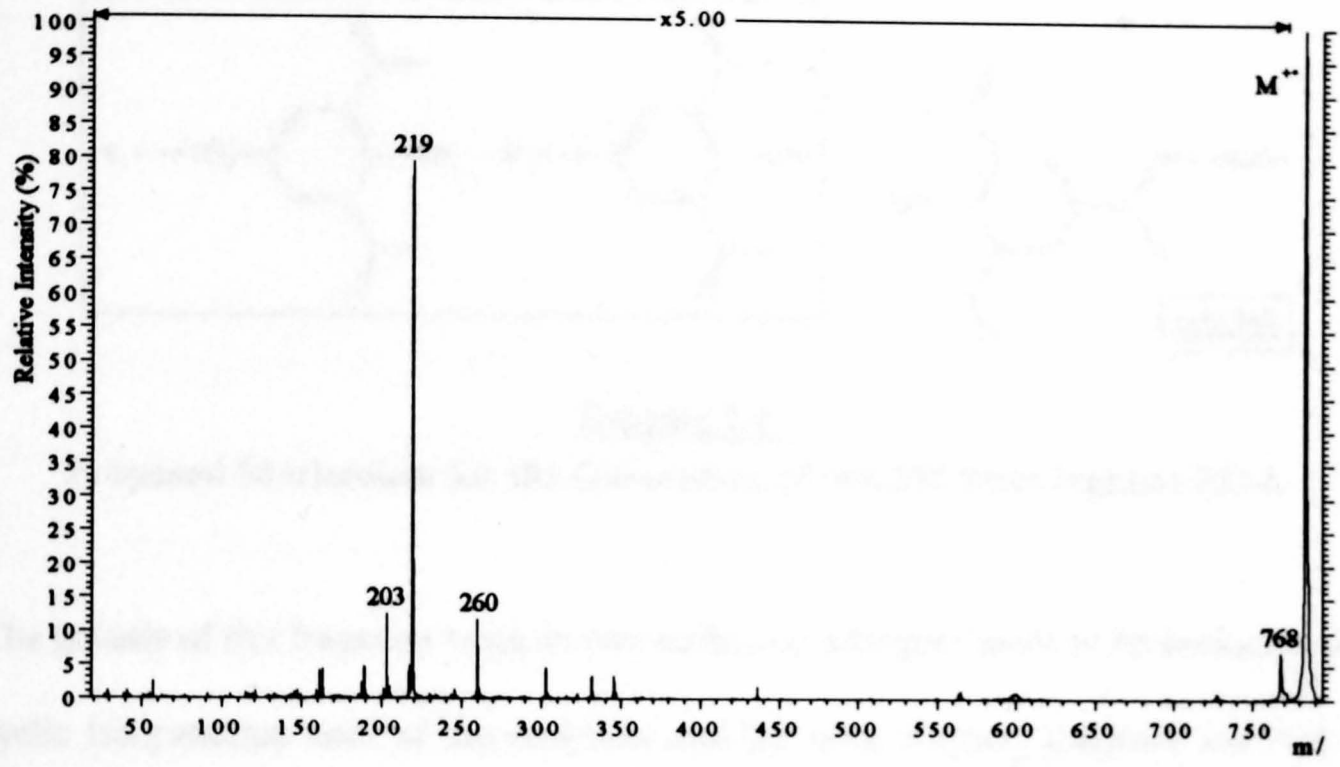

Figure 7.15.
LSIMS-MS/MS Spectrum of Irganox 3114, $M^{+\bullet}$ m/z 783, from an Equimolar Mixture of Polymer Additives.

A fragment ion peak of high intensity is also seen at m/z 219 in the low energy MS/MS spectrum of the same compound [12]. There is also an intense fragment ion peak at m/z 260 in the high energy MS/MS spectrum which can be assigned the structure shown with the proposed mechanism in Scheme 7.4. This fragment ion was observed in the EI-low energy MS/MS spectrum but no structure or mechanism of formation

was proposed [12]. The proposed structure shown in Scheme 7.4 is consistent, however, with the empirical formula that was calculated from accurate mass data [12].

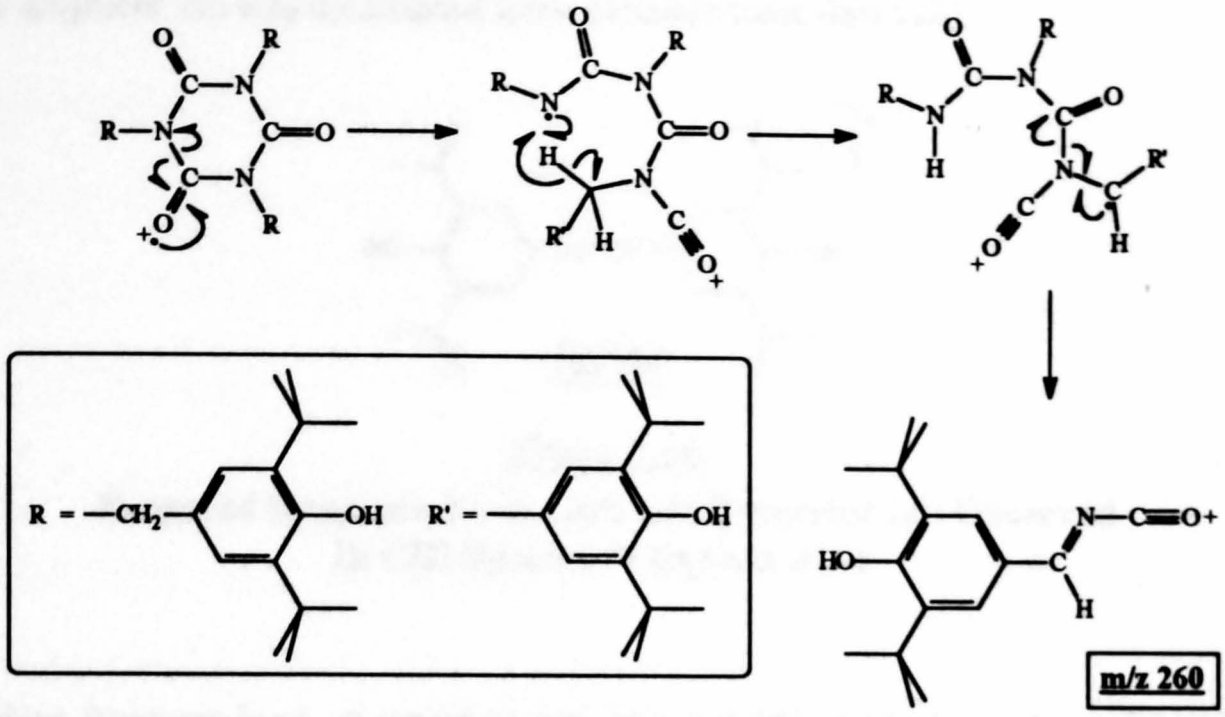

Scheme 7.4.

Proposed Mechanism for the Generation of m/z 260 from Irganox 3114.

The genesis of this fragment requires two carbon-to-nitrogen bonds to be broken in the cyclic isocyanurate core of the molecule and the even electron fragment ion that is generated requires the cleavage of three bonds within the precursor ion. Ring opening *via* homolytic cleavage is followed by a hydrogen rearrangement and the breaking of another carbon-to-nitrogen bond. A requirement for the mechanism of generation for this fragment ion is that the site of ionisation is a carbonyl oxygen, adjacent to the isocyanurate ring. Other even electron fragment ions, formation of which require opening of the isocyanurate ring, are observed at m/z 303 and m/z 332.

An intense fragment ion is observed at m/z 768 which is generated by loss $CH_3^{\bullet}$ from the precursor ion. The ion of low abundance at m/z 727 may be generated by loss of *iso*-C_4H_8 from a tertiary butyl group of Irganox 3114. Furthermore, the fragment ion

at m/z 438, also of low abundance in the high energy LSIMS-MS/MS spectrum has been proposed to have the structure shown in Figure 7.16 [12]. The empirical formula of this fragment ion was determined from accurate mass data [12].

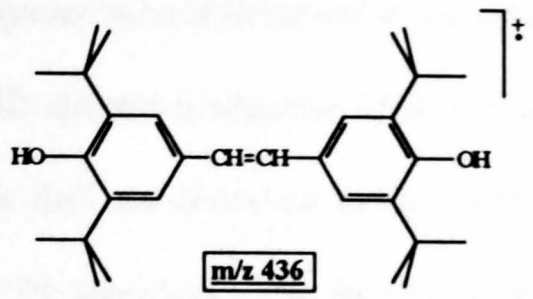

Figure 7.16.
Proposed Structure for the m/z 436 Fragment Ion Observed in CID Spectra of Irganox 3114.

Abundant fragment ions, observed at m/z 565 and 346 in the low energy EI-MS/MS spectrum of Irganox 3114 [12], are only seen at low abundance in the high energy experiments. These ions were proposed to have the structures shown in Figure 7.17(a) and 7.17(b) [12]. Furthermore, a fragment ion is also seen at m/z 564 in Figure 7.15 which probably has the structure indicated by Figure 7.17(c) and is generated by loss of R˙ from the precursor ion, where R has the structure shown in Scheme 7.4.

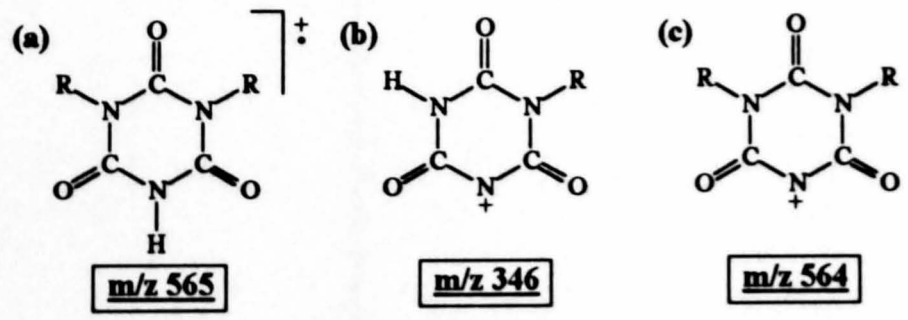

Figure 7.17.
The Proposed Structures of Fragment Ions of Irganox 3114 Observed at: (a) m/z 565; (b) m/z 346 and (c) m/z 564.

The m/z 564 ion is probably an intermediate in the generation of the m/z 346 fragment ion as loss of a radical followed by a neutral is a more favourable process than initial

expulsion of a neutral to generate m/z 565, an odd electron ion, prior to loss of a radical $R^{\bullet}$ to form m/z 346.

A similar distribution of fragment ions is observed at low m/z ratios (<m/z 200) to that found in the high energy CID spectra of Irganox 1010 and Irganox 1076. The relative intensities of fragment ions that are observed in the LSIMS-MS spectrum are very similar to that seen in the CID spectrum. The formation of fragment ions with higher m/z ratios is more favoured in the EI-MS spectrum. This is probably a consequence of the higher critical energies that are required for generation of many ions of higher m/z ratios for Irganox 3114, as multiple bond cleavages are required to form these ions.

7.4.(ii) Hostanox 03. The most intense fragment ions in the high energy CID spectrum of Hostanox 03 (Figure 7.18) are those observed at m/z 325 and m/z 309.

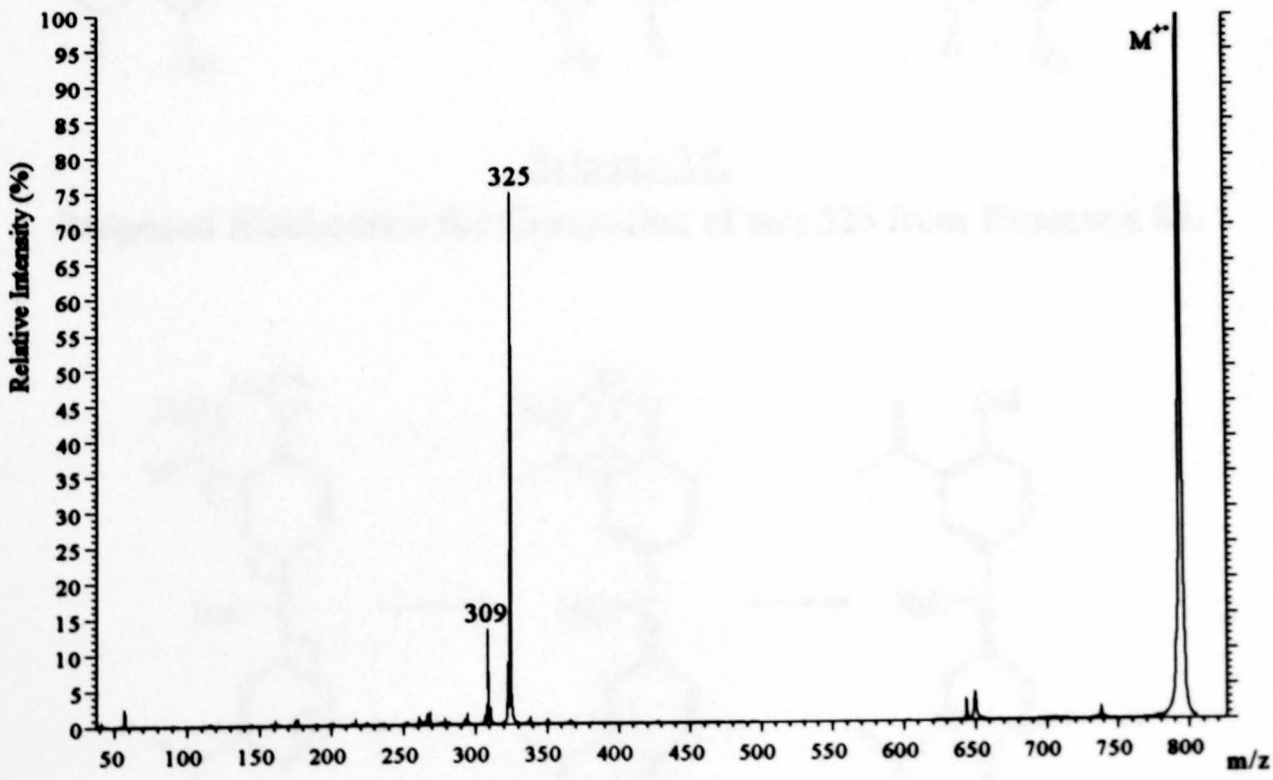

Figure 7.18.

LSIMS-MS/MS Spectrum of Hostanox 03, $M^{+\bullet}$ m/z 794, from an Equimolar Mixture of Polymer Additives.

The proposed structures of these ions and the mechanisms of their formation are shown in Schemes 7.5 and 7.6. The ion at m/z 325 is formed by β-cleavage to the hindered phenol rings. The generation of these ions is analogous to that of β-cleavage and loss of methane from the Irganox compounds studied. Loss of methane from the *tert*-butyl group of the m/z 325 ion gives the fragment at m/z 309. A precursor ion scan of m/z 309 generated a spectrum dominated by m/z 325 and m/z 794, in accordance with the mechanism in Scheme 7.5. The high relative intensity of the m/z 325 and 309 peaks may be a consequence of the highly conjugated structures, and therefore stability, of these fragment ions.

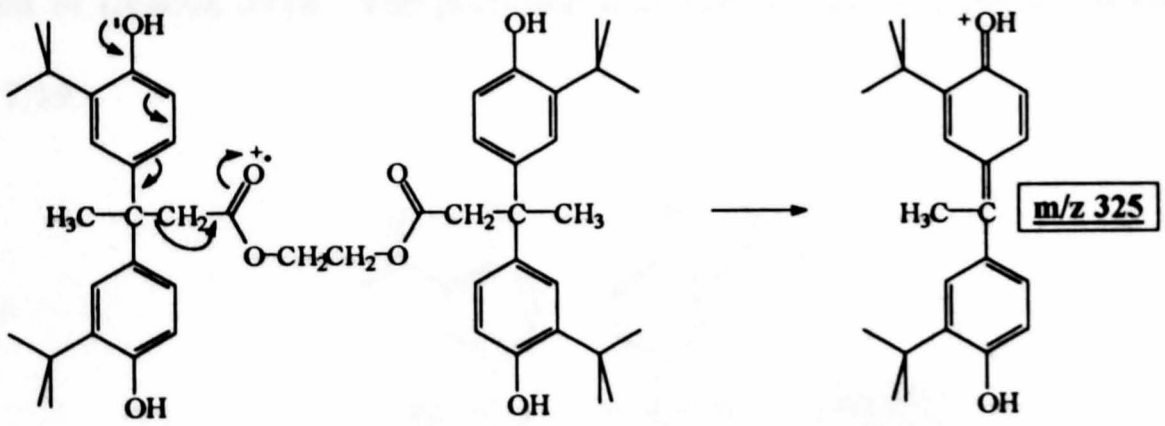

Scheme 7.5.

Proposed Mechanism for Generation of m/z 325 from Hostanox 03.

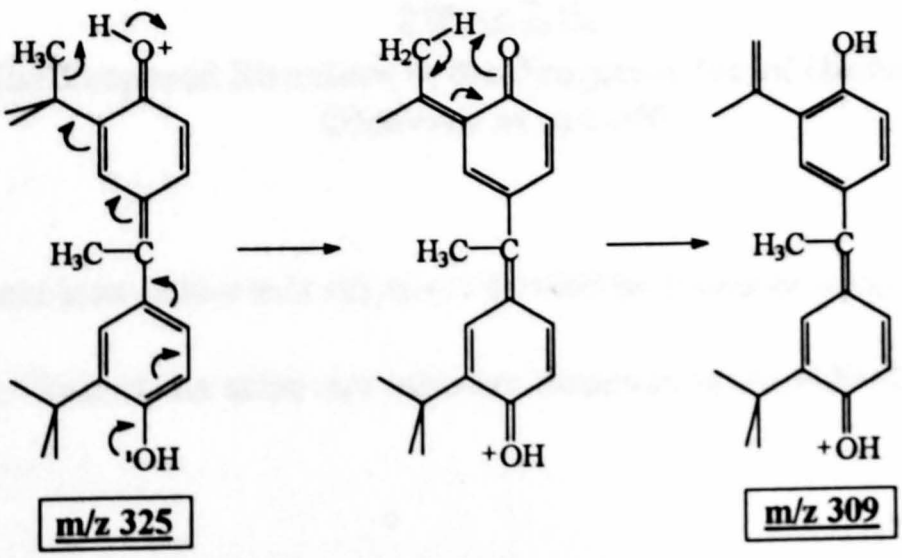

Scheme 7.6.

Proposed Mechanism for Generation of m/z 309 from Hostanox 03.

Fragment ions of low relative intensity are observed at m/z 728 and 644 in Figure 7.18. These ions are presumed to be generated from the precursor ion by rearrangement processes as they have even m/z ratios and therefore are odd electron ions. Expelling *iso*-C_4H_8 or 2,6-di-*tert*-butylphenol from the precursor ion by means of 1,3-hydrogen rearrangements is proposed to generate the ions observed at m/z 728 and 644 respectively.

A fragment ion seen at m/z 650 is possibly formed by an internal rearrangement similar to that required to generate the m/z 436 product ion that is observed in the MS/MS spectrum of Irganox 3114. The proposed structure of this fragment ion is shown in Figure 7.19.

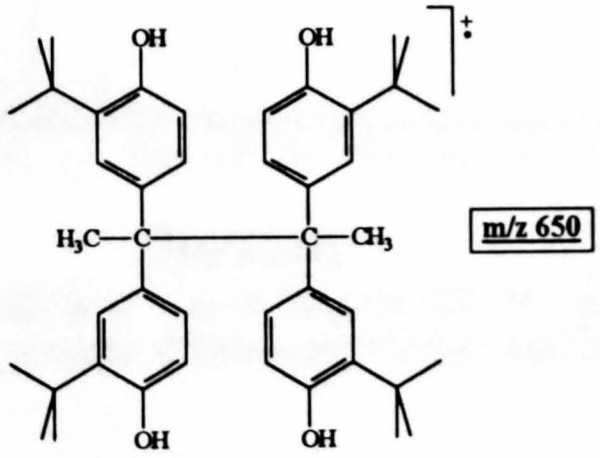

Figure 7.19.

The Proposed Structure of the Fragment Ion of Hostanox 03 Observed at m/z 650.

Other fragment ions at low m/z ratios are formed by losses of neutral species from the m/z 325 ion. Ions of the same m/z ratio are observed in the MS/MS spectrum of m/z 325.

The EI-MS and LSIMS-MS spectra of Hostanox 03 are very similar to the CID spectrum. The generation of ions which are formed by rearrangement processes is more favoured by means of LSIMS ionisation.

7.4.(iii) Timuvin 327. The CID spectrum of Tinuvin 327 is shown in Figure 7.20.

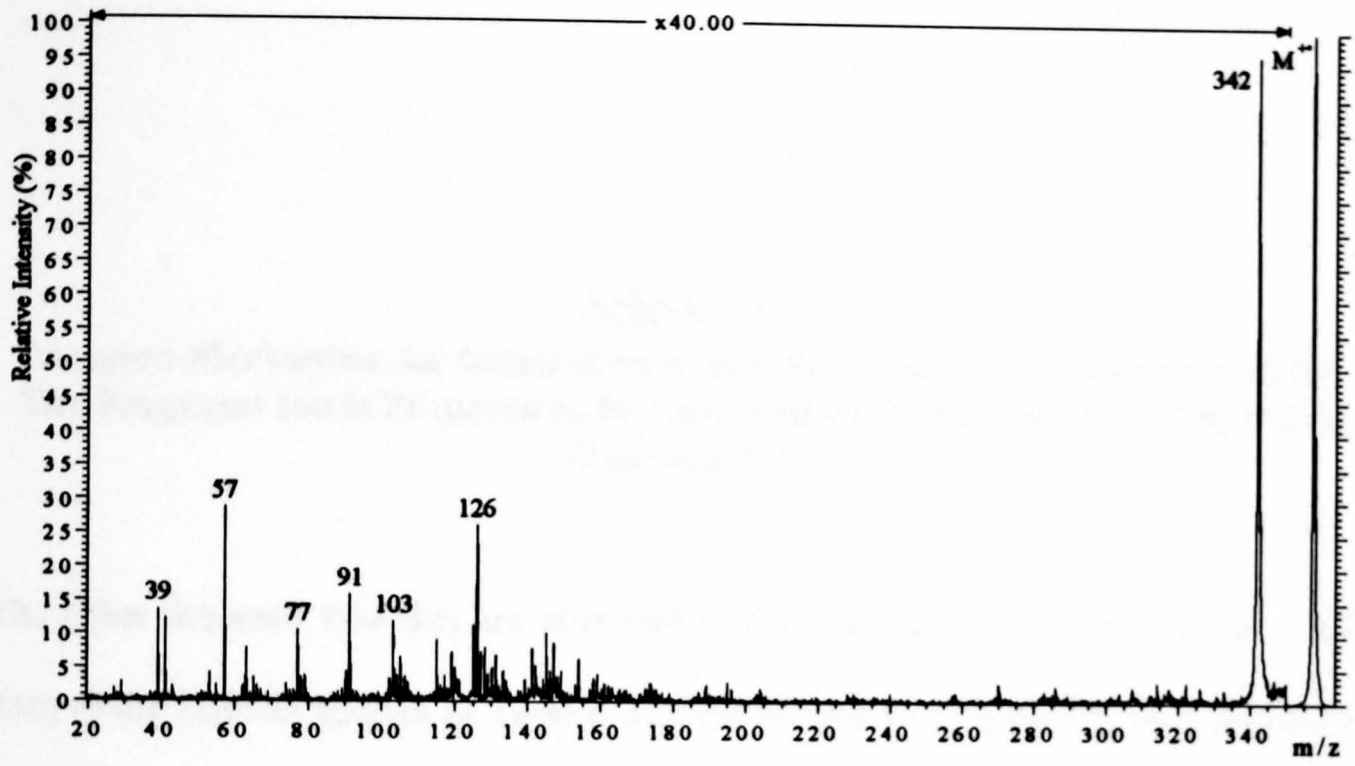

Figure 7.20.

LSIMS-MS/MS Spectrum of Tinuvin 327, $M^{+\bullet}$ m/z 357, from an Equimolar Mixture of Polymer Additives.

The most intense fragment ion in the spectrum is that due to a loss of a radical of mass 15 Da from the precursor ion and is observed at m/z 342. This has been assigned as the loss of a methyl radical from the *tert*-butyl group (Scheme 7.7). The ion that is generated is possibly stabilised by the formation of an oxonium ion (Scheme 7.7). A similar mechanism possibly occurs to stabilise the $[M^{+\bullet} - CH_3^{\bullet}]$ fragment ion observed in the CID spectrum of Irganox 1076 (Figure 7.10).

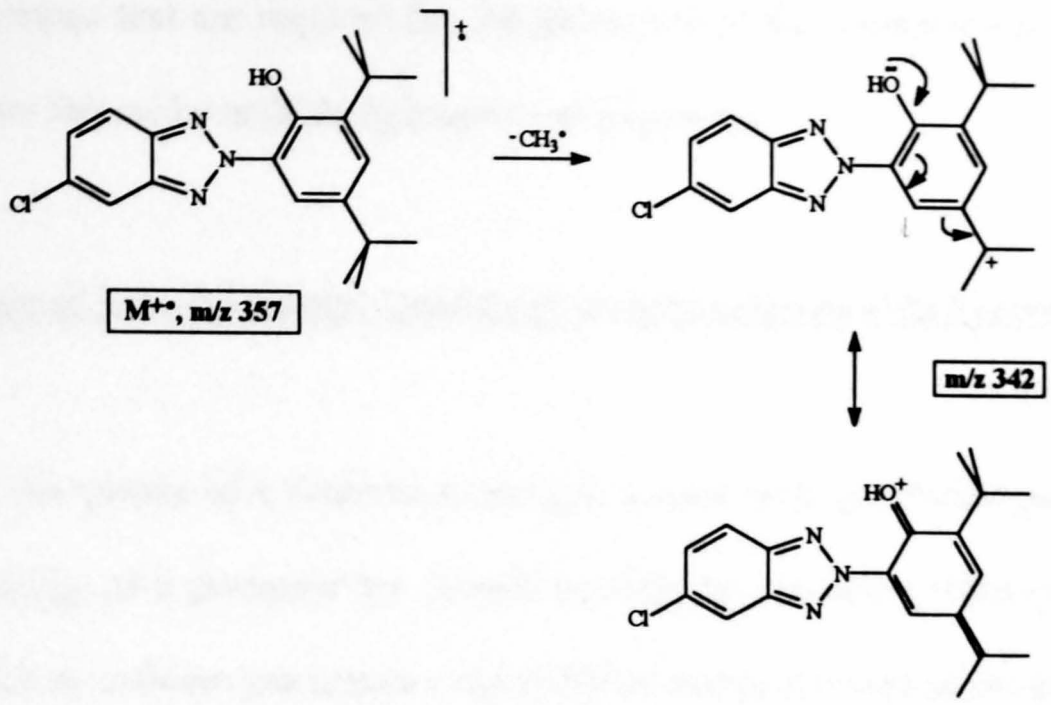

Scheme 7.7.

Proposed Mechanism for Generation of m/z 342 Fragment Ion of Tinuvin 327. The Fragment Ion is Proposed to be Stabilised by Generation of a Substituted Oxonium Ion.

The other fragment ions that are observed in the lower end of the mass range (<m/z 250) in the MS/MS spectra of Tinuvin 327 are formed *via* complex rearrangements of two or more hydrogens. This is indicated by the various series of fragment ion peaks separated by 1 Da. Ions of the same mass-to-charge ratio are also seen in the EI-MS spectrum of this compound, differing only in relative intensity. A possibility for hydrogen rearrangement from the hydroxyl group to the triazole ring, generating the carbonyl isomer of Tinuvin 327, is possibly the first process in the generation of many of the fragment ions. The carbonyl isomer of these types of compounds has been observed for similar compounds in the excited state [54].

The EI-MS spectrum is very similar to the CID spectrum but very little fragmentation is observed in the LSIMS-MS spectrum. This is probably a consequence of the high

critical energies that are required for the generation of the fragment ions of Tinuvin 327 that are formed by multiple hydrogen rearrangements.

7.5. Effects of Internal Energy Deposition by Ionisation on CID Spectra.

Fragment ion spectra of a compound can give a reasonable qualitative picture of the internal energy of a precursor ion formed by different ionisation techniques if other factors such as collision gas pressure and collision energy are kept constant. The CID spectra from the $M^{+\cdot}$ ion of Irganox 1076 generated by EI, LSIMS, ammonia-CI and FD ionisation are shown in Figure 7.21.

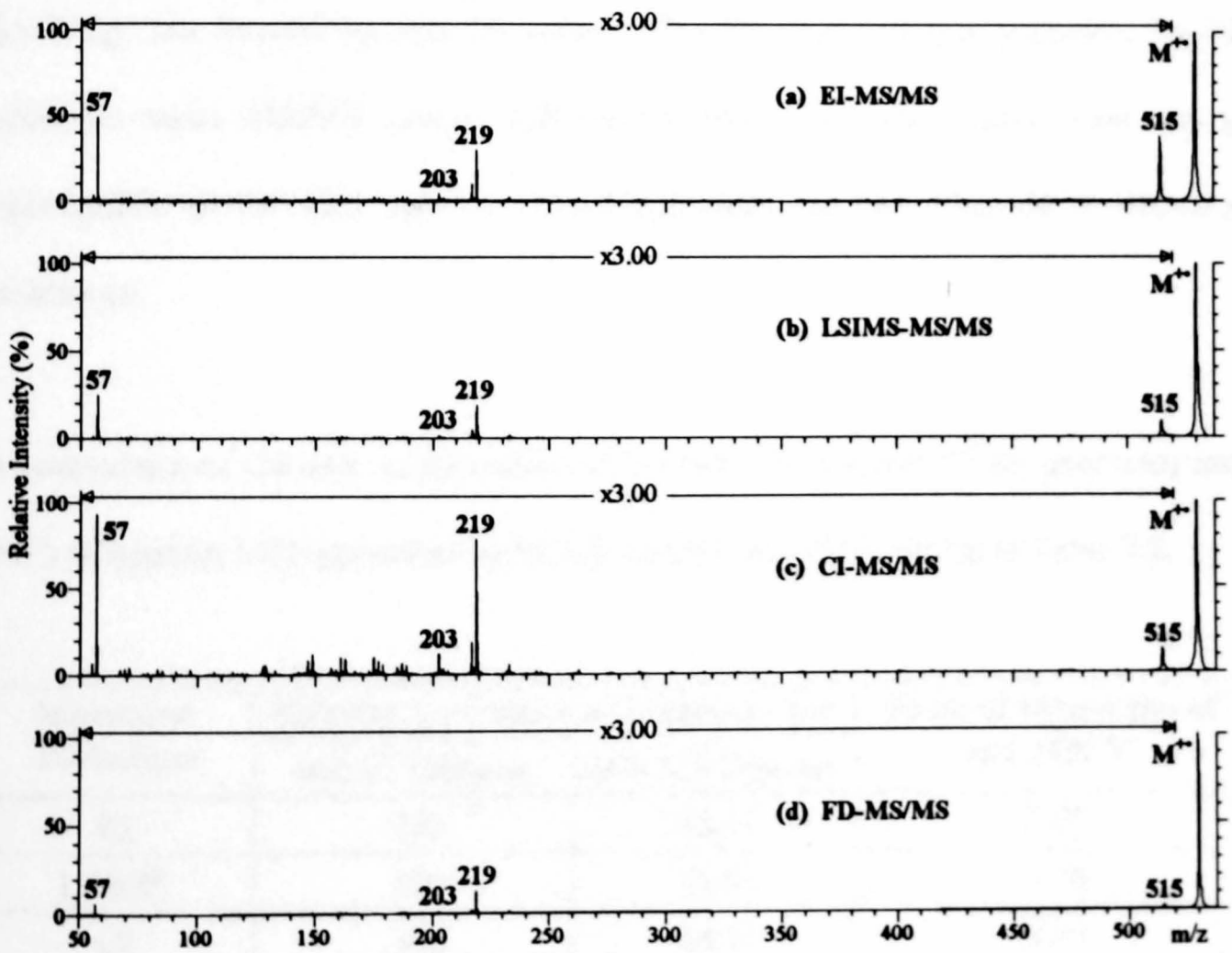

Figure 7.21.

MS/MS Spectra of Irganox 1076, $M^{+\cdot}$ m/z 530, Generated by: (a) EI; (b) LSIMS; (c) CI and (d) FD.

The distribution of fragment ions observed in CID spectra is presumed to be affected less by the internal energy deposited during the ionisation process than by that transferred as a consequence of collisional activation in a collision cell. The spectra in Figure 7.21 show that fragment ions of Irganox 1076 are observed at the same m/z ratios from precursor ions generated by all four ionisation techniques. These data (Figure 7.21) indicate that the internal energy of the precursor ion has some, but very little, qualitative effect on the CID spectra of the polymer additives. Furthermore, the similarity of the spectra suggests that molecular ions of polymer additives generated by EI, LSIMS, CI and FD may have a common structure. This implies that the ions generated by ammonia-CI are the radical cation, $M^{+\bullet}$, and not a fragment of the $[M+NH_4]^+$ ion formed by loss of water. The low ion currents generated by FD ionisation made MS/MS spectra difficult to obtain and the results were not as reproducible as for CID spectra of ions generated by the other three ionisation techniques.

A comparison of the ratio of intensities of the m/z 219 and m/z 57 for precursor ions ($M^{+\bullet}$) of Irganox 1076 generated by EI, CI, LSIMS and FD is shown in Table 7.2.

Ionisation Technique	Relative Intensities of Fragment Ion		Ratio of Intensities of m/z 219: 57
	m/z 57 Daltons	m/z 219 Daltons	
EI	100	60.11	0.60
LSIMS	100	74.84	0.75
CI	100	84.15	0.84
FD	54.69	100	1.83

Table 7.2.

The Ratio of Relative Intensities of the Fragment Ion at m/z 219 to that at m/z 57 from the EI, LSIMS, CI and FD-MS/MS Spectra of Irganox 1076.

These ions are generated by loss of radicals from the molecular ion in the collision region. The m/z 57 ion is formed by charge transfer from the phenyl ring to the *tert*-butyl group of the molecule, generating $C_4H_9^+$. Cleavage β to the phenyl ring generates the ion at m/z 219, proposed to have the structure shown in Figure 7.12(b).

The effects of varying the ionisation technique on the CID spectra are very small as a consequence of the greater contribution of internal energy by collisional activation processes. The amount of internal energy deposited by collisional activation of the precursor ion predominantly determines the degree of fragmentation observed in CID spectra. This may be rationalised by comparing the CID spectra generated when the pressure of the gas in the collision cell is varied. Increasing the gas pressure should increase the average number of collisions between the precursor ions and the target gas atoms. The internal energy uptake of the precursor ions should therefore also increase.

The m/z 57 fragment ion peak is relatively less intense than that at m/z 219 when no collision gas is allowed into the CID cell, compared to that obtained when an attenuation of the precursor ion beam of 80% with argon is employed. The internal energy of precursor ions increases with a higher gas pressure in the collision cell, giving a lower precursor ion transmission to the second analyser as more fragment ions are generated. The intensity of the m/z 57 fragment ion would therefore be expected to increase with respect to the m/z 219 ion as the internal energy of the precursor rises. Figure 7.22 shows a line graph of the ratio of relative intensities of m/z 219: m/z 57 for the four ionisation techniques. The ratio of m/z 219: m/z 57 increases when the ionisation technique is changed from EI to FD through LSIMS and CI.

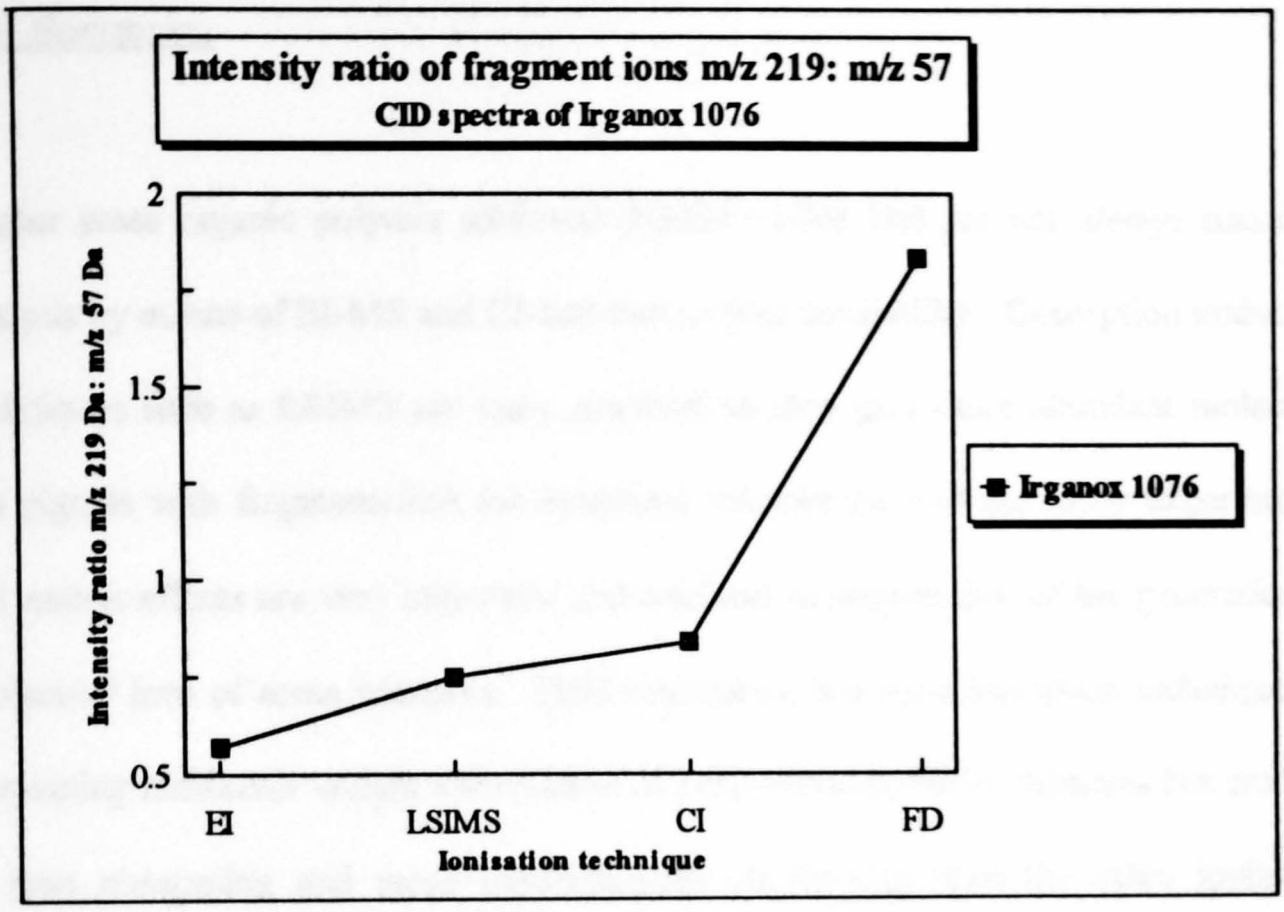

Figure 7.22.

Line Graph Comparing the Change in Intensity of the Ratio of m/z 219: m/z 57 in the CID Spectra of Irganox 1076 when the Ionisation Technique is Different.

The observed trend follows that expected for the four ionisation techniques. Ions generated by means of EI ionisation have high amounts of internal energy on average and are therefore likely to fragment more readily than those formed by the other techniques. FD generates ions with very low amounts of internal energy and so less fragmentation is expected. Ions with intermediate quantities of internal energy are formed by means of LSIMS and CI ionisation.

7.6. Summary.

Higher mass organic polymer additives (RMM >1000 Da) are not always suited to analysis by means of EI-MS and CI-MS due to their involatility. Desorption ionisation techniques such as LSIMS are more practical as they give more abundant molecular ion signals with fragmentation for structural information and are facile experiments, but matrix effects are very important and can lead to suppression of the generation of molecular ions of some additives. Field desorption is a good ionisation technique for generating molecular weight information of polymer additives in mixtures but analysis is time consuming and more experimentally challenging than the other ionisation techniques. Predominantly $[M+Ag]^+$ ions are generated by means of UV-MALDI ionisation and often some clusters are observed which could make assignment of unknowns more complex than for analysis by means of FD. Furthermore, matrix effects are also important. Analysis by means of UV-MALDI-MS is rapid and the experiment is simple but the instrumental capability for CID experiments is far from being widely available.

The low ion currents generated by FD make MS/MS spectra difficult to obtain. LSIMS is therefore a more suitable ionisation technique for analysis of mixtures by means of tandem mass spectrometry. High energy MS/MS of the molecular ions of additives in a mixture aids structural elucidation as these molecules often dissociate to generate characteristic fragment ions such as m/z 219 and 203 for the Irganox compounds analysed in these experiments and m/z 325 and 309 for Hostanox 03. These ions are not always prominent in the low energy MS/MS spectra of the same

compounds [21]. The mechanisms proposed indicate that many of the fragment ions generated from the additives studied here may have substituted oxonium ion structures.

LSIMS-MS/MS experiments may therefore be used in conjunction with FD-MS as screen to determine the class, molecular weight and structure of mixtures of organic polymer additives.

1 R. P. Lattimer and R. E. Harris, *Mass Spectrom. Rev.*, **4**, 369 (1985).

2 A. M. Wims and S. J. Swarin, *J. Appl. Poly. Science*, **19**, 1243 (1975).

3 J. Lehotay, J. Danecek, O. Líska, J. Lesko and E. Brandsteterová, *J. Appl. Poly. Science*, **25**, 1943 (1980).

4 P. Rudewicz and B. Munson, *Anal. Chem.*, **58**, 358 (1986).

5 J. D. Vargo and K. L. Olson, *Anal. Chem.*, **57**, 672 (1985).

6 R. P. Lattimer, R. E. Harris, C. K. Rhee and H.-R. Schulten, *Anal. Chem.*, **58**, 3188 (1986).

7 T. L. Riley, T. J. Prater, J. L. Gerlock, J. E. deVries and D.. Schuetzle, *Anal. Chem.*, **56**, 2145 (1984).

8 R. P. Lattimer, R. E. Harris, D. B. Ross and H. E. Diem, *Rubber Chem. Technol.*, **57**, 1013 (1984).

9 C. L. Johlman, C. L. Wilkins, J. D. Hogan, T. L. Donovan, D. A. Laude, Jr. and M.-J. Youssefi, *Anal. Chem.*, **62**, 1167 (1990).

10 J. O. Lay and B. J. Miller, *Anal. Chem.*, **59**, 1323A (1987).

11 R. P. Lattimer, R. E. Harris, D. B. Ross and H. E. Diem, *Rubber Chem. Technol.*, **57**, 1013 (1984).

12 R. P. Lattimer, *J. Anal. Appl. Pyrolysis*, **26**, 65 (1993).

13 A. T. Hsu and A. G. Marshall, *Anal. Chem.*, **60**, 932 (1988).

14 B. Asamato, J. R. Young and R. J. Citerin, *Anal. Chem.*, **62**, 61 (1990).

15 J. E. Hunt, K. R. Lykke and M. J. Pellin in *Methods and Mechanisms for Producing Ions from Large Molecules* (K. G. Standing, Ed.), Plenum Press, New York, 309 (1991).

16 M. P. Mawn, R. W. Linton, S. R. Bryan, B. Hagenhoff, U. Jürgens and A. Benninghoven, *J. Vac. Sci. Technol.*, **A9**, 1307 (1991).

17 M. P. Mawn, A. M. Belu, R. W. Linton and A. Benninghoven, *Proceedings of 40th Annual Conference on Mass Spectrometry and Allied Topics, Washington, DC*, ASMS, Santa Fe (1992).

18 J. H. Scrivens, *Proceedings of the 13th ICMS Conference*, Budapest (1994).

19 R. P. Lattimer, *Rubber Chem. Technol.*, **61**, 658 (1988).

20 R. P. Lattimer, H. Muenster and H. Budzikiewicz, *Rubber Chem. Technol.*, **63**, 298 (1990).

21 S. W. Chen and G. R. Her, *Applied Spectroscopy*, **47**, 844 (1993).

22 J. M. Curtis, C. D. Bradley, P. J. Derrick and M. M. Sheil, *Org. Mass Spectrom.*, **27**, 502 (1992).

23 M. M. Sheil, G. W. Kilby, J. M. Curtis, C. D. Bradley and P. J. Derrick, *Org. Mass Spectrom.*, **28**, 574 (1993).

24 W. Brand and K. Levsen, *Int. J. Mass Spectrom. Ion Phys.*, **35**, 1 (1980).

25 C. Fenslau and R. J. Cotter, *Chem. Rev.*, **87**, 501 (1987).

26 D. Renner and G. Spiteller, *Biomed. Environ. Mass Spectrom.*, **13**, 401 (1986).

27 E. Schroder, H. Munster and H. Budikiewicz, *Org. Mass Spectrom.*, **21**, 707 (1986).

28 G. J. C. Paul, R. Theberge, M. J. Bertrand, R. Feng and M. D. Bailey, *Org. Mass Spectrom.*, **28**, 1329 (1993).

29 G. J. C. Paul, S. Bourg and M. J. Bertrand, *J. Am. Soc. Mass Spectrom.*, **4**, 493 (1993).

30 G. Dube, *Org. Mass Spectrom.*, **19**, 242 (1984).

31 E. Egestad and P. Sjoberg, *Rapid Commun. Mass Spectrom.*, 7, 812 (1993).

32 H. Nakata and K. Tanaka, *Org. Mass Spectrom.*, **29**, 283 (1994).

33 H. Nakata, N. Arakawa and R. Mizuno, *Org. Mass Spectrom.*, **29**, 192 (1994).

34 S. J. Pachuta and R. G. Cooks, *Chem. Rev.*, **87**, 647 (1987).

35 C. Bojeson and M. Moller, *Int. J. Mass Spectrom. Ion Proc.*, **66**, 239 (1986).

36 Q.-W. Huang and G.-L. Wu, *Int. J. Mass Spectrom. Ion Proc.*, **70**, 145 (1986).

37 E. Clayton and A. J. C. Wakefield, *J. Chem. Soc., Chem. Commun.*, 969 (1984).

38 L. D. Detter, O. W. Hand, R. G. Cooks and R. A. Walton, *Mass Spectrom. Rev.*, 7, 465 (1988).

39 D. H. Williams, A. F. Findeis, S. Naylor and B. W. Gibson, *J. Am. Chem. Soc.*, **109**, 1980 (1987).

40 S. Kurono, T. Tani, T. Hirano, K. Tsujimoto and M. Ohashi, *Org. Mass Spectrom.*, **27**, 1365 (1992).

41 R. Theberge and M. J. Bertrand, *J. Mass Spectrom.*, **30**, 163 (1995).

42 D. H. Williams, A. F. Findeis, S. Naylor and B. W. Gibson, *J. Am. Chem. Soc.*, **109**, 1980 (1987).

43 D. H. Williams and S. Naylor, *J. Chem. Soc., Chem. Commun.*, 1408 (1987).

44 L. Kelner and S. P. Markey, *Int. J. Mass Spectrom. Ion Proc.*, **59**, 157 (1984).

45 T. Keough and A. J. DeStefano, *Org. Mass Spectrom.*, **16**, 527 (1981).

46 R. Yamalagni and P. Kerbarle, *J. Am. Chem. Soc.*, **95**, 1320 (1976).

47 J. L. Gower, R. T. Edser and G. D. Risbridger, *Int. J. Mass Spectrom. Ion Proc.*, **47**, 467 (1983).

48 K. P. Madhusudanan, *J. Mass Spectrom.*, 30, 639 (1995).

49 L. M. Mallis and D. H. Russell, *Anal. Chem.*, **58**, 1076 (1986).

50 J. Adams and M. L. Gross, *Anal. Chem.*, **59**, 1576 (1987).

51 H. Budzikiewicz, C. Djerassi and D. H. Williams, *Interpretation of Mass Spectra of Organic Compounds*, Holden-Day, San Francisco, chapter 9 (1964).

52 J. Adams and M. L. Gross, *J. Am. Chem. Soc.*, **108**, 6915 (1986).

53 J. Adams and M. L. Gross, *Anal. Chem.*, **59**, 1576 (1987).

54 F. Gugumus in *Plastics Additives Handbook*, R. Gächter and H. Müller (Eds.), Hanser, Munich, 180 (1990).

CHAPTER 8.

ELECTROSPRAY-LOW ENERGY TANDEM MASS SPECTROMETRY OF POLYMER ADDITIVES.

8.1. Introduction.

8.1.(i) Electrospray Ionisation of Polymer Additives. There are few reports in the literature of the analysis of polymer additives by means of ESI-MS or ESI-MS/MS. This prompted a preliminary investigation into the effectiveness of this technique for analysing the same group of polymer additives as that studied by means of high energy experiments (Chapter 7). Furthermore, these experiments also enable a comparison of the high energy and low energy CID spectra of polymer additives to be made. Tinuvin 327 was not suitable for to analysis by ESI, however, and it is presumed that this compound is more likely to be compatible with atmospheric pressure chemical ionisation (APCI). APCI is often of wider applicability than ESI to the analysis of compounds with a low RMM.

A plasticiser that is commonly used in polymeric systems such as poly vinyl chloride (PVC), Emkarate 3020, was also studied by means of ESI-MS/MS. This additive is a mixture of phthalate esters that has the basic structure given in Figure 8.1. The unbranched hydrocarbon chains R are predominantly 13 carbon atoms in length with a distribution of other chains with similar dimensions (Figure 8.1).

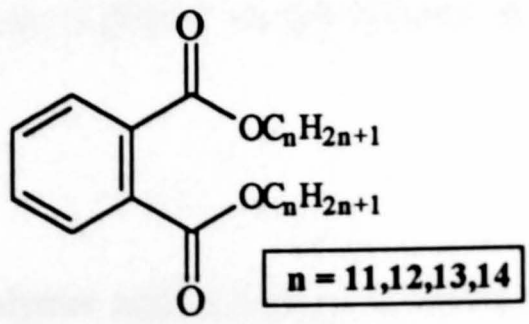

Figure 8.1.
The Structure of Emkarate 3020, a Phthalate Ester.

8.1.(ii) Sample Preparation. Samples for analysis by means of ESI were dissolved in methanol (MeOH)/tetrahydrofuran (THF) (1:1 *v/v*, 100 pmol μL^{-1}) and mixed with ammonium chloride (0.5%). Enough water was added to the MeOH/THF to dissolve the ammonium chloride which is insoluble in MeOH/THF. The mobile phase employed was MeOH/THF and the pumping speed was 5 $\mu L\ min^{-1}$.

8.2. ESI-Low Energy Mass Spectrometry of Polymer Additives.

A number of factors contribute to the intensity and distribution of the peaks observed in the mass spectra of ions generated by ESI. These factors include the amount of salt added to the analyte to aid ionisation and the value of the cone voltage. The amount of salt (NH_4Cl) added to the sample partially determines the intensity of the analyte peaks observed which are typically of the form $[M+NH_4]^+$. Furthermore, clusters of salt are always seen in the ESI mass spectra with the general formula $[(NH_4)_{n+1}Cl_n]^+$. A distribution of peaks due to the presence of the two isotopes of chlorine is observed for every value of n. These clusters were more intense when increased concentrations of ammonium salt were added to the sample and the analyte peaks were observed at reduced intensity. The concentration of salt employed in these experiments generated intense analyte signals with the minimum of salt clusters as shown by Campana and coworkers [1].

The molecular ions from polymer additives seen in the mass spectra were all singly charged species and were predominantly clusters with an ammonium ion, namely $[M+NH_4]^+$. Clusters of two molecules of analyte with ammonium ions ($[2M+NH_4]^+$)

were also observed in all ESI mass spectra of these compounds. The $[2M+NH_4]^+$ ions were more intense for polymer additives with a low RMM. Multiply charged ions were not observed for any of the samples analysed. This is probably due to the molecular shape and low RMM of the polymer additives. The low number of basic binding sites in the polymer additives for association with NH_4^+ is also an important factor as multiply charged ions are often observed in the ESI mass spectra of peptides with similar RMM [2].

Singly charged protonated molecules (MH^+) of phthalate esters were observed at high abundances in the mass spectrum of Emkarate 3020 (Figure 8.2).

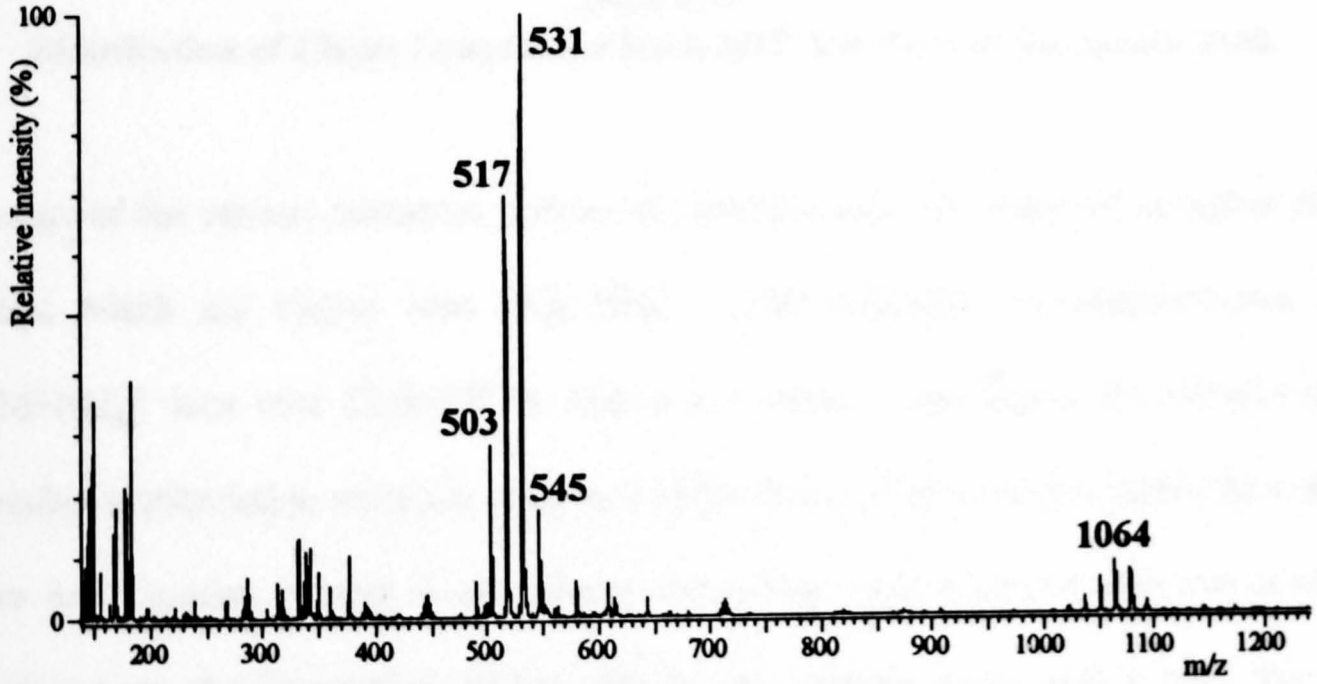

Figure 8.2.

ESI-MS Spectrum of Emkarate 3020. Cone Voltage = 57 V.

Ion peaks corresponding to $[M+NH_4]^+$ were also seen at low intensities. The distribution of MH^+ peaks indicates the presence of phthalate esters with chains R of 10-14 carbon atoms in length (Figure 8.1). The m/z ratio of each ion and the corresponding hydrocarbon chain length of the phthalate esters in the observed

distribution are shown in Table 8.1. The percentages of phthalate esters with each chain length present in the mixture could be estimated by means of a statistical approach as employed by Scrivens and coworkers for the analysis of commercial lubricants which often contain a complex mixture of esters [3].

Mass-to-Charge Ratio (m/z)	Length of Carbon Chains R (No. of Carbon Atoms in Chain)
475	11,11
489	11,12
503	12,12; 11,13
517	12,13; 11,14
531	13,13; 12,14
545	14,13
559	14,14

Table 8.1.

Distribution of Chain Lengths for Each MH^+ Ion Peak of Emkarate 3020.

Dimers of the various molecular species of phthalate ester are observed at higher m/z ratios which are cluster ions with NH_4^+. This indicates the predominance of $[2M+NH_4]^+$ ions over $[2M+H]^+$ at higher m/z ratios. The high mass clusters are possibly tetrahedral in structure with each of the four carbonyl oxygen atoms from the two ester species present in the cluster interacting with a central ammonium ion. Furthermore, the interactions of two species of phthalate esters with a NH_4^+ ion to produce the dimers also gives a broader distribution of ion peaks than that given by the MH^+ species. This phenomenon is observed as a consequence of an increase in the statistical distribution of hydrocarbon chain lengths in phthalate esters that may contribute to each cluster ion peak.

The most important factor that influences the distribution of molecular and fragment ions in the ESI mass spectra of polymer additives is the cone voltage. The mass spectra obtained from Hostanox 03 when the cone potential was set at 30 and 89 V are shown in Figure 8.3. At low cone voltages little or no fragmentation occurs but dissociations of the ionised species become prominent as the potential is increased. This is indicated in Figure 8.3(a) as no decomposition of Hostanox 03 occurs in the source region when the cone voltage is 30 V. At a cone potential of 89 V, however, considerable fragmentation is observed in the ESI mass spectrum (Figure 8.3(b)). The ions labelled in Figure 8.3(b) are all fragments from $[M+NH_4]^+$ of Hostanox 03.

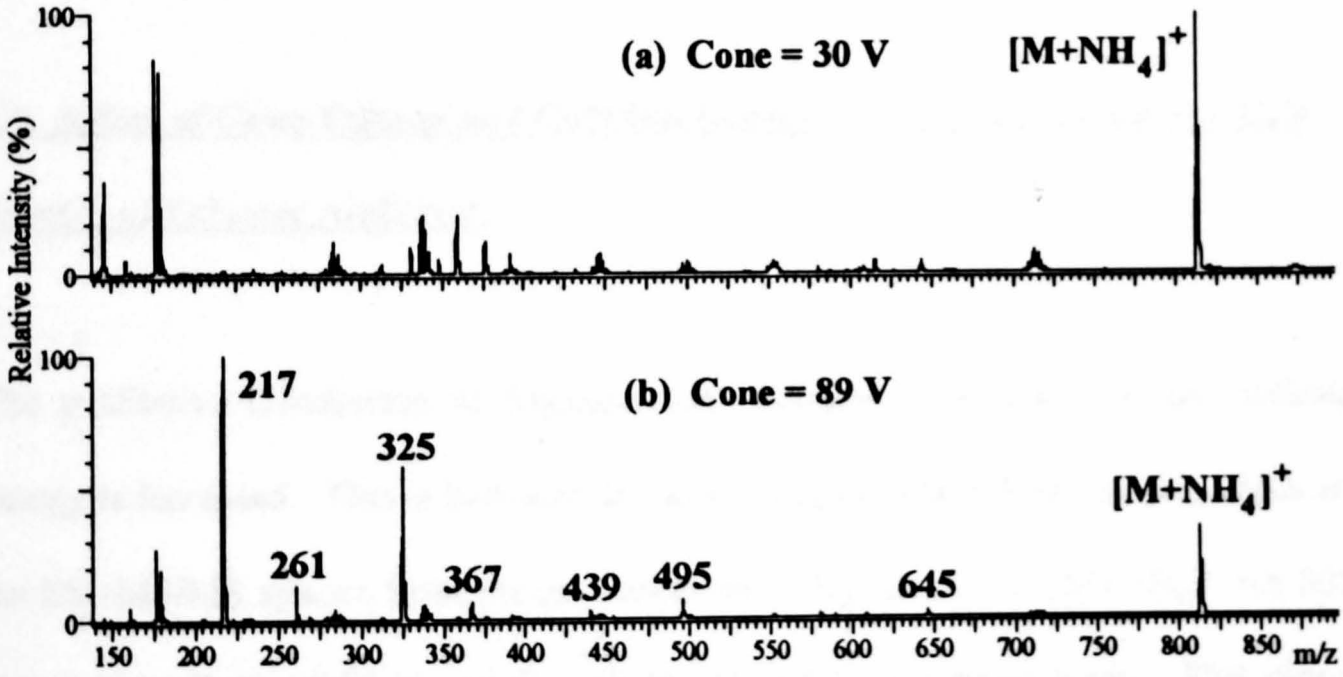

Figure 8.3.

ESI-MS Spectrum of Hostanox 03 at a Cone Voltage of (a) 30 V and (b) 89 V.

The cone voltage at which decomposition is induced is dependent on the RMM of the precursor ion. Fragmentation of species with low RMM is induced at low cone voltages whereas polymer additives with higher RMM require a greater input of internal energy and therefore only start to fragment at high values of cone potential. Furthermore, peaks are observed at 32 and 72 Da greater than that of many fragment

ions. These peaks arise due to formation of clusters of fragment ions with solvent molecules, namely MeOH and THF which have an RMM of 32 and 72 Da respectively. Clusters of solvent with analyte have been observed in the ESI mass spectra of some species of synthetic polymers [4]. The ion-molecule reactions which are a prerequisite for the generation of these ions would be expected to be more prominent at lower values of the cone potential but these clusters are not observed under these conditions as no fragmentation occurs. It is presumed that these ions are formed only with certain fragment ions which have low steric hindrance. This will be discussed further in Section 8.4.

8.3. Effect of Cone Voltage and Collision Energy on the ESI-Low Energy CID Spectra of Polymer Additives.

The qualitative distribution of fragment ions changes considerably as the collision energy is increased. This is indicated by comparing Figures 8.4(a) and (b), which are the ESI-MS/MS spectra from the precursor ion of Irganox 3114, $[M+NH_4]^+$ m/z 802, at a cone voltage of 36 V and E_{coll} of 15 eV and 85 eV respectively. This clearly shows the shift in m/z ratios of fragment ions at higher collision energies. Larger collision energies were required to generate optimum CID spectra of polymer additives with higher RMM. This is a consequence of the increasing number of degrees of freedom with RMM of the polymer additives. More internal energy is therefore required for dissociation to occur.

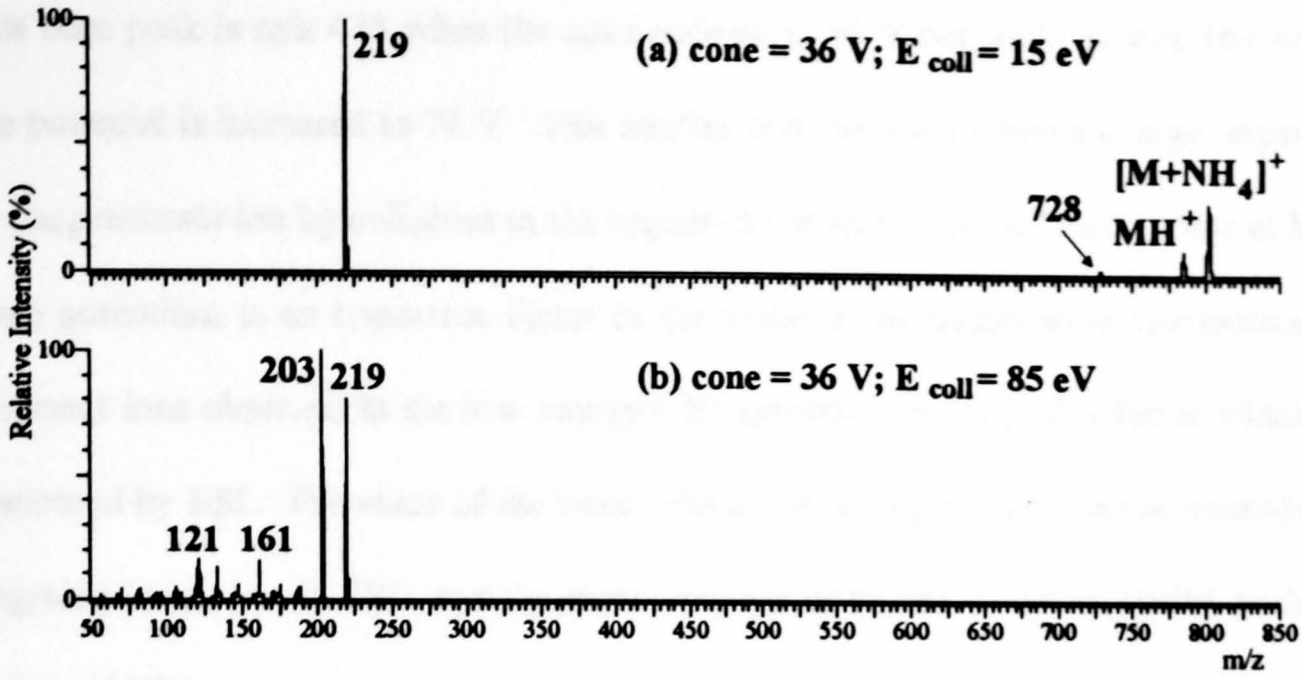

Figure 8.4.

ESI-MS/MS Spectra of Irganox 3114, $[M+NH_4]^+$ m/z 801, at Cone Voltage 36 V and Collision Energy (a) 15 eV and (b) 85 eV.

The CID spectrum of Irganox 1076, $[M+NH_4]^+$ m/z 549, obtained at a collision energy of 10 eV and cone voltages of 46 and 74 V (Figures 8.5(a) and (b) respectively) show the effect of the cone potential on the distribution of fragment ions observed in the low energy CID spectra of polymer additives.

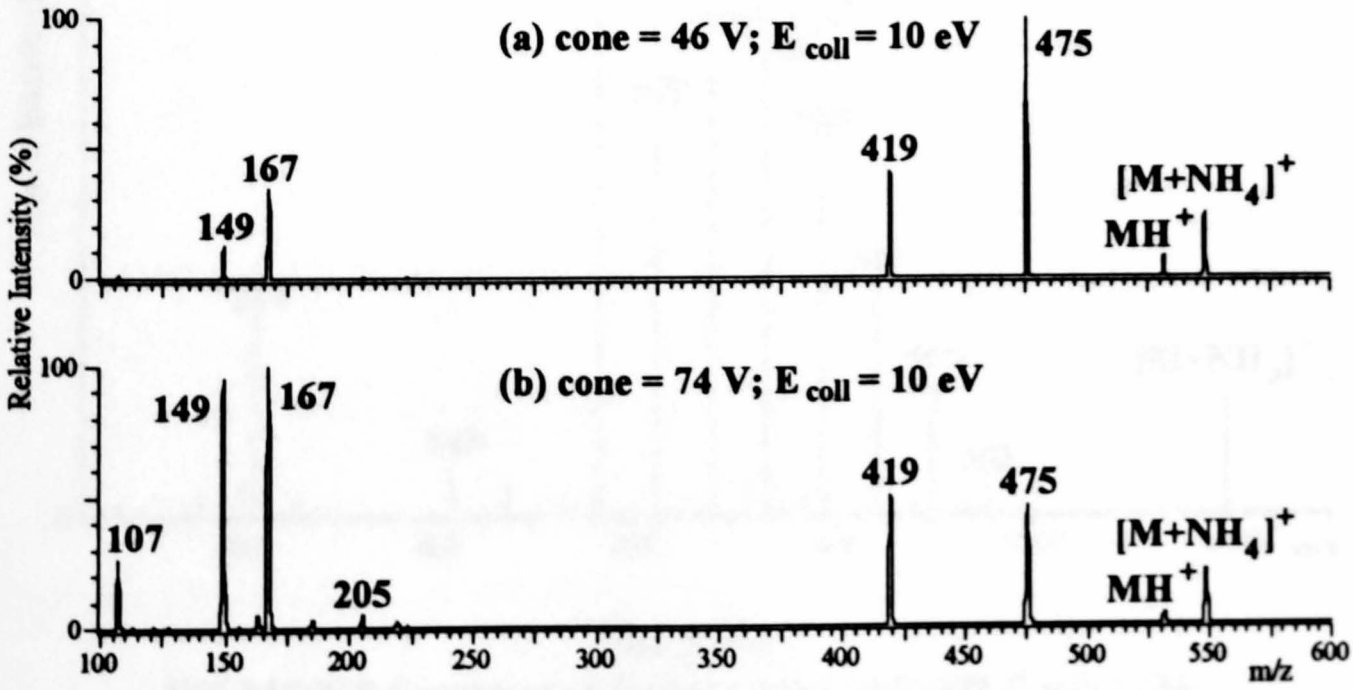

Figure 8.5.

ESI-MS/MS Spectra of Irganox 1076, $[M+NH_4]^+$ m/z 548, at Collision Energy 10 eV and Cone Voltage (a) 46 V and (b) 74 V.

The base peak is m/z 475 when the cone voltage is 46 V but shifts to m/z 167 when the potential is increased to 74 V. This implies that the extra internal energy imparted to the precursor ion by collisions in the region of the sample cone, which occur at high cone potentials, is an important factor in determining the quantitative distribution of fragment ions observed in the low energy CID spectra from ions of polymer additives generated by ESI. The value of the cone voltage has a larger effect on the intensity of fragment ions seen in CID spectra from polymer additives of lower RMM such as Irganox 1076.

8.4. ESI-Low Energy CID of Polymer Additives.

8.4.(i) Irganox 1010. Figure 8.6 is the fragment ion spectrum from the ammoniated molecule ion ($[M+NH_4]^+$) of Irganox 1010 at a collision energy of 35 eV.

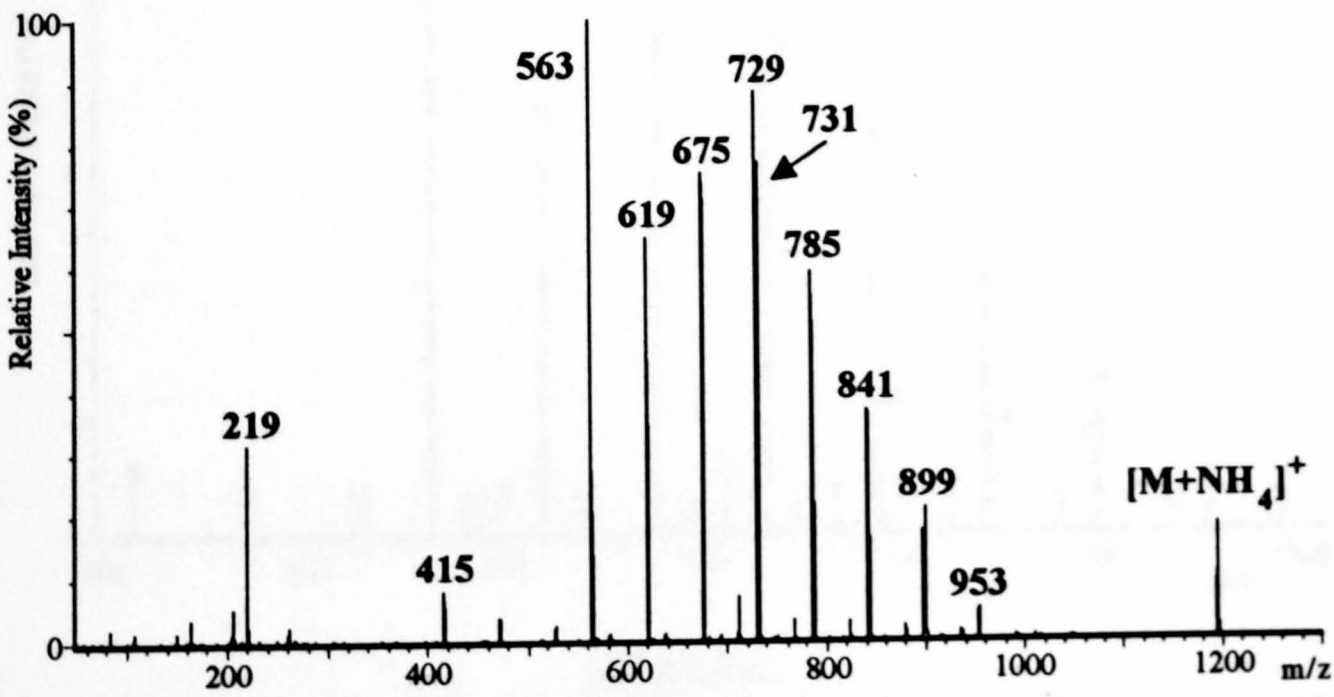

Figure 8.6.

ESI-MS/MS Spectrum of Irganox 1010, $[M+NH_4]^+$ m/z 1194, at Cone Voltage 67 V and Collision Energy 35 eV.

The low energy CID spectrum from the same precursor ion generated by means of desorption chemical ionisation (DCI) is similar [5]. It is interesting to note that the spectrum in Figure 8.6 is comparable with that generated by means of LSIMS-MS under high energy conditions. This indicates that the internal excitation energy deposited in the LSIMS ionisation process is similar to that by means of ESI-low energy CID under the conditions used in these experiments. LSIMS is thought to impart an average of approximately 1-2 eV of internal excitation energy during the ionisation process [6,7,8].

The low energy CID spectrum is dominated by two series of peaks, differing by 56 Da, in the centre of the mass range (m/z 500-900). An expanded view of the m/z 400-1000 region of the spectrum is shown in Figure 8.7.

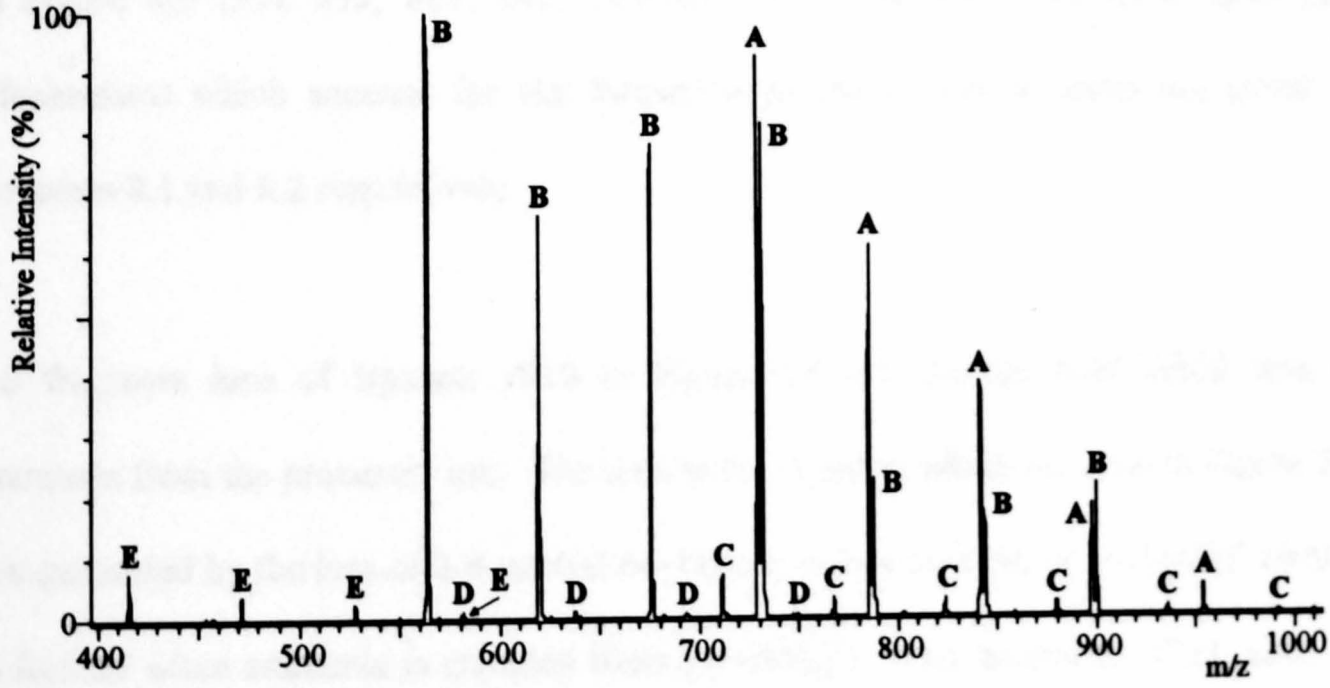

Figure 8.7.

Expanded Region (m/z 400-1000) of the ESI-MS/MS Spectrum of Irganox 1010, $[M+NH_4]^+$ m/z 1194, at Collision Energy 35 eV.

Closer examination of this region indicates that five series are present, which are labelled A-E in Figure 8.7. All ions in each series have a sequential mass difference of

56 Da. The m/z ratios of all of the fragment ions in the five series which are observed in the CID spectrum are shown in Table 8.2.

Series	Assignment	m/z Ratios of Fragment ions Observed
A	$[M+NH_4]^+ - NH_3 - (56)_n$	1065; 1009; 953; 897; 841; 785; 729
B	$[M+NH_4]^+ - NH_3 - 278 - (56)_n$	899; 843; 787; 731; 675; 619; 563
C	$[M+NH_4]^+ - NH_3 - 18 - (56)_n$	1103; 1047; 991; 935; 879; 823; 767; 711
D	$[M+NH_4]^+ - NH_3 - 260 - (56)_n$	805; 749; 693; 637; 581
E	$[M+NH_4]^+ - NH_3 - 538 - (56)_n$	639; 583; 527; 471; 415

Table 8.2.

The Assignment and m/z Ratios of the Various Series of Fragment Ions Observed in the CID Spectrum of Irganox 1010.

A general structure for the ions of the B series (m/z 899, 843, 787, 731, 675, 619 and 563) was postulated by Chen et al. [5] but no mechanism was forwarded. The observation of ions from the A series in the DCI-CID spectrum, which are very intense in Figure 8.6 (m/z 953, 897, 841, 785 and 729), was not commented upon [5]. Mechanisms which account for the formation of the A and B series are given in Schemes 8.1 and 8.2 respectively.

All fragment ions of Irganox 1010 in Figure 8.6 are formed with initial loss of ammonia from the precursor ion. The ions in the A series which are seen in Figure 8.6 are generated by the loss of 2-8 neutral *iso*-butene units (*iso*-C_4H_8) from $[MH]^+$ (which is formed when ammonia is expelled from $[M+NH_4]^+$). The neutral *iso*-C_4H_8 units of mass 56 Da are generated by a 1,3-hydrogen rearrangement from a methyl substituent of the *tert*-butyl groups to the substituted phenol ring. The ions formed are proposed to have the structures shown in Scheme 8.1. Loss of a carboxylic acid from ions in the A series yields the B series. This mechanism requires the site of protonation

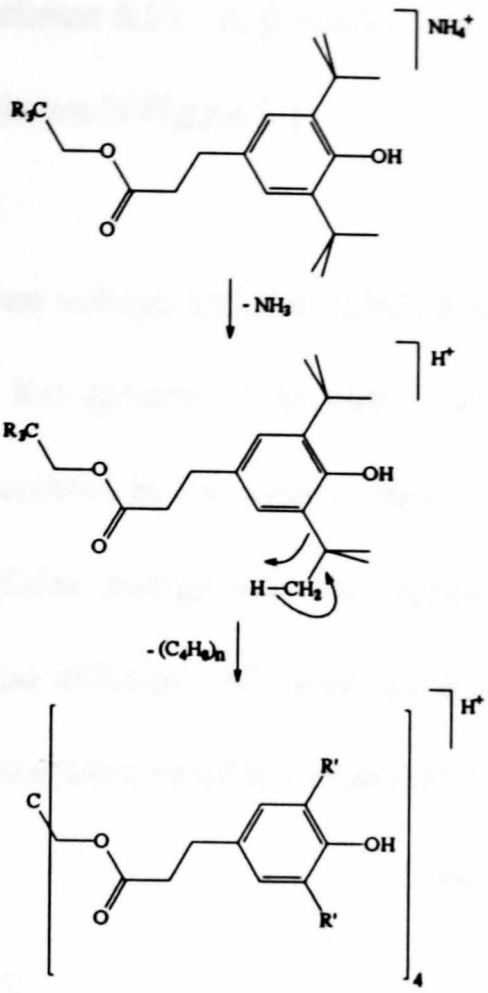

A Series
1065(w), 1009(w), 953, 897, 841, 785, 729

R' = H, $C(CH_3)_3$

Scheme 8.1.

Proposed Mechanism for Generation of the A Series Observed in the ESI-MS/MS Spectrum of Irganox 1010, $[M+NH_4]^+$ m/z 1194.

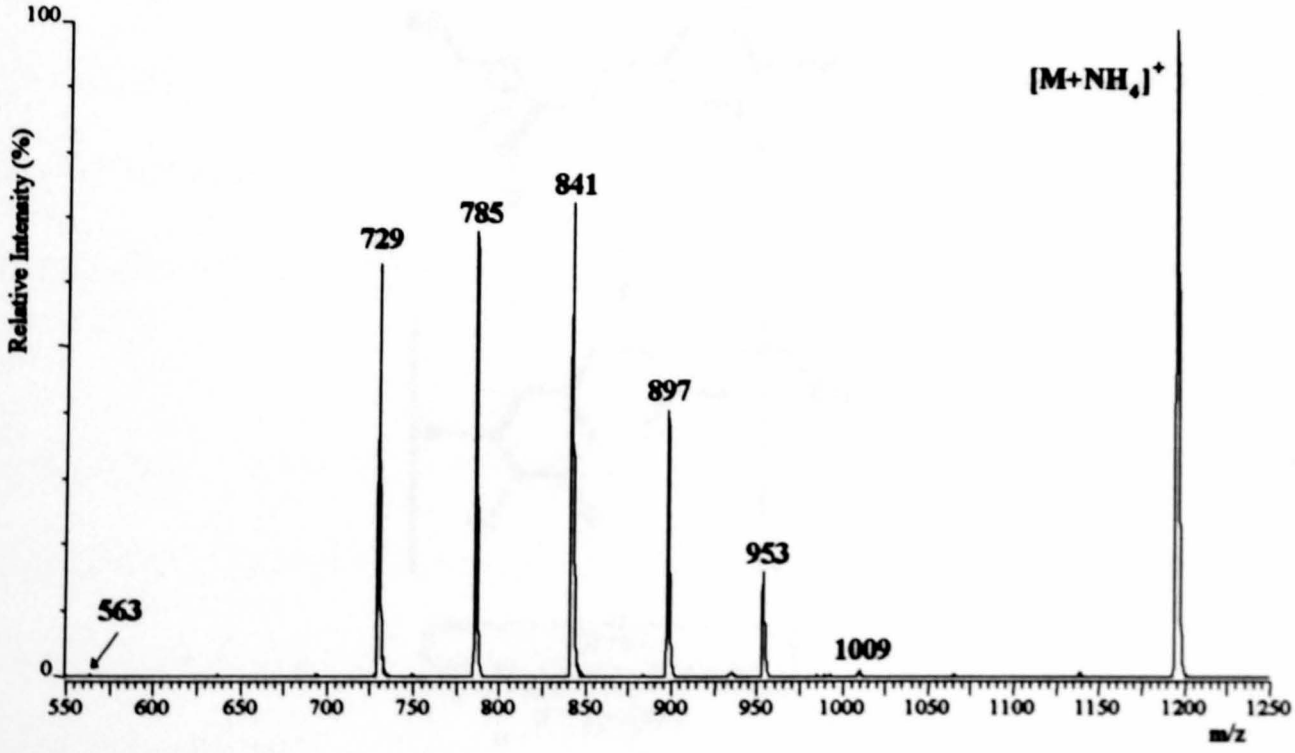

Figure 8.8.

Precursor ion Spectrum of m/z 563 from the B Series in the Product Ion Spectrum of Irganox 1010.

to be a carbonyl oxygen (Scheme 8.2). A precursor ion scan of m/z 563, the lowest mass ion of the B series, is shown in Figure 8.8.

Optimisation of both the cone voltage and the collision energy were important in the generation of all precursor ion spectra. The cone voltage was increased until the fragment ion of interest, generated in the source region, was at optimum intensity at the first detector. The collision energy was also adjusted so that the yield of the product ion generated in the collision cell from all precursors was maximised, as recorded at the second detector situated after the second quadrupole mass analyser.

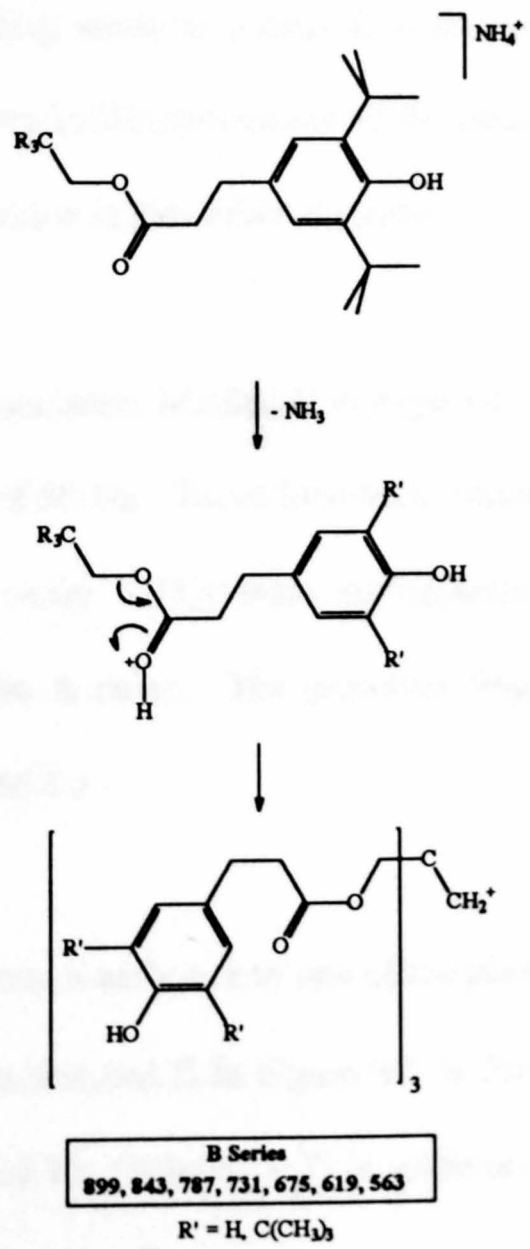

Scheme 8.2.

Proposed Mechanism for Generation of the B Series Observed in the ESI-MS/MS Spectrum of Irganox 1010, $[M+NH_4]^+$ m/z 1194.

Precursor ion peaks are observed in Figure 8.8 at masses corresponding to the A series. These data are consistent with the fragmentation pathway indicated in Scheme 8.2 where initial loss of ammonia is followed by sequential losses of *iso*-C_4H_8 and finally a carboxylic acid. Precursor ion scans of higher mass ions in the B series (see Appendix C) also support the proposed mechanism.

Another sequence of ions, labelled C in Figure 8.7, is formed by loss of water from the A series. These losses are common from protonated phenols, indicating that the phenolic oxygen is the preferred site of the charge when this process occurs and hence the final cleavage, generating water as a neutral, is charge-induced. This is the only series of peaks that requires initial protonation of the phenolic oxygen, indicating that the favoured site for the proton is the carbonyl oxygen.

A series of ions of low abundance, labelled D in Figure 8.7, is observed from m/z 805 to 581 with a separation of 56 Da. These ions have masses corresponding to the loss of 260 Da from the A series. This mass corresponds to an alkene and carbon monoxide from ions of the A series. The proposed fragmentation pathway for this process is shown in Scheme 8.3.

A 1,4-hydrogen transfer from a carbon α to one of the phenol rings generates alcoholic fragment ions. The series denoted E in Figure 8.5 is formed by sequential losses of 278 (Scheme 8.2) and 260 Da (Scheme 8.3) in addition to *iso*-C_4H_8 units and NH_3 from the precursor ion.

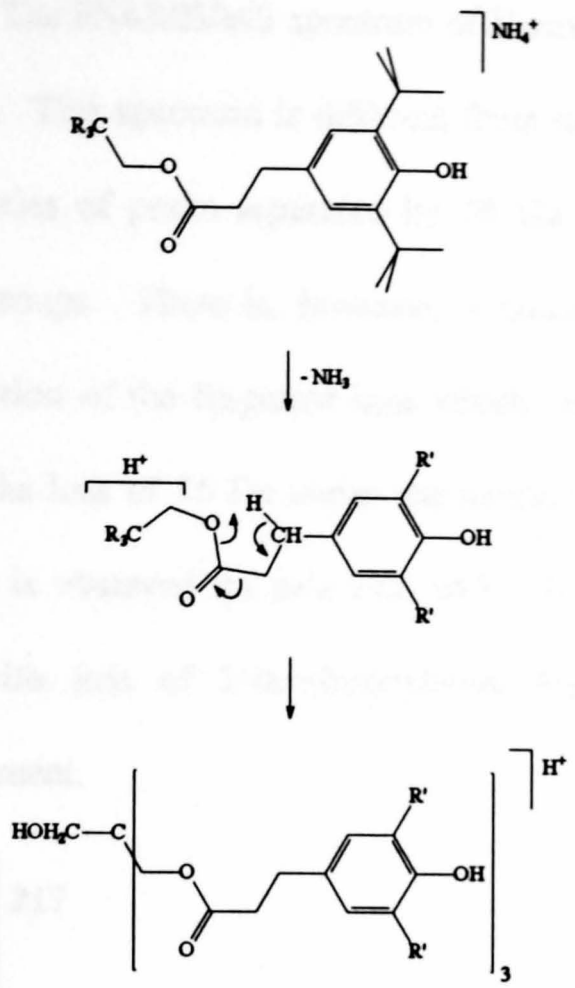

Scheme 8.3.

Proposed Mechanism for Generation of the D Series Observed in the ESI-MS/MS Spectrum of Irganox 1010, $[M+NH_4]^+$ m/z 1194.

The only other intense fragment ion observed under the conditions employed here is that at m/z 219. An ion with the same m/z ratio is the base fragment ion peak in the high energy CID spectrum of the same compound and the proposed mechanism for this process is shown in Scheme 7.1. Other intense fragment ions in the high energy CID spectrum such as those observed at m/z 203 and 57 are not present under these conditions. The m/z 203 and 57 ions are observed, however in the low energy CID spectrum when the collision energy is increased. Furthermore, no ions are seen above m/z 219 Da at the increased value of E_{coll} which indicates that m/z 203 and 57 are generated by high energy processes.

8.4.(ii) Hostanox 03. The ESI-MS/MS spectrum of Hostanox 03 at an E_{coll} of 22 eV is shown in Figure 8.9. This spectrum is different from that generated from Irganox 1010 as there is no series of peaks separated by 56 Da even though Hostanox 03 contains 4 *tert*-butyl groups. There is, however, a common separation of 150 Da between a high proportion of the fragment ions which indicates that this process is more favourable than the loss of 56 Da under the conditions employed. A series of three losses of 150 Da is observed for m/z 795, 645, 495 and 345. This process is proposed to occur with loss of 2-*tert*-butylphenol from a fragment ion by a 1,3-hydrogen rearrangement.

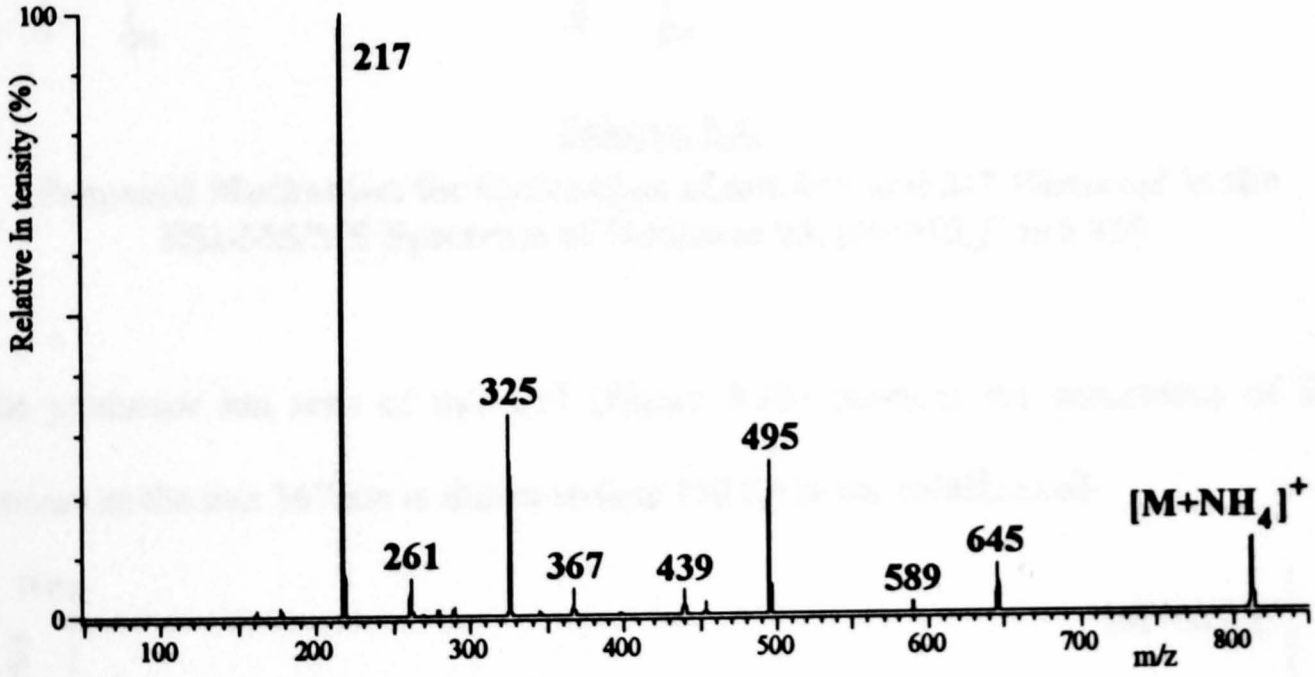

Figure 8.9.

ESI-MS/MS Spectrum of Hostanox 03, $[M+NH_4]^+$ m/z 812, at Cone Voltage 36 V and Collision Energy 22 eV.

Furthermore, there are also several rearrangement processes occurring which require the site of protonation to be a carbonyl oxygen after initial loss of ammonia from $[M+NH_4]^+$. An example is the generation of m/z 367 which occurs via a charge-induced 1,5-hydrogen rearrangement with initial protonation at one of the carbonyl oxygen atoms. Loss of 150 Da from m/z 367 generates the m/z 217 fragment

which is the base peak in the CID spectrum. Furthermore, loss of *iso*-C_4H_8 from m/z 217 generates the m/z 161 ion via a similar mechanism to that shown in Scheme 8.1. The m/z 217 fragment ion is highly conjugated and the resulting stability probably explains its peak intensity in the fragment ion spectrum. The proposed mechanism of generating both the m/z 367 and 217 fragment ions is shown in Scheme 8.4.

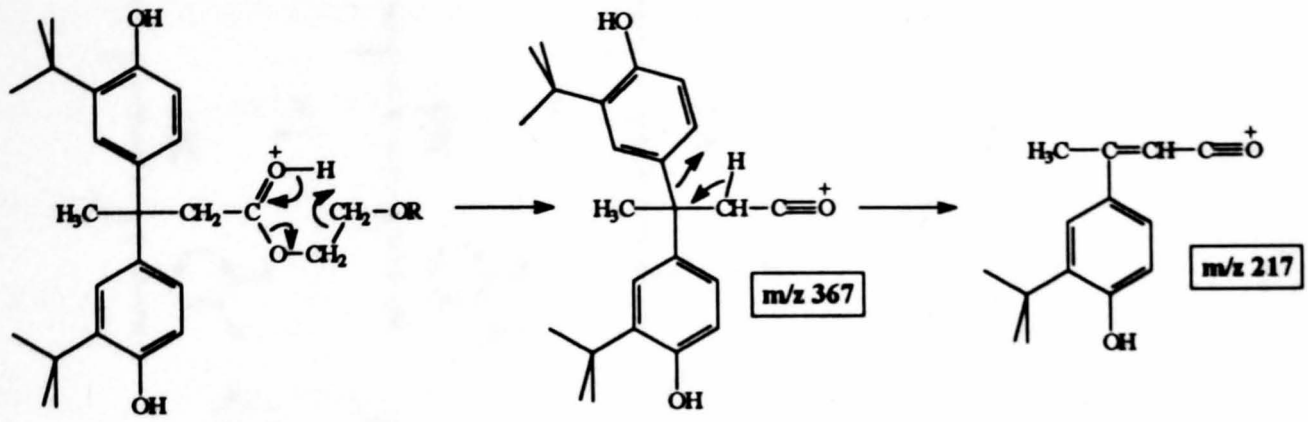

Scheme 8.4.

Proposed Mechanism for Generation of m/z 367 and 217 Observed in the ESI-MS/MS Spectrum of Hostanox 03, $[M+NH_4]^+$ m/z 812.

The precursor ion scan of m/z 217 (Figure 8.10) indicates the occurrence of this process as the m/z 367 ion is shown to lose 150 Da in the collision cell.

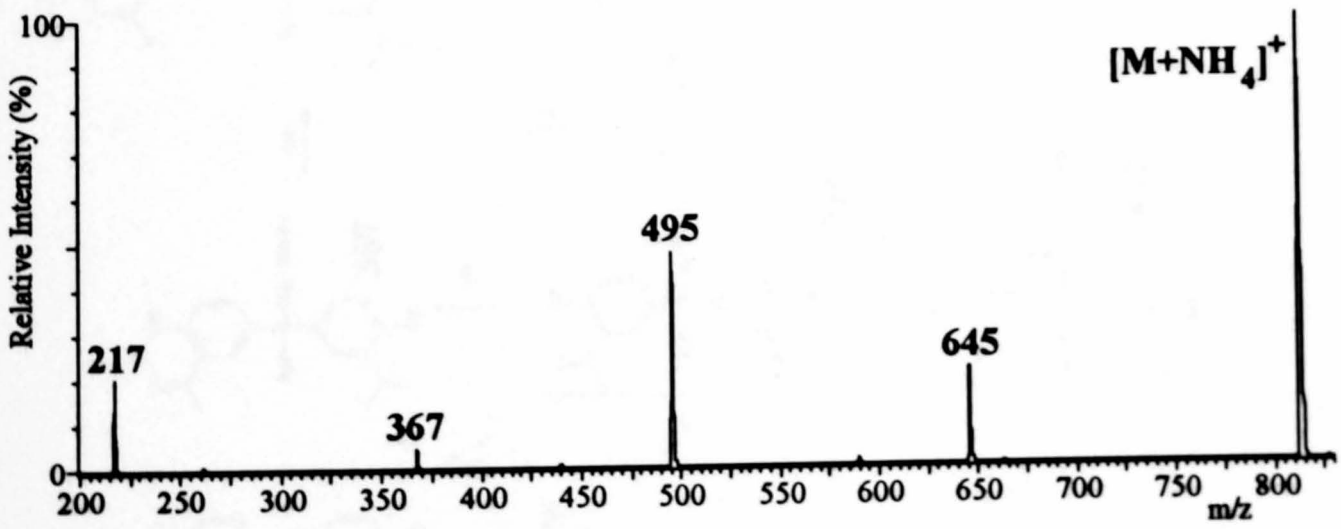

Figure 8.10.

Precursor ion Spectrum of m/z 217 from the Product Ion Spectrum of Hostanox 03.

Scheme 8.5.

The Proposed Fragmentation Pathways of Hostanox 03 by means of ESI-MS/MS.

This spectrum also indicates that the m/z 217 fragment ion may be generated by a more complicated pathway. These pathways are summarised in Scheme 8.5 which shows the proposed main fragmentation routes of Hostanox 03 which are observed by means of ESI-low energy MS/MS. The pathways shown have been determined from the various precursor ion scans which have fragments of Hostanox 03 as the product ion generated in the collision cell. These precursor ion scans are shown in Appendix C. More conclusive evidence for these pathways could be obtained from reaction intermediate scans but utilisation of this technique is not possible on tandem quadrupole instruments unless there are at least three mass analysers and two collision cells (such as with a pentaquadrupole instrument [9,10,11]).

A mechanism to account for the generation of m/z 261 is shown in Scheme 8.6.

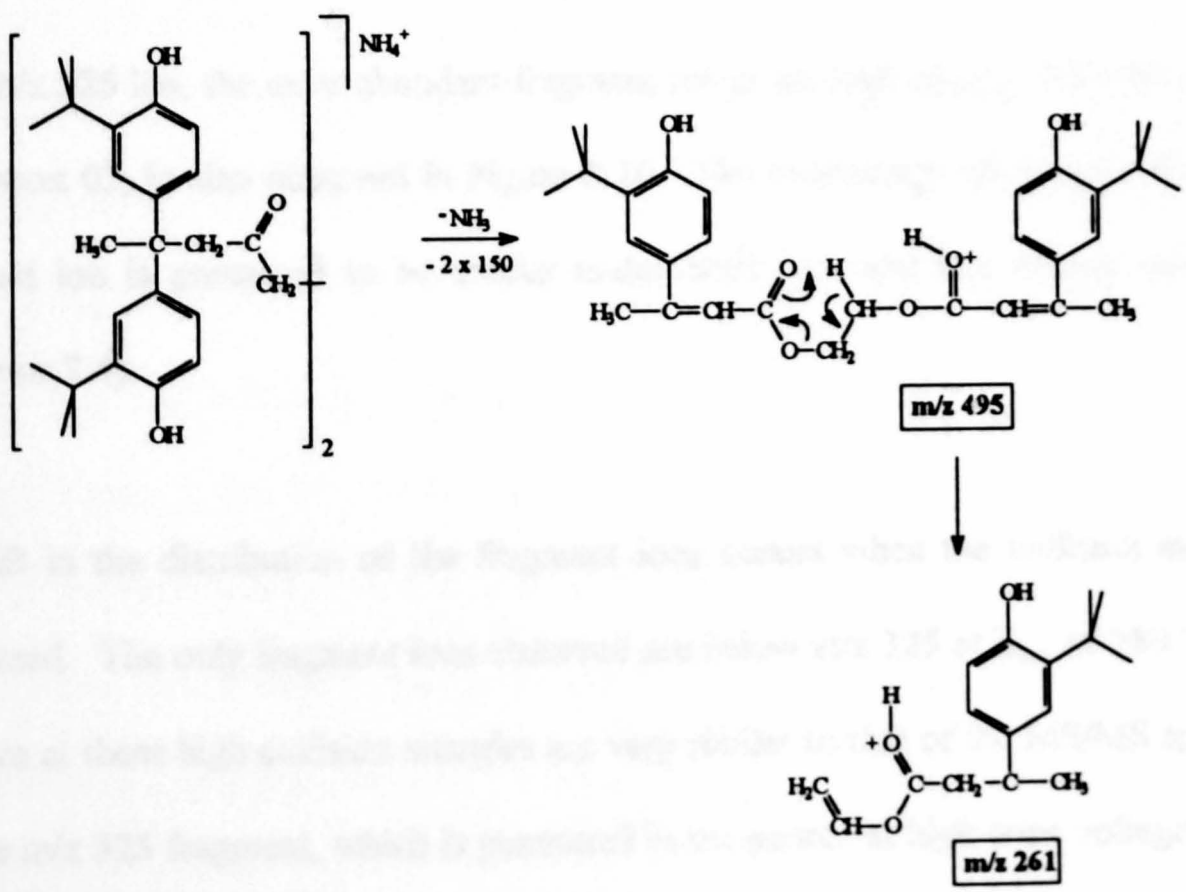

Scheme 8.6.

Proposed Mechanism for Generation of m/z 495 and 261 Observed in the ESI-MS/MS Spectrum of Hostanox 03, $[M+NH_4]^+$ m/z 812.

This process occurs with loss of ammonia and two units of 2-*tert*-butylphenol followed by a 1,5-hydrogen rearrangement with expulsion of a carboxylic acid. The peaks observed in the precursor ion spectrum of m/z 261 (Figure 8.11) are consistent with this fragmentation pathway.

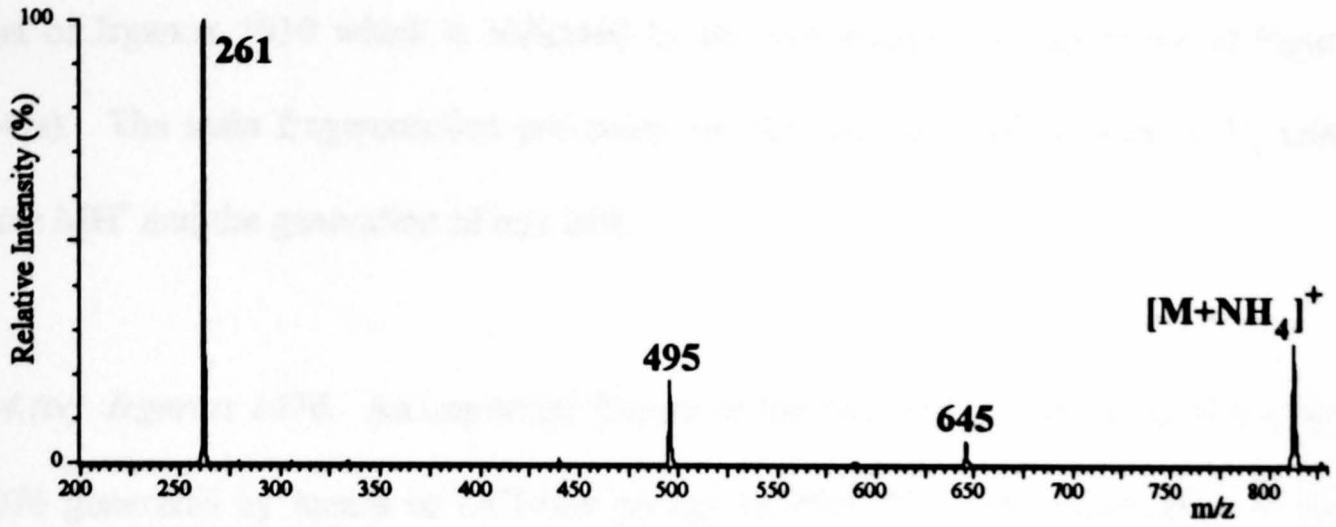

Figure 8.11.

Precursor ion Spectrum of m/z 261 from the Product Ion Spectrum of Hostanox 03.

The m/z 325 ion, the most abundant fragment ion in the high energy CID spectrum of Hostanox 03, is also observed in Figure 8.10. The mechanism for generation of this product ion is presumed to be similar under both high and low energy conditions (Scheme 7.4).

A shift in the distribution of the fragment ions occurs when the collision energy is increased. The only fragment ions observed are below m/z 325 at E_{coll} of >80 V. The spectra at these high collision energies are very similar to that of the MS/MS spectrum of the m/z 325 fragment, which is generated in the source at high cone voltages. This phenomenon is similar to that observed for Irganox 3114 (Figure 8.4) and indicates that a narrow range of internal energies is imparted into the precursor ion by collisional

activation under low collision energy conditions. This is in agreement with the results of Cooks and coworkers [12].

8.4.(iii) Irganox 3114. The main decomposition process of Irganox 3114 is similar to that of Irganox 1010 which is indicated by the low energy CID spectrum in Figure 8.4(a). The main fragmentation processes are the loss of a series of *iso*-C_4H_8 units from MH^+ and the generation of m/z 219.

8.4.(iv) Irganox 1076. An important feature of the fragment ion spectrum of Irganox 1076 generated by means of DCI-low energy MS/MS [5] is the observation of two ions at m/z 167 and 149. These ions are typically observed at high abundance in the EI and fragment ion spectra of phthalate esters [13,14,15,16,17,18,19,20]. Furthermore, the RMM of Irganox 1076 is the same as that of a phthalate ester with two hydrocarbon chains containing 13 carbon atoms each (Figure 8.1). As a consequence it was necessary to compare the CID spectra of these two compounds to verify that the CID spectrum acquired by Chen and Her [5] was obtained from pure Irganox 1076 and not from a phthalate ester with the same RMM. The spectra obtained (Figures 8.5 and 8.12) indicate that the compound employed by Chen and Her was indeed Irganox 1076 as the spectra obtained by means of ESI (Figure 8.5) and DCI-MS/MS [5] are very similar. Furthermore, the CID spectrum from the phthalate ester (Figure 8.12) with the same RMM is considerably different from that generated from the antioxidant.

The main fragmentation pathways of Irganox 1076 by means of ESI-low energy CID are shown in Scheme 8.7. These dissociation routes were generated from the data

Scheme 8.7.

The Proposed Fragmentation Pathways of Irganox 1076 by Means of ESI-MS/MS.

provided by the precursor ion spectra shown in Appendix C. Initial losses of NH_3 followed by *iso*-C_4H_8 units from the precursor ion are prominent and are observed as fragment ions at m/z 531, 475 and 419 respectively. The mechanisms for these processes are the same as those proposed for generation of the A series from Irganox 1010 (Scheme 8.1).

Many peaks were observed in the precursor ion spectra at a m/z ratio which was 32 (F+32) or 72 (F+72) Da higher than that of certain fragment ions of Irganox 1076. Furthermore, the F+32 and F+72 peaks were not seen in the product ion spectra of Irganox 1076 (Figure 8.5). These ions are clusters of the fragment ions of Irganox 1076 with solvent, either MeOH (RMM 32 Da) or THF (RMM 72 Da), which were also observed in the ESI mass spectra when the cone voltage was similar to that employed for precursor ion scanning experiments.

The structures of the m/z 167 and 149 fragment ions observed in the DCI-MS/MS spectrum of Irganox 1076 were proposed but no mechanisms of generation were forwarded [5]. The structure proposed by Chen and Her for the m/z 149 ion requires cleavage α to the benzene ring which is a high energy process. The mechanism forwarded for m/z 149 (Scheme 8.8) is very similar to that proposed for generation of the m/z 367 fragment in the low energy MS/MS spectrum of Hostanox 03 (Scheme 8.4). This process occurs via a 1,5-hydrogen rearrangement from the protonated carbonyl oxygen to the β-carbon of the alkyl chain to generate formaldehyde and an alkane as neutral species. This is a much lower energy process than that proposed by Chen and Her [5] which is a direct bond cleavage.

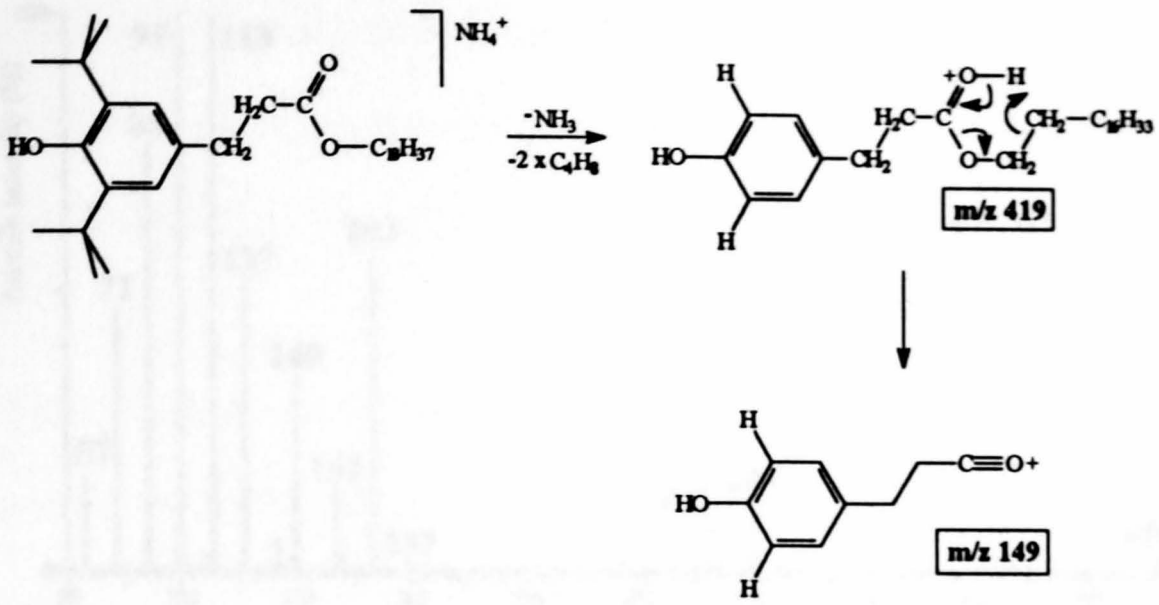

Scheme 8.8.

Proposed Mechanism for Generation of m/z 419 and 149 Observed in the ESI-MS/MS Spectrum of Irganox 1076, $[M+NH_4]^+$ m/z 548.

A 1,5-hydrogen rearrangement is also proposed to generate the m/z 167 fragment ion (Scheme 8.9) which has a protonated carboxylic acid structure.

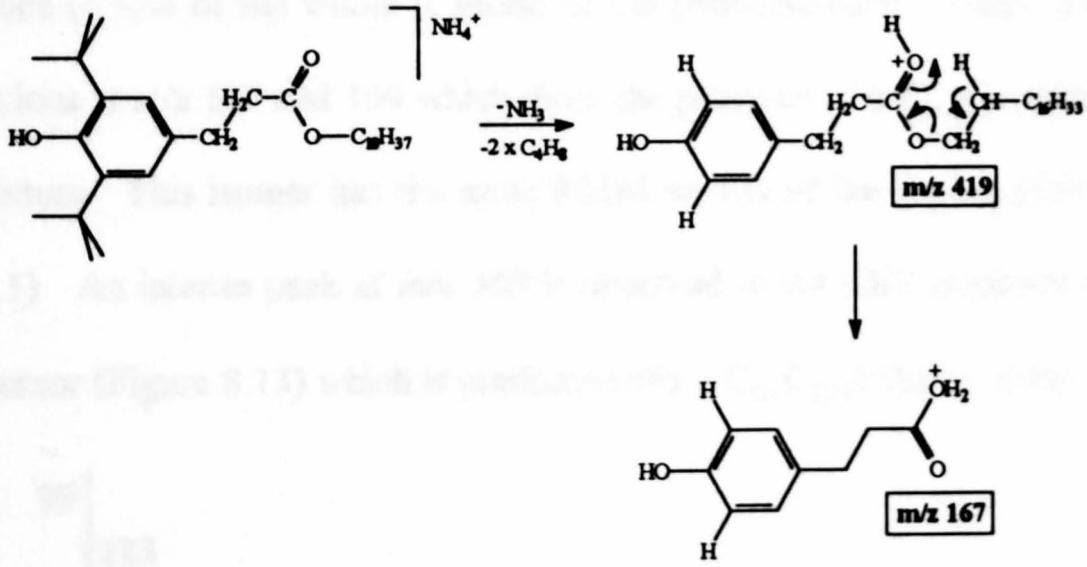

Scheme 8.9.

Proposed Mechanism for Generation of m/z 419 and 167 Observed in the ESI-MS/MS Spectrum of Irganox 1076, $[M+NH_4]^+$ m/z 548.

8.4.(v) Emkarate 3020. The low energy CID spectrum of the m/z 531 ion (MH^+) from Emkarate 3020 (Figure 8.12) is dominated by a series of hydrocarbon fragment ions with the formula $[C_nH_{2n+1}]^+$ observed at lower m/z ratios.

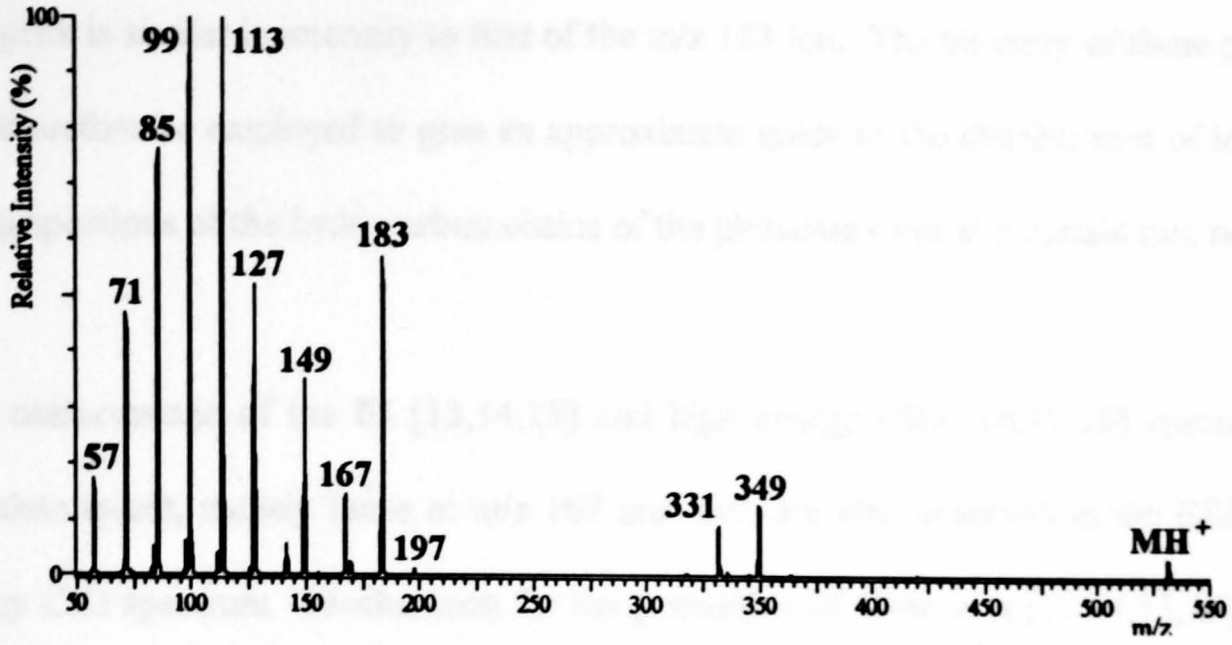

Figure 8.12.

ESI-MS/MS Spectrum of Emkarate 3020, MH^+ m/z 531, at Cone Voltage 36 V and Collision Energy 15 eV.

These ions are generated by loss of the whole or part of the hydrocarbon chain from the phthalate ester. The ions formed include a prominent ion (m/z 183) which corresponds to loss of the whole R group of the phthalate ester. There are also less abundant ions at m/z 197 and 169 which show the presence of a C_{14},C_{12} phthalate ester in the mixture. This isomer has the same RMM as that of the C_{13},C_{13} phthalate ester (Table 8.1). An intense peak at m/z 169 is observed in the CID spectrum of the m/z 517 precursor (Figure 8.13) which is predominantly a C_{13},C_{12} phthalate ester.

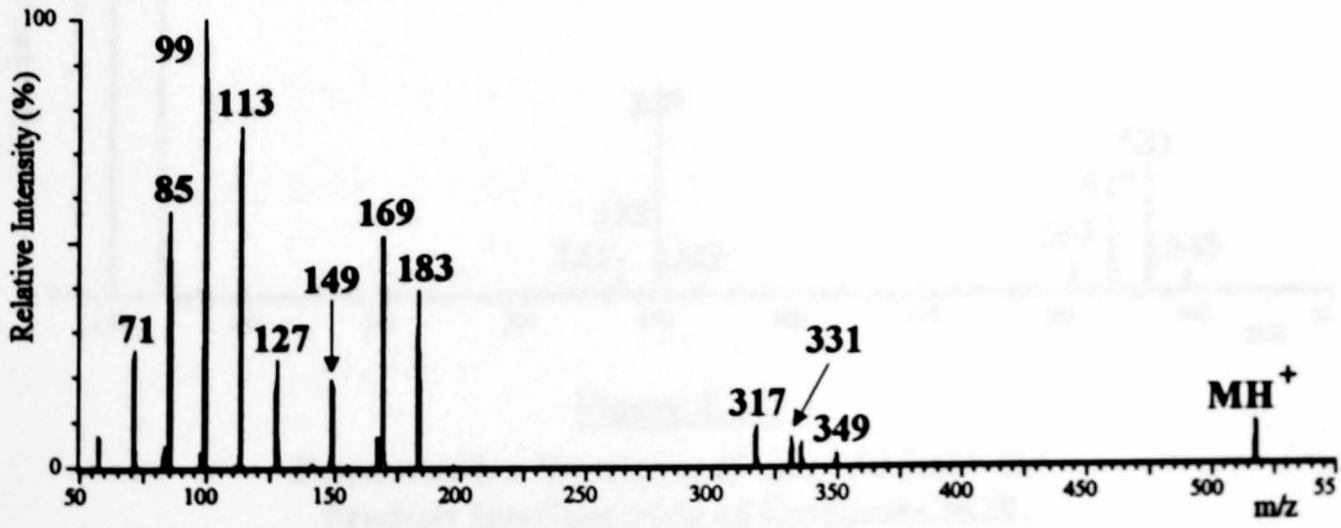

Figure 8.13.

ESI-MS/MS Spectrum of Emkarate 3020, MH^+ m/z 517, at Cone Voltage 36 V and Collision Energy 13 eV.

This peak is similar in intensity to that of the m/z 183 ion. The intensity of these peaks may therefore be employed to give an approximate guide to the distributions of length and proportions of the hydrocarbon chains of the phthalate ester at a certain m/z ratio.

Ions characteristic of the EI [13,14,15] and high energy CID [16,17,18] spectra of phthalate esters, namely those at m/z 167 and 149, are also observed in the ESI-low energy CID spectrum. Mechanisms for the generation of these ions [13,14,15,16] and fragmentation pathways [15,18] have been proposed for the dissociation of phthalate esters. Other prominent fragment ion peaks in Figure 8.12 are those at m/z 349 and 331 which are generated with loss of one of the hydrocarbon chains of the phthalate ester [19,20]. Peaks of weak intensity are also observed at m/z 317, 335, 345 and 363 which correspond to the losses of C_{14} or C_{12} chains from the precursor ion. These again indicate the presence of the mixture of phthalate esters which make up each ion peak in the mass spectrum. The precursor ion scan of m/z 149 (Figure 8.14) indicates that this fragment ion may be generated by the pathway shown in Scheme 8.8.

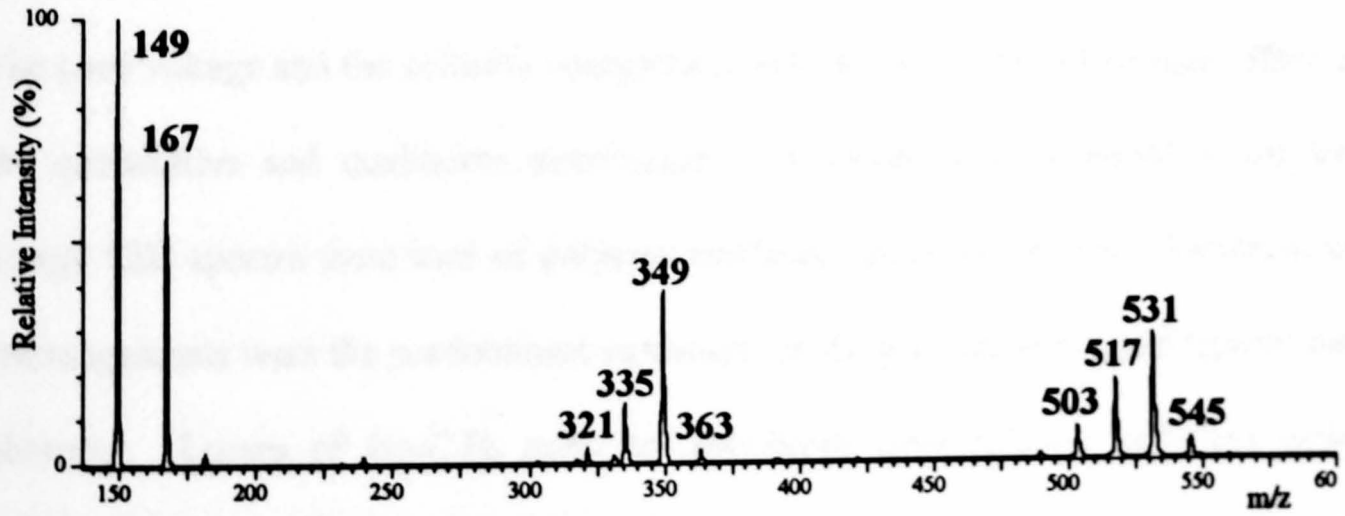

Figure 8.14.

Precursor ion Spectrum of m/z 149 from the Product Ion Spectrum of Emkarate 3020.

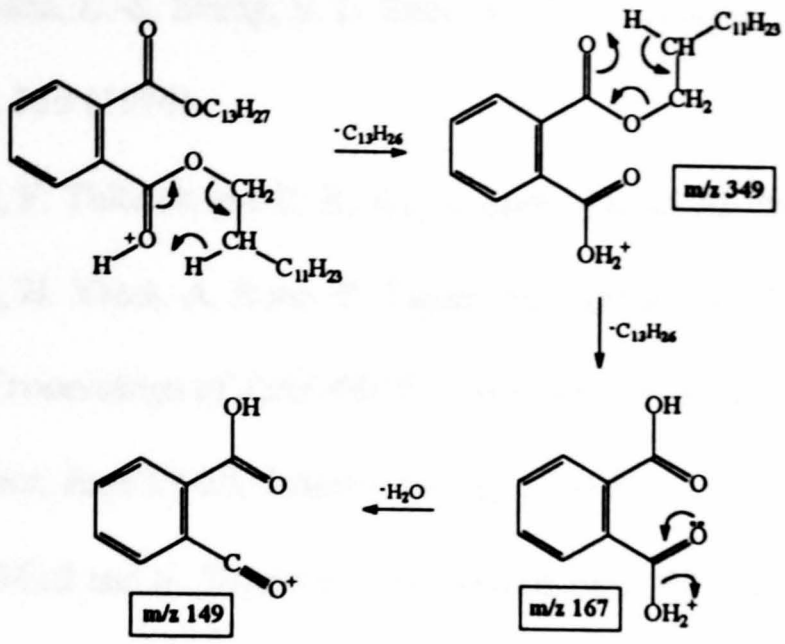

Scheme 8.10.

Proposed Mechanism for Generation of m/z 349, 167 and 149 Observed in the ESI-MS/MS Spectrum of Emkarate 3020, $[M+NH_4]^+$ m/z 548.

The m/z 149 ion may be generated from a phthalate ester with any chain length as indicated by Figure 8.14 and the pathways proposed previously [13,14,15,18].

8.5. Summary.

The cone voltage and the collision energy have been shown to have a marked effect on the quantitative and qualitative distribution of fragment ions observed in the low energy CID spectra from ions of polymer additives generated by ESI. Furthermore, rearrangements were the predominant pathways for the generation of the fragment ions observed. Losses of *iso*-C_4H_8 units are prominent from polymer additives which contain *tert*-butyl groups while losses of 2-*tert*-butylphenol were also observed in the CID spectra of Hostanox 03.

1 J. E. Campana, L.-S. Sheng, S. L. Shew and B. E. Winger, *Trac/Trends Anal. Chem.*, **13**, 239 (1994).

2 X.-J. Tang, P. Thibault and R. K. Boyd, *Anal. Chem.*, **65**, 2824 (1993).

3 J. Scrivens, H. Yates, A. Bunn, P. Tayler, M. Beckett, M. Taylor and R. Jennings, *Proceedings of 43rd ASMS Conference on Mass Spectrometry and Allied Topics*, June 21-26, Atlanta, Georgia (1995).

4 R. Saf, C. Mirtl and K. Hummel, *Tetrahedron Lett.*, **35**, 6653 (1994).

5 S. W. Chen and G. R. Her, *Appl. Spectrosc.*, **47**, 844 (1993).

6 D. H. Williams, A. F. Findeis, S. Naylor and B. W. Gibson, *J. Am. Chem. Soc.*, **109**, 1980 (1987).

7 D. H. Williams and S. Naylor, *J. Chem. Soc., Chem. Commun.*, 1408 (1987).

8 L. Kelner and S. P. Markey, *Int. J. Mass Spectrom. Ion Proc.*, **59**, 157 (1984).

9 J. D. Morrison, D. A. Stanney and J. Tedder, *Proceedings of 34th ASMS Conference on Mass Spectrometry and Allied Topics*, June 8-13, Cincinnati, Ohio, 222 (1986).

10 C. Beaugrand, G. Devant, D. Jaouen, H. Mestdagh, N. Morin and C. Rolando, *Adv. Mass Spectrom.*, **11**, 256 (1989).

11 J. C. Schwarz, K. L. Schey and R. G. Cooks, *Int. J. Mass Spectrom. Ion Proc.*, **101**, 1 (1990).

12 H. I. Kenttämaa and R. G. Cooks, *J. Am. Chem. Soc.*, **107**, 1881 (1985).

13 F. W. McLafferty and R. S. Gohlke, *Anal. Chem.*, **31**, 2076 (1959).

14 E. M. Emery, *Anal. Chem.*, **32**, 1495 (1960).

15 C. Djerassi and C. Fenselau, *J. Am. Chem. Soc.*, **87**, 5756 (1965).

16 D. F. Hunt, J. Schabanowitz and A. B. Giordani, *Anal. Chem.*, **52**, 386 (1980).

17 D. F. Hunt, J. Schabanowitz, T. M. Harvey and M. Coates, *Anal. Chem.*, **57**, 525 (1985).

18 J. Yinon, *Org. Mass Spectrom.*, **23**, 755 (1988).

19 H. Cohen, C. Charrier and J. Sarfaty, *Arch. Environ. Contam. Toxicol.*, **20**, 437 (1991).

20 W. C. Brumley, E. M. Schafter and P. E. Tillander, *J. AOAC International*, **77**, 1230 (1994).

CHAPTER 9.

AVERAGE MASS VALUES AND END GROUP INFORMATION OF POLYMERS.

9.1. Introduction.

The introduction of soft ionisation techniques such as matrix-assisted laser desorption ionisation (MALDI) [1] and developments in instrumentation have increased the interest in the analysis of polymers by means of mass spectrometry [2,3,4,5,6,7,8,9,10, 11,12, 13,14,15]. Mass spectra produced by MALDI give mean mass values and mass envelopes that often correlate well with other analytical techniques such as gel permeation chromatography (GPC) [16,17]. The low resolution and mass accuracy of the technique when combined with time-of-flight (TOF) analysers, however, means that the determination of the mass and structure of polymer end groups is often not possible. Currently, very few laboratories are able to undertake tandem mass spectrometry experiments with ions generated by MALDI and it is therefore difficult to obtain end group information. It is possible, however, to perform CID experiments in TOF instruments by means of post source decay.

The combination of accurate average mass measurements, mass envelopes and end group information can, however, be achieved by carrying out two experiments. The average mass values are initially obtained from MALDI spectra. Ions of the same mass as those present in MALDI spectra are then generated by liquid secondary ion mass spectrometry (LSIMS) in a sector instrument and collision induced dissociation (CID) experiments performed yielding fragment ions in the CID spectra that can give end group information. The mass envelopes of polymers observed in LSIMS-MS spectra are typically centred at lower m/z ratios, compared to that seen by means of

MALDI-MS, as a consequence of fragmentation and reduced ionisation efficiency at high mass.

The classes of synthetic polymers studied were polymethylmethacrylates (PMMA) and polystyrenes (PS). The structures of these polymers are shown in Figure 9.1.

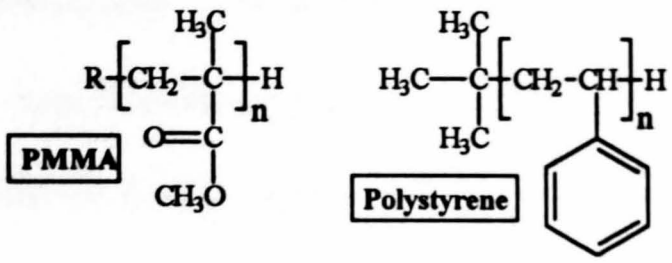

Figure 9.1.

The Structure of the Polystyrenes and Polymethylmethacrylates Employed.

The different end groups R of the PMMA polymers studied are shown in Figure 9.2.

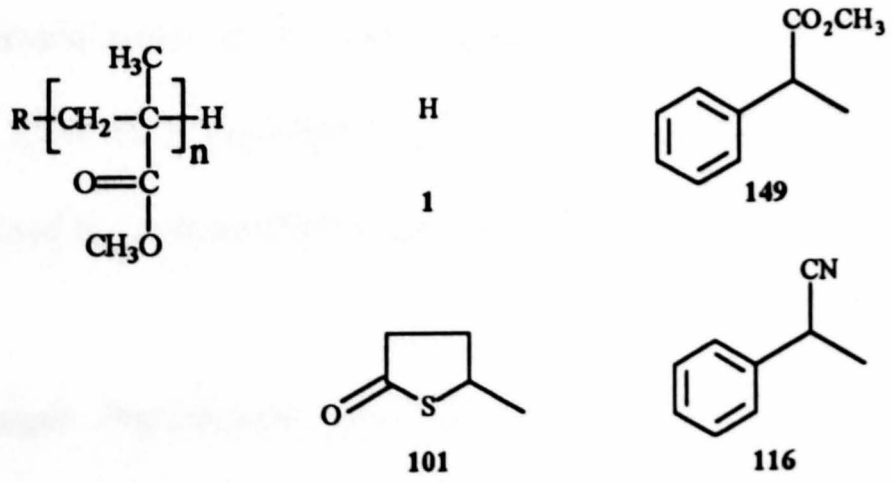

Figure 9.2.

The End Groups of the PMMA Samples Studied.

A few studies of polystyrene [2,7] and PMMA [2,4] have been performed by means of MALDI-MS. The structural determination of synthetic polymers by means of

LSIMS-MS/MS [18,19,20,21,22,23] has been almost totally limited to polyglycols [18,19,21,22,23].

9.2. Experimental.

9.2.(i) Mass Spectrometry. UV-MALDI spectra were obtained by means of the TOFSPEC mass spectrometer operated in linear or reflectron mode with an accelerating potential of 25 kV. Approximately 50-100 laser shots were employed to obtain the mass spectra under control of the OPUS data system.

LSIMS spectra were acquired by means of the ZAB-T tandem mass spectrometer operating at an accelerating potential of 8 kV. Precursor ions for CID experiments were selected at greater than unit mass resolution by MS1. The ion beam was attenuated by 80 % with argon at 4 keV collision energy in the mid-point collision cell. The microchannel plates of the array detector were held at the maximum electrical potential of 1.875 kV. Acquisition of 5-20 scans under control of the OPUS data system was used to produce the fragment ion spectra.

9.2.(ii) Sample Preparation. For MALDI spectra of cationated species, silver trifluoroacetate or sodium iodide solution (10 mg mL^{-1}/MeOH) was added to the matrix solution (10 mg mL^{-1}/MeOH) and the sample solution (10 mg mL^{-1}/MeOH) in a 1:10:1 ratio. Dithranol was the matrix of choice for experiments with polystyrene and indole acrylic acid (IAA) was employed with PMMA samples. The structures of the matrices employed for MALDI experiments are shown in Figure 9.3. *Meta*-nitrobenzyl

alcohol (NBA) was the matrix for analysis by means of LSIMS-MS. The addition of sodium iodide (NaI) or silver trifluoroacetate promoted the generation of cationated adducts.

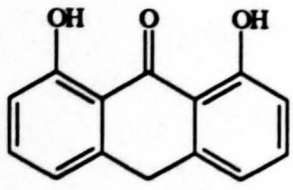

Dithranol
RMM 226.2

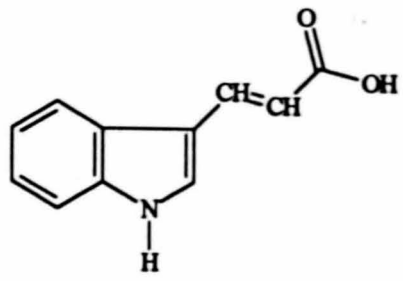

3-Indoleacrylic Acid (IAA)
RMM 187.2

Figure 9.3.
The Structures and RMM of the Matrices Employed in MALDI Experiments.

9.3. MALDI-Mass Spectrometry of Polymers.

9.3.(i) Calibration for MALDI Experiments. The accuracy of an external calibration in MALDI experiments was optimum when the calibrant was close to the sample in structure. Synthetic polymers as calibrants, in this case a mixture of three polystyrene samples, generate a better calibration file than that obtained from biopolymers. The samples employed were polystyrene 1700, 5050 and 10200 as they generated MALDI spectra with peaks covering the mass range of interest, 1000-15,000 Da. The mixture of polystyrene samples employed as the calibration mixture generated the MALDI spectrum shown in Figure 9.4. This mass spectrum was obtained in linear mode.

The calibration file was generated by employing seven peaks from the mass spectrum which were spread across the mass range of interest. The higher mass samples employed were at a higher concentration in the mixture. The same method was used

to generate calibration files in the reflectron mode of operation. The reduced detection efficiency in reflectron mode, however, made the generation of spectra with peaks from all three polymer samples problematical.

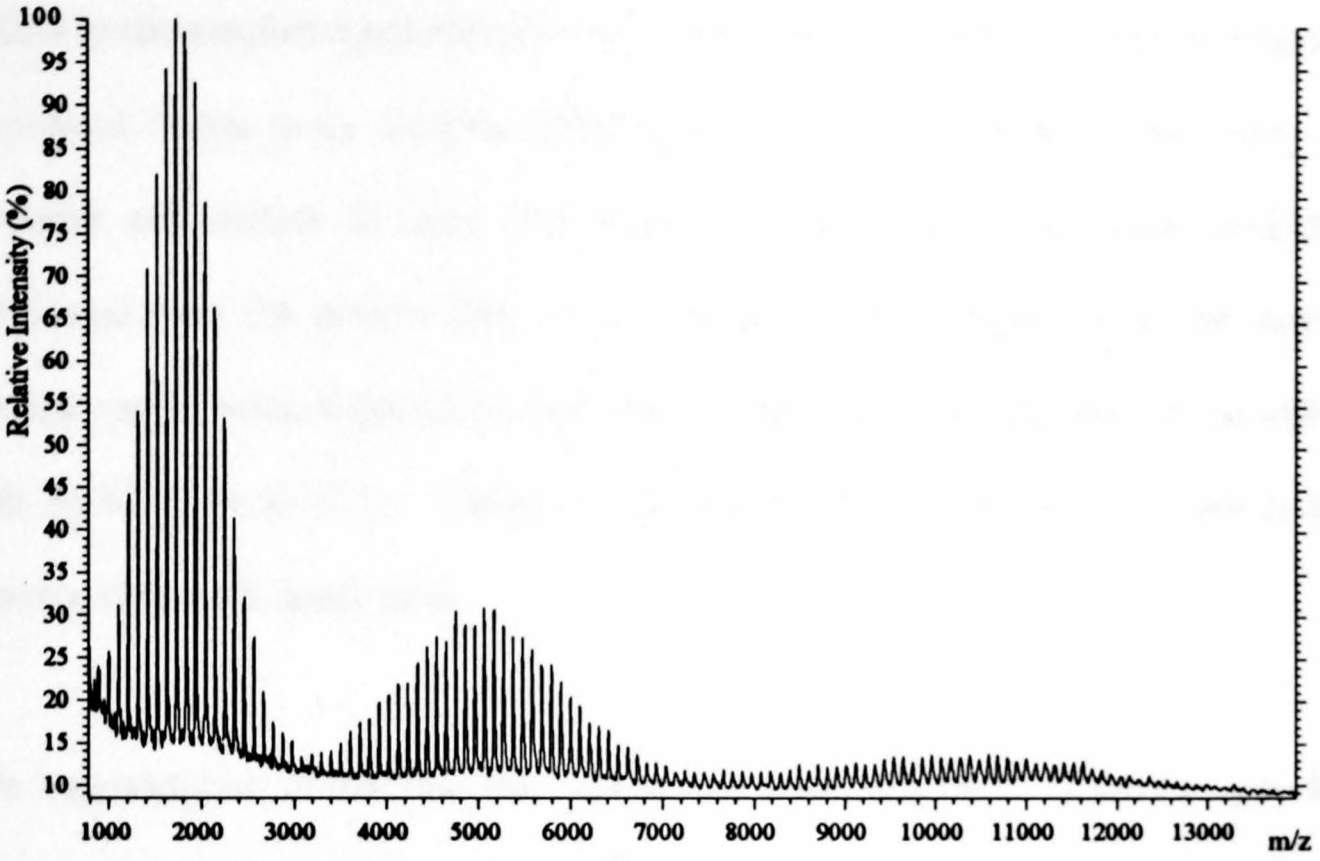

Figure 9.4.

MALDI Spectrum of Mixture of Polystyrene Standards (1700, 5050 and 10200) Employed for Calibration (Linear Mode, IAA/Acetone/Silver Trifluoroacetate).

The mass accuracy obtained for some polymers with the calibration file generated from this mixture is discussed below. Improvements in mass accuracy could be obtained with an internal calibration, where the calibrant selected would have an average mass close to that of the sample of interest.

9.3.(ii) MALDI-MS of Polymethylmethacrylate (PMMA) Standards. Figures 9.5 and 9.6 show the MALDI mass spectra of PMMA 2010, a GPC standard, generated in reflectron and linear modes, respectively. Similar distributions are observed in both

modes. The spectra are dominated by two series of ion peaks which correspond to $[M+Na]^+$ and $[M+K]^+$ species of intact oligomers. Previous studies have shown that Li^+ and Na^+ are approximately equally efficient at ionising PMMA when a metal salt is added to the sample/analyte mixture [24]. Furthermore, it has been suggested that the cationised matrix is the ionising agent [24]. No salt was added to the matrix to promote cationisation in these experiments and hence the metal cations probably originated from the sample disk, sample containers or as impurities in the matrix. Similar species were observed in spectra of PMMA standards, acquired with no added salt, by Lloyd et al. [17]. Cations of the metals, Na^+ and K^+, are also seen in the spectra along with matrix ions.

No fragmentation of the oligomer adduct ions were observed. Ions are seen for oligomeric species from the 7-mer to the 35-mer of the polymer in both linear and reflectron modes of operation. The observed resolution is improved approximately three times in reflectron mode over linear mode. The $[M+Na]^+$ and $[M+K]^+$ peaks are fully resolved for all oligomeric adduct ions in reflectron mode but are not in linear mode. The low resolution in linear mode leads to the generation of one peak for $[M+Na]^+$ and $[M+K]^+$ ions at higher m/z ratios in the spectrum. A comparison of the mass accuracy obtained by means of the two modes was undertaken and is summarised below. The calibration files employed were those generated by the method described above.

Table 9.1 shows the mean masses of $[M+Na]^+$ ions obtained from three spectra acquired from the same sample spot in reflectron mode.

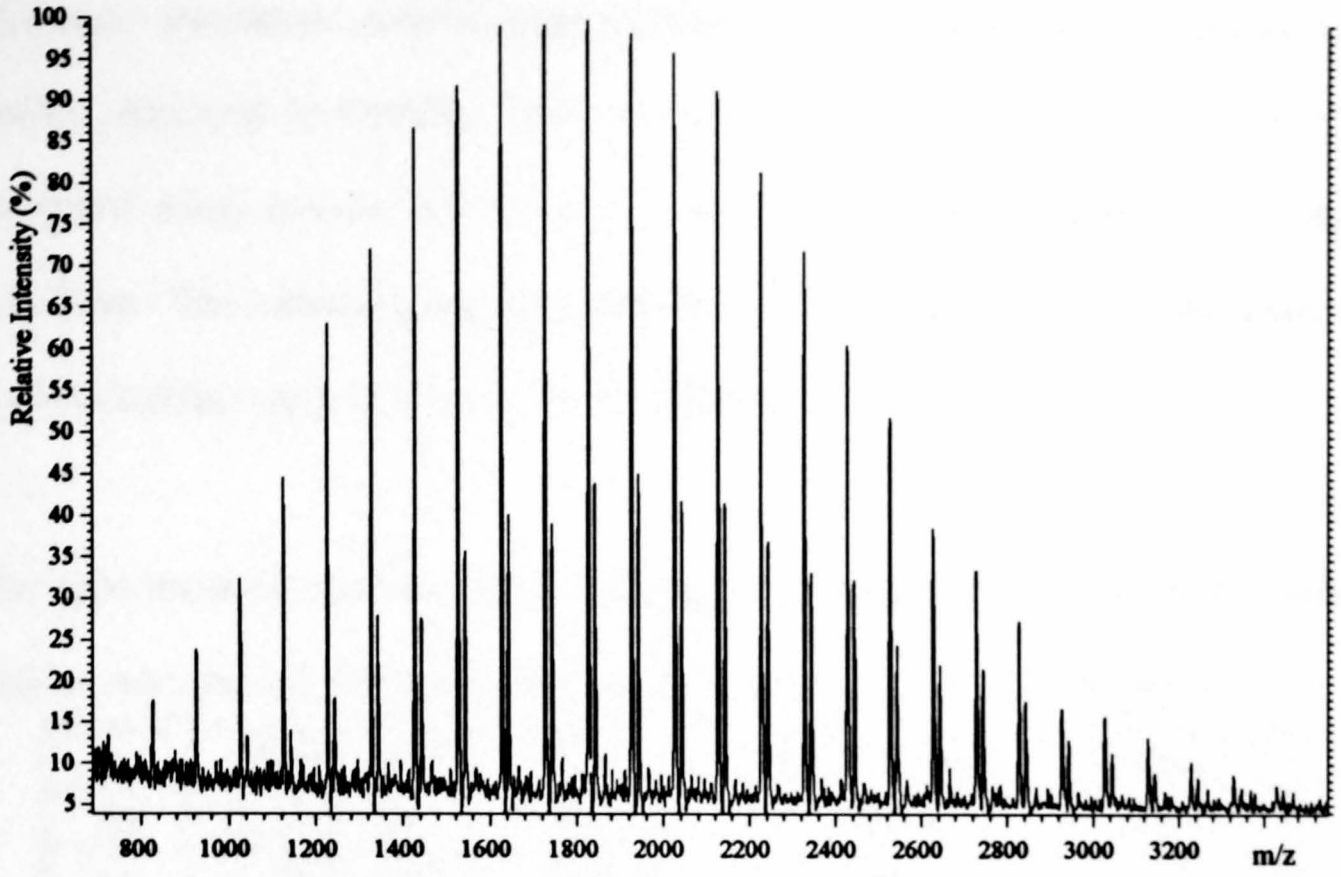

Figure 9.5.

MALDI Spectrum of PMMA 2010 (Reflectron Mode, IAA/Acetone).

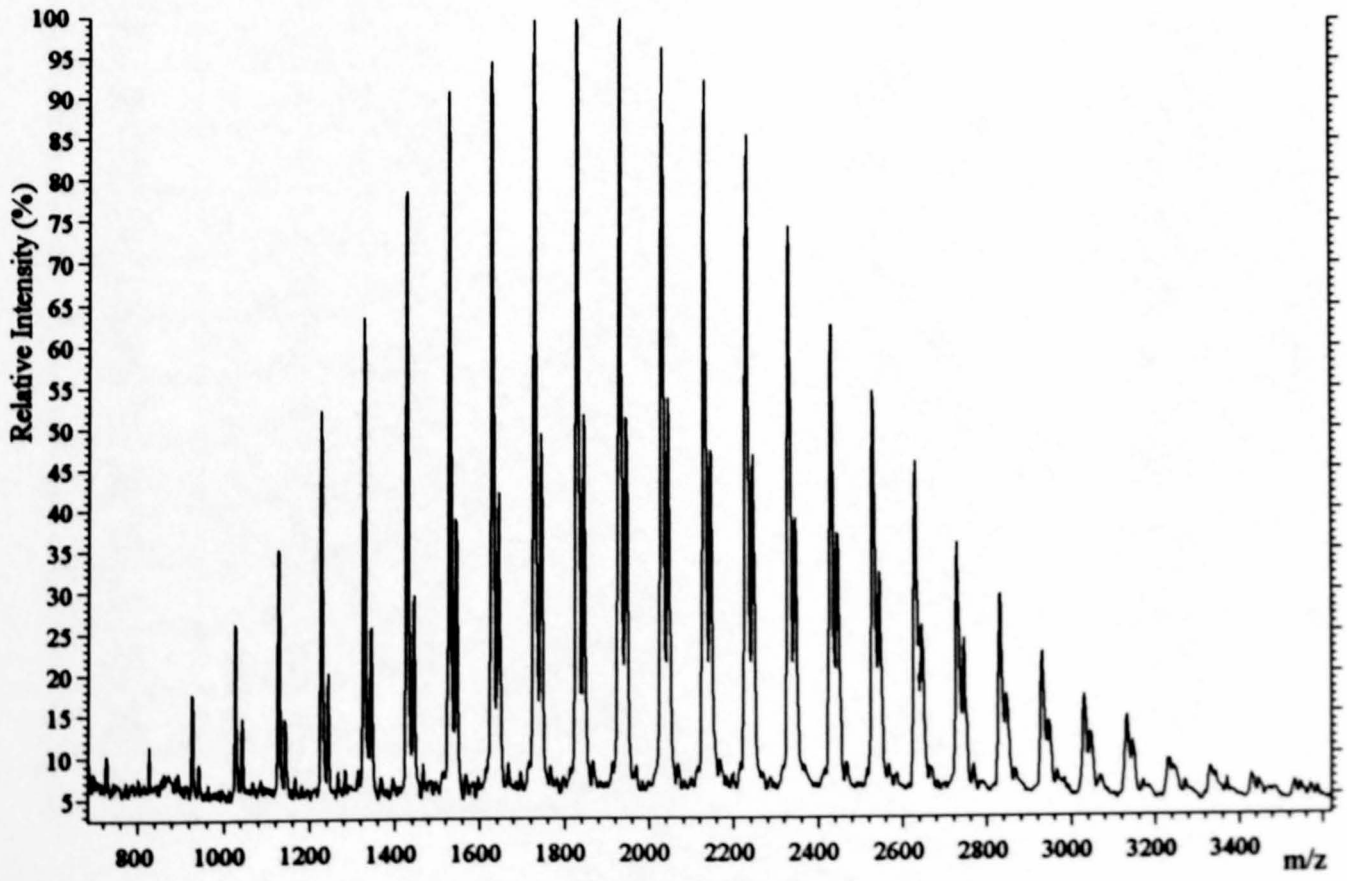

Figure 9.6.

MALDI Spectrum of PMMA 2010 (Linear Mode, IAA/Acetone).

The mean percentage error in mass calculated by averaging values generated for twenty oligomers is 0.020%. The percentage errors in mass, compared to the calculated mass, are also presented for each oligomer and an average for twenty oligomers. The corresponding calculated average percentage error for linear mode is 0.058% and the computations are shown in Table 9.2.

The mass accuracy was found to be reduced by the doping of the matrix with sodium iodide. Adducts with Na^+ were observed in the spectra with no $[M+K]^+$ series.

n	Formula	$Mass_{calc}$	$Mass_{exp}$(mean)	% Error
10	$C_{50}H_{82}O_{20}Na^+$	1025.96	1026.3	33e-3
11	$C_{55}H_{90}O_{22}Na^+$	1126.09	1126.48	20e-3
12	$C_{60}H_{98}O_{24}Na^+$	1226.21	1226.48	22e-3
13	$C_{65}H_{106}O_{26}Na^+$	1326.34	1326.62	21e-3
14	$C_{70}H_{114}O_{28}Na^+$	1426.46	1426.75	20e-3
15	$C_{75}H_{122}O_{30}Na^+$	1526.59	1526.88	19e-3
16	$C_{80}H_{130}O_{32}Na^+$	1626.71	1626.96	15e-3
17	$C_{85}H_{138}O_{34}Na^+$	1726.84	1727.05	12e-3
18	$C_{90}H_{146}O_{36}Na^+$	1826.96	1827.3	19e-3
19	$C_{95}H_{154}O_{38}Na^+$	1927.08	1927.38	16e-3
20	$C_{100}H_{162}O_{40}Na^+$	2027.21	2027.49	14e-3
21	$C_{105}H_{170}O_{42}Na^+$	2127.33	2127.74	19e-3
22	$C_{110}H_{178}0_{44}Na^+$	2227.45	2227.82	17e-3
23	$C_{115}H_{186}O_{46}Na^+$	2327.57	2327.96	17e-3
24	$C_{120}H_{194}O_{48}Na^+$	2427.69	2428.15	19e-3
25	$C_{125}H_{202}O_{50}Na^+$	2527.81	2528.46	26e-3
26	$C_{130}H_{210}O_{52}Na^+$	2627.92	2628.56	24e-3
27	$C_{135}H_{218}O_{54}Na^+$	2728.04	2728.6	21e-3
28	$C_{140}H_{226}O_{56}Na^+$	2828.18	2828.74	20e-3
29	$C_{145}H_{234}O_{58}Na^+$	2928.29	2929.17	30e-3
			% Error (Mean)	20e-3

Table 9.1.

Mass Accuracy Values of Polymethylmethacrylate 2010 (Reflectron Mode).

Furthermore, the observed resolution was much lower in the spectra when the sample was doped. The addition of 18-crown-6-ether to the matrix/analyte solution has been found to promote the generation of spectra with only $[M+Na]^+$ series as the potassium ions complex with the additive [25]. Employing a composite matrix has also generated spectra dominated by $[M+Na]^+$ ions [25]. Furthermore, the removal of either cation may be caused by running the matrix/analyte solution through an ion exchange column [25]. These methods of cationisation were not found to degrade the observed resolution or mass accuracy [25].

n	Formula	$Mass_{calc}$	$Mass_{exp}$(mean)	% Error
10	$C_{50}H_{82}O_{20}Na^+$	1025.96	1026.91	93e-3
11	$C_{55}H_{90}O_{22}Na^+$	1126.09	1126.92	74e-3
12	$C_{60}H_{98}O_{24}Na^+$	1226.21	1226.94	60e-3
13	$C_{65}H_{106}O_{26}Na^+$	1326.34	1327.16	62e-3
14	$C_{70}H_{114}O_{28}Na^+$	1426.46	1427.26	56e-3
15	$C_{75}H_{122}O_{30}Na^+$	1526.59	1527.37	51e-3
16	$C_{80}H_{130}O_{32}Na^+$	1626.71	1627.45	45e-3
17	$C_{85}H_{138}O_{34}Na^+$	1726.84	1727.68	49e-3
18	$C_{90}H_{146}O_{36}Na^+$	1826.96	1827.76	44e-3
19	$C_{95}H_{154}O_{38}Na^+$	1927.08	1927.96	46e-3
20	$C_{100}H_{162}O_{40}Na^+$	2027.21	2028.2	49e-3
21	$C_{105}H_{170}O_{42}Na^+$	2127.33	2128.36	48e-3
22	$C_{110}H_{178}0_{44}Na^+$	2227.45	2228.52	48e-3
23	$C_{115}H_{186}O_{46}Na^+$	2327.57	2328.79	52e-3
24	$C_{120}H_{194}O_{48}Na^+$	2427.69	2428.97	53e-3
25	$C_{125}H_{202}O_{50}Na^+$	2527.81	2529.33	60e-3
26	$C_{130}H_{210}O_{52}Na^+$	2627.92	2629.64	65e-3
27	$C_{135}H_{218}O_{54}Na^+$	2728.04	2729.7	61e-3
28	$C_{140}H_{226}O_{56}Na^+$	2828.18	2830.07	67e-3
29	$C_{145}H_{234}O_{58}Na^+$	2928.29	2930.48	75e-3
			% Error (Mean)	58e-3

Table 9.2.

Mass Accuracy Values of Polymethylmethacrylate 2010 (Linear Mode).

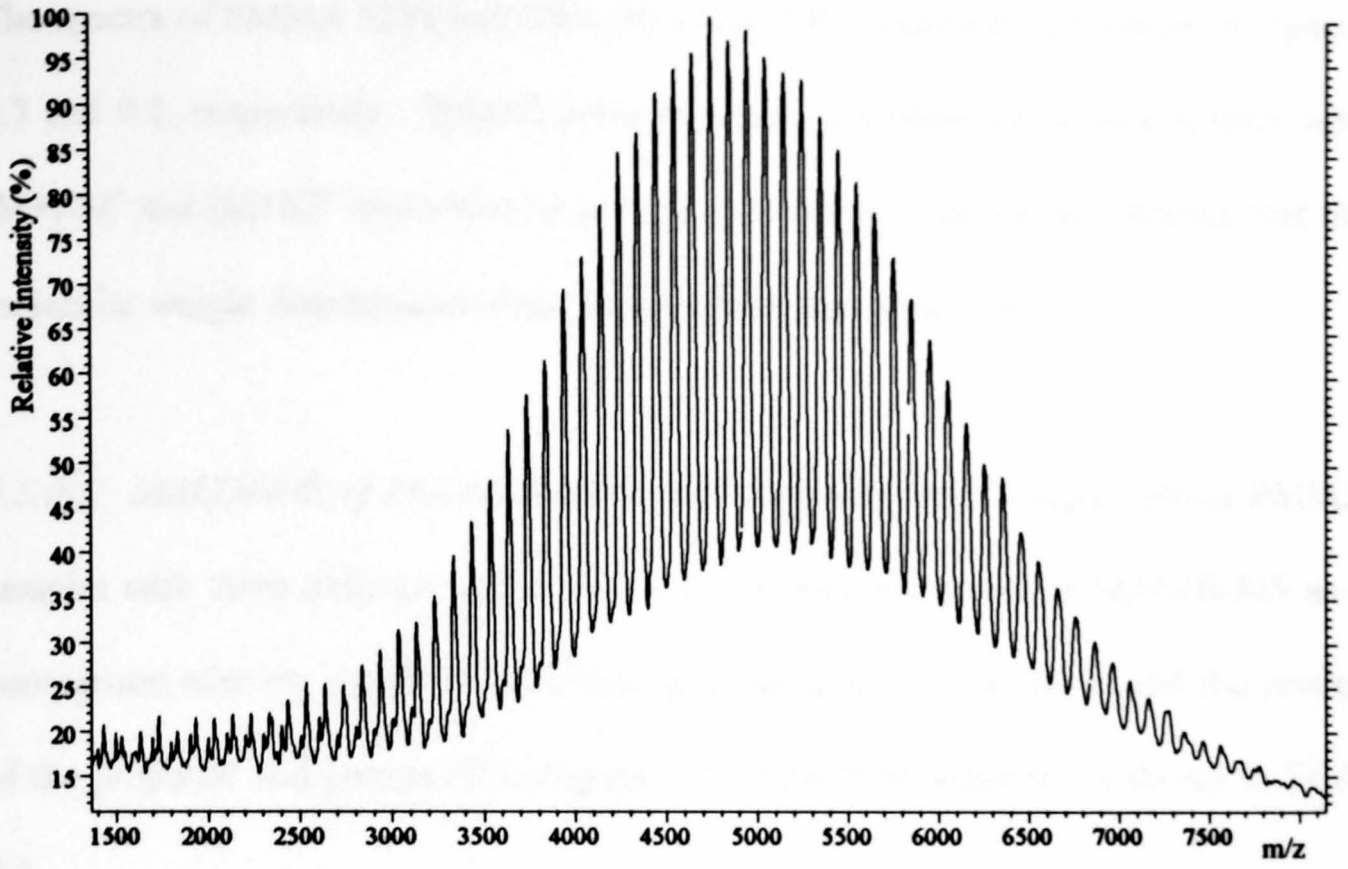

Figure 9.7.

MALDI Spectrum of PMMA 5270 (Linear Mode, IAA/Acetone).

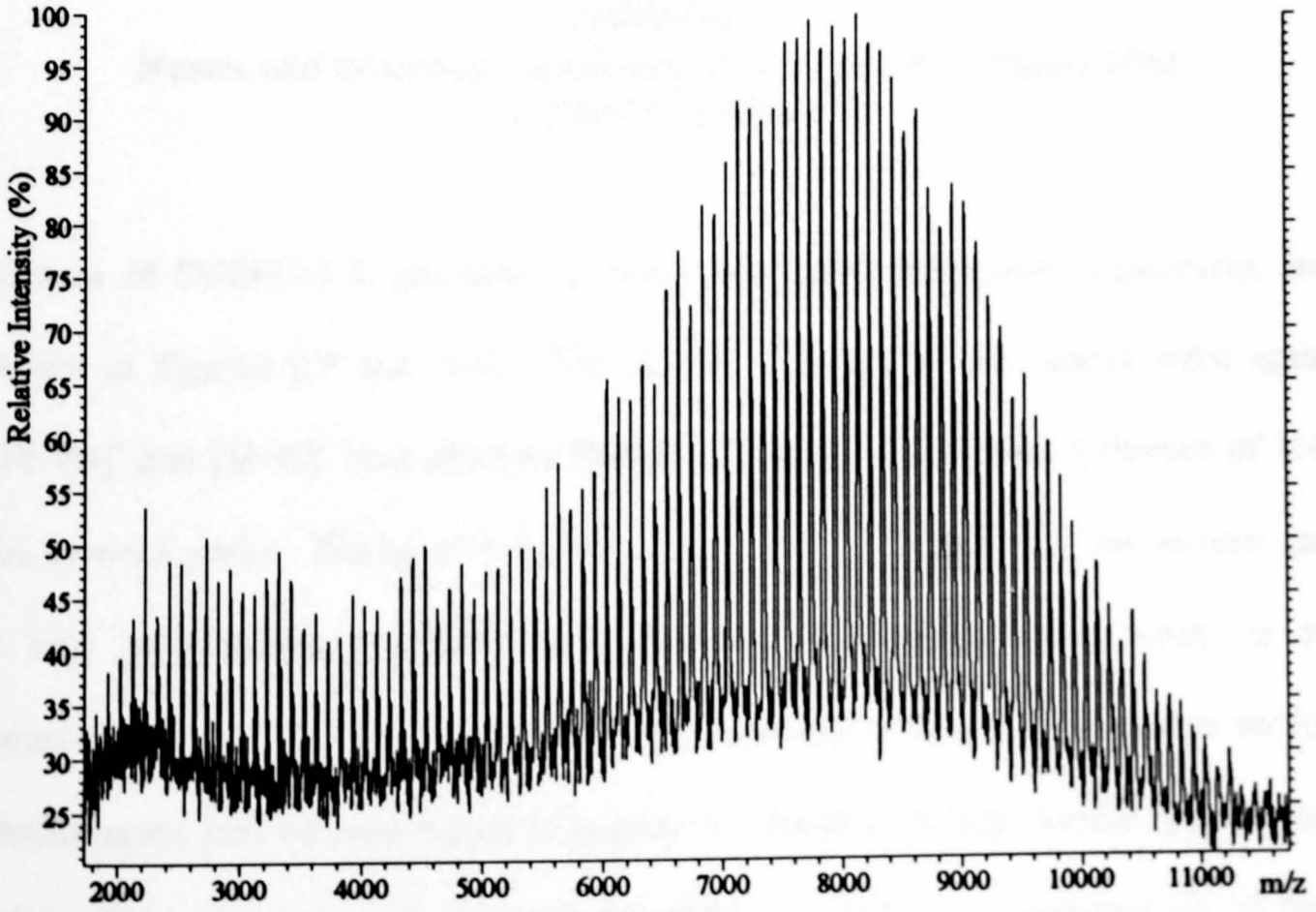

Figure 9.8.

MALDI Spectrum of PMMA 9200 (Reflectron Mode, IAA/Acetone).

The spectra of PMMA 5270 and 9200, both also GPC standards, are shown in Figures 9.7 and 9.8, respectively. Smooth mass envelopes are observed in both spectra with $[M+Na]^+$ and $[M+K]^+$ ions resolved at lower m/z ratios. The spectra indicate that the molecular weight distributions of the samples have low mass tails.

9.3.(iii) MALDI-MS of PMMA Samples with Different End Groups. Novel PMMA samples with three different end groups were analysed by means of MALDI-MS as a comparison with the standards with hydrogen end groups. The names and the masses of the proposed end groups (R in Figure 9.2) of the three samples are shown in Table 9.3.

Name	Mass of End Group R (Da)
ERCT9B	101
PEGFC9.5	149
PEGFC11.5	116

Table 9.3.
Names and Proposed End Group (R in Figure 9.2) Masses (Da) of PMMA Samples.

Spectra of PEGFC11.5, generated in linear and reflectron modes respectively, are shown in Figures 9.9 and 9.10. The species observed in the spectra were again $[M+Na]^+$ and $[M+K]^+$ ions of intact PMMA oligomers with a mass difference of 100 Da between peaks. The broad mass envelopes observed indicate that the polymer has a high polydispersity. Higher oligomers are observed in linear mode up to approximately 12,000 Da compared to approximately 9000 Da in reflectron mode Furthermore, ions of these higher oligomers are observed at low abundances in linear mode. These ions are not observed in reflectron mode as a consequence of the

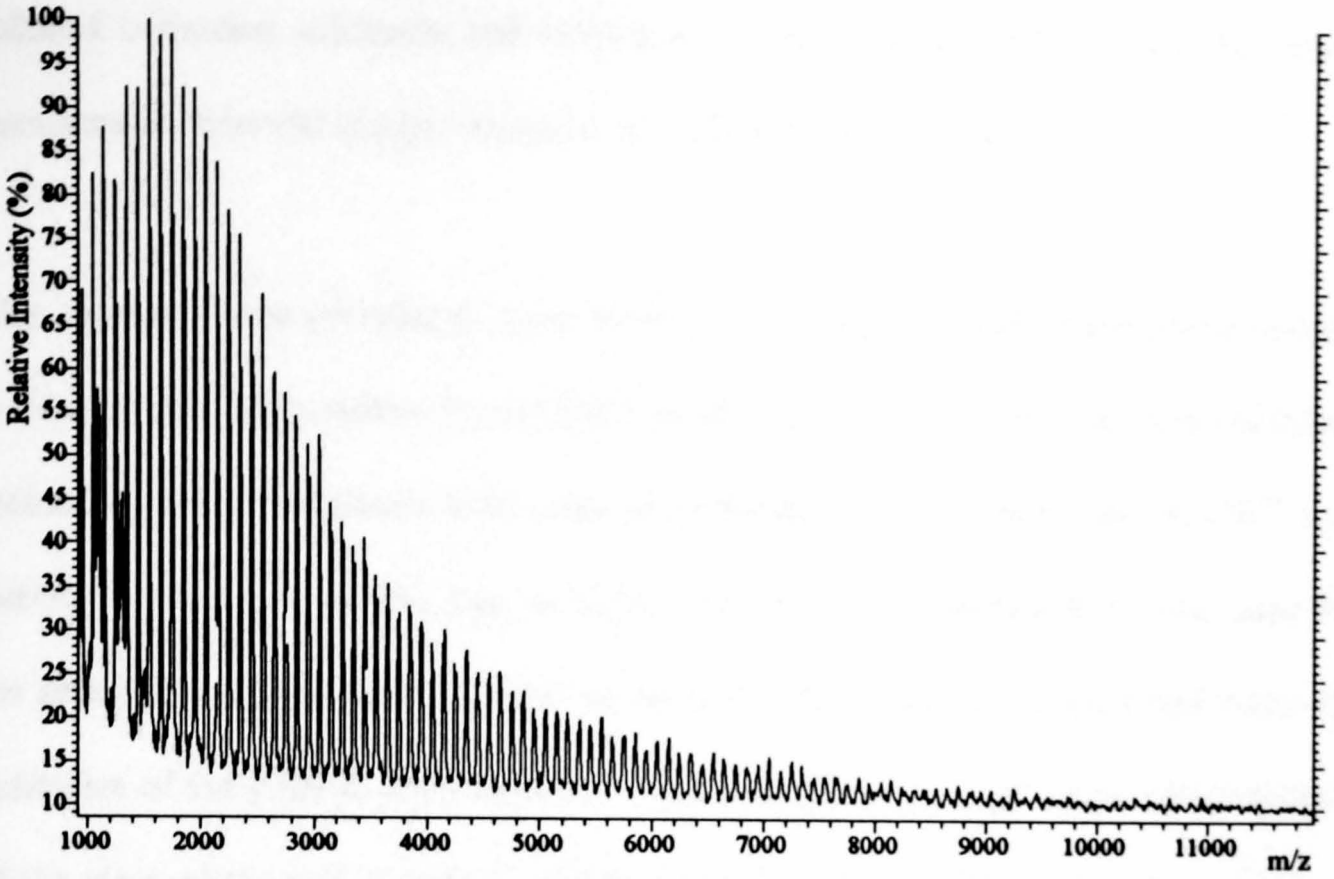

Figure 9.9.

MALDI Spectrum of PEGFC11.5 (Linear Mode, IAA/Acetone).

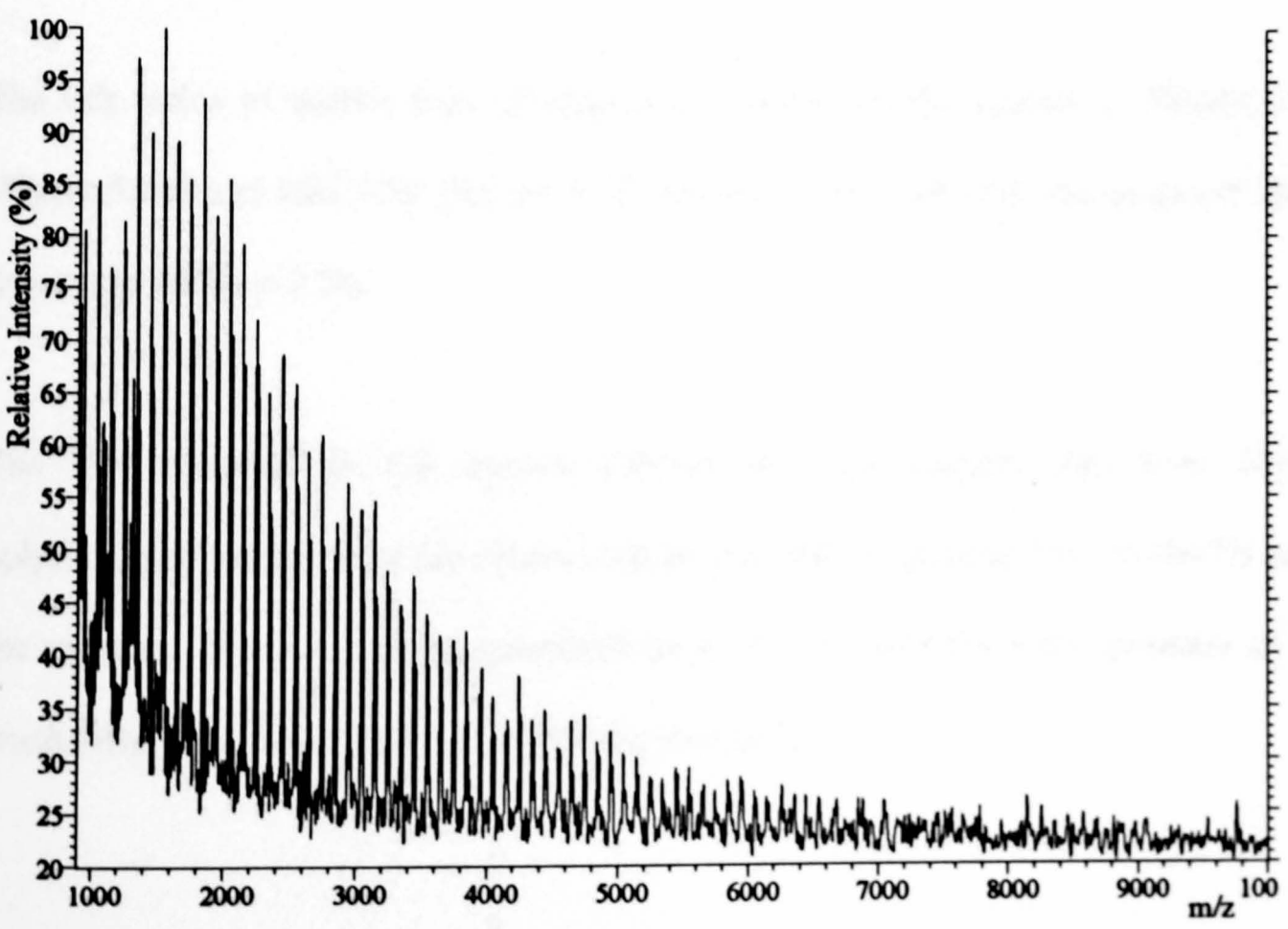

Figure 9.10.

MALDI Spectrum of PEGFC11.5 (Reflectron Mode, IAA/Acetone).

reduced collection efficiency and detection efficiency in reflectron mode. The peak maximum is observed at approximately m/z 1800 in both modes.

The optimum mean percentage error between the calculated and experimental masses is 0.014 and 0.045 in reflectron and linear modes respectively. The m/z ratios of lower molecular weight oligomers were used to generate these values as the $[M+Na]^+$ and $[M+K]^+$ peaks were not resolved at higher values. The experimental masses used for the above calculations were the best obtained for this group of samples and were not indicative of the general mass accuracy. The m/z ratios observed allow determination of the mass of the end groups to within approximately ± 1 Da. The values obtained are consistent with the structure of the end group shown in Figure 9.2 but do not provide unequivocal determination of the mass.

The m/z ratios of adduct ions of oligomers observed in the spectra of PEGFC9.5 (Figure 9.11) and ERCT9B (Figure 9.12) are also consistent with the proposed end groups, to within ± 2 Da.

The ions observed in the spectra indicate that the samples also have large polydispersity values. Ions are observed from m/z 1000 to greater than 10,000 Da for the samples. The ion currents generated from all three samples were generally of a much lower abundance than for the PMMA standards.

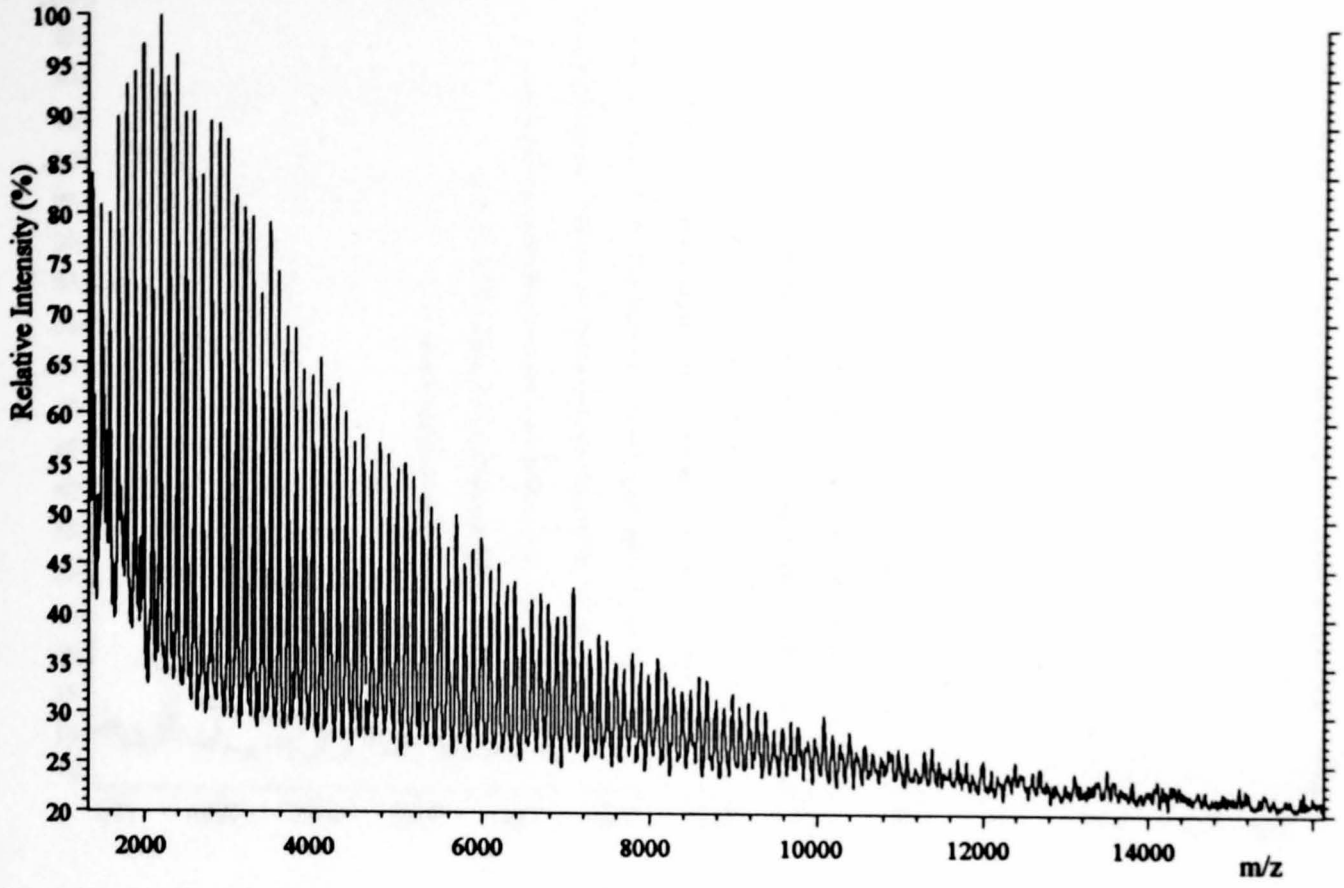

Figure 9.11.

MALDI Spectrum of PEGFC9.5 (Reflectron Mode, IAA/Acetone).

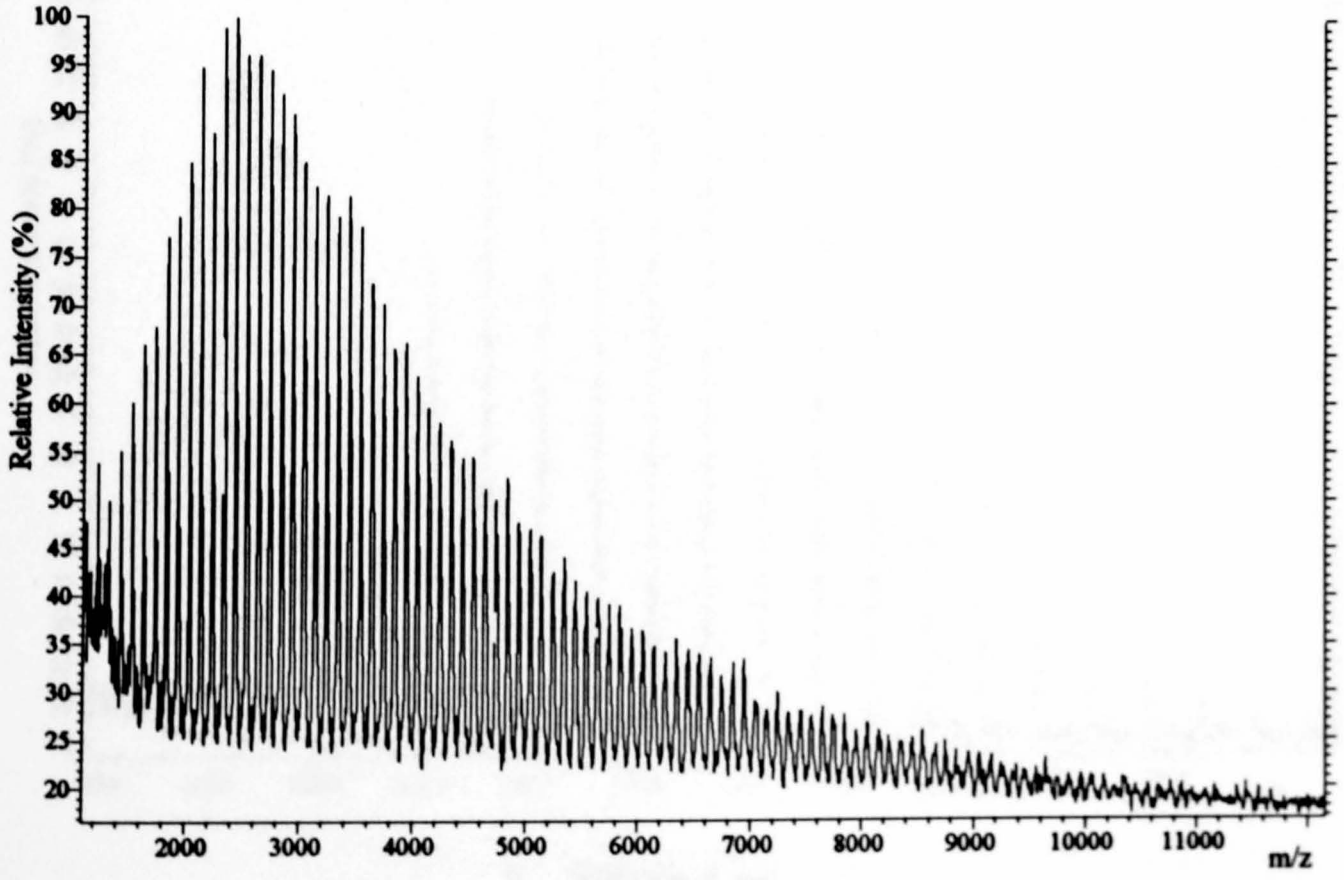

Figure 9.12.

MALDI Spectrum of ERCT9B (Linear Mode, IAA/Acetone).

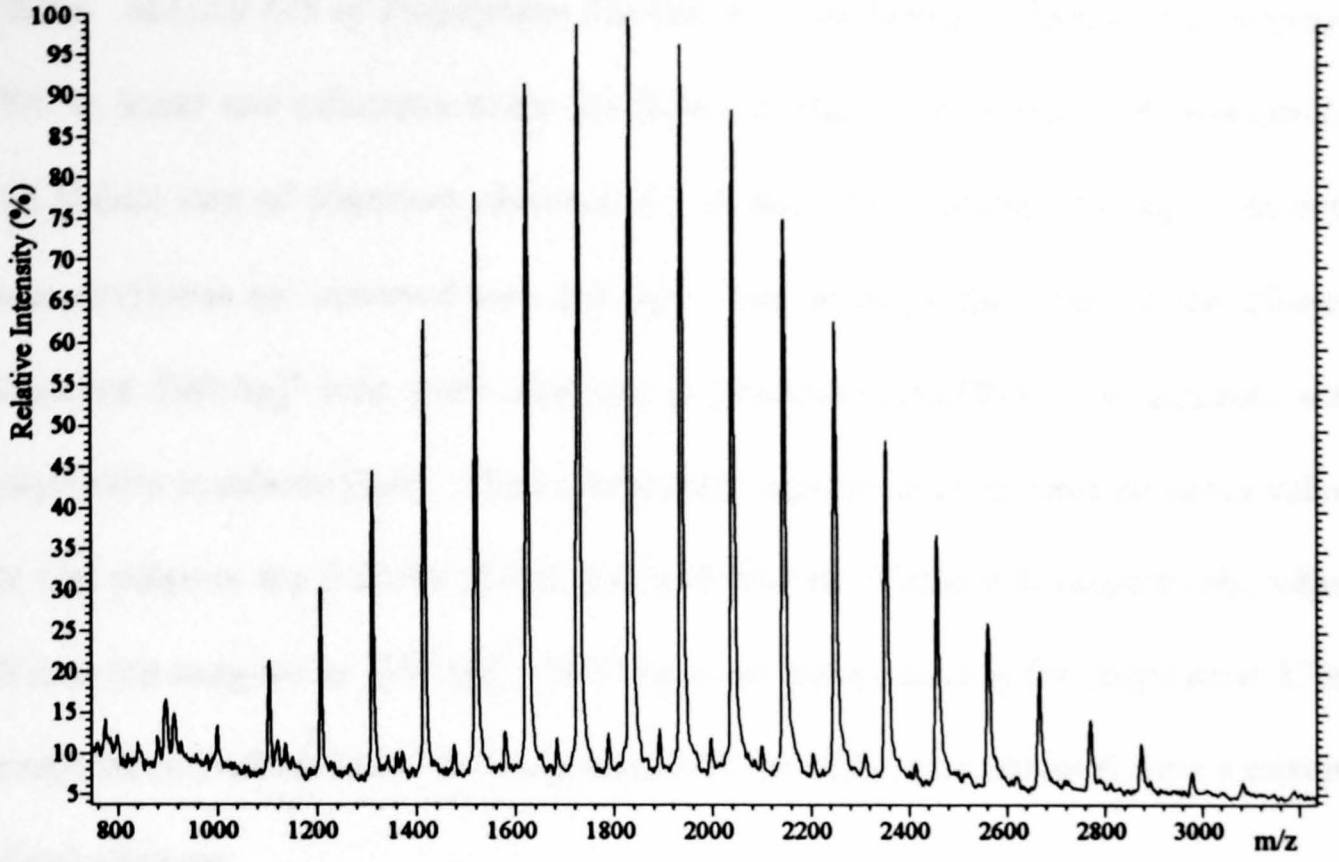

Figure 9.13.

MALDI Spectrum of Polystyrene 1700 (Linear Mode, IAA/Acetone/Silver Trifluoroacetate).

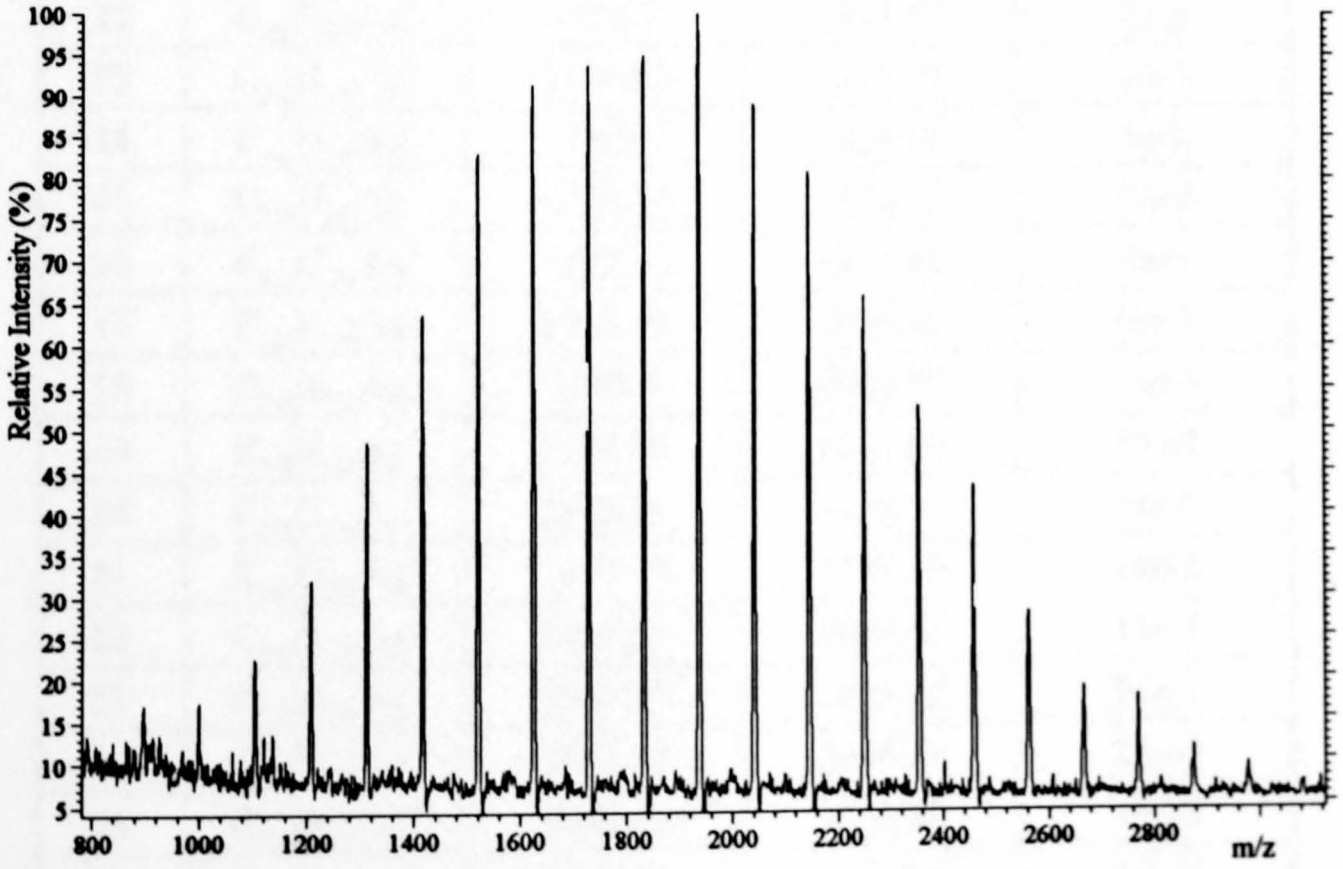

Figure 9.14.

MALDI Spectrum of Polystyrene 1700 (Reflectron Mode, IAA/Acetone/Silver Trifluoroacetate).

9.3.(iv) MALDI-MS of Polystyrene Standards. The MALDI spectra of polystyrene 1700 in linear and reflectron mode are shown in Figures 9.13 and 9.14 respectively. The adduct ions of oligomers observed are all the silver adducts, $[M+Ag]^+$. Smooth mass envelopes are observed with $[M+Ag]^+$ ions given by the 6-mer to the 29-mer. Abundant $[M+Ag]^+$ ions were observed in previous MALDI-MS experiments with polystyrene standards [2,4]. The experimental average error in mass accuracy values for this polymer are 0.013% (Table 9.4) and 0.033% (Table 9.5) respectively, where all ions are assigned as $[M+Ag]^+$. The improved mass accuracy for polystyrene 1700, compared to PMMA 2010, is as expected with the calibration obtained from a mixture of polystyrenes.

n	Formula	$Mass_{calc}$	$Mass_{exp}$(mean)	% Error
9	$C_{76}H_{82}Ag^+$	1103.29	1103.1	17e-3
10	$C_{84}H_{90}Ag^+$	1207.42	1207.38	3e-3
11	$C_{92}H_{98}Ag^+$	1311.56	1311.61	4e-3
12	$C_{100}H_{106}Ag^+$	1415.7	1415.77	5e-3
13	$C_{108}H_{114}Ag^+$	1519.85	1519.97	8e-3
14	$C_{116}H_{122}Ag^+$	1624	1624.08	5e-3
15	$C_{124}H_{130}Ag^+$	1728.15	1728.32	10e-3
16	$C_{132}H_{138}Ag^+$	1832.3	1832.46	9e-3
17	$C_{140}H_{146}Ag^+$	1936.45	1936.66	11e-3
18	$C_{148}H_{154}Ag^+$	2040.6	2040.89	14e-3
19	$C_{156}H_{162}Ag^+$	2144.76	2145.07	14e-3
20	$C_{164}H_{170}Ag^+$	2248.91	2249.15	11e-3
21	$C_{172}H_{178}Ag^+$	2353.07	2353.39	14e-3
22	$C_{180}H_{186}Ag^+$	2457.22	2457.61	16e-3
23	$C_{188}H_{194}Ag^+$	2561.37	2561.92	21e-3
24	$C_{196}H_{202}Ag^+$	2665.52	2666.14	23e-3
25	$C_{204}H_{210}Ag^+$	2769.69	2770.05	13e-3
26	$C_{212}H_{218}Ag^+$	2873.84	2874.86	35e-3
			% Error (mean)	13e-3

Table 9.4.

Mass Accuracy Values of Polystyrene 1700 (Reflectron Mode).

n	Formula	$Mass_{calc}$	$Mass_{exp}$(mean)	% Error
9	$C_{76}H_{82}Ag^+$	1103.29	1103.26	3e-3
10	$C_{84}H_{90}Ag^+$	1207.42	1207.8	31e-3
11	$C_{92}H_{98}Ag^+$	1311.56	1312.64	82e-3
12	$C_{100}H_{106}Ag^+$	1415.7	1416.17	76e-3
13	$C_{108}H_{114}Ag^+$	1519.85	1520.39	36e-3
14	$C_{116}H_{122}Ag^+$	1624	1624.17	10e-3
15	$C_{124}H_{130}Ag^+$	1728.15	1728.2	3e-3
16	$C_{132}H_{138}Ag^+$	1832.3	1832.47	9e-3
17	$C_{140}H_{146}Ag^+$	1936.45	1936.76	16e-3
18	$C_{148}H_{154}Ag^+$	2040.6	2040.88	14e-3
19	$C_{156}H_{162}Ag^+$	2144.76	2145.07	14e-3
20	$C_{164}H_{170}Ag^+$	2248.91	2249.41	22e-3
21	$C_{172}H_{178}Ag^+$	2353.07	2354.07	42e-3
22	$C_{180}H_{186}Ag^+$	2457.22	2459.12	77e-3
23	$C_{188}H_{194}Ag^+$	2561.37	2561.29	3e-3
24	$C_{196}H_{202}Ag^+$	2665.52	2667.77	84e-3
25	$C_{204}H_{210}Ag^+$	2769.69	2769.35	12e-3
26	$C_{212}H_{218}Ag^+$	2873.84	2875.73	66e-3
			% Error (mean)	33e-3

Table 9.5.

Mass Accuracy Values of Polystyrene 1700 (Linear Mode).

The MALDI spectra of polystyrene 7600 generated in linear and reflectron modes are shown in Figures 9.15 and 9.16. The spectra contain ions which are silver adducts, $[M+Ag]^+$ from below 5000 Da to above 11,000 Da differing by 104 Da, the mass of the repeat unit of polystyrene.

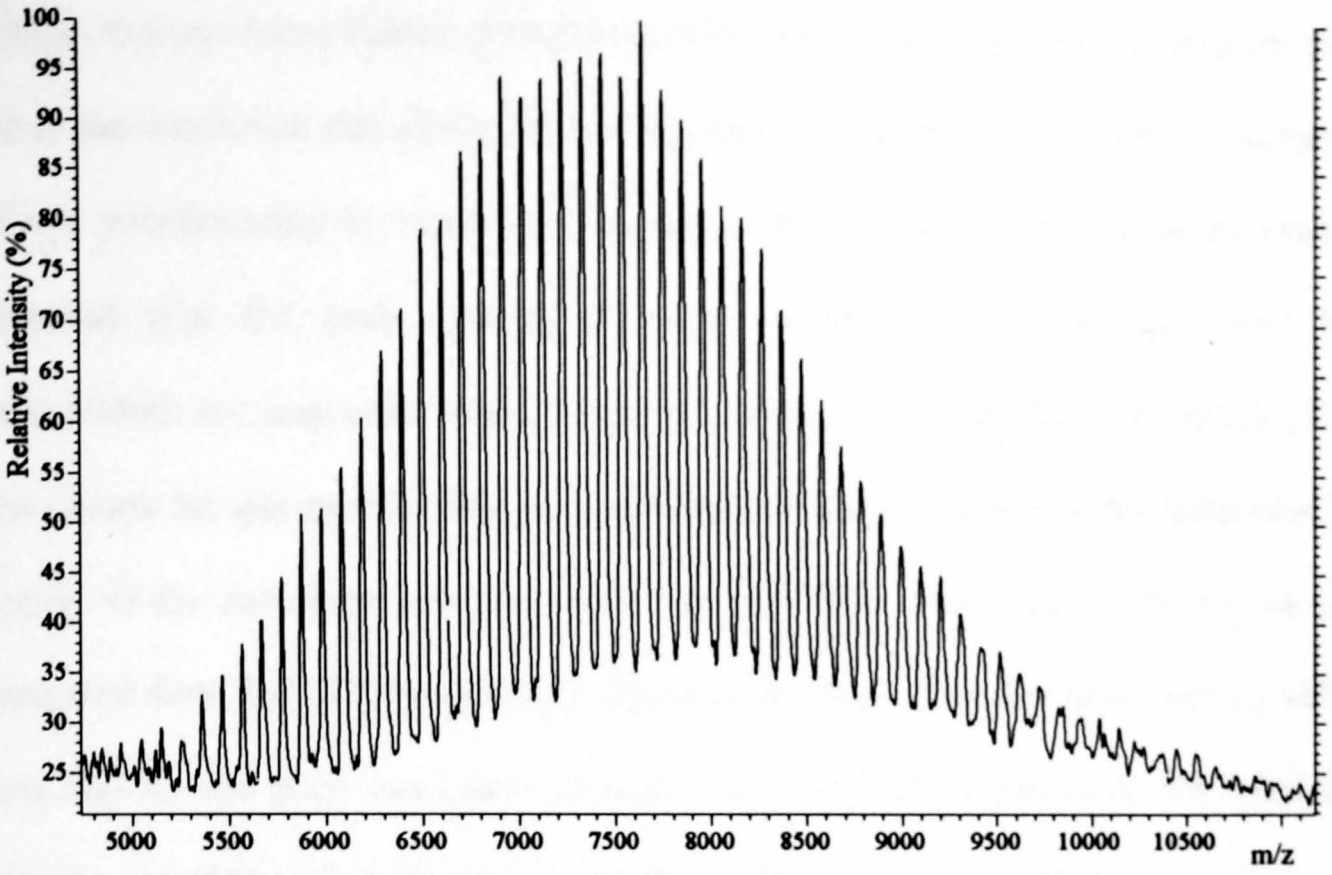

Figure 9.15.

MALDI Spectrum of Polystyrene 7600 (Linear Mode, IAA/Acetone/Silver Trifluoroacetate).

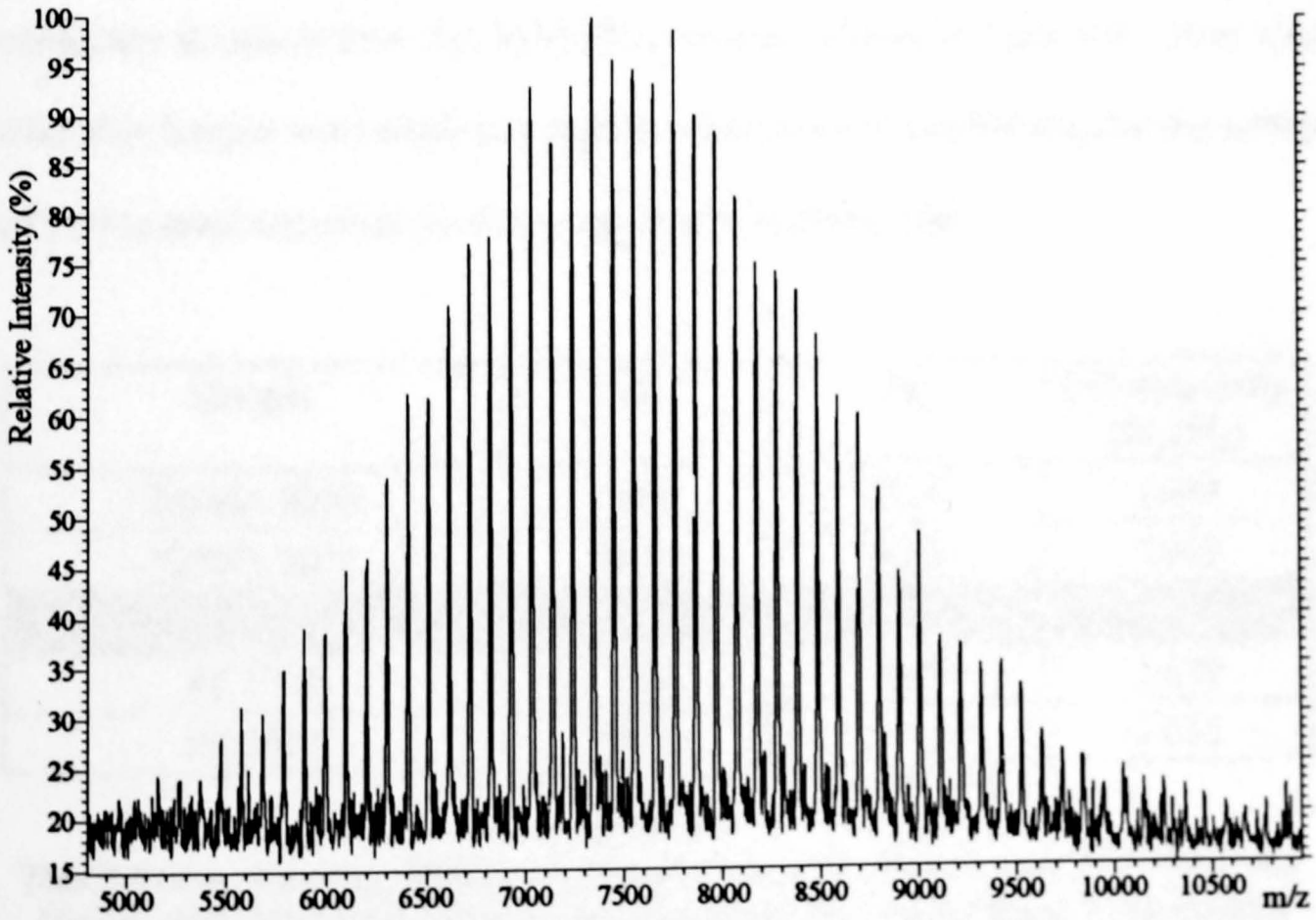

Figure 9.16.

MALDI Spectrum of Polystyrene 7600 (Reflectron Mode, IAA/Acetone/Silver Trifluoroacetate).

9.3.(v) Average Mass Values of PMMA and PS. Previous comparisons have generally led to the conclusion that similar M_n and M_w values are generated for polymer samples of low polydispersity by means of GPC and MALDI-MS [16,17]. A recent report indicated that the peak average molecular weight (M_p) values generated by MALDI-MS are inaccurate when the polymer has a high polydispersity (PDi) [13]. The reason for this anomaly has been explained as a consequence of the difference in display of the data from that of MALDI spectra [26]. Furthermore, the M_p values generated from MALDI spectra were found to be lower than that generated by GPC data due to the poor resolution of higher m/z ions of oligomers in the MALDI experiment and the relatively high sensitivity of GPC at high mass [26].

The average mass (M_n and M_w) and polydispersity values calculated for PMMA and polystyrene standards from the MALDI spectra are shown in Table 9.6. Peak areas rather than heights were employed as these account more satisfactorily for the isotope and instrumental contributions that cause peak broadening [26].

Sample	M_n	M_w	Polydispersity (M_w/M_n)
PMMA 2010	1894	2035	1.074
PMMA 5270	4829	5018	1.039
PS 1700	1885	2035	1.079
PS 7600	7484	7606	1.016

Table 9.6.

The Number Average, Weight Average Molecular Masses and Polydispersity Values of PMMA and Polystyrene Standards Generated from MALDI-MS Experiments.

The low polydispersity values calculated are consistent with the narrow distribution of peaks which are observed in the spectra of PMMA and polystyrene standards.

9.4. LSIMS-Mass Spectrometry of Polymers.

9.4.(i) LSIMS-MS of PMMA. An intense distribution of peaks corresponding to $[M+Na]^+$ ions of intact oligomers is observed in the LSIMS mass spectrum of PMMA 2010 (Figure 9.17). These sodiated ions have the same m/z ratios as those observed in the MALDI spectra of the same compound. This envelope of ions start at m/z 625 (the 6-mer) and extends to greater than m/z 3000. The distribution centres at approximately m/z 1400 which is approximately 400 Da less

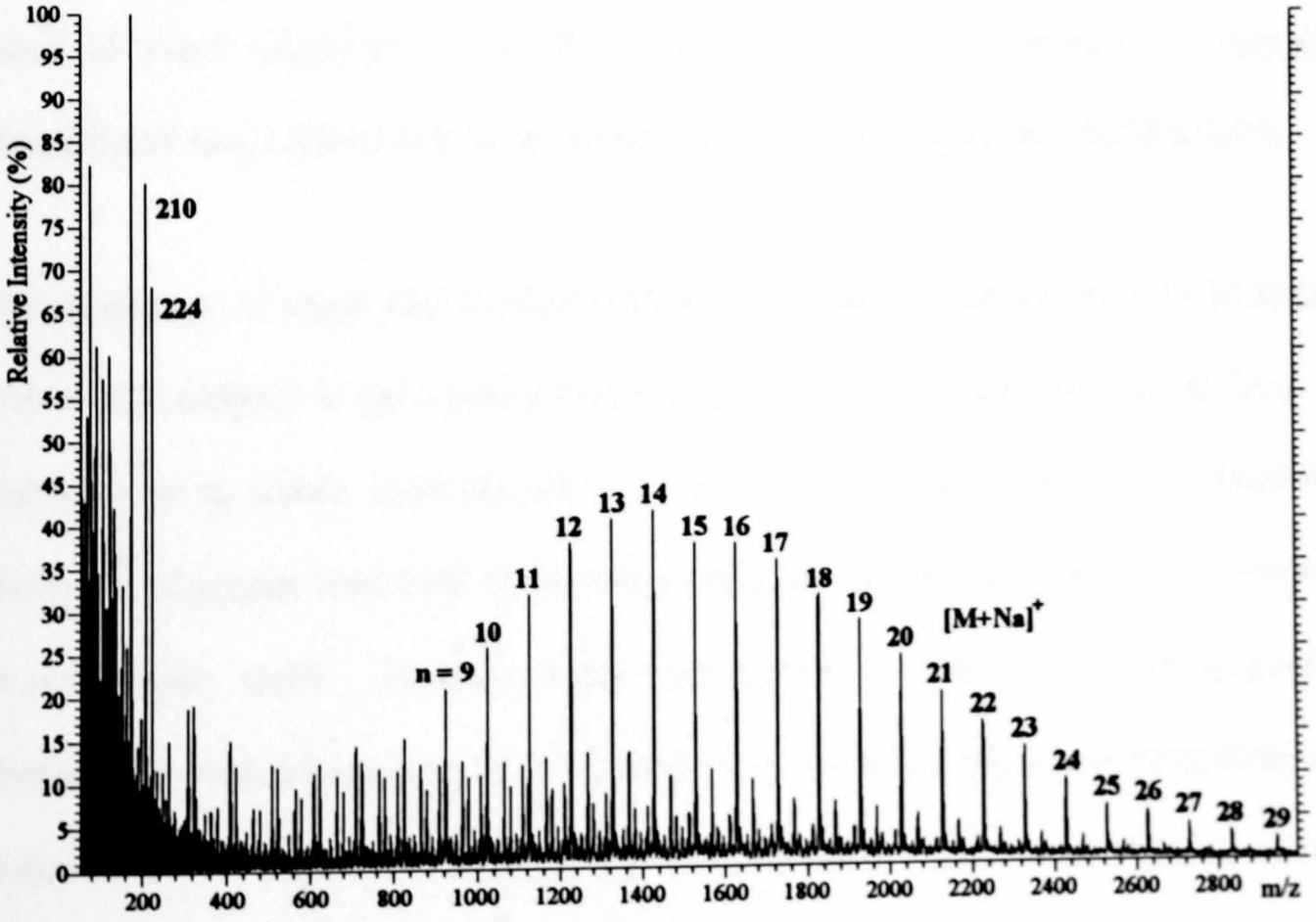

Figure 9.17.

LSIMS Spectrum of PMMA 2010 (NBA Matrix/NaI).

than that found by MALDI-MS. Higher mass oligomers are observed at reduced relative intensity in the LSIMS spectrum in comparison to that observed by MALDI-MS. The skewed nature of this distribution is probably a consequence of two factors. One determinant is the reduced efficiency of ionisation of higher molecular weight materials by means of LSIMS ionisation. A second factor is the fragmentation observed in the LSIMS spectrum. Various series of fragment ions are observed in the mass spectrum and their origin will be discussed in the next section.

The reduced ionisation efficiency of oligomers with higher molecular weights by LSIMS is probably the most important factor in the observation of a mass envelope centring at lower m/z values in comparison to those given by MALDI-MS. There is no evidence that fragmentation of oligomers is more prevalent for high mass species and that these ions dissociate to generate fragment ions with the same m/z ratios as those of intact oligomers. For these reasons it is more reasonable to employ MALDI-MS over LSIMS-MS for generating average mass values for PMMA 2010.

One advantage of employing LSIMS with a sector mass spectrometer over MALDI with a TOF analyser is the improved mass accuracy. The experiments on the ZAB-T enabled one to obtain mass accuracy of ±0.1 Da for oligomers with a dynamic resolution of greater than 1000 (10% valley definition) under the conditions employed in the present work. Accurate mass measurements would enable the empirical formulae for each oligomer to be a calculated and hence aid end group determination as the structure of the repeat unit of the polymer is known. These experiments would be made problematical by the short lived ion currents for polymers generated by LSIMS.

The generation of intense ion signals from polymers by LSIMS is made difficult by the sample preparation. The spectra generated are not very reproducible and high concentrations are required to obtain intense ion signals from the sample. The signals obtained are also very short lived. When the LSIMS ion gun is turned on intense signals are observed which reduce very rapidly.

The LSIMS mass spectrum of PEGFC9.5 (Figure 9.18) is dominated by fragment ions. Adducts of intact oligomers with sodium are observed at low abundance with a maximum at approximately m/z 1600. Peaks are observed at m/z 219, 530 ($M^{+\bullet}$) and 553 ($[M+Na]^+$) which indicates that Irganox 1076 is present as an additive in the sample.

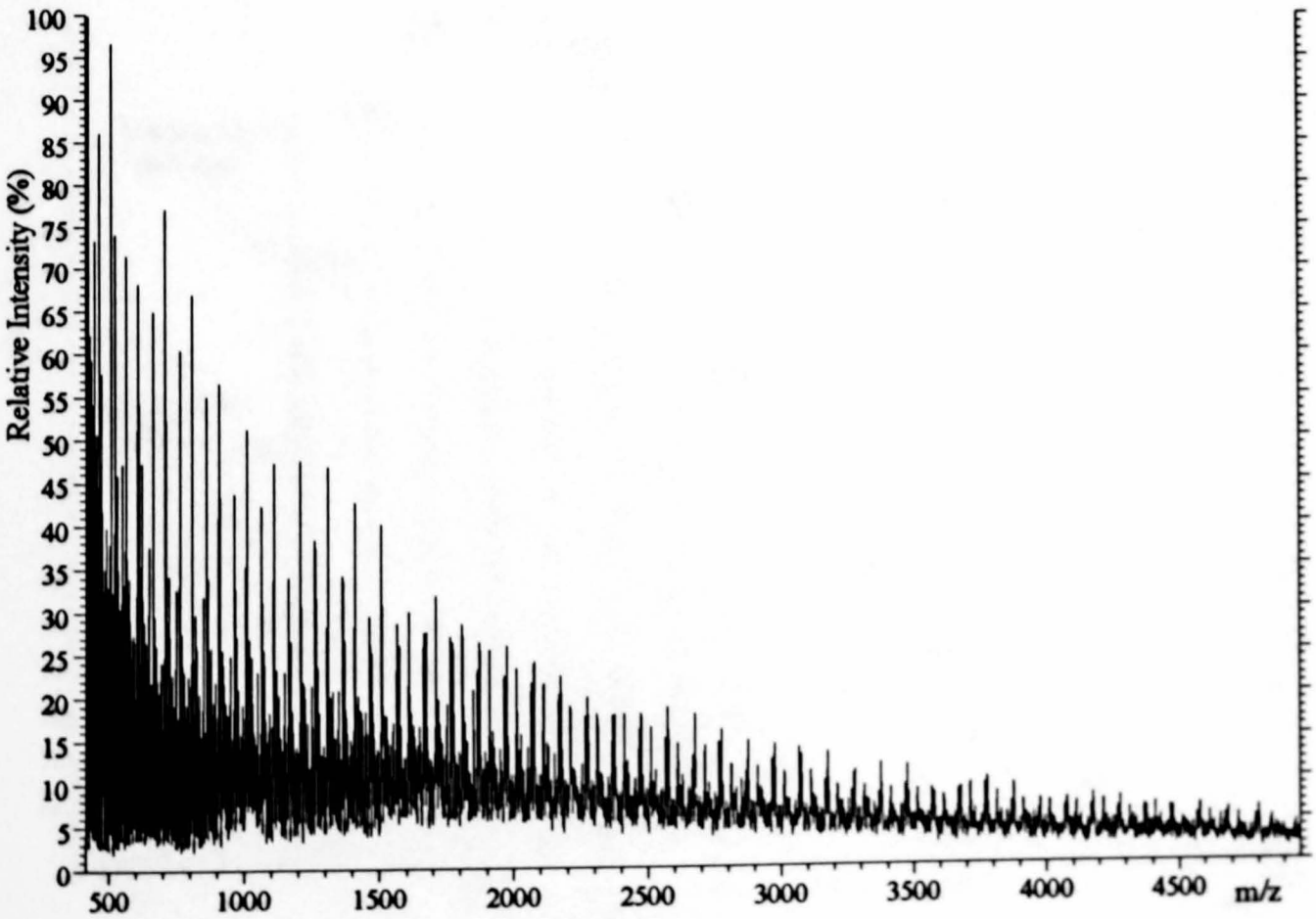

Figure 9.18.

LSIMS Spectrum of PEGFC9.5 (NBA Matrix/NaI).

9.4.(ii) LSIMS-MS of Polystyrene. The LSIMS mass spectrum of PS 1700 is dominated by peaks at low m/z ratios which correspond to dissociation of the polymer, matrix ions and fragmentation of polymer additives.

Adduct ions of intact oligomers with silver ($[M+Ag]^+$) were observed at low abundance between m/z 1000 and 3000. This expanded region of the spectrum is shown in Figure 9.19. Other series of ions are observed in this region of spectrum which probably correspond to oxidation of the polymer on the probe tip. This phenomenon is often found when NBA is employed as the matrix for LSIMS ionisation. The presence of silver adducts in the spectrum is indicated by a comparison

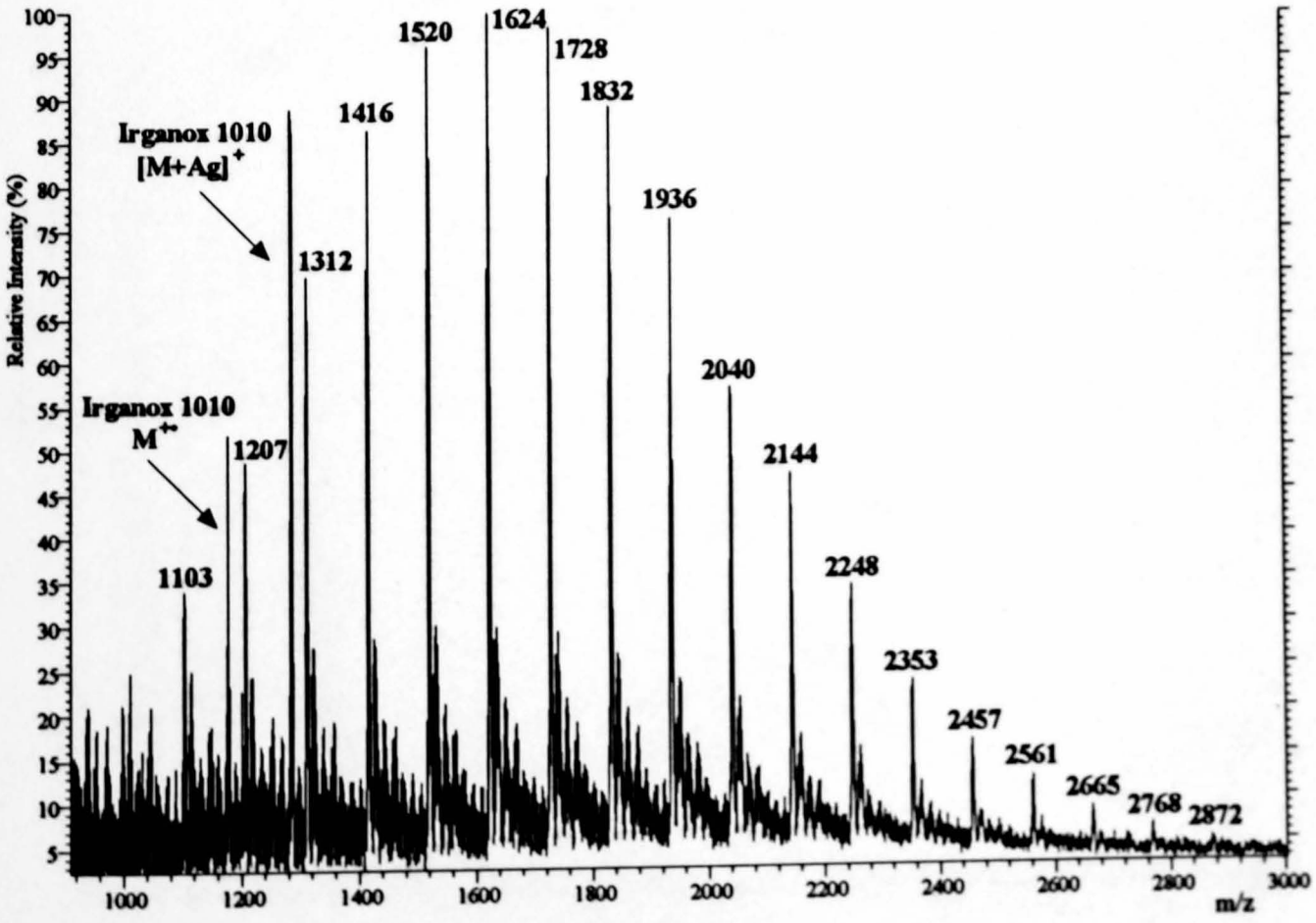

Figure 9.19.

Partial LSIMS Spectrum (m/z 1000-3000) of Polystyrene 1700 (NBA Matrix/Silver Trifluoroacetate).

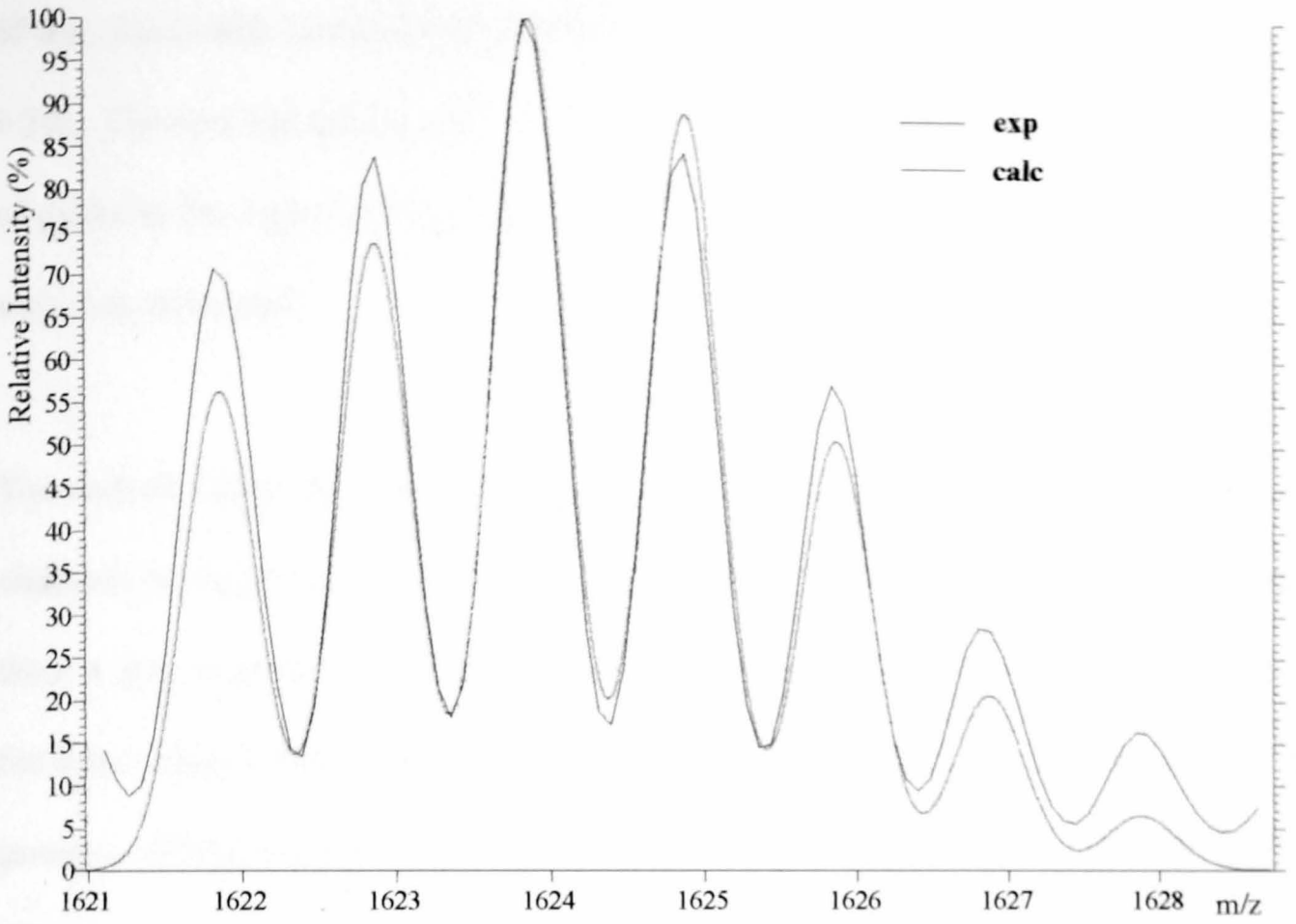

Figure 9.20.

Calculated and Experimental (LSIMS Spectrum) Isotope Distributions of the 15-mer of Polystyrene 1700.

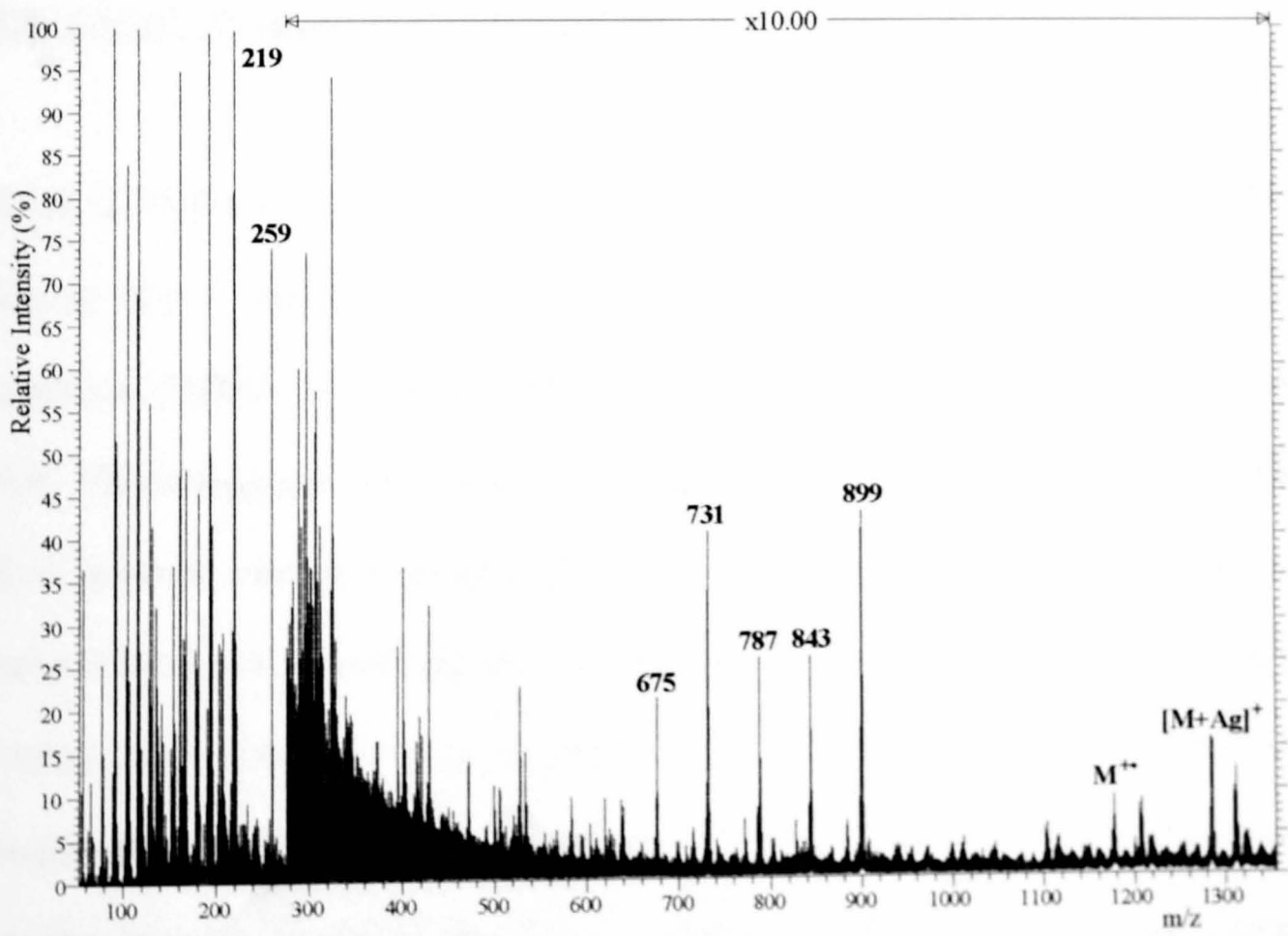

Figure 9.21.

Partial LSIMS Spectrum (m/z 50-1350) of Polystyrene 1700 (NBA Matrix/Silver Trifluoroacetate).

of the theoretical isotope distribution with that observed in the experiment (Figure 9.20). The two isotopes of silver, ^{107}Ag and ^{109}Ag, give rise to an extended distribution of peaks in the region of the adducts. The experimental distribution gives a good fit with that calculated.

The radical cation $M^{+\cdot}$ and the silver adduct ($[M+Ag]^+$) of Irganox 1010 are also observed in Figure 9.19. The intensity of the additive peaks reduces very quickly after the ion gun is turned on, relative to those from oligomeric adducts. An expansion of the lower region of the LSIMS spectrum is shown in Figure 9.21 which indicates the presence of fragment ions of Irganox 1010. The origin of these ions is discussed in Chapters 7 and 8.

9.5. LSIMS-Tandem Mass Spectrometry of Polymers.

9.5.(i) LSIMS-MS/MS of PMMA. Figures 9.22, 9.23 and 9.24 are the LSIMS-MS/MS spectra of m/z 1825.7, 2025.8 and 2526.0, $[M+Na]^+$, from PMMA 2010. The CID spectra of PMMA 2010 are dominated by fragment ions at low m/z ratio, below m/z 500. These fragment ions are generated by direct cleavage of the polymer backbone. Two series of ions are observed, both differing in m/z ratio by 100 Da which is the mass of the repeat unit of PMMA. These ions have m/z ratios of 110 + 100n and 124 +100n where n = 0-4. These fragment ions aid end group identification and were observed in the CID spectra obtained from all oligomers of PMMA 2010 studied ranging from the 14-mer to the 25-mer. These fragmentation pathways are shown in Scheme 9.1.

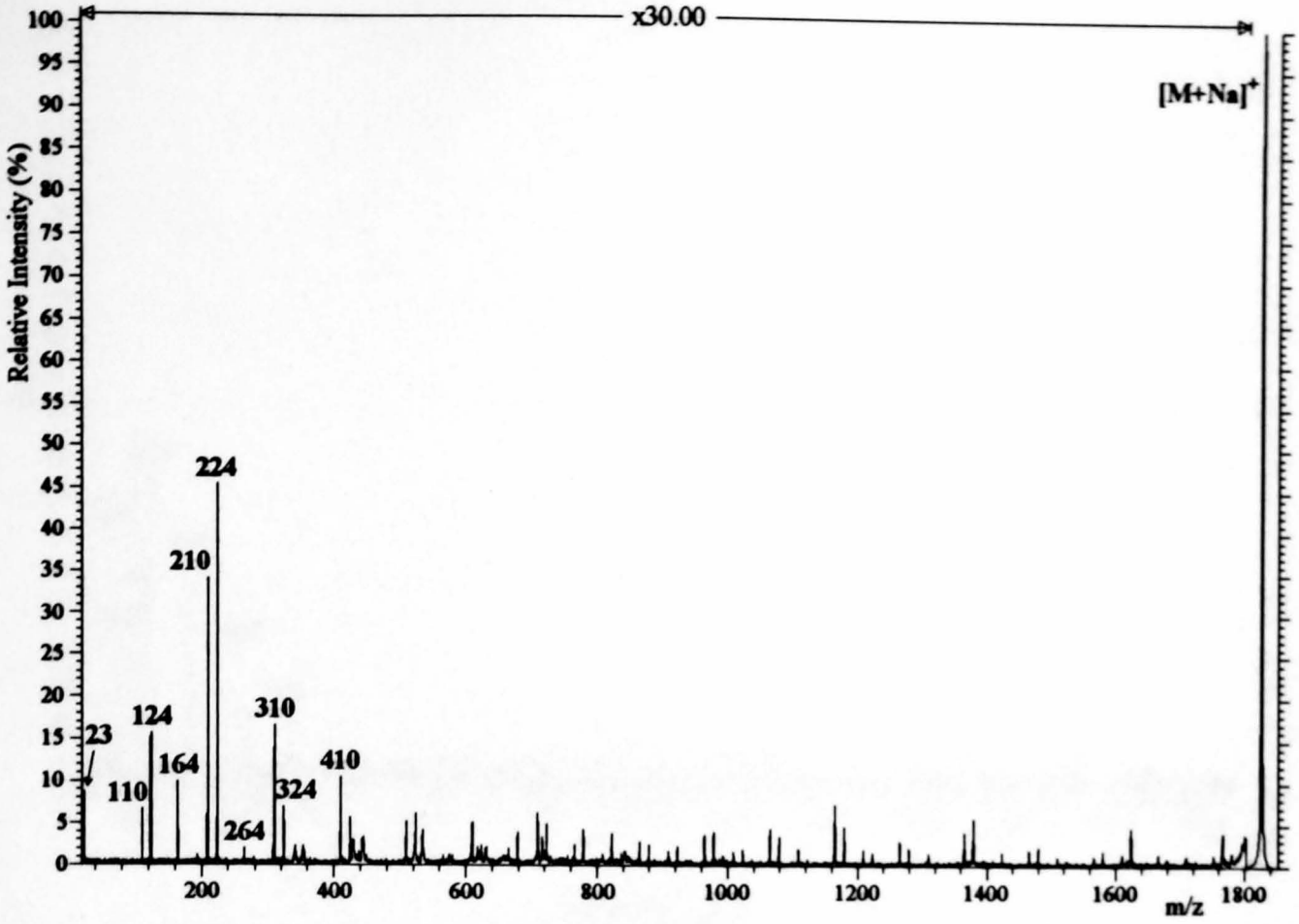

Figure 9.22.

LSIMS-MS/MS Spectrum of PMMA 2010, $[M+Na]^+$ m/z 1825.7 (NBA Matrix/NaI).

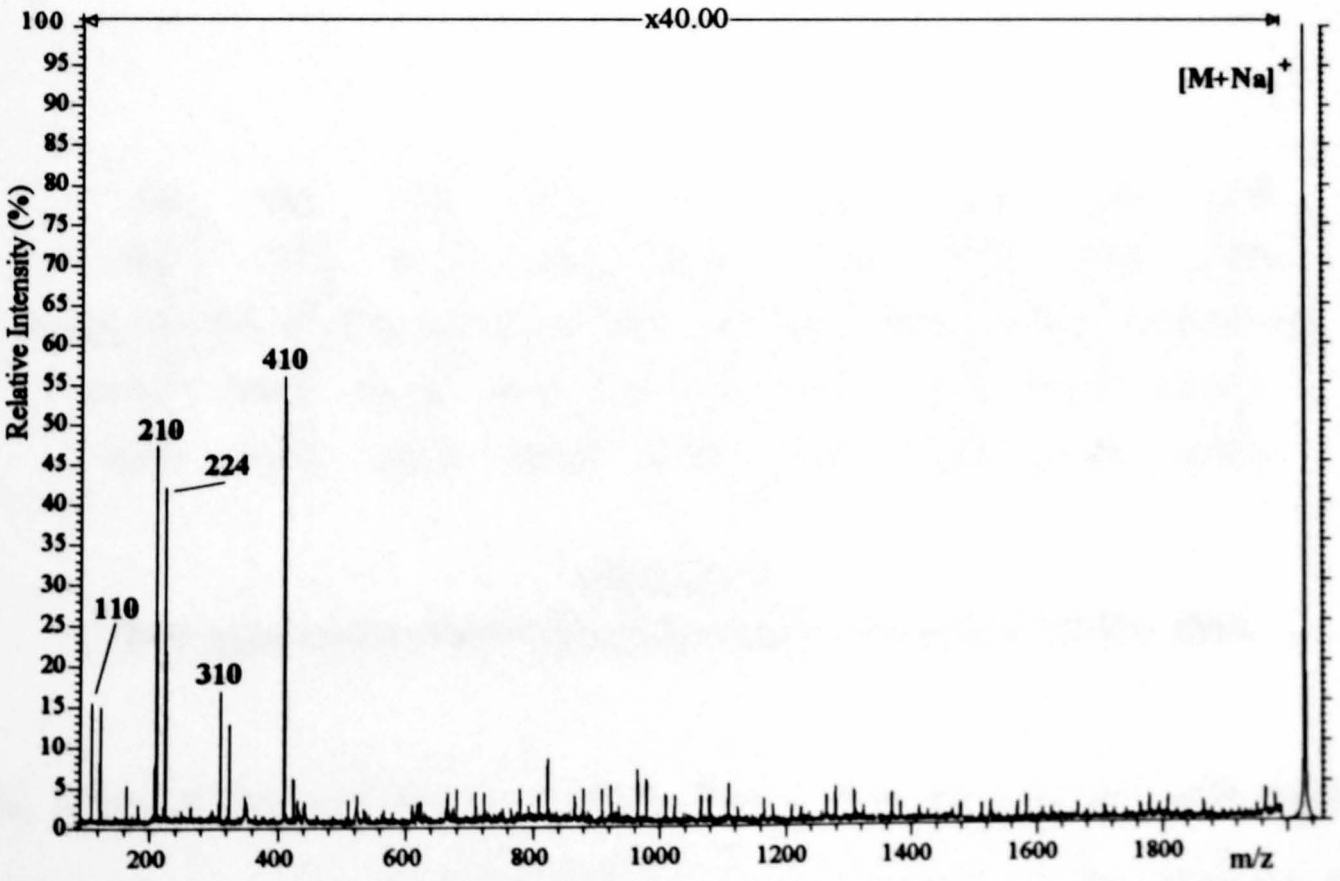

Figure 9.23.

LSIMS-MS/MS Spectrum of PMMA 2010, $[M+Na]^+$ m/z 2025.8 (NBA Matrix/NaI).

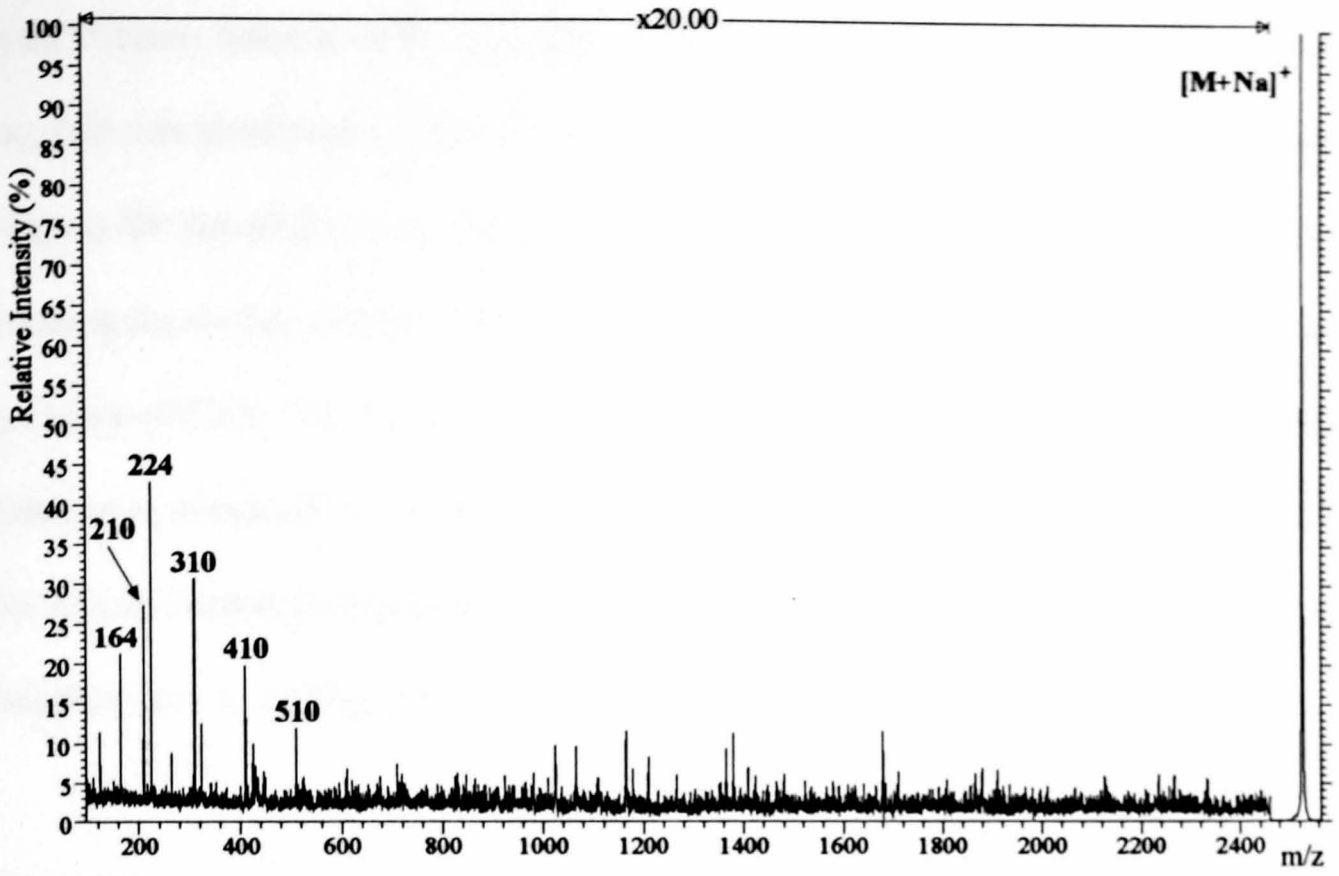

Figure 9.24.

LSIMS-MS/MS Spectrum of PMMA 2010, $[M+Na]^+$ m/z 2526.0 (NBA Matrix/NaI).

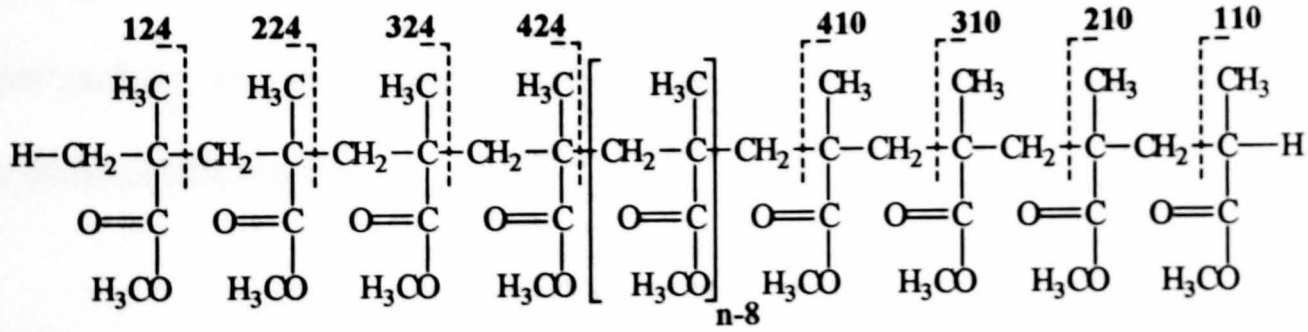

Scheme 9.1.

CID Fragmentation Pathways of the Sodiated n-mer of PMMA 2010.

The origin of ions with m/z ratio 110 + 100n is from chain scission with charge retention (Na^+) on one side of the polymer. The ions of m/z ratio 124 + 100n may be generated by cleavage and charge retention on either end of the polymer backbone.

Initial random scission of the polymer backbone followed by depolymerisation of the fragment ion generated to give the ions observed in the CID spectra is one possible pathway for the origin of the abundant fragment ions at low m/z ratios. This pathway is analogous to that proposed by Craig et al. [27] for the decomposition of polystyrene by means of CID. The loss of monomer units from the fragment ions formed by initial cleavage is presumed to be close to a thermoneutral process in this mechanism [27]. The site of homolytic cleavage was proposed by Lattimer, however, to be at, or near, the chain ends for polyglycols [22].

These ions are radical cations and may possibly be distonic ions with the radical situated on the polymer backbone. Ions of this type were observed in the CID spectra of alkali metal cationated polyglycols by Lattimer [22]. Furthermore, radical cations were also found at low m/z ratios in the CID spectra of fatty alcohols [28] and fatty acids [29]. The proposed structures of the two main series of fragment ions that are observed at low m/z ratios are shown in Figure 9.25. The m/z 124 fragment ion is most probably that shown in Figure 9.25(a) as a tertiary carbon is the more stable site for the unpaired electron.

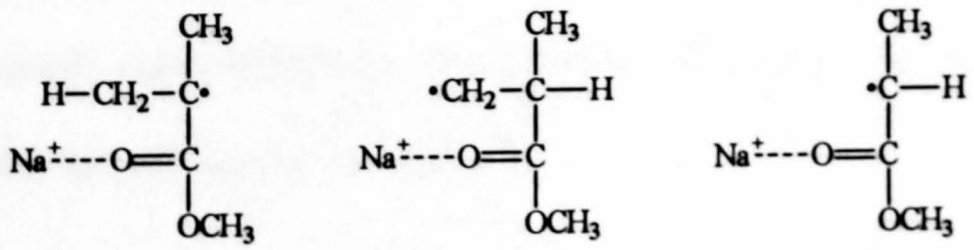

Figure 9.25.

The Proposed Structures of m/z 124 and m/z 110 Fragment Ions Observed in the CID Spectra of PMMA 2010.

Odd electron fragment ions are also generated by loss of methanol and carbon monoxide from the m/z 224 and 324 products. A mechanism to account for this process is shown in Scheme 9.2.

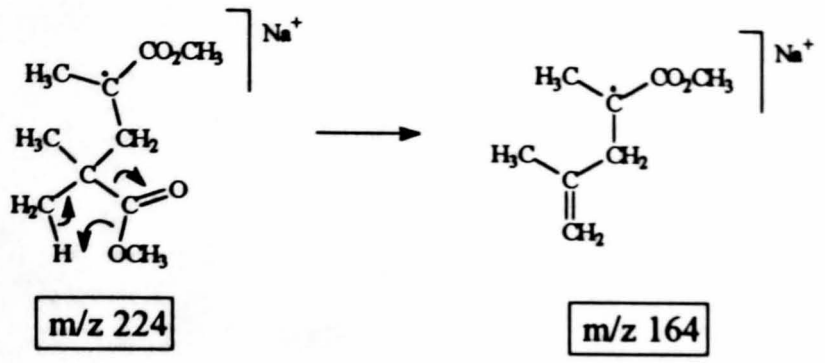

Scheme 9.2.

The Proposed Mechanism of Generation of m/z 164.

A 1,4-hydrogen rearrangement from the methyl side chain of the m/z 224 fragment ion generates the m/z 164 ion with concurrent expulsion of carbon monoxide and methanol. Observation of a fragment ion at $[M+Na-60]^+$ gives credence to this mechanism where carbon monoxide and methanol are expelled concurrently with homolytic cleavage of the polymer backbone.

All fragment ions observed in the CID spectra of PMMA 2010 retain the cation (Na^+). The sodium ion is presumed to be bound to the carbonyl oxygen of one of the ester groups of the side chains of PMMA. The presence of the cation, Na^+, in the precursor ion is indicated by the fragment ion at m/z 23.

Four series of ions are observed in the region of the spectra between m/z 500 and the precursor ion as shown in the expanded region of the CID spectrum of m/z 1825.7

(Figure 9.26). These series of even electron fragment ions have odd m/z ratios and are separated by 100 Da, the mass of the repeat unit of the polymer. The m/z ratios at which these ions appear are given in Table 9.7.

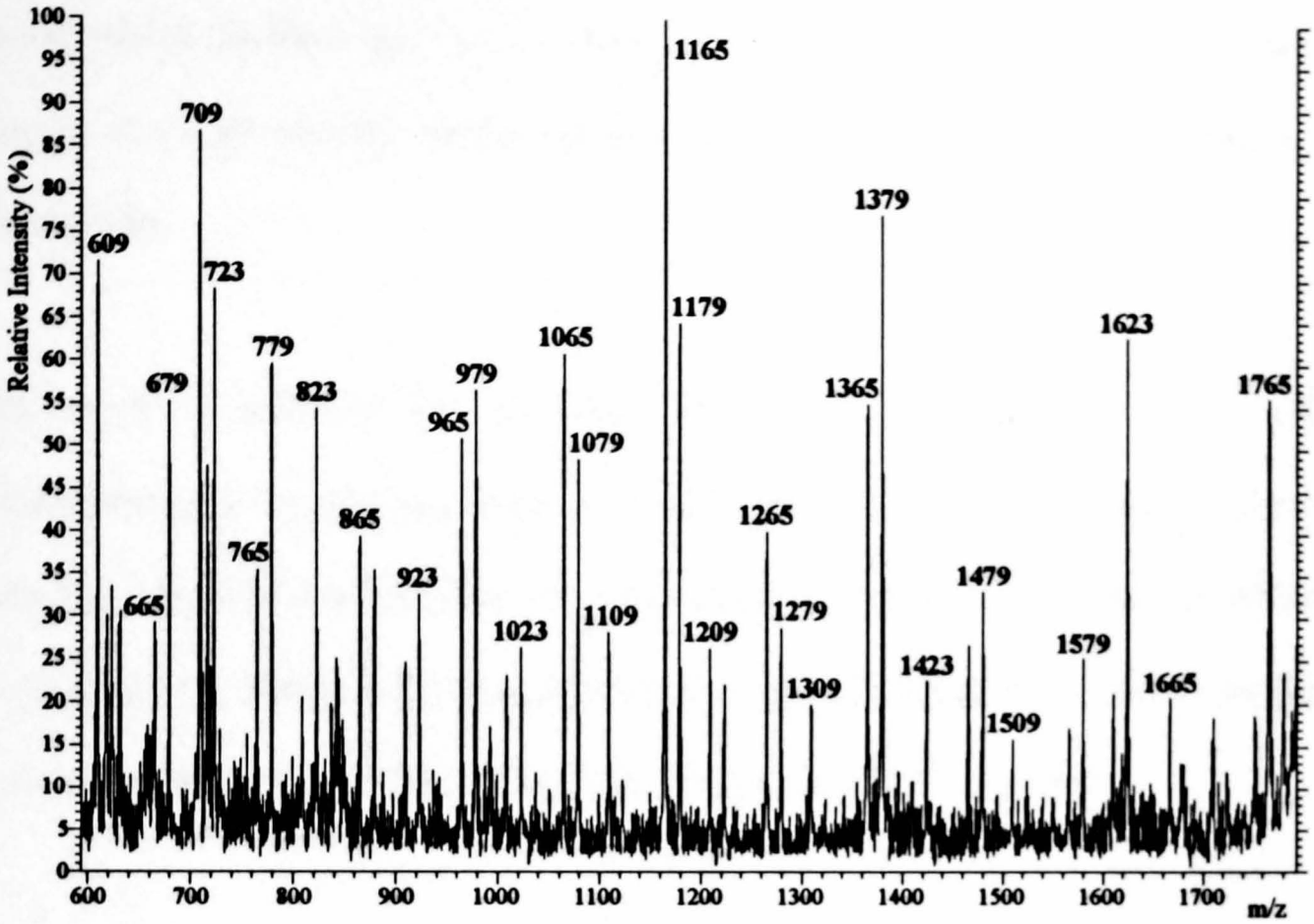

Figure 9.26.

Expanded Region (m/z 600-1800) of the LSIMS-MS/MS Spectrum of PMMA 2010, $[M+Na]^+$ m/z 1825.7 (NBA Matrix/NaI).

Series	m/z Ratio
A	100n + 9
B	100n + 23
C	100n + 65
D	100n + 79

Table 9.7.

The m/z Ratios of the A-D Series Observed in the MS/MS Spectra of $[M+Na]^+$ Ions from PMMA 2010.

All four series, A-D, are generated by rearrangement processes. These fragment ions again all retain the cation. The low abundance of the ions generated by rearrangement processes in comparison to that of ions formed by direct cleavages indicates the prevalence of the latter types of processes under high energy CID conditions. This is due to the high internal energy uptake on collision and the fast time frame of dissociation.

The A and B series of ions are observed at m/z 109 + 100n and 123 + 100n respectively and are both proposed to be generated by 1,5-hydrogen rearrangements between two methylene carbons of the polymer backbone. A fragment ion with an unsaturated end group is formed with loss of a methylmethacrylate monomer unit and part of the main chain of the polymer, as shown in Schemes 9.3 and 9.4.

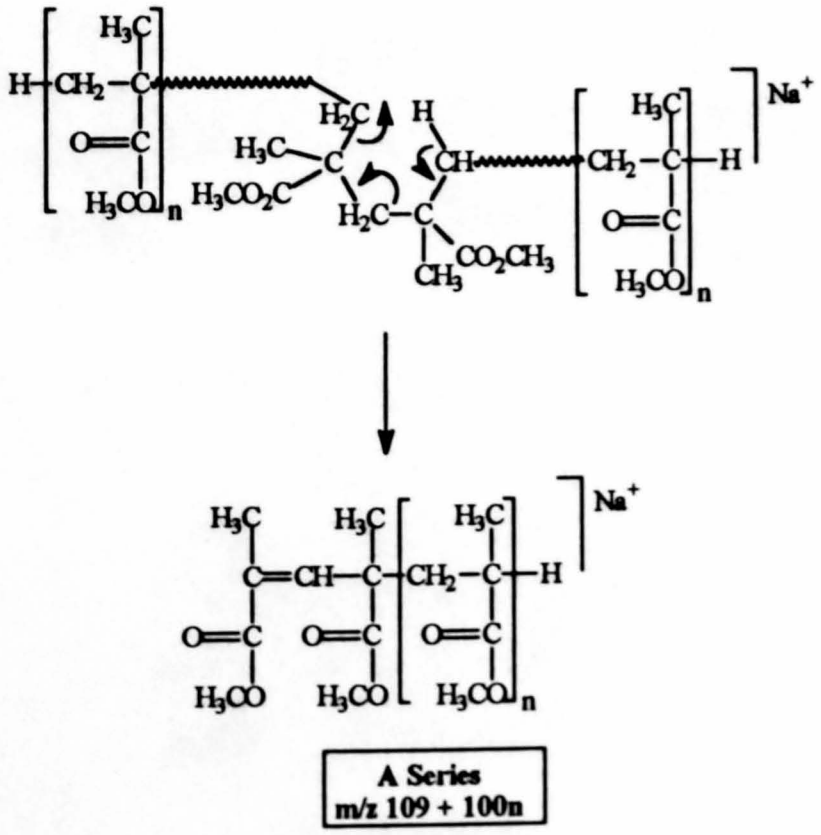

Scheme 9.3.

Proposed Mechanism for Generation of the A Series from PMMA 2010.

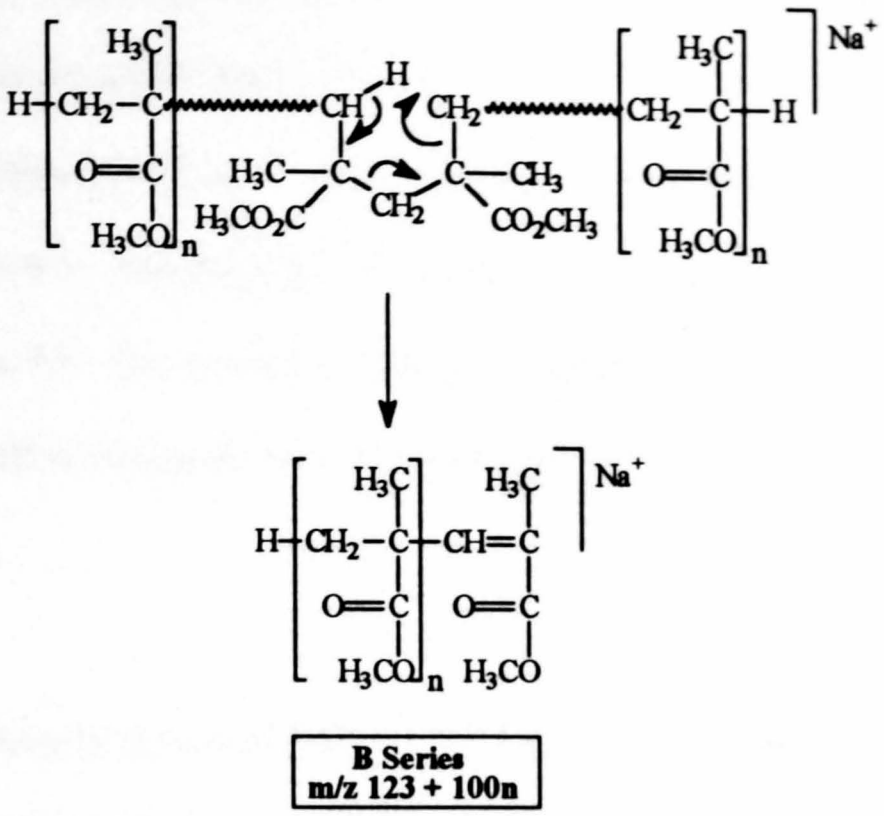

Scheme 9.4.

Proposed Mechanism for Generation of the B Series from PMMA 2010.

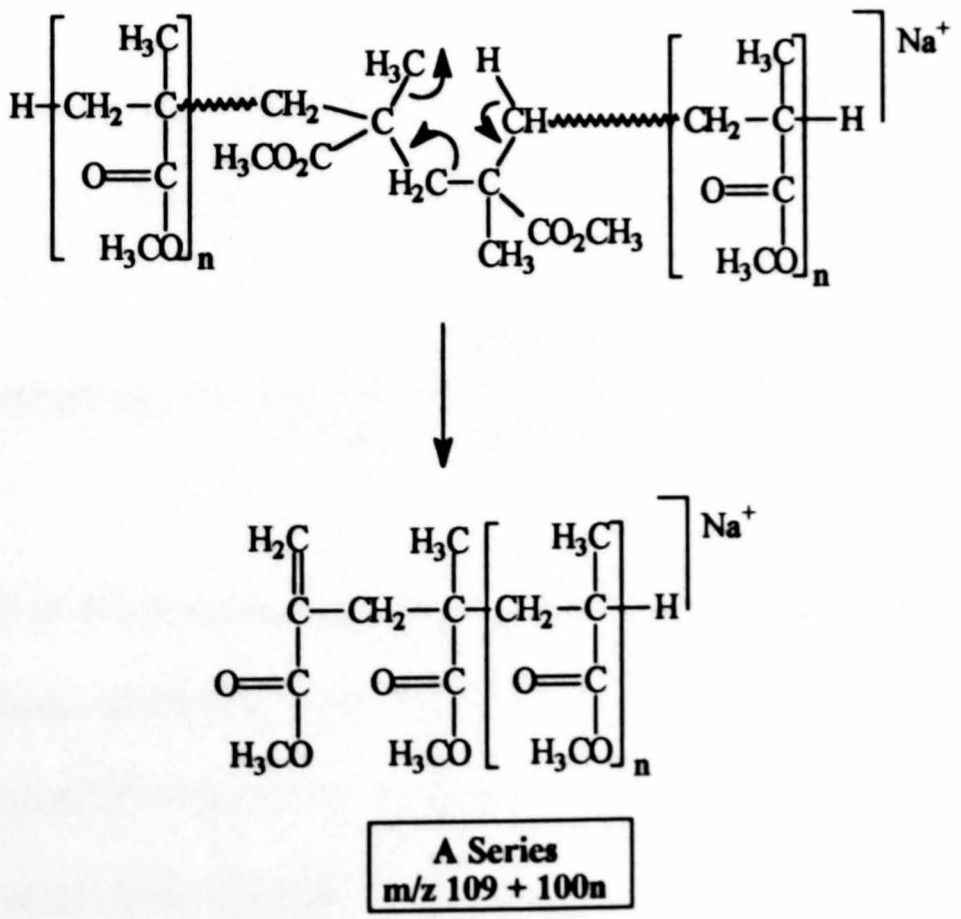

Scheme 9.5.

An Alternative Mechanism for Generation of the A Series from PMMA 2010.

Another possible mechanism for generation of the A and B series involves a 1,5-hydrogen rearrangement from a methyl carbon of a side-chain to a methylene carbon of the polymer backbone. An example of this mechanism for the A series is shown in Scheme 9.5. The fragment ion generated has a structure different from that shown in Scheme 9.3. The unsaturated group is situated between a methylene carbon of a side-chain and a tertiary carbon of the polymer backbone at an end of the chain of the fragment ion.

Loss of carbon dioxide, prior to a similar 1,5-hydrogen rearrangement to that proposed for generation of the A and B series, accounts for the formation of the C and D series observed in the CID spectra of PMMA. The proposed mechanism for the loss of carbon dioxide from a methacrylate side-chain is shown in Scheme 9.6.

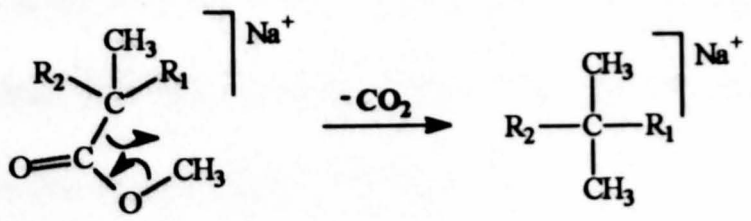

Scheme 9.6.

Proposed Mechanism for Loss of Carbon Dioxide from the Methacrylate Side-chains of PMMA 2010.

All of the series of ions generated by rearrangement processes are also observed in the LSIMS spectrum of PMMA 2010 (Figure 9.17). These series of fragment ions must also be generated by chain scission as they are more abundant at lower m/z ratios. The ions generated by direct cleavages of the polymer are also observed in Figure 9.17.

The observation of facile chain scission from the $[M+Na]^+$ precursor ions formed by LSIMS is inconsistent with that from MH^+ ions generated by field desorption [30]. CID of MH^+ ions generated predominantly fragment ions where a part or the whole of the side chains of the polymer had been lost [30]. The fragment ions observed were hence seen mainly at high m/z ratios. No multiple losses of side chains were observed in the LSIMS-CID spectra. One possible explanation for this phenomenon is that MH^+ ions generated by FD are cyclic in structure and hence two cleavages of the polymer backbone would be required for depolymerisation type reactions to occur. This would be a much higher energy process than losses of part or whole of the side chains and would explain the predominance of high m/z fragment ions in the CID spectra of MH^+ ions. The $[M+Na]^+$ ions that are generated by LSIMS are almost certainly linear in structure and chain scission to form fragment ions is therefore more facile. Cyclic peptide ions have been proposed to be generated by means of FD ionisation while linear species were formed by means of LSIMS [31]. The observation of only single side chain losses from $[M+Na]^+$ precursor ions indicates that these losses may occur predominantly from the end groups of the polymer.

The CID spectrum of the natriated 15-mer, $[M+Na]^+$ m/z 1673.8, of PEGFC9.5 is shown in Figure 9.27. The signal-to-noise ratio is very low in comparison to that observed for PMMA 2010 as a consequence of the low abundance of the former precursor ion. The fragment ions observed at low m/z ratios aid end group identification of the polymer, however, and the fragmentation pathways of the polymer adduct are shown in Scheme 9.7.

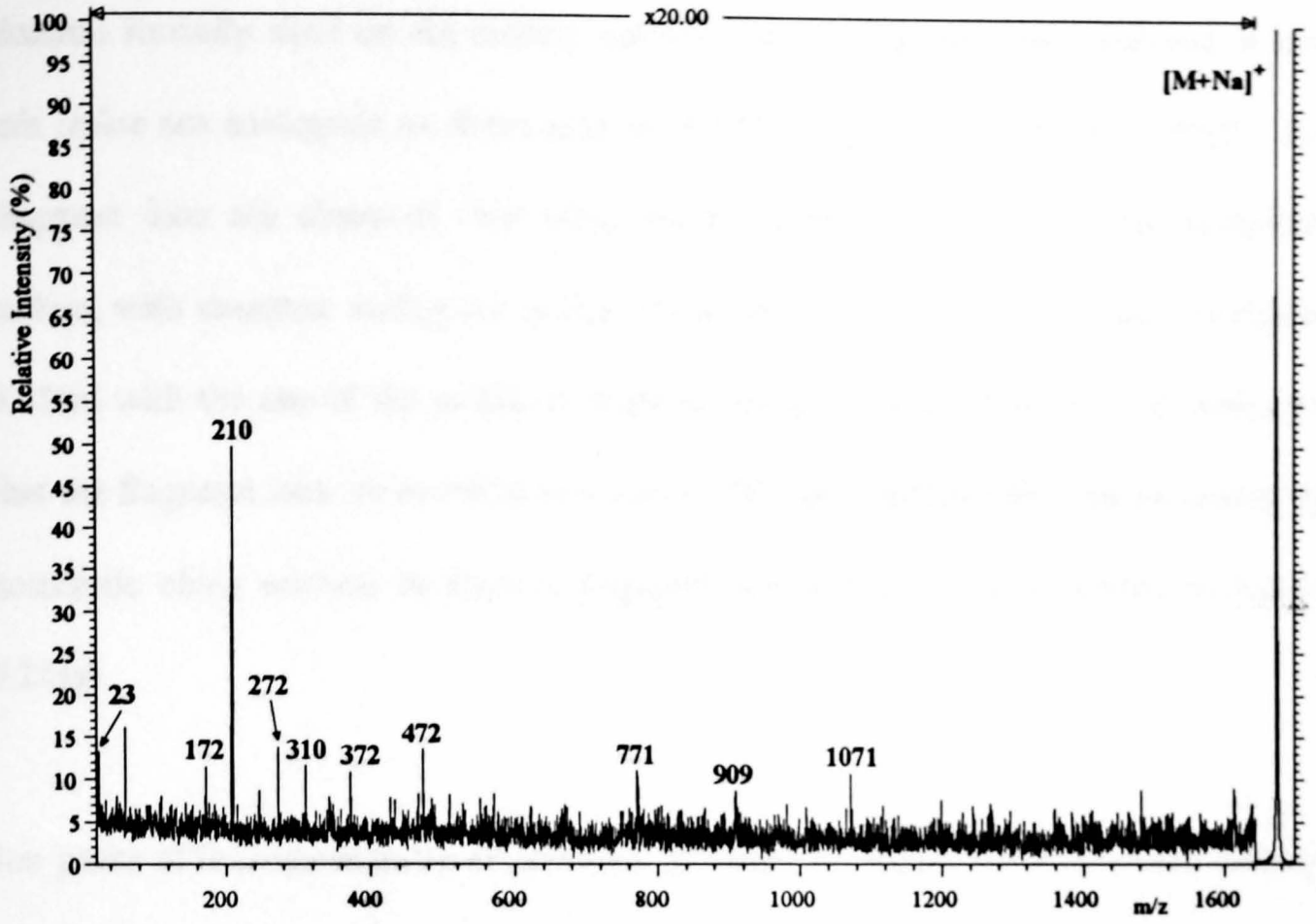

Figure 9.27.

LSIMS-MS/MS Spectrum of PEGFC9.5, $[M+Na]^+$ m/z 1673.8 (NBA Matrix/NaI).

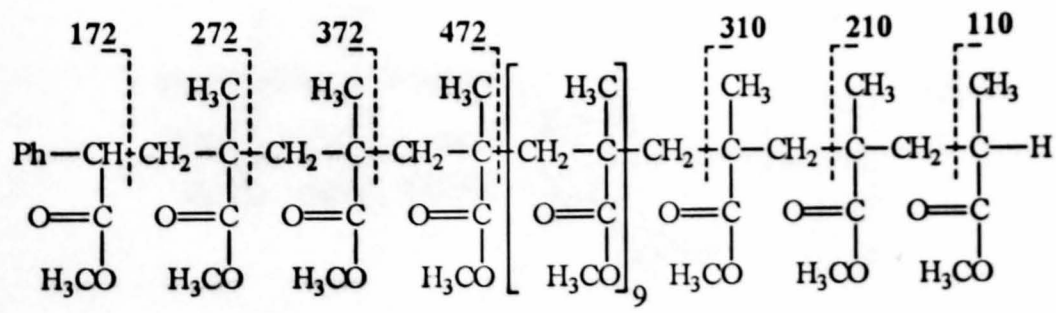

Scheme 9.7.

CID Fragmentation Pathways of the Sodiated 15-mer of PEGFC9.5.

Ions are observed at m/z 110 + 100n and 172 +100n, differing in m/z ratio by the mass of the polymer repeat unit. The fragment ions in these two series are generated from cleavages adjacent to a tertiary carbon and hence have a structure with the unpaired

electron formally sited on the tertiary carbon. These fragment ions observed at low m/z ratios are analogous to those seen in the CID spectra from PMMA 2010. No fragment ions are observed that result from cleavages adjacent to the methylene carbon, with structure analogous to that of the m/z 100n + 124 ions shown in Figure 9.25(b) with the site of the unpaired electron being a primary carbon. This indicates that the fragment ions observed at m/z 124 + 100n for PMMA 2010 are generated by homolytic chain scission to form a fragment ion with a structure shown in Figure 9.25(a).

Ion peaks of low intensity are observed in the central portion of the spectrum that are generated by hydrogen rearrangements. These ions have m/z ratios of 109 + 100n and 171 + 100n. The proposed mechanisms for the generation of these ions are shown in Schemes 9.8 and 9.9 respectively. A 1,5-hydrogen rearrangement generates the fragment ions with an alkene end group.

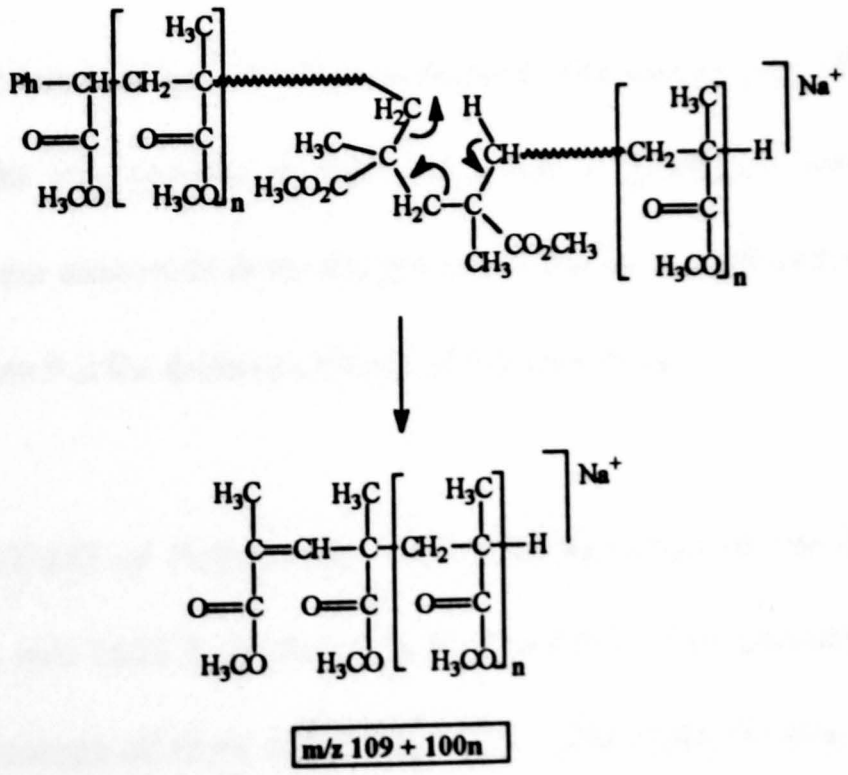

Scheme 9.8.

Proposed Mechanism for Generation of m/z 109 + 100n Fragment Ions Observed in the CID Spectra from $[M+Na]^+$ Ions of PEGFC9.5.

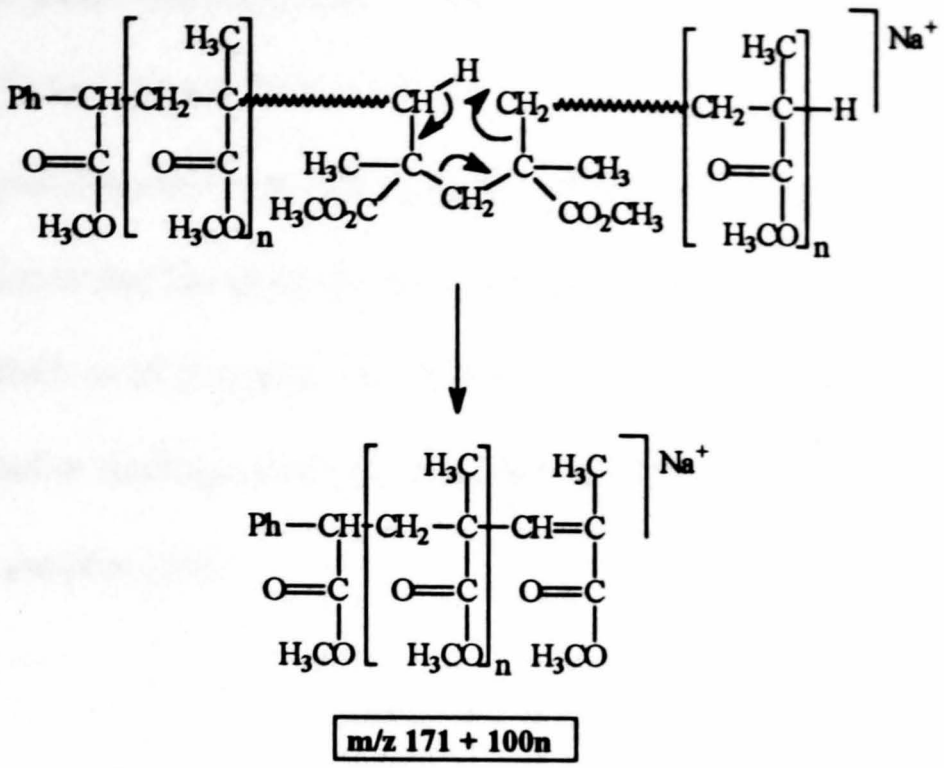

Scheme 9.9.

Proposed Mechanism for Generation of m/z 171 + 100n Fragment Ions Observed in the CID Spectra from $[M+Na]^+$ Ions of PEGFC9.5.

These fragment ions are generated by mechanisms that are analogous to those for the A and B series of PMMA 2010 (Scheme 9.3, 9.4 and 9.5)

Only one fragment ion is observed which is formed with loss of part of a side chain of the polymer. This ion appears at m/z 1613 and is generated with liberation of methanol and carbon monoxide from the precursor ion by a mechanism similar to that proposed in Scheme 9.2 for decompositions of PMMA 2010.

9.5.(ii) LSIMS-MS/MS of Polystyrene. The CID spectrum of the $[M+Ag]^+$ ion of polystyrene 1700, m/z 1621.7, is shown in Figure 9.28. This precursor ion contains the cation of the isotope of silver with RMM 107. The fragment ions observed in the spectrum are predominantly adducts with silver except for three ions at low m/z ratios.

These three ion peaks were also seen at high intensity in the CID spectra of $M^{+\bullet}$ ions generated by FD ionisation (Chapter 10) [27]. These ions appear at m/z 91, 161 and 193 and their possible structures will be discussed in Chapter 10. The observation of these ions indicates that the silver ion is less tightly bound to polystyrene than sodium ions are to PMMA as all fragment ions in the CID spectra of the latter polymer retain the cation. Weaker binding of cations with higher RMM is also observed for adducts of metals with peptides [32].

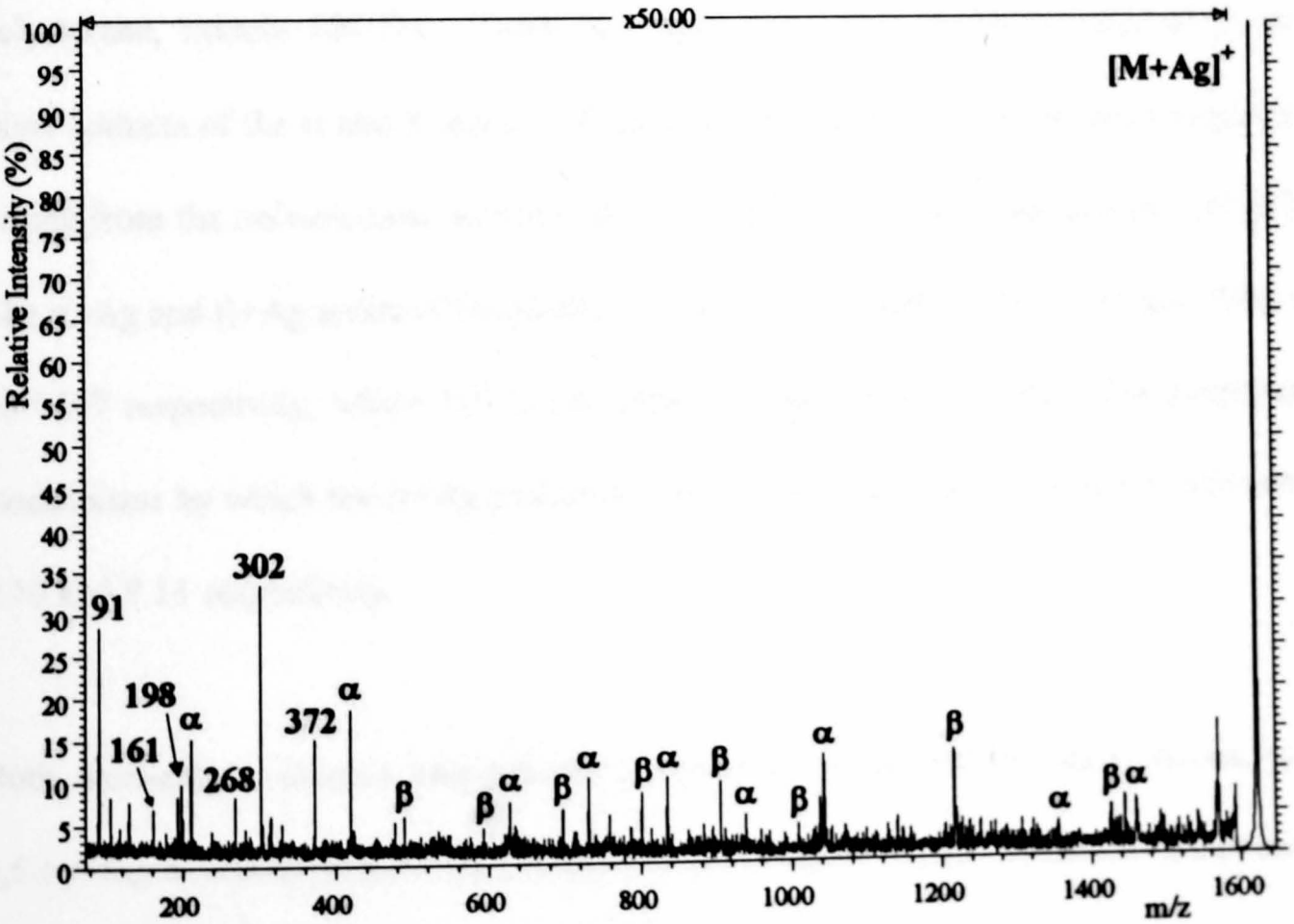

Figure 9.28.

LSIMS-MS/MS Spectrum of Polystyrene 1700, $[M+Ag]^+$ m/z 1621.7 (NBA Matrix/Silver Trifluoroacetate).

Five other ions at low m/z ratios are silver adducts of ions that are observed in the CID spectra of $M^{+\bullet}$ ions and are observed at m/z 198, 211, 268, 302 and 372 in Figure 9.28. The respective fragment ions observed in the CID spectra from the $[M+Ag]^+$ precursor ion have a m/z ratio which is 107 Da higher, corresponding to the addition of the ^{107}Ag isotope. Adduct ions containing silver are observed at much higher intensity when more than one phenyl ring is present in the structure. It is therefore a possibility that the silver ion is bound to two phenyl rings which would explain the pronounced increase in intensity of the silver adduct fragment ions containing two rings.

Two series of ions are also observed in the central region of the spectrum, between approximately m/z 400 and the precursor ion, which are separated by the repeat unit of polystyrene, namely 104 Da. These ions have m/z ratios which correspond to the silver adducts of the α and β series of fragment ions observed in the MIKES spectrum arising from the unimolecular decomposition of molecular ions of polystyrene [27,33]. The α+Ag and β+Ag series of fragment ions have m/z ratios of 104n + 107 and 104n + 70 +107 respectively, where 107 is the relative atomic mass of silver. The proposed mechanisms by which the α+Ag and β+Ag series are generated are shown in Schemes 9.10 and 9.11 respectively.

Both mechanisms involve energetically favourable six membered intermediates and 1,5-hydrogen rearrangements to produce adduct ions of alkene terminated fragments with silver. The neutrals lost in generation of the α+Ag and β+Ag series were observed as ions in the MIKES spectrum arising from the unimolecular decomposition when the charge was retained on the side of the polymer backbone to other than that

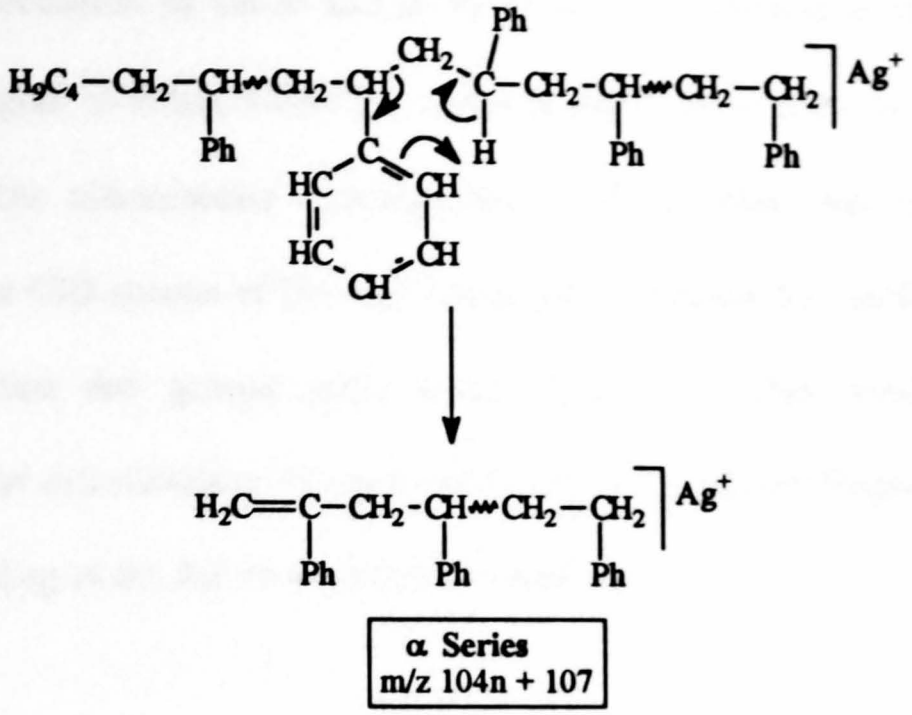

Scheme 9.10.

Proposed Mechanism of Generation of the α+Ag Series from the CID Spectrum of Polystyrene 1700.

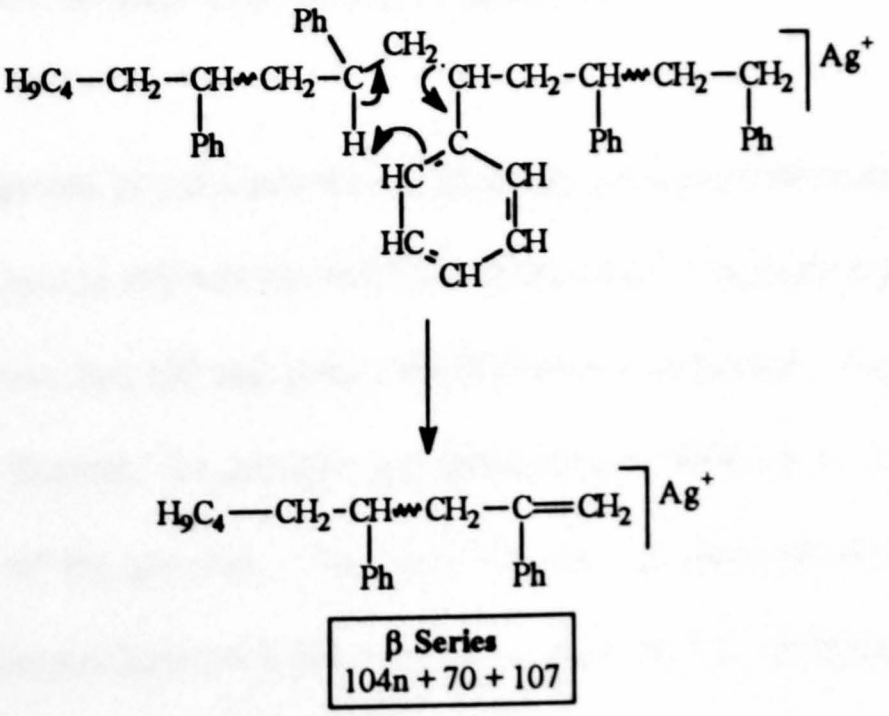

Scheme 9.11.

Proposed Mechanism of Generation of the β+Ag Series from the CID Spectrum of Polystyrene 1700.

required for formation of the α and β series [27]. Furthermore, these ions were observed at higher abundance than that of the α and β series in the MIKES spectrum arising from the unimolecular decomposition. These other two series were not observed in the CID spectra of $[M+Ag]^+$ series which indicate the stability of fragment ions with alkene end groups under these conditions. This stability may be a consequence of delocalisation of electrons in the silver adduct fragment ions which would aid binding of the Ag^+ to the polymer fragment.

9.6. Summary.

A variety of synthetic polymers, differing in both average mass and end group, have been analysed by MALDI-MS. The mass accuracy of the peaks generated by MALDI is improved approximately 2-3 times when spectra are obtained in reflectron rather than linear mode. Standard sample preparation techniques for polystyrene and PMMA polymers with low average mass have been determined.

LSIMS mass spectra of polymers do not generally give good mass envelopes but the ions generated can be selected for MS/MS experiments. Fragment ions are generated in MS/MS spectra that aid end group identification of polymers. Series of fragment ions are often formed, the product ion peak masses differing by the mass of the monomer unit of the polymer. Fragment ions of low mass dominate the MS/MS spectra. Mechanisms have been proposed to account for the rearrangement processes that occur. Fragment ions with unsaturated chain ends are preferentially generated by rearrangement processes.

1 M. Karas, D. Bachmann, U. Bahr and F. Hillenkamp, *Int. J. Mass Spectrom. Ion Proc.*, **78**, 53 (1987).

2 U. Bahr, A. Deppe, M. Karas, F. Hillenkamp and U. Giessmann, *Anal. Chem.*, **64**, 2866 (1992).

3 P. O. Danis, D. E. Karr, F. Mayer, A. Holle and C. H. Watson, *Org. Mass Spectrom.*, **27**, 843 (1992).

4 P. O. Danis and D. E. Karr, *Org. Mass Spectrom.*, **28**, 923 (1993).

5 H. M. Bürger, H.-R. Müller, D. Seebach, K. O. Börnsen, M. Schär and H. M. Widmer, *Macromolecules*, **26**, 4783 (1993).

6 G. Montaudo, M. S. Montaudo, C. Puglisi and F. Samperi, *Rapid Commun. Mass Spectrom.*, **8**, 981 (1994).

7 G. Montaudo, M. S. Montaudo, C. Puglisi and F. Samperi, *Rapid Commun. Mass Spectrom.*, **8**, 1011 (1994).

8 M. Eggert and R. Freitag, *J. Poly. Sci. Part A. Poly. Chem.*, **32**, 803 (1994).

9 R. Freitag, T. Baltes and M. Eggert , *J. Poly. Sci. Part A. Poly. Chem.*, **32**, 3019 (1994).

10 G. Montaudo, M. S. Montaudo, C. Puglisi and F. Samperi, *Anal. Chem.*, **66**, 4366 (1994).

11 H. S. Sahota, P. M. Lloyd, S. G. Yeates, P. J. Derrick, P. C. Taylor and D. M. Haddleton, *J. Chem. Soc., Chem. Comm.*, 2445 (1994)

12 M. Dey, J. A. Castoro and C. L. Wilkins, *Anal. Chem.*, **67**, 1575 (1995).

13 G. Montaudo, M. S. Montaudo, C. Puglisi and F. Samperi, *Rapid Commun. Mass Spectrom.*, **9**, 453 (1995).

14 G. Montaudo, M. S. Montaudo, C. Puglisi and F. Samperi, *Macromolecules*, **28**, 4562 (1995).

15 P. O. Danis, D. E. Karr, W. J. Simonsick, Jr. and D. T. Wu, *Macromolecules*, **28**, 1229 (1995).

16 B. Hanley, D. Parees, S. Hanton, R. King and K. Owens, *Proceedings of 43rd ASMS Conference on Mass Spectrometry and Allied Topics*, May 21-26, Atlanta, Georgia (1995).

17 P. M. Lloyd, K. G. Sudaby, J. E. Varney, E. Scrivener, P. J. Derrick and D. M. Haddleton, *Eur. Mass Spectrom.*, accepted for publication.

18 R. P. Lattimer, H. Münster and H. Budzikiewicz, *Int. J. Mass Spectrom. Ion Proc.*, **90**, 119 (1989).

19 R. P. Lattimer, *J. Am. Soc. Mass Spectrom.*, **3**, 225 (1991).

20 G. Montaudo, *Rapid Commun. Mass Spectrom.*, **5**, 95 (1991).

21 R. P. Lattimer, *Int. J. Mass Spectrom. Ion Proc.*, **116**, 23 (1992).

22 R. P. Lattimer, *J. Am. Soc. Mass Spectrom.*, **5**, 1072 (1994).

23 T. L. Selby, C. Wesdemiotis and R. P. Lattimer, *J. Am. Soc. Mass Spectrom.*, **5**, 1072 (1994).

24 R. King, R. Goldschmidt, Y. Xiong and K. Owens, *Proceedings of 43rd ASMS Conference on Mass Spectrometry and Allied Topics*, May 21-26, Atlanta, Georgia (1995).

25 X. Tang, A. Vertes, P. Dreifuss, C. Hull and W. Dutton, *Proceedings of 43rd ASMS Conference on Mass Spectrometry and Allied Topics*, May 21-26, Atlanta, Georgia (1995).

26 C. McEwen, C. Jackson and B. Larsen, *Proceedings of 43rd ASMS Conference on Mass Spectrometry and Allied Topics*, May 21-26, Atlanta, Georgia (1995).

27 A. G. Craig and P. J. Derrick, *Aust. J. Chem.*, **39**, 1421 (1986).

28 J. Adams and M. L. Gross, *J. Am. Chem. Soc.*, **108**, 6915 (1986).

29 J. Adams and M. L. Gross, *Anal. Chem.*, 59, 1576 (1987).

30 W. W. Hope, PhD Thesis, University of New South Wales, Australia (October 1988).

31 J. M. Curtis, C. D. Bradley, P. J. Derrick and M. M. Sheil, *Org. Mass Spectrom.*, **27**, 502 (1992).

32 L. M. Mallis and D. H. Russell, *Int. J. Mass Spectrom. Ion Proc.*, **78**, 148 (1987).

33 A. G. Craig and P. J. Derrick, *J. Am. Chem. Soc.*, **107**, 6707 (1985).

CHAPTER 10.

FIELD DESORPTION OR PYROLYSIS-FIELD IONISATION COMBINED WITH TANDEM MASS SPECTROMETRY FOR THE ANALYSIS OF POLYMERIC MATERIALS.

10.1. Introduction.

Field desorption (FD) ionisation has been used for many polymeric systems to generate accurate mass envelopes of intact oligomers [1,2,3], including polystyrene [4,5,6,7,8,9]. Few papers have been published on collision induced dissociation (CID) of polymeric precursor ions generated by FD [10] due to the relatively low ion currents generated by this ionisation technique. The high energy band pass of the second mass spectrometer of the ZAB-T enables fragment ions spectra to be acquired from precursor ions with inherently low ion currents such as those generated by FD. The application of FD-MS/MS by means of this instrument to aid structural elucidation and end group determination of oligomers from polymers based on polystyrene is described in this chapter.

The thermal degradation or pyrolysis (py) of synthetic polymers is widely used as a method of obtaining information on their structures. When this is combined with field ionisation (FI), a soft ionisation technique that produces mainly ions of the type MH^+ or $M^{+\cdot}$, py-FI/MS allows one to obtain molecular ions of the pyrolyzates formed [11] and therefore gives information on the molecular weight distribution of these polymer fragments. In the present work, py-FI-MS has been employed to analyse a polypropylene sample and the spectra obtained have been compared to that of Lattimer [12]. Furthermore, structural information on the pyrolyzates observed was generated by means of py-FI-MS/MS. The fragment ion peaks observed are discussed in relation to the proposed structures of the pyrolyzates of polypropylene [12].

The addition of high molecular weight, oligomeric, organic polymer additives is becoming more common in many polymeric materials. The analysis of these mixtures of additives by means of mass spectrometry is limited to desorption techniques as a consequence of the inherent involatility of the systems. It was previously suggested that the most suitable ionisation technique for analysing these types of additives is FD [12]. Molecular ions are predominantly generated by FD ionisation with little fragmentation induced and tandem mass spectrometry must be employed to obtain structural information. FD-MS/MS has therefore also been applied to the structural determination of polymer additives from the five component mixture described in chapter 7 (Figure 7.1) as a preliminary investigation into the suitability of this technique for the analysis of oligomeric polymer additives.

Polystyrene 1700 was the sample used in these experiments. The structure of this polymer is shown in Figure 10.1.

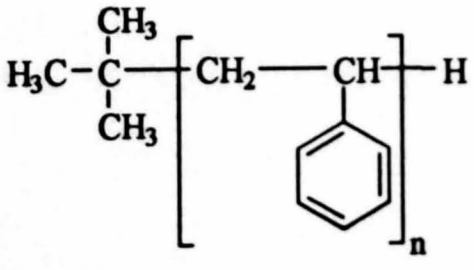

Figure 10.1.

The Structure of Polystyrene 1700, Including *Tert*-Butyl and Hydrogen End Groups.

The end groups of the polymer are a *tert*-butyl group and hydrogen atom. The fragment ions observed in the FD-MS/MS spectra of polystyrene 1700 are discussed with relevance to the mechanisms of fragmentation proposed by Craig et al. [10].

A novel solid product was obtained when 2,3,5,6-tetrafluoro-4-hydroxystyrene was polymerised. The polymer formed was presumed to have the structure given in Figure 10.2.

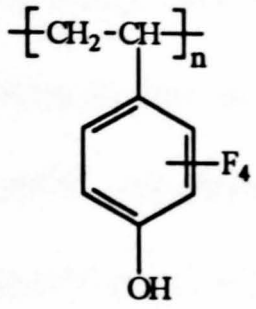

Figure 10.2.

The Proposed Structure of Polymerised 2,3,5,6-Tetrafluoro-4-hydroxystyrene.

This proposed structure is a modification of the structure for polystyrene. These types of modifications have been shown to give polymers with many different properties [13]. In the present work, FD-MS was employed to generate molecular weight information for the polymer and structural determination was aided by FD-MS/MS experiments.

10.2. Experimental.

10.2.(i) Sample Preparation. A solution of polystyrene 1700 in acetone was placed on the emitter and the solvent allowed to evaporate. One droplet of solution from a syringe was used to get an even coating of polymer on the emitter. Similar emitter coating techniques were employed for poly(TFHS) in THF. Finely ground polypropylene pellets were deposited in the quartz crucible of a direct insertion probe for py-FI experiments. An equimolar mixture (10 nmol μL^{-1}) of Tinuvin 327, Irganox

1076, Irganox 3114, Hostanox 03 and Irganox 1010 was employed for analysis of polymer additives.

10.2.(ii) Mass spectrometry. All analyses were performed by means of the ZAB-T tandem mass spectrometer. A heating current of 0-2.5 A was employed to generate pyrolyzates of polypropylene in py-FI experiments. Selection of precursor ions, generated by FD, in tandem mass spectrometry experiments was performed by careful noting of emitter currents with their appearance in the mass spectra. The emitter current values were used to enable one to produce the highest possible ion currents for CID of the ion of interest. The emitter was 'flashed' at 60 mA, to remove absorbed species, during the inter-scan period of 2 s in py-FI-MS experiments. The temperature of desorption was noted and this value was employed to generate the most intense precursor ion signals for py-FI-MS/MS experiments. The collision gas employed in MS/MS experiments was argon with a primary ion beam reduction of approximately 80%. The electrical potential applied to the microchannel plates of the photodiode array detector was 1.75 kV except where stated.

10.3. FD and Pyrolysis-FI-MS of Polymers.

10.3(i) FD-MS of Polystyrene 1700. The FD mass spectrum of polystyrene 1700 is shown in Figure 10.3. It shows a distribution of intact singly charged oligomers, with a maximum at approximately m/z 1550. The peak maximum falls at approximately two oligomers lower than that observed by MALDI-MS (Figures 9.13 and 9.14). Furthermore, the ions observed in the MALDI-MS spectrum were the silver adducts

$[M+Ag]^+$ but radical cations ($M^{+\bullet}$) are the dominant species in the FD-MS spectrum (Figure 10.3). There is also a distribution of peaks of lower intensity which corresponds to doubly charged species of intact polystyrene oligomers. No multiply charged species were observed by means of MALDI-MS (Chapter 9). Rollins et al. noted that distributions ions with up to six charges were present in the FD mass spectra of polystyrenes of high average molar mass [9]. The generation of $M^{+\bullet}$, M^{2+}, $M^{3+\bullet}$ and higher charge states of polystyrene has been proposed to occur *via* the ion evaporation mechanism [10]. The charge results from electron deficiency at the surface which is generated by the electric field [14]. This field also encourages evaporation of the charged species to form gas phase ions [14,15].

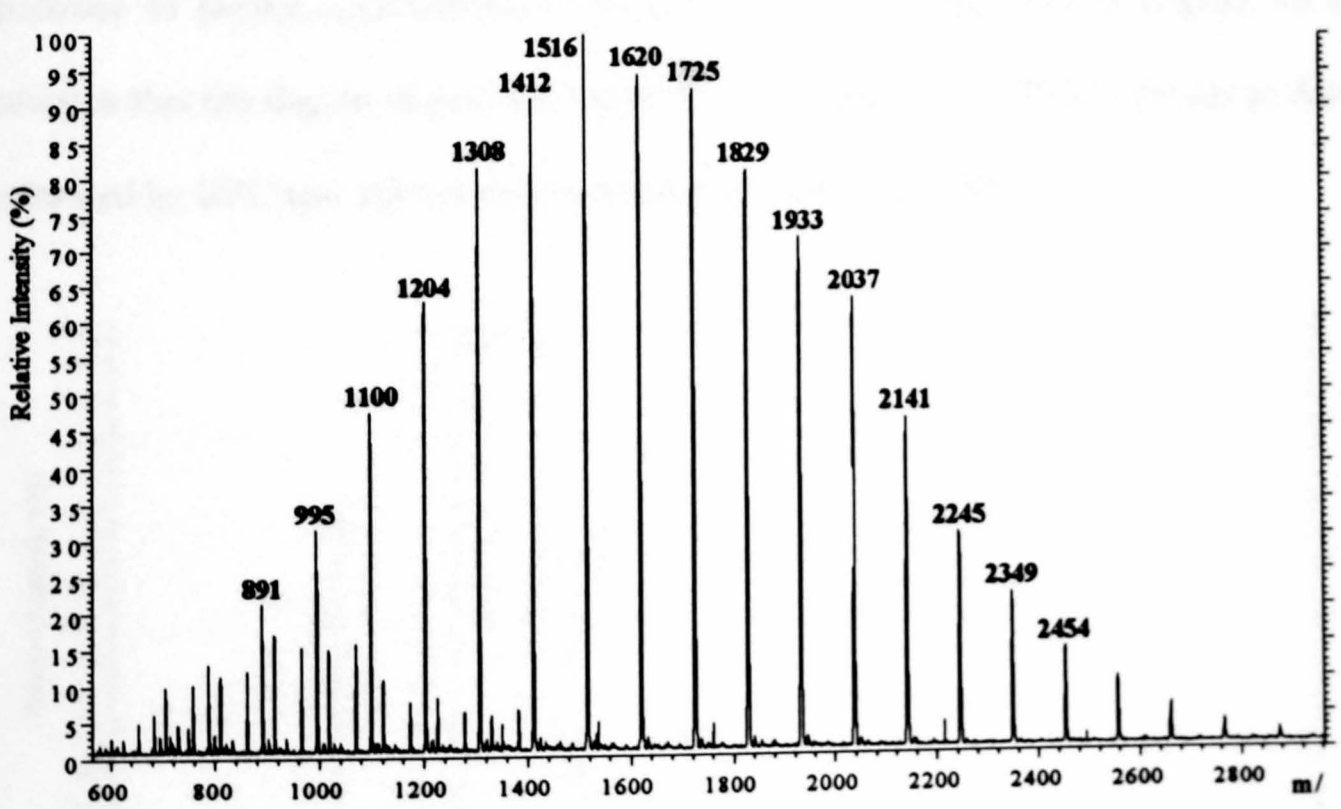

Figure 10.3.

Partial FD-MS Spectrum of Polystyrene 1700.

Singly charged ions are observed in Figure 10.3 corresponding to molecular ions ($M^{+\bullet}$) of the 6-mer (m/z 683) to the 28-mer (m/z 2973). The most intense isotope peak

(K_{max}) of the molecular ions may be calculated by employing the formula derived by Matsuo et al. [5] which is shown in Equation 10.1.

$$K_{max} = 0.01108\ i + 0.007825\ j \qquad \text{(Equation 10.1)}$$

The 0.01108 factor accommodates the natural abundances of ^{13}C and the 0.007825 factor corrects for the natural isotopes of hydrogen. The data derived from this equation agree with the experimental values observed in the FD mass spectrum of polystyrene 1700 (Figure 10.3).

10.3(ii) FD-MS of Poly(2,3,5,6-tetrafluoro-4-hydroxystyrene). The FD mass spectrum of poly(2,3,5,6-tetrafluoro-4-hydroxystyrene) (poly(TFHS)) (Figure 10.4) indicates that the degree of polymerisation is approximately 10. This is similar to data generated by GPC and other mass spectrometric techniques [16].

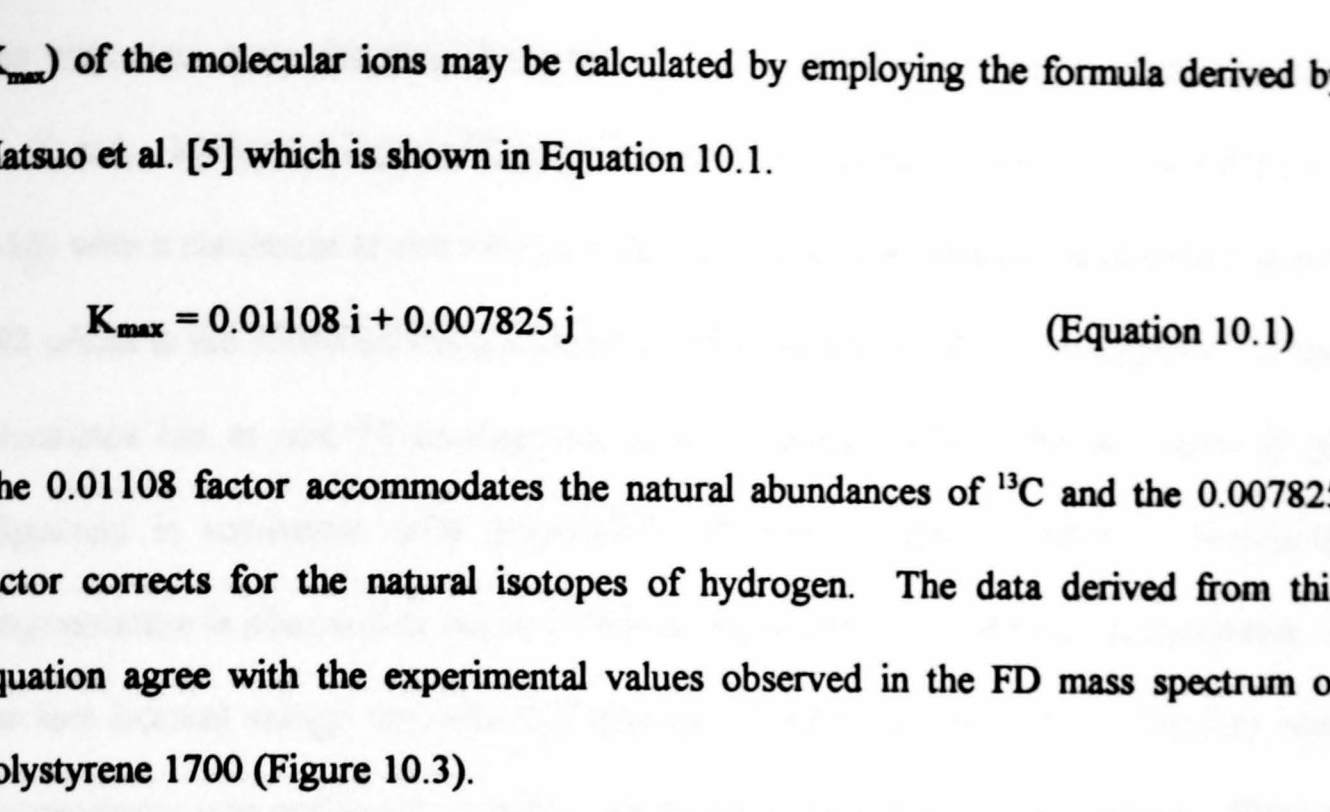

Figure 10.4.

FD-MS Spectrum of Poly(2,3,5,6-tetrafluoro-4-hydroxystyrene).

The oligomers were desorbed from the emitter at heating currents of approximately 30-60 mA. Molecular ions ($M^{+\cdot}$) are observed for oligomers with m/z 384-1921 (n = 2-10) with a maximum at m/z 576 (n = 3). A peak of low intensity is observed at m/z 192 which is the RMM of the monomer, 2,3,5,6-tetrafluoro-4-hydroxystyrene. A low abundance ion at m/z 72 corresponds to the solvent, THF. The m/z ratio of the oligomers is consistent with poly(TFHS) having a cyclic structure. Negligible fragmentation is observed in the spectrum as expected by FD-MS as a consequence of the low internal energy deposition during the ionisation process [17]. Tandem mass spectrometry was employed to obtain structural information for the polymer (Section 10.4).

10.3(iii) Pyrolysis-FI-MS of Polypropylene. The py-FI spectrum of polypropylene acquired over a temperature range of 350-450 °C is shown in Figure 10.5. This spectrum differs from that obtained by Lattimer [12] in that ions of pyrolyzates are observed at every carbon number in Figure 10.5 up to approximately m/z 2500. The spectrum generated by Lattimer was dominated by ions below m/z 1000 [12]. This phenomenon could be a consequence of the lower efficiency of the pyrolysis processes in the quartz tube of the direct insertion probe of the ZAB-T, where pyrolyzates are generated *in vacuo*.

Two main series of ions are observed in Figure 10.5 which were termed the A and E series by Lattimer [12]. The proposed structures of the A series of ions are shown in Figure 10.6.

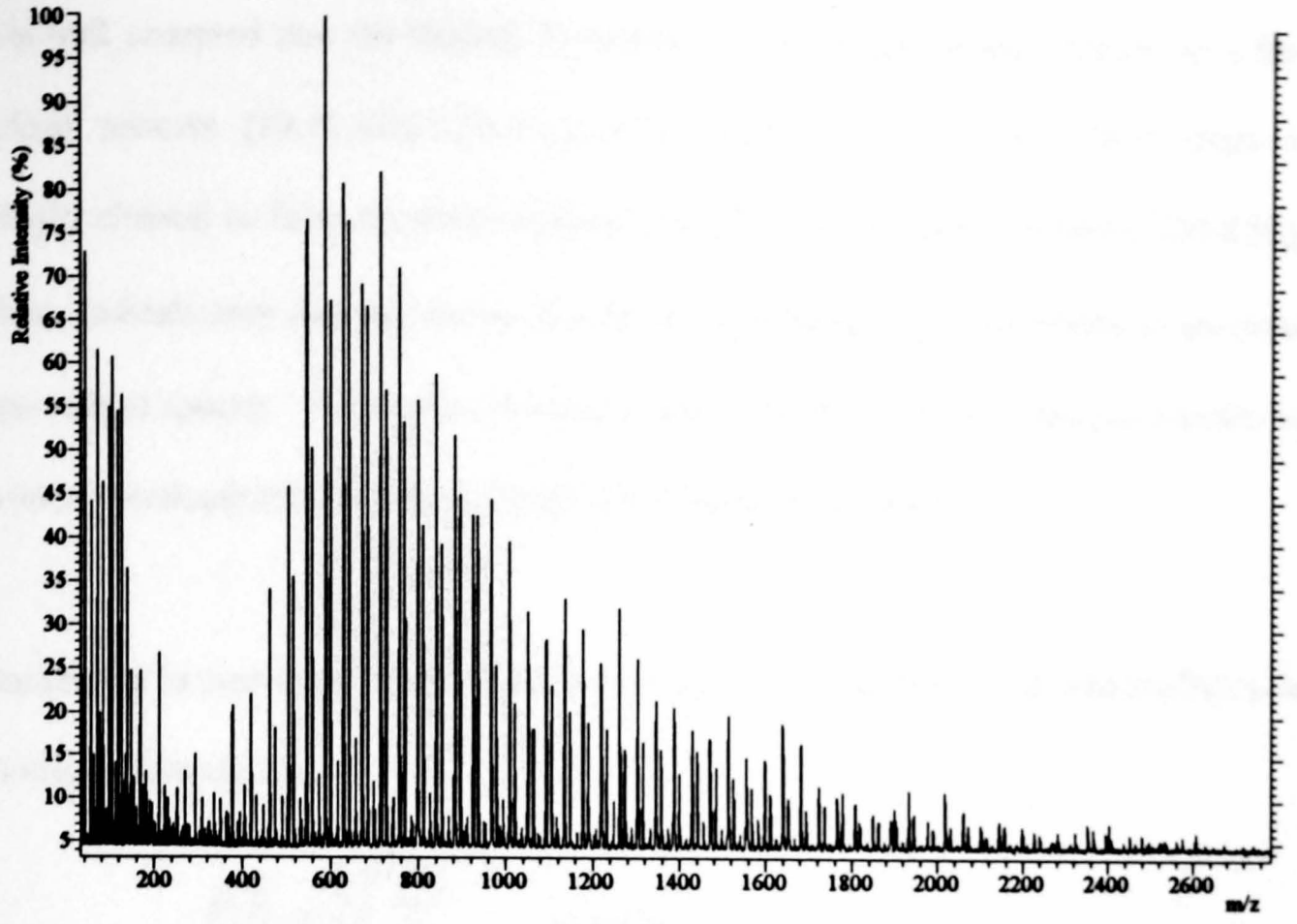

Figure 10.5.

Pyrolysis-FI-MS Spectrum of Polypropylene.

Structure I

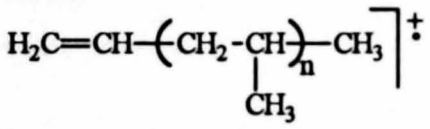

Structure II

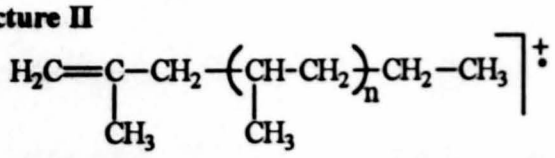

Figure 10.6.

Structures of the A Series of Ions from Pyrolysis-FI-MS of Polypropylene.

This series, which was only observed at low intensities above m/z 500 by Lattimer [12], is the dominant series in Figure 10.5 to greater than m/z 2000. The E series was observed at a much higher intensity than the A series in the spectrum of Lattimer [12] but is always of weaker intensity than the adjacent ions of the A series in Figure 10.5.

It is well accepted that the thermal decomposition of polypropylene occurs *via* a free radical process [18,19,20,21,22,23,24,25,26,27,28]. The polypropylene chain is initially cleaved to form a primary radical ($-CH_2^{\cdot}$) and a secondary radical ($-^{\cdot}CH-CH_3$). These radicals may decompose via β-scission or undergo rearrangements to generate new radical species. A common rearrangement process occurs by hydrogen transfer to produce predominantly tertiary radicals and is termed 'backbiting'.

'Backbiting' is presumed to occur preferentially via six-membered ring intermediates, as shown in Scheme 10.1.

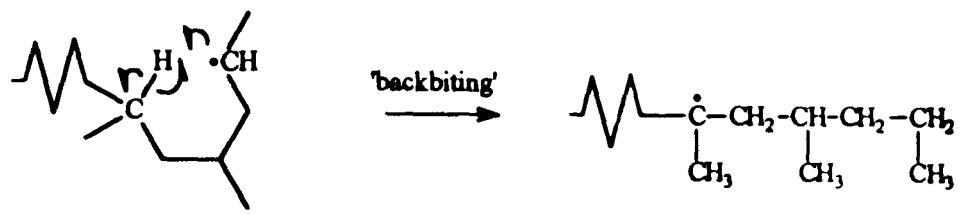

Scheme 10.1.
'Backbiting' Processes *via* a Six-Membered Ring Intermediate.

A 1,5-hydrogen transfer from a methine hydrogen to a secondary radical generates a pyrolyzate with a tertiary radical and a saturated end group. Transfer of a methine hydrogen is much more favoured than that of a methylene hydrogen due to the extra stability of the tertiary radical generated. Furthermore, the backbiting process may occur many times so that the site of the radical is distanced from the end of the chain.

The various proposed pathways of formation for ions of the A series are shown in Scheme 10.2 [12].

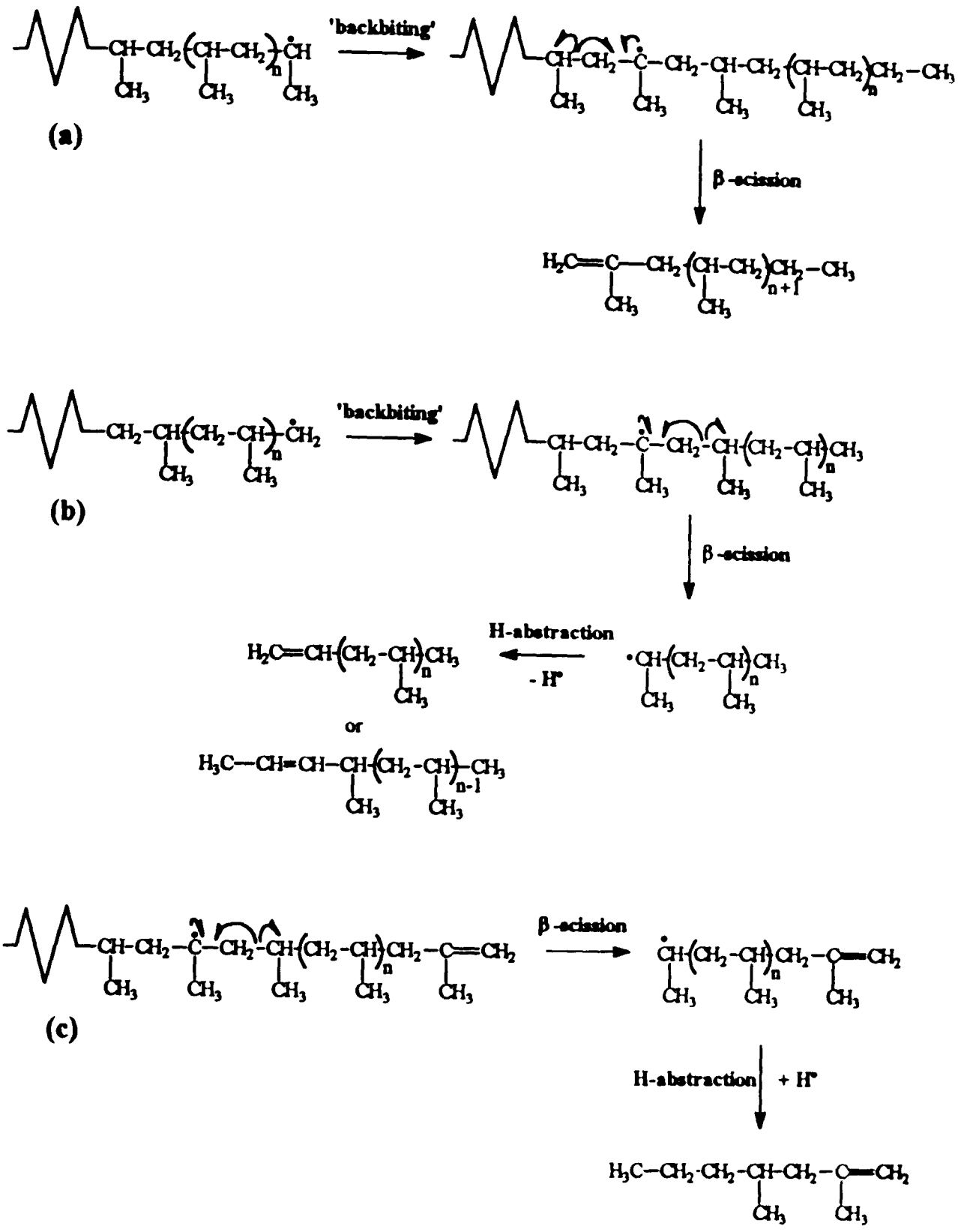

Scheme 10.2.

Pyrolysis Pathways of Polypropylene Generating Ions of the A Series.

All mechanisms involve initial generation of primary or secondary radical species which rearrange to form tertiary radicals by backbiting processes [12]. Subsequent β-scission produces the ions of the A series shown in Scheme 10.2(a) [12]. The tertiary radical

with an unsaturated group, which is an intermediate in the generation of ions of the A series in Scheme 10.2(c), is generated from the tertiary radical shown in 10.2(a) via β-scission. The unsaturated tertiary radical which is an intermediate in the process shown in Scheme 10.2(c) is also involved in the generation of ions from the E series. These ions have doubly unsaturated end groups as shown in Table 10.1. Furthermore, hydrogen abstraction subsequent to β-scission was proposed to be the mechanism for two possible pathways for generation of ions of the A series (Scheme 10.2(b) and (c)) [12]. These processes generate ions which have the same m/z ratios but differ in structure (Figure 10.6).

Four other series of ions of low intensity are observed at intensities lower than that of the A and E series and are termed the B, C, D, and F series [12]. Their RMM and proposed structures are shown in Table 10.1.

Series	RMM	Proposed Structure
B	$42_{(n+1)} + 14$	$H_2C{=}\underset{\displaystyle H_3C}{\overset{\displaystyle |}{C}}{-}\left(CH_2{-}\underset{\displaystyle CH_3}{\overset{\displaystyle |}{CH}}\right)_n{-}CH_3$
C	$42_{(n+1)} + 28$	$H_3C{-}CH{=}CH{-}\left(\underset{\displaystyle CH_3}{\overset{\displaystyle |}{CH}}{-}CH_2\right)_n{-}CH_3$
D	$42_{(n+1)} + 30$	$H_3C{-}CH_2{-}CH_2{-}\left(\underset{\displaystyle CH_3}{\overset{\displaystyle |}{CH}}{-}CH_2\right)_n{-}CH_3$
E	$42_{(n+2)} + 12$	$H_2C{=}\underset{\displaystyle H_3C}{\overset{\displaystyle |}{C}}{-}\left(CH_2{-}\underset{\displaystyle CH_3}{\overset{\displaystyle |}{CH}}\right)_n{-}CH_2{-}\underset{\displaystyle CH_3}{\overset{\displaystyle |}{C}}{=}CH_2$
F	$42_{(n+1)} + 40$	$H_2C{=}CH{-}\left(CH_2{-}\underset{\displaystyle CH_3}{\overset{\displaystyle |}{CH}}\right)_n{-}CH_2{-}\underset{\displaystyle CH_3}{\overset{\displaystyle |}{C}}{=}CH_2$

Table 10.1.

Proposed Structures and RMM of Pyrolyzates of Polypropylene Observed in the Py-FI Mass Spectrum.

The B, C and D series are observed as ions from pyrolyzates at low m/z ratios whereas ions of the F series are only seen at greater than m/z 400. The E and F series are both doubly unsaturated pyrolyzates that are observed only at higher m/z ratios and are generated from singly unsaturated tertiary radicals. Furthermore, it was noted that ions of the E and F series are observed only at lower heating temperatures and that the py-FI experiment was able to detect these ions due to the soft ionisation by FI, the in-source sample heating and the short distance between the pyrolysis crucible and the point of ionisation at the field emitter [12]. These higher RMM pyrolyzates were not observed in earlier polypropylene pyrolysis studies [15,16,17,18,19,20,21,22,23,24, 25].

10.4. FD and Pyrolysis-FI-MS/MS of Polymers.

10.4(i) FD-MS/MS of Polystyrene 1700. The CID spectrum of the 11-mer from polystyrene, m/z 1203, is shown in Figure 10.7. The emitter current required for desorption of the oligomer was 38-40 mA. This anode temperature generated intense and stable molecular ions for the 11-mer. Furthermore, occasional sparks in the source generated increased ion signals from the precursor ion and hence improved fragment ion abundances also. Approximately 30 scans were summed to generate the spectrum shown in Figure 10.7. The CID spectrum of the m/z 1307 oligomer of polystyrene 1700 (Figure 10.8), obtained at emitter heating currents of 40-42 mA, is very similar to that of the m/z 1203 oligomer.

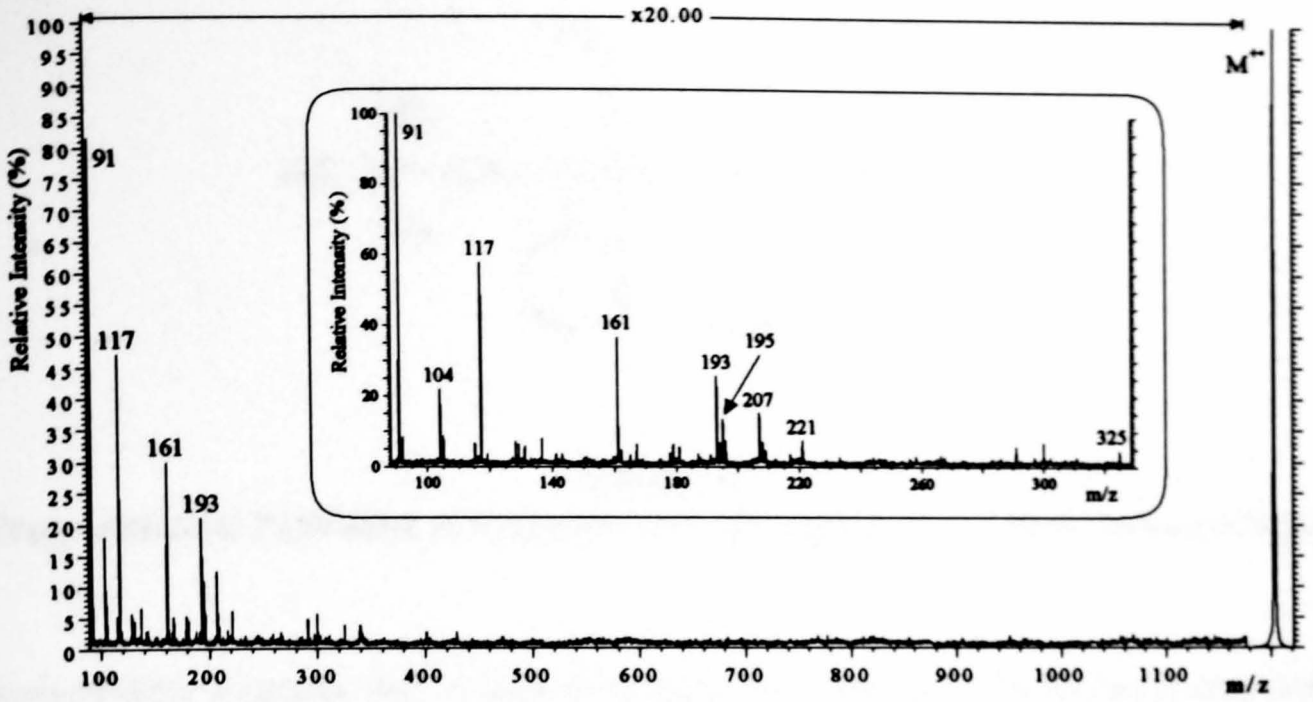

Figure 10.7.

FD-MS/MS Spectrum of Polystyrene 1700, $M^{+\cdot}$ m/z 1203. The m/z 80-330 Region of the Spectrum is Expanded.

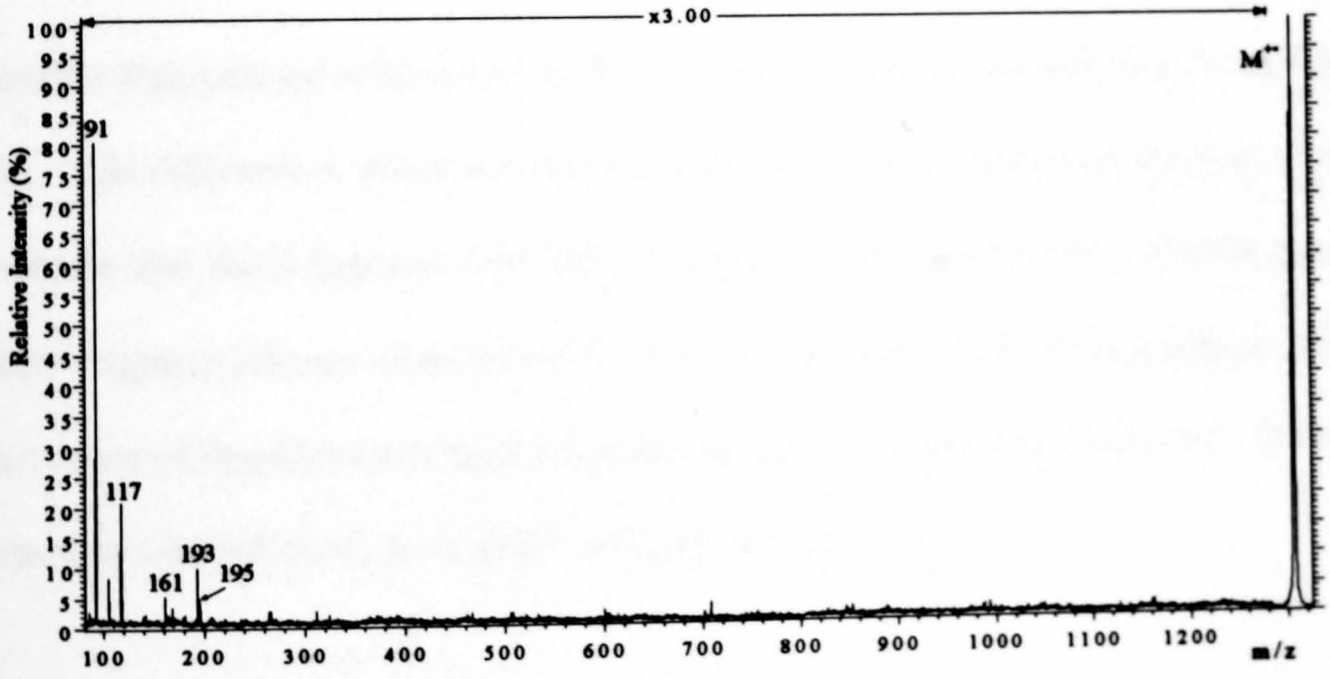

Figure 10.8.

FD-MS/MS Spectrum of Polystyrene 1700, $M^{+\cdot}$ m/z 1307.

Two of the fragment ions, at m/z 91 and m/z 161, aid the confirmation of the end groups of the polymer (see Figure 10.9).

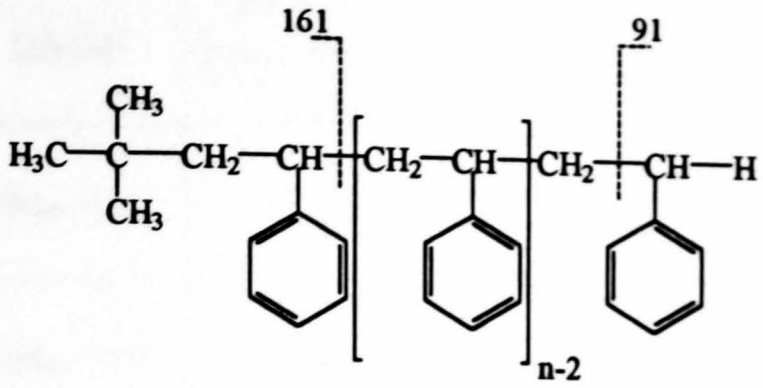

Figure 10.9.

Fragmentation Pathways of Polystyrene 1700 Aiding End Group Determination.

Each of these fragment ions is formed by homolytic cleavage of a carbon-carbon bond in the backbone of the polymer, β-cleavage to the phenyl ring. The product ion at m/z 91 is presumed to be a tropylium ion, $C_7H_7^+$, the structure of which is well documented in the literature [29,30].

Another fragment ion is observed at m/z 195 which is 104 Da greater than the m/z 91 ion. This difference is the mass of the repeat unit of the polymer and therefore it is probable that these fragment ions differ in structure by a styrene unit. Furthermore, other fragment ions are observed which differ by the repeat unit of the polymer. The m/z ratios of these ions and their proposed structures are given in Table 10.2. These ions were labelled the C, D, E and F series by Craig et al. [10].

The C and D series include the m/z 91, 195 and 161 fragment ions, the generation of which is described above. The E series was proposed to be generated by loss of benzene from ions of the C series [10]. The expulsion of benzene is probably by a 1,3-hydrogen rearrangement from a methylene carbon of the polymer backbone to the tertiary carbon of the phenyl ring.

Series	RMM	Observed Fragment Ions (m/z)	Proposed Structure
C	104n + 91	91, 195	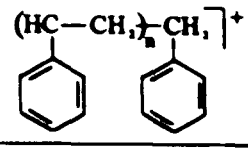
D	104n + 57	161	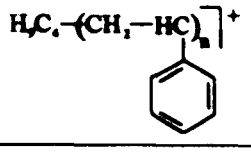
E	104n + 13	117, 221, 325	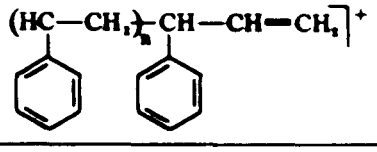
F	104n	104, 208	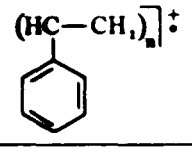

Table 10.2.

Structures and RMM of the C, D, E and F Series of Fragment Ions Observed in Product Ion Spectra of Polystyrene.

The fragment ions observed in CID spectra of polystyrene were proposed to be generated by initial random chain scission followed by depolymerisation reactions [10]. Depolymerisation reactions involve the expulsion of styrene units from the initially generated fragments of the precursor ion. These reactions were proposed to be an approximately thermoneutral process and hence go to near completion, which explains the predominance of fragment ions at low m/z ratios. Furthermore, the generation of fragment ions at m/z 104 and 208 (F series, Table 10.2) may be rationalised by charge retention at these fragments during depolymerisation reactions.

The fragment ions generated are predominantly observed at less than m/z 300. This phenomenon is similar to that observed by Craig et al. [10] in the MIKES-CID spectra from radical cation precursor ions of polystyrene oligomers. Collision induced dissociation of polystyrene ion was proposed to occur *via* multiple consecutive

reactions [10]. This mechanism is different from that which was proposed by Lattimer [31] for CID of polyglycols in which the preference for cleavage was near chain ends. No explanation was given, however, for this preference.

The lack of fragment ions at m/z above 500 from polymers in CID experiments from $M^{+\bullet}$ precursor ions is different to that observed from cationated species (Chapter 9). The fragment ions in CID spectra observed from cationated precursor ions $[M+Ag]^+$ of polystyrene result from both random initial chain scission followed by depolymerisation and by rearrangement processes. The rearrangement reactions are similar to those proposed for the unimolecular dissociation of polystyrene radical cations [32].

10.4(ii) FD-MS/MS of Poly(2,3,5,6-tetrafluoro-4-hydroxystyrene). The product ion spectrum of the m/z 576 oligomer (n = 3) of poly(TFHS) is shown in Figure 10.10.

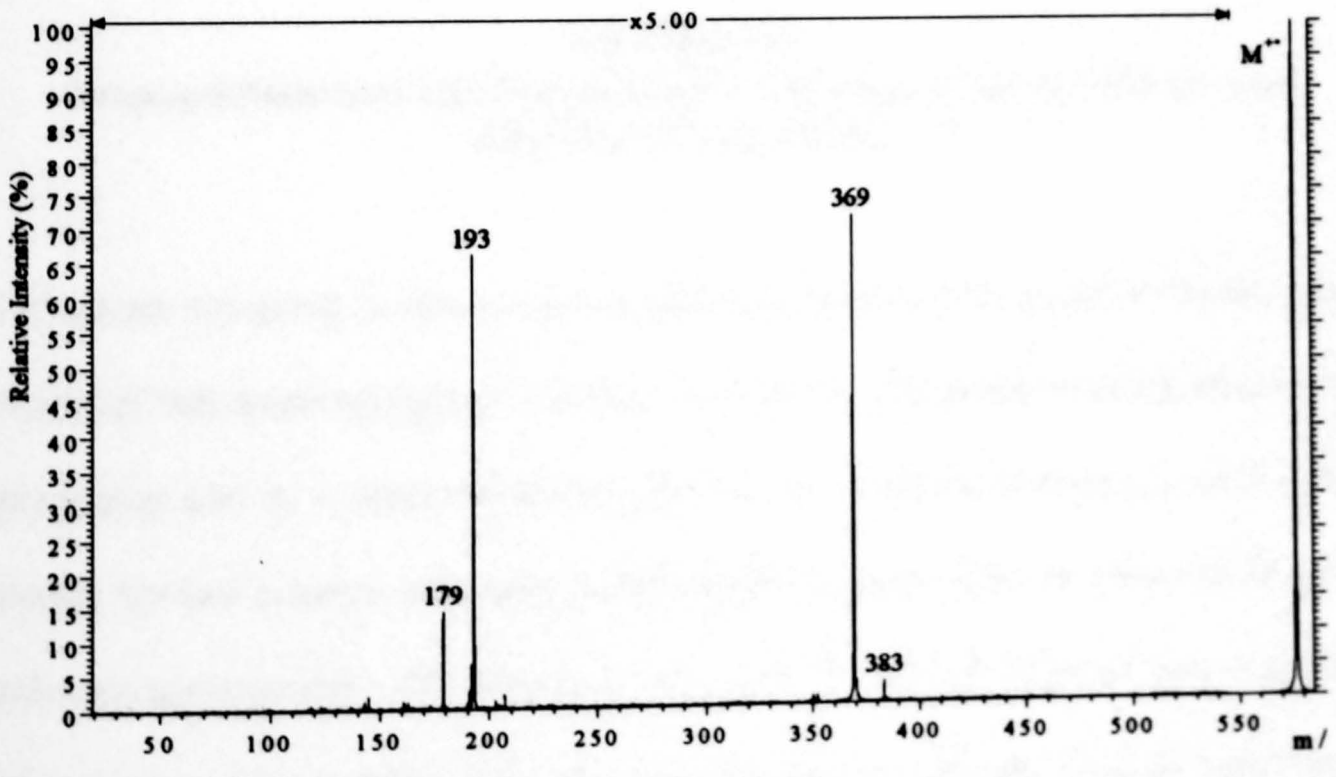

Figure 10.10.

FD-MS/MS Spectrum of Poly(2,3,5,6-tetrafluoro-4-hydroxystyrene), $M^{+\bullet}$ m/z 576.

The emitter currents employed were 35-38 mA. Abundant fragment ions are observed at m/z 179, 191, 193, 369 and 383. This series of fragment ions is not consistent with the polymer having the cyclic structure originally proposed. A linear structure with either a ketone or styrenyl end group is consistent with the fragmentation pathways observed. It is unlikely that poly(TFHS) contains a styrenyl end group, however, as the polymer is formed by coupling reactions between chain radicals [33]. A more probable structure for the m/z 576 oligomer with a ketone end group is shown in Scheme 10.3 with the proposed fragmentation pathways.

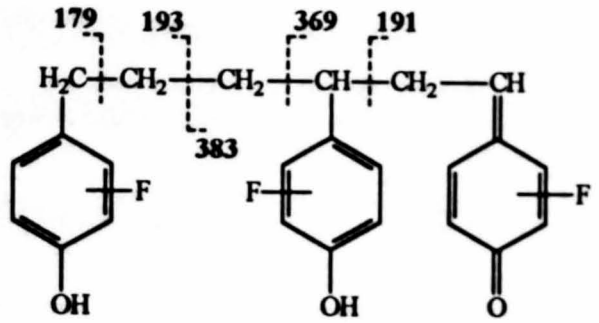

Scheme 10.3.

Proposed Structure and Fragmentation Pathways of the m/z 576 (n = 3) Oligomer of Poly(TFHS).

The ketone end group is also consistent with data generated by means of NMR which suggested that an alkenyl group is present in solution. The presence of the ketone end group may also be a factor in limiting the degree of polymerisation [33] and hence explain the low average molecular weight of the polymer which is observed by GPC and mass spectrometry. The intensity of the m/z 179 and 369 fragment ions may be a consequence of the stability of the species generated by cleavage β to the substituted benzene ring. The most abundant ions in the CID spectra generated from molecular ions of polystyrene also occur via cleavage β to the benzene ring. There were no

observed losses of 2,3,5,6-tetrafluorophenol from fragment ions of poly(TFHS), however, which would be analogous to the loss of benzene from product ions of polystyrene. This may be a consequence of the greater steric hinderance to hydrogen rearrangements, which are required for the loss of benzene from polystyrene, in poly(TFHS). All fragment ions may be generated by chain scission and/or initial cleavage further along the backbone of the polymer followed by depolymerisation reactions, as proposed for the fragmentation of polystyrene by means of CID [10].

The m/z 179, 193, 369 and 383 fragment ions are also observed in the product ion spectrum from the m/z 1152 oligomer (n = 6) of poly(TFHS), generated at an emitter heating current of 42-45 mA (Figure 10.11). These fragment ions are consistent with a general structure for the polymer which is shown in Figure 10.12.

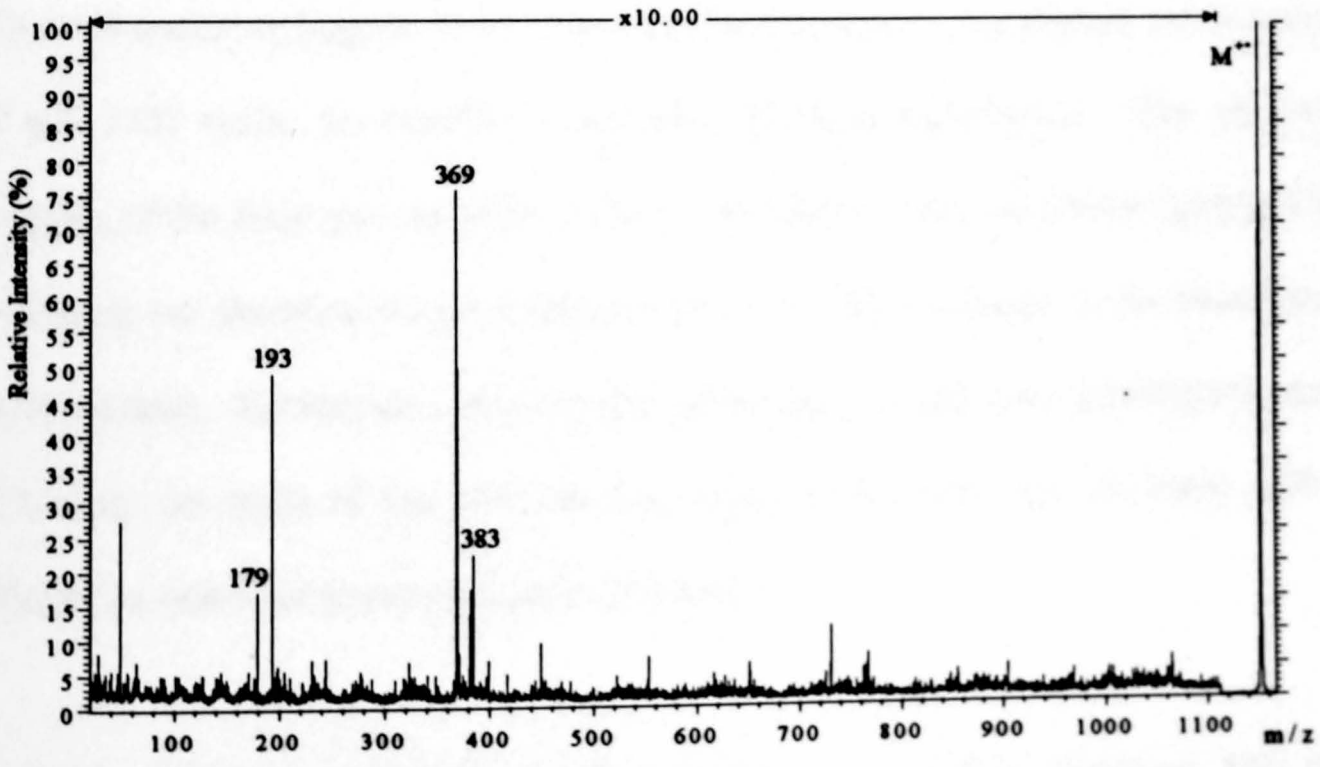

Figure 10.11.

FD-MS/MS Spectrum of Poly(2,3,5,6-tetrafluoro-4-hydroxystyrene), $M^{+\bullet}$ m/z 1152.

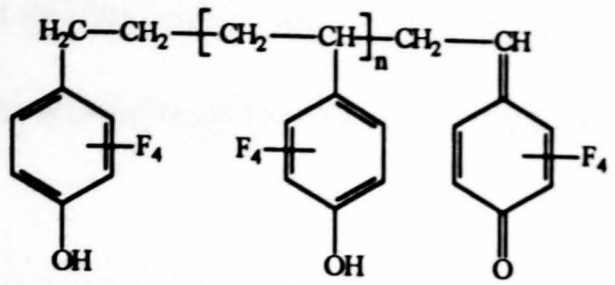

Figure 10.12.
The proposed Structure of Poly(TFHS).

The dominant fragment ions were observed at low m/z ratios. This phenomenon is similar to that seen in product ion spectra of polystyrene. This indicates that fragmentation pathways either involve initial random cleavage of the polymer backbone followed by depolymerisation [10] or scission near to chain ends [31].

The low intensity of fragment ion peaks observed in the spectrum from the m/z 1152 oligomer is a consequence of the low abundance of the precursor ion, as seen in the FD mass spectrum (Figure 10.4). The noise level is high in the product ion spectrum of m/z 1152 under the conditions employed for these experiments. The observed intensity of the fragment ion peaks at the array detector may have been improved by increasing the electrical potential between the microchannel plates of the photodiode array detector. Furthermore, the detection efficiency may also have been improved by increasing the angle of the microchannel plates to the incoming ion beam with a concurrent reduction in the resolution obtainable.

10.4(iii) Pyrolysis-FI-MS/MS of Polypropylene. It would be expected from the pyrolysis fragmentation pathways proposed by Lattimer that the fragment ion spectrum of an ion from a pyrolyzate of the A series of polypropylene would indicate the

presence of two different structures for these ions. The CID spectrum of the m/z 756 pyrolyzate of the A series of polypropylene is shown in Figure 10.13.

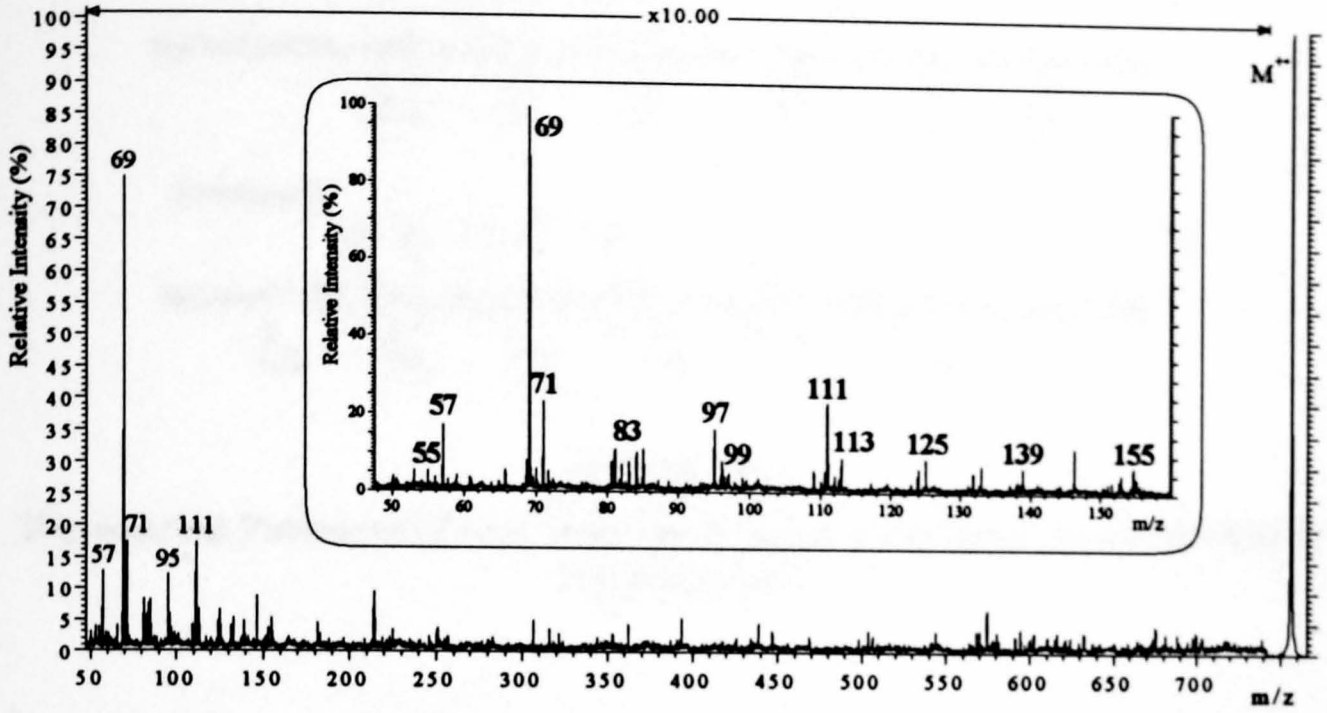

Figure 10.13.

Pyrolysis-FI-MS/MS Spectrum of Polypropylene, $M^{+\bullet}$ m/z 756 of the A Series.

A poor signal-to-noise ratio is observed in the fragment ion spectrum as a consequence of the low ion currents generated from pyrolyzates of polypropylene. Approximately 30 scans were summed to obtain the spectrum shown in Figure 10.13. The fragment ions observed are consistent with the two proposed structures for the A series as shown in Scheme 10.4, which also shows the dissociation pathways of the pyrolyzates subsequent to collisional activation.

Various series of ions are observed in the fragment ion spectrum that differ in m/z ratios by a polypropylene monomer unit. All fragment ions observed in the CID spectrum are generated by simple cleavage of the backbone of the pyrolyzate. A

preference for generation of fragment ions with alkene end groups is observed (Scheme 10.4).

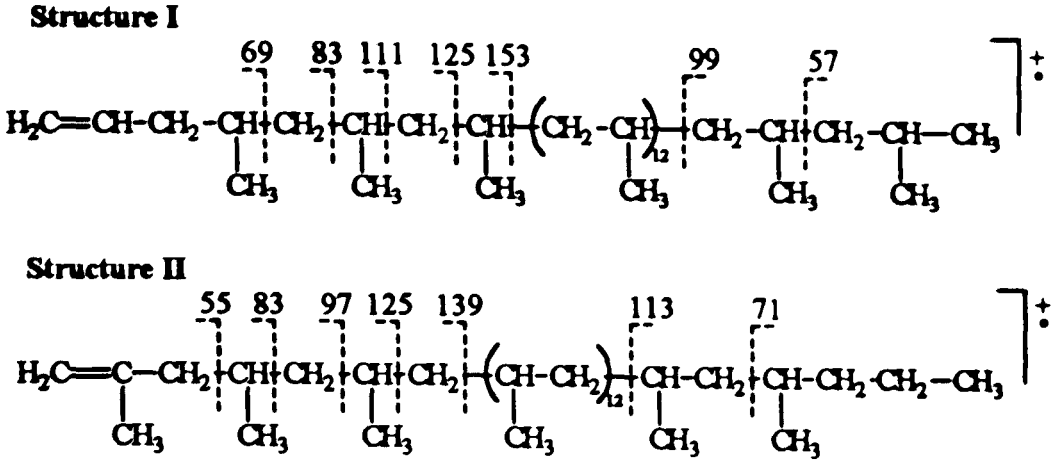

Scheme 10.4.

Dissociation Pathways of Ions from the A Series from Pyrolysis-FI-MS/MS of Polypropylene.

The fragment ions are again observed predominantly at low m/z ratios. This indicates that to generate the fragment ions that are seen in the spectrum, the cleavage of pyrolyzates either occurs near chain ends [31] or that random chain scission is followed by depolymerisation [10].

10.4(d) FD-MS/MS of Polymer Additives. The FD-MS/MS spectra of the molecular ions $M^{+\bullet}$ of Irganox 1076 (Figure 10.14) and Irganox 1010 (Figure 10.15), from an equimolar mixture of polymer additives, are similar to those generated by means of LSIMS-MS/MS (see Chapter 7.3). The characteristic fragment ions observed in the LSIMS-MS/MS spectra from Irganox compounds, such as the ions appearing at m/z 219 and 203, are also found in the FD-MS/MS spectra. These ions aid confirmation of the structure of the polymer additive selected. The signal-to-noise ratio is lower, however, in the FD-MS/MS spectra when compared to that observed in the respective

LSIMS-MS/MS spectra. Furthermore, some of the less abundant fragment ions seen in the LSIMS-product ion spectra are not observed in the respective FD spectra.

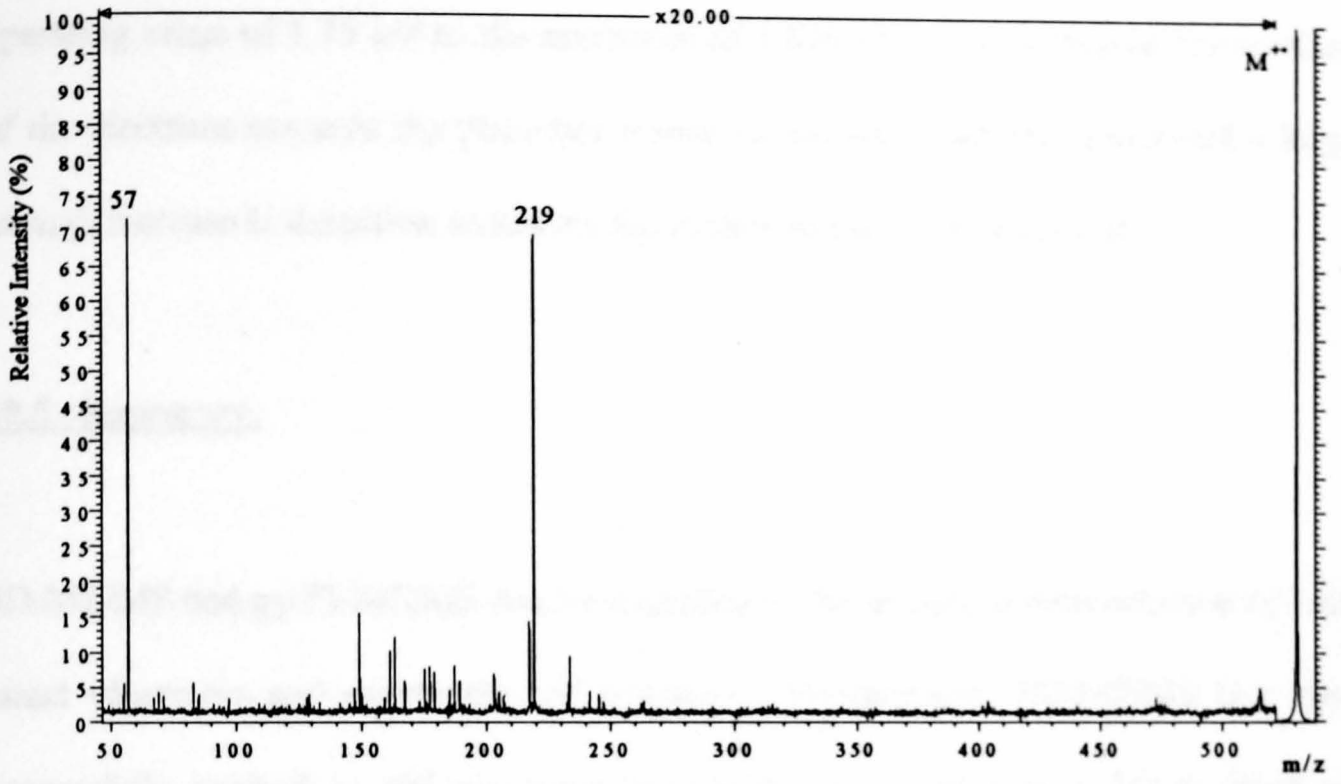

Figure 10.14.

FD-MS/MS Spectrum of Irganox 1076, $M^{+\bullet}$ m/z 530.

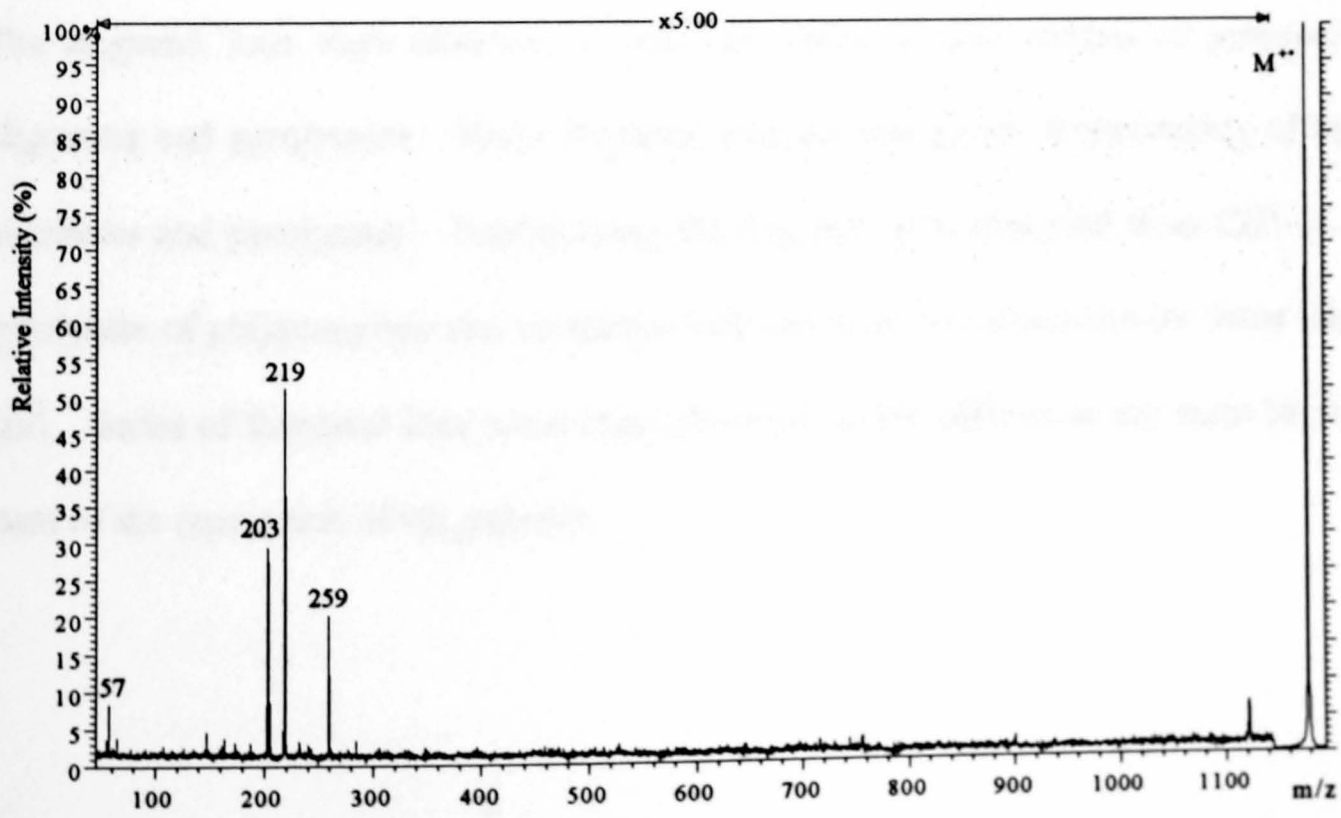

Figure 10.15.

FD-MS/MS Spectrum of Irganox 1010, $M^{+\bullet}$ m/z 1177.

The fragment ions were observed only in the FD-MS/MS spectra from the equimolar mixture of polymer additives when the electrical potential held between the microchannel plates of the photodiode array detector was increased from the normal operating value of 1.75 kV to the maximum of 1.875 kV. The increased acceleration of the electrons towards the phosphor screen of the array detector generated a large enough increase in detection sensitivity for improved data to be acquired.

10.5. Summary.

FD-MS/MS and py-FI-MS/MS has been applied to the structural determination of both intact oligomers and pyrolyzates of polymers. Furthermore, FD-MS/MS has been successfully applied to aid structural determination of polymer additives from an equimolar mixture.

The fragment ions were observed at low m/z ratios in CID spectra of polymeric oligomers and pyrolyzates. These fragment ions aid end group determination of the oligomers and pyrolyzates. Furthermore, the fragment ions observed from CID of a pyrolyzate of polypropylene are consistent with the proposed structures for these ions [10]. Series of fragment ions were often observed which differed in m/z ratio by the mass of the repeat unit of the polymer.

1 R. P. Lattimer and H.-R. Schulten, *Int. J. Mass Spectrom. Ion Phys.*, **52**, 105 (1983).

2 R. P. Lattimer and G. E. Hansen, *Macromolecules*, **14**, 776 (1981).

3 H.-R. Schulten and R. P. Lattimer, *Mass Spectrom. Rev.*, **3**, 231 (1984).

4 R. P. Lattimer, D. J. Harmon and K. R. Welch, *Anal. Chem.*, **51**, 1293 (1979).

5 T. Matsuo, H. Matsuda and I. Katakuse, *Anal. Chem.*, **51**, 1331 (1979).

6 R. P. Lattimer, D. J. Harmon and G. E. Hansen, *Anal. Chem.*, **52**, 1808 (1980).

7 J. Saito, S. Toda and S. Tanaka, *Bunseki Kagaku*, **30**, 706 (1981).

8 A. I. Tottszer, G. M. Neumann, P. J. Derrick and G. D. Willett, *J. Phys. D: Appl. Phys.*, **21**, 1713 (1988).

9 K. Rollins, J. H. Scrivens, M. J. Taylor and H. Major, *Rapid Commun. Mass Spectrom.*, **4**, 355 (1990).

10 A. G. Craig and P. J. Derrick, *Aust. J. Chem.*, **39**, 1421 (1986).

11 B. Plage, H.-R. Schulten, J. Schneider and H. Ringsdorf, *Macromolecules*, **23**, 3417 (1990).

12 R. P. Lattimer, *J. Anal. Appl. Pyrolysis*, **26**, 65 (1993).

13 E. M. Pearce and T. K. Kwei, *J. Macromol. Sci., Chem.*, **A28**, 1207 (1991).

14 P. J. Derrick, *Fresnius' Z. Anal. Chem.*, **324**, 486 (1986).

15 S. C. Davis, V. Natoli, G. M. Neumann and P. J. Derrick, *Int. J. Mass Spectrom. Ion Proc.*, **78**, 17 (1987).

16 M. J. Taylor, PhD Thesis, University of Wales Swansea, U.K. (1995).

17 W. Brand and K. Levsen, *Int. J. Mass Spectrom. Ion Phys.*, **35**, 1 (1980).

18 S. L. Madorsky, *Thermal Degradation of Organic Polymers*, Wiley, New York, (1964).

19 Y. Tsuchiya and K. Sumi, *J. Polym. Sci., Part A-1*, 7, 1599 (1969).

20 D. O. Hummel, H.-D. Schueddemage and K. Ruebenacker, in *Polymer Spectroscopy* (D. O. Hummel, Ed.), Verlag Chemie, Weinheim (1974).

21 E. Kiran and J. K. Gillham, *J. Appl. Polym. Sci.*, **20**, 2045 (1976).

22 J. K. Y. Kiang, P. C. Uden and J. C. W. Chien, *Polym. Deg. Stab.*, **2**, 113 (1980).

23 T. Szekely, F. Till, G. Varhegyi and M. Blaszo, *J. Polym. Sci., Polym. Symp.*, **67**, 115 (1980).

24 M. T. Sousa Pessoa de Amorim, C. Comel and P. Vermande, *J. Anal. Appl. Pyrolysis*, **4**, 73 (1982).

25 M. Ishiwatari, *J. Polym. Sci., Polym. Lett. Ed.*, **22**, 83 (1984).

26 H. Ohtani, S. Tsuge, T. Ogawa and H.-G. Elias, *Macromolecules*, **17**, 465 (1984).

27 T. Szekely, G. Varhegyi, F. Till, P. Szabo and E. Jakab, *J. Anal. Appl. Pyrolysis*, **11**, 83 (1987).

28 T. Kojima, *Mem. Natl. Def. Acad., Math., Phys., Chem. Eng.*, **28**, 139 (1989).

29 P. N. Rylander, S. Meyerson and H. M. Grubb, *J. Am. Chem. Soc.*, **79**, 842 (1957).

30 C. Lifshitz, *Acc. Chem. Res.*, **27**, 138 (1994).

31 R. P. Lattimer, *J. Am. Soc. Mass. Spectrom.*, **5**, 1072 (1994).

32 A. G. Craig and P. J. Derrick, *J. Am. Chem. Soc.*, **107**, 6707 (1985).

33 Personal communication.

CHAPTER 11.

CONCLUSIONS AND FUTURE WORK.

11.1. SID of Peptides.

Sequence information was generated by means of SID for four peptides that differed only in the residue at the C-terminus. It would be problematical to generate fragment ion spectra for polymeric materials from this technique as a consequence of the relatively low ion currents that are generally generated for these compounds by FD and LSIMS ionisation. The low collection efficiency of fragment ions after collision with the surface and ion neutralisation on collision with the surface may account for the low fragment ion currents that were observed. Increasing the angle of collision and therefore reducing the ion neutralisation may increase the overall efficiency of the SID process in the four sector mass spectrometer. Furthermore, employing a liquid perfluoropolyether or a surface assembled monolayer surface may also induce higher relative fragment ion currents.

11.2. Comparison of High and Low Energy CID of Polymer Additives.

The MS/MS spectra of the same polymer additive often differ greatly in the high and low energy regimes. Low energy spectra are dominated by peaks arising from hydrogen rearrangements whereas direct cleavages are more favoured in high energy experiments. The fragment ions observed in the high energy MS/MS spectra are often characteristic of the type of polymer additive whereas the peaks seen in low energy experiments are highly dependent on the collision energy employed.

The conclusion drawn from these experiments is that the ideal methodology for the mass spectrometric analysis of polymer additives is a FD mass spectrum of the mixture and LSIMS-MS/MS of the ions observed. A reasonable quantitative picture is generated by means of FD ionisation as there are no matrix effects. LSIMS-MS/MS aids structural elucidation as characteristic fragmentation is often observed in the spectra.

11.3. MALDI of Polymers.

UV-MALDI spectra of some PMMA and polystyrene standards have been shown to give average mass values of these polymers. Molecular ions were observed with no fragmentation. Most of the polymers employed, however, had low polydispersity values and it is more problematical to generate UV-MALDI spectra when samples of high polydispersity are used. This may be a consequence of the inhomogeneity in the sample-matrix-salt lattice. Improvements in sample preparation procedures may lead to greater reproducibility. Polymers with high polydispersity values may also be more fully characterised by means of GPC-MALDI-MS.

11.4. CID of Oligomeric Ions of Polymers.

MS/MS spectra have been shown to generate end group information and structural information of polymers. Fragment ion peaks are generally observed at low m/z values in the CID experiments. Peaks arising from cleavages of the polymer nearer to the centre of the polymer backbone are seen when cationated precursors are employed

APPENDIX A.

EI-MS AND LSIMS-MS SPECTRA OF POLYMER ADDITIVES.

The EI-MS AND LSIMS-MS spectra of Tinuvin 327, Irganox 3114, Hostanox 03 and Irganox 1010 are shown below. The conditions used were the same as stated in Section 7.2.

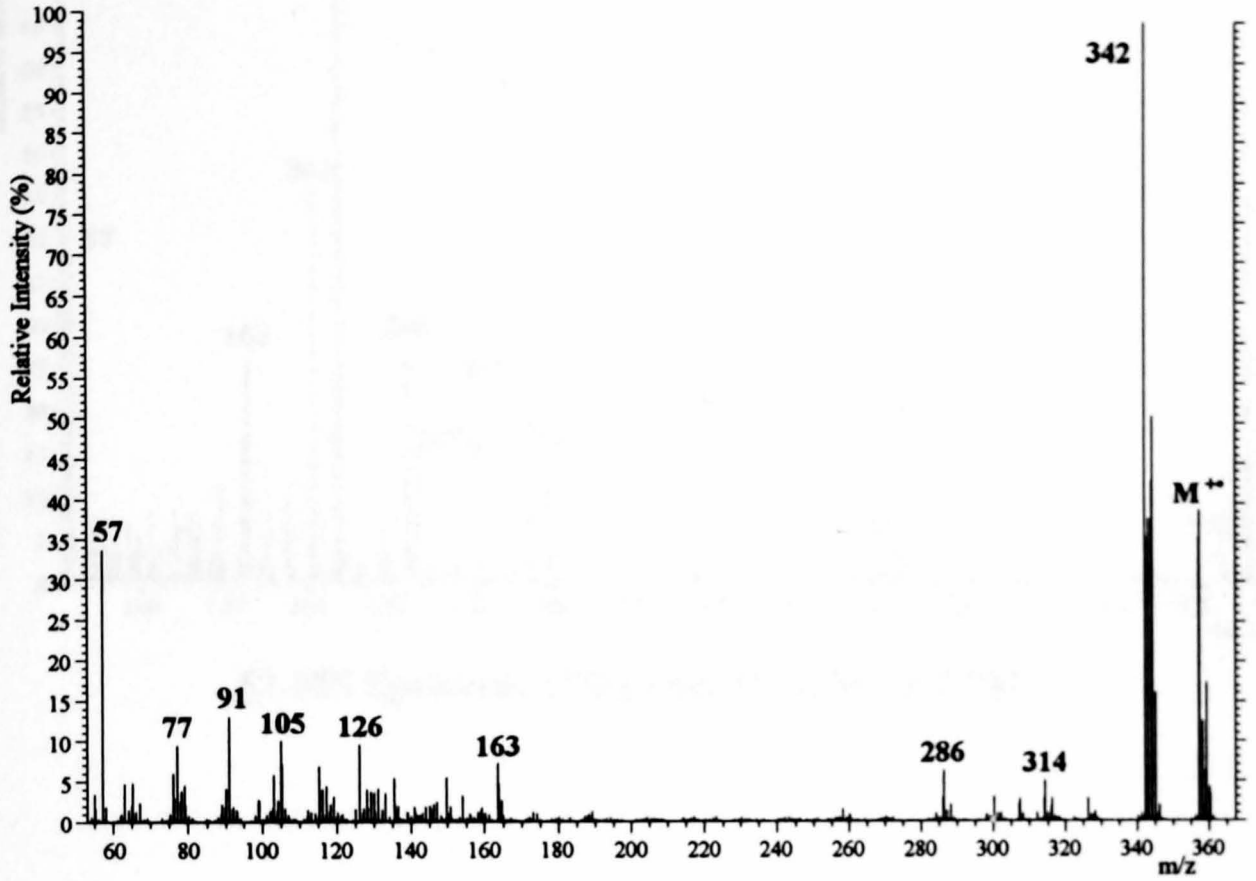

EI-MS Spectrum of Tinuvin 327, $M^{+\bullet}$ m/z 357.

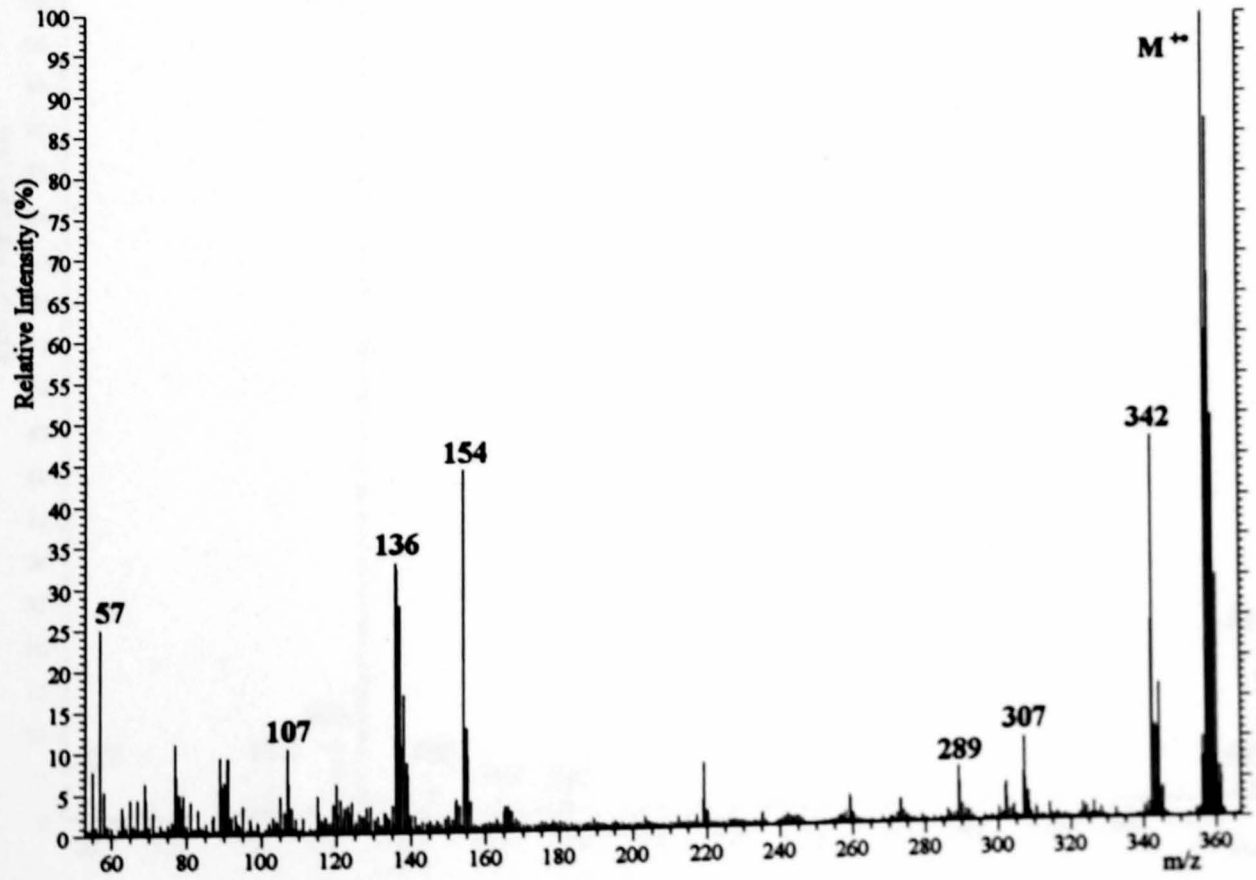

LSIMS-MS Spectrum of Tinuvin 327, $M^{+\bullet}$ m/z 357.

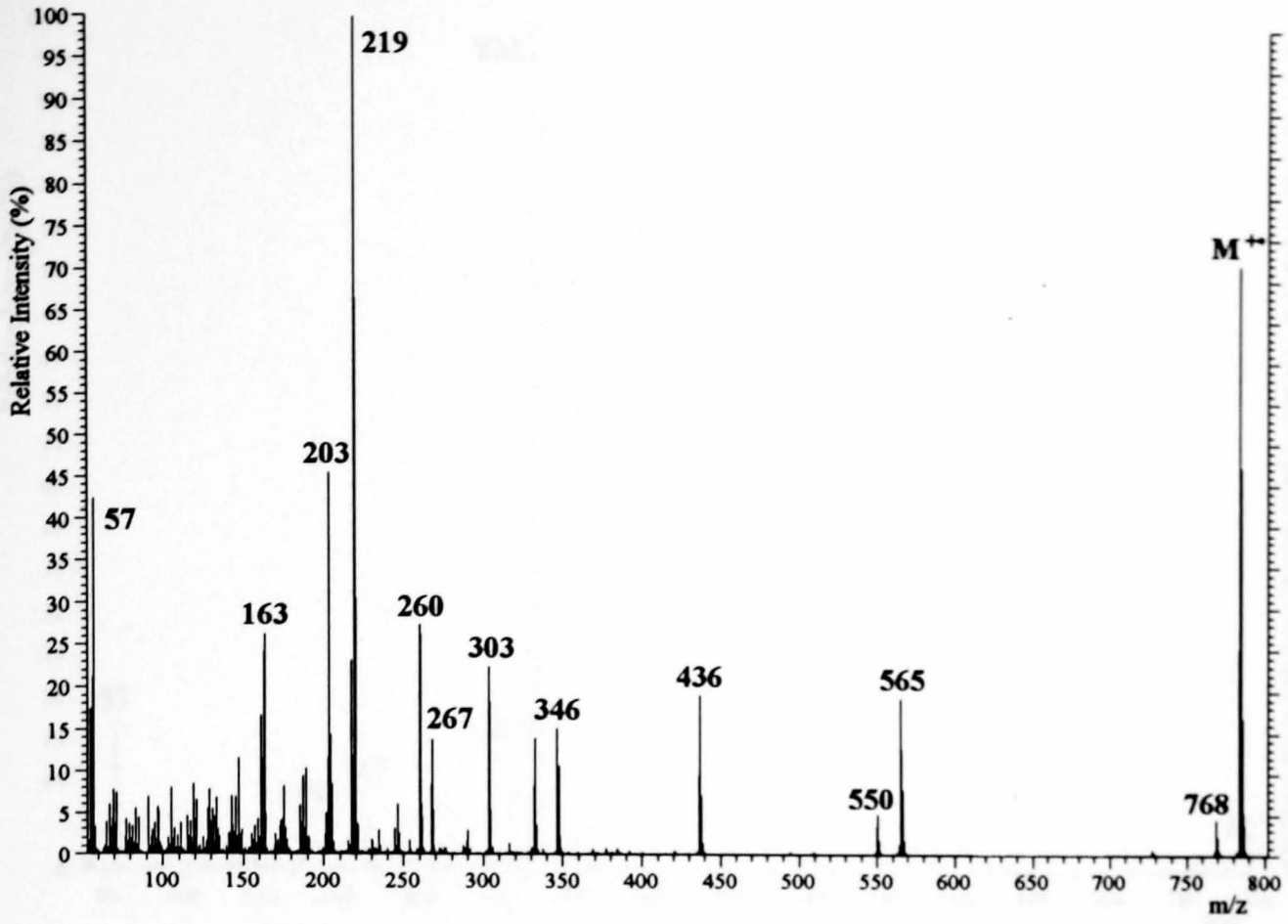

EI-MS Spectrum of Irganox 3114, $M^{+\bullet}$ m/z 783.

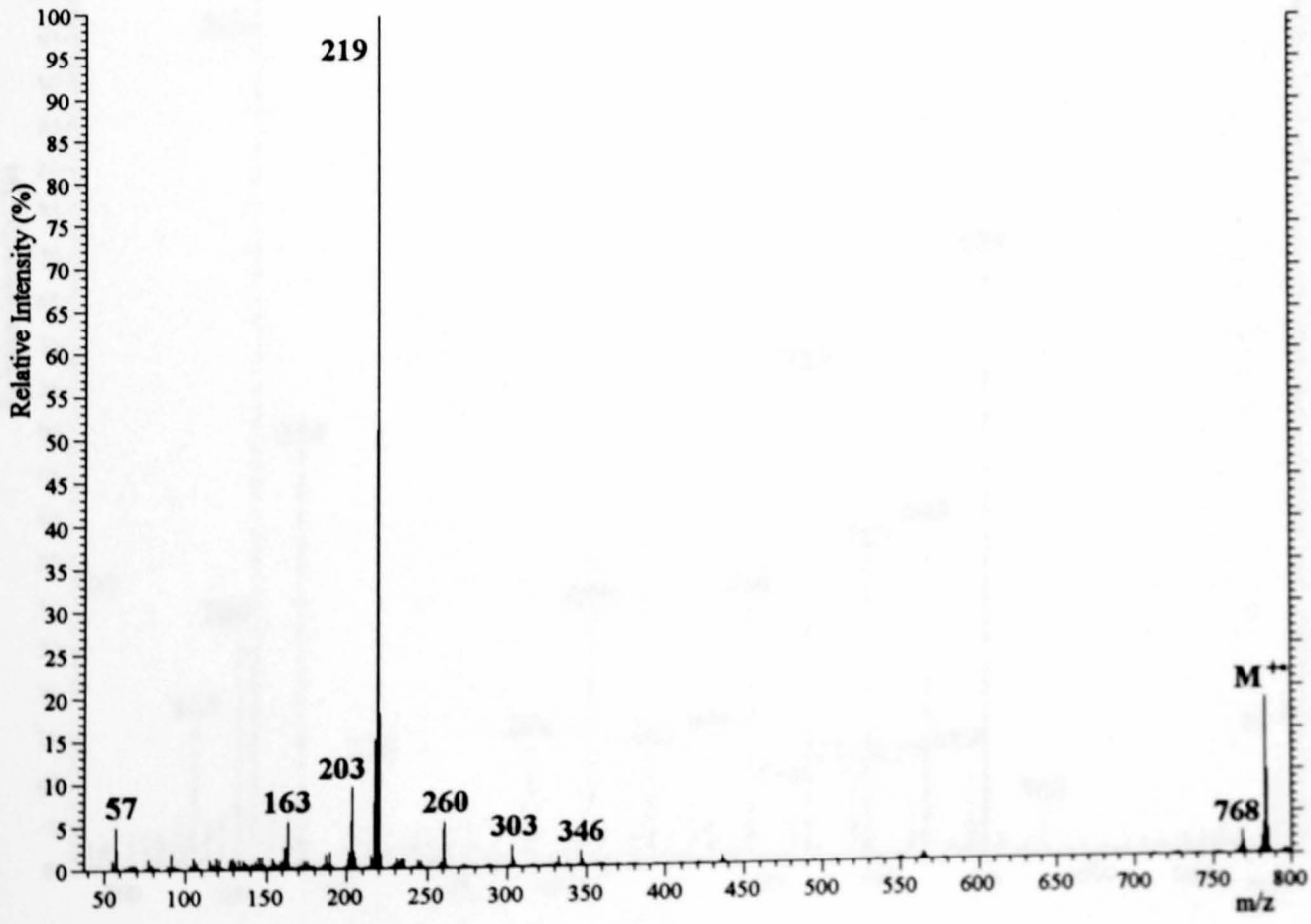

LSIMS-MS Spectrum of Irganox 3114, $M^{+\bullet}$ m/z 783.

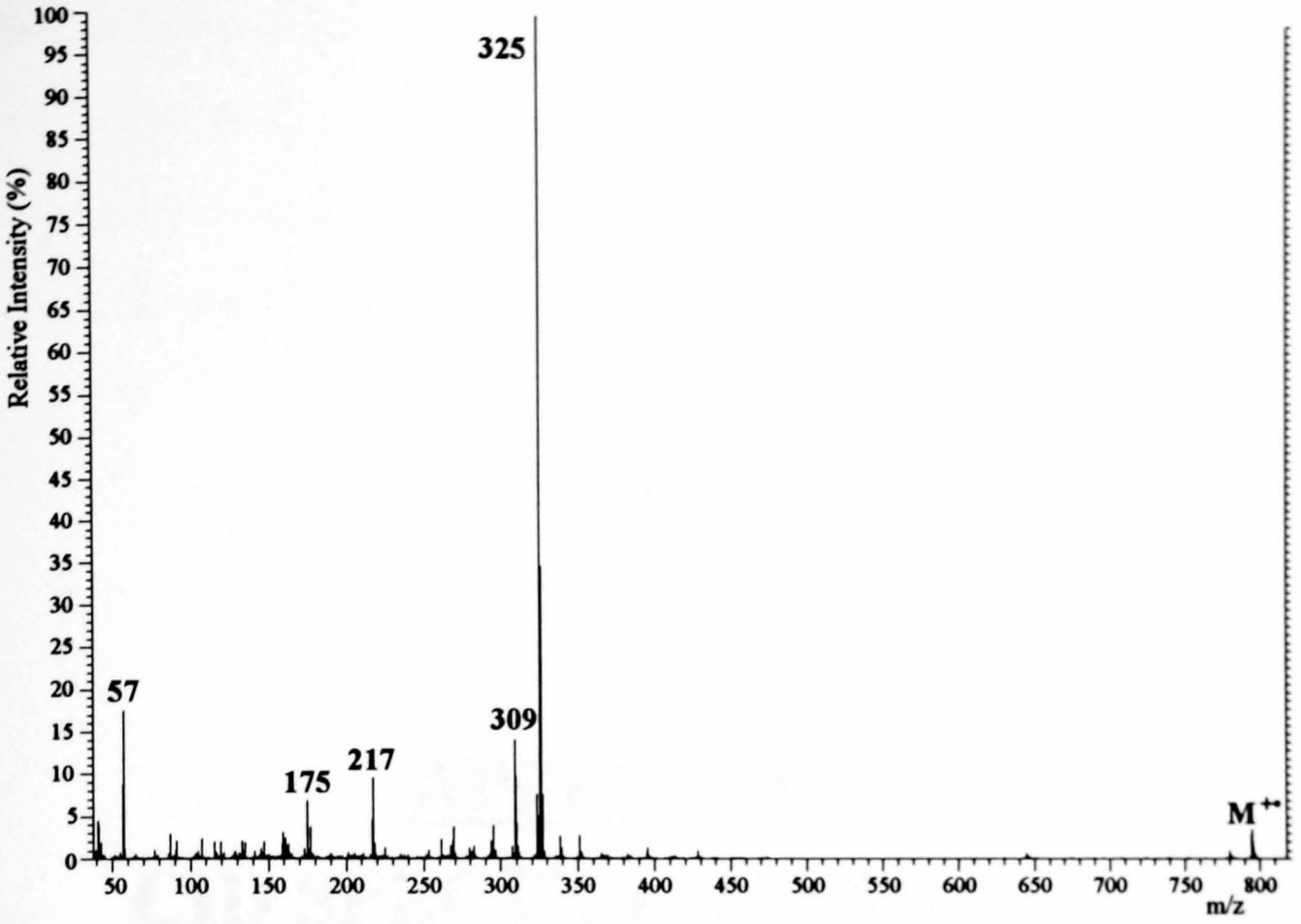

EI-MS Spectrum of Hostanox 03, $M^{+\bullet}$ m/z 794.

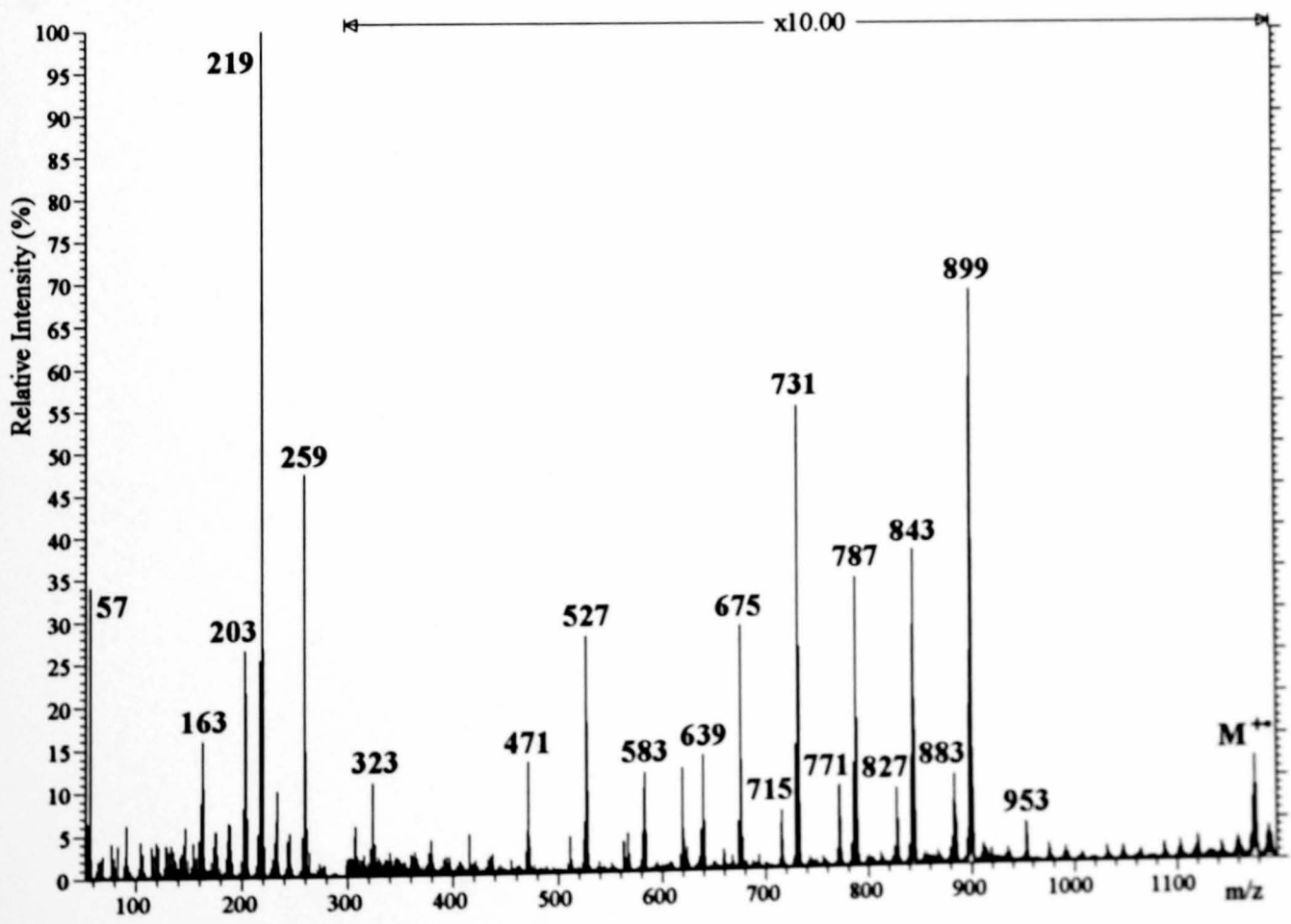

LSIMS-MS Spectrum of Irganox 1010, $M^{+\bullet}$ m/z 1177.

APPENDIX B.

CID SPECTRA OF IRGANOX COMPOUNDS.

The CID spectra of Irganox 1222, Irganox 1024, Irganox 1098 and Irganox 1330 are shown below. These compounds all have the base structure shown in Figure 7.9. The conditions used were the same as stated in Section 7.2. The characteristic ions at m/z 219 and 203 (Section 7.4) are observed in the spectra.

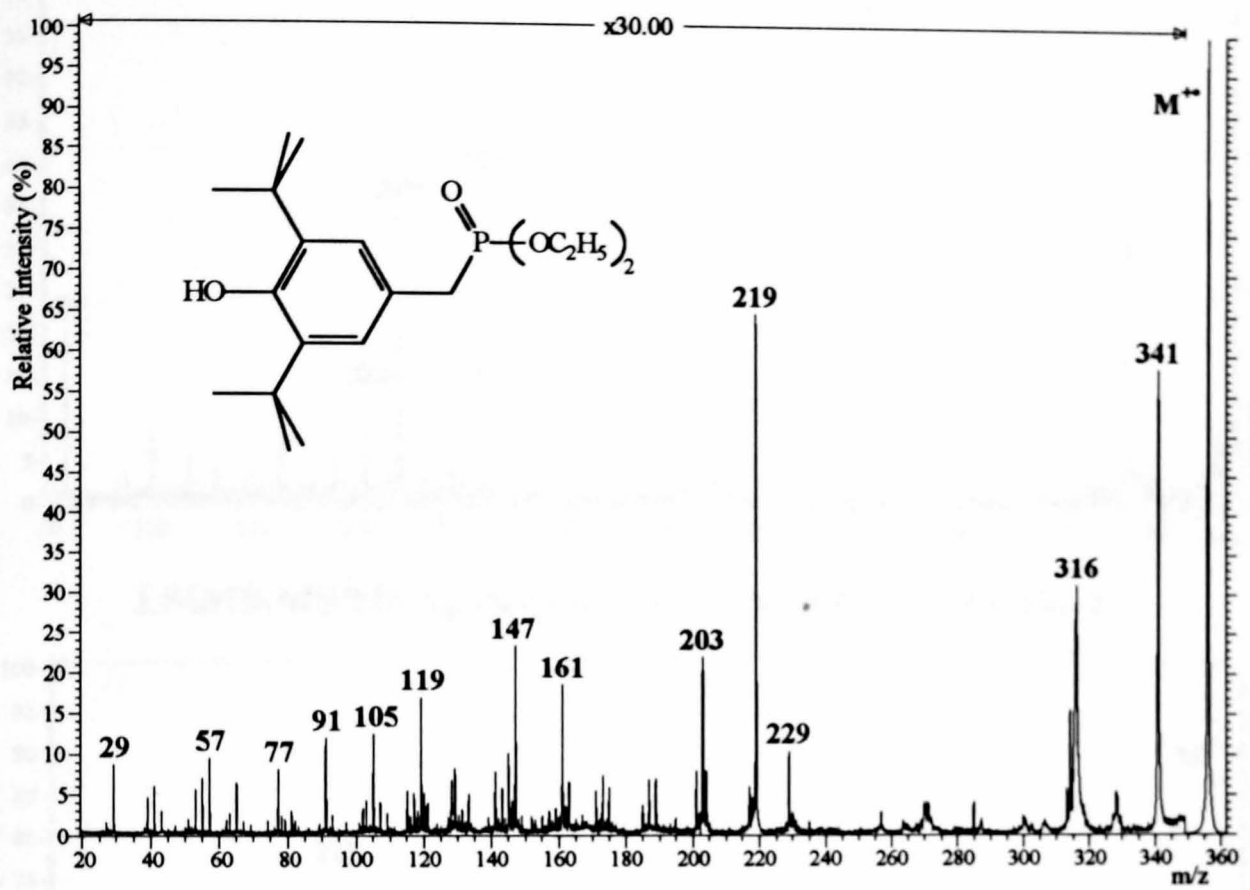

LSIMS-MS/MS Spectrum of Irganox 1222, $M^{+\bullet}$ m/z 356.1.

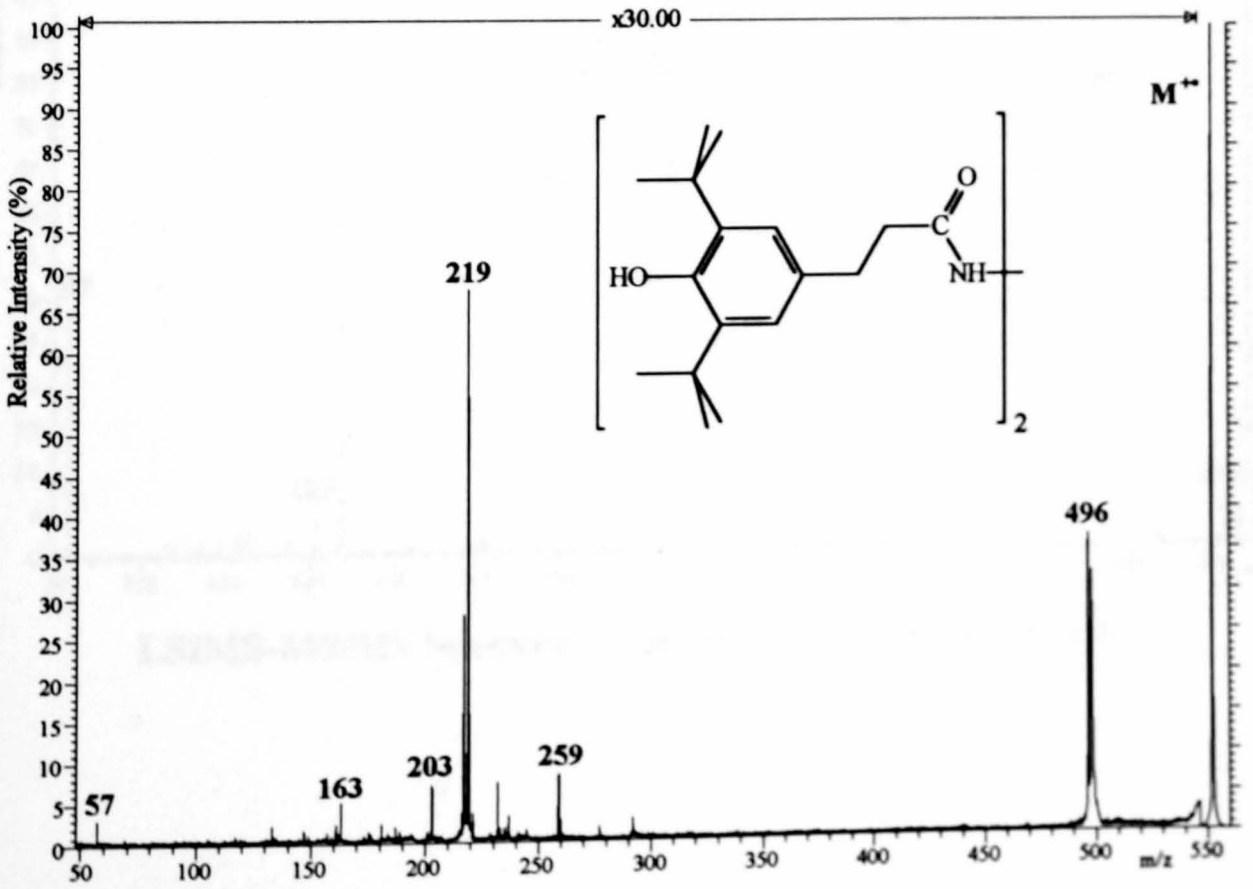

LSIMS-MS/MS Spectrum of Irganox 1024, $M^{+\bullet}$ m/z 552.2.

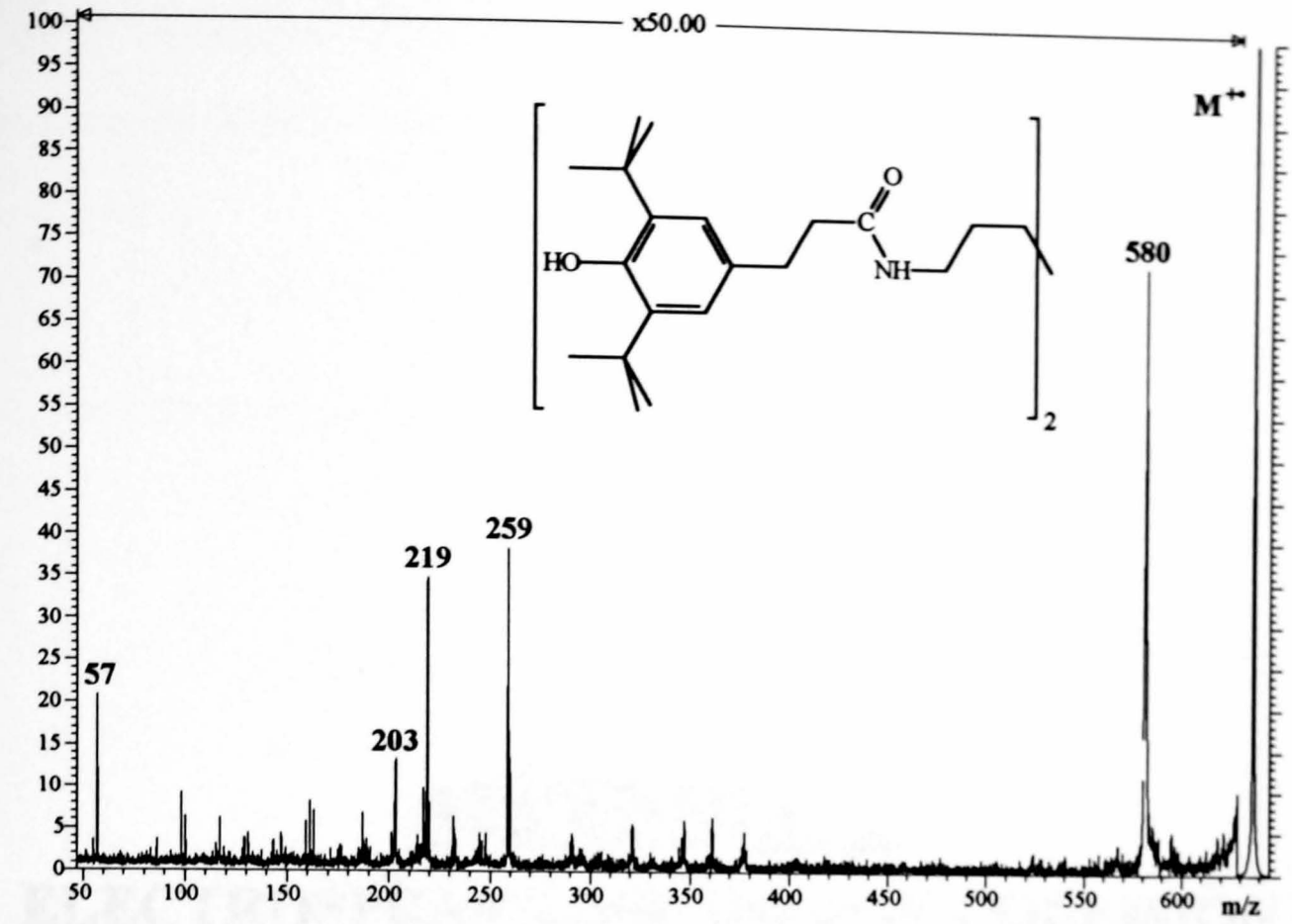

LSIMS-MS/MS Spectrum of Irganox 1098, $M^{+\bullet}$ m/z 636.3.

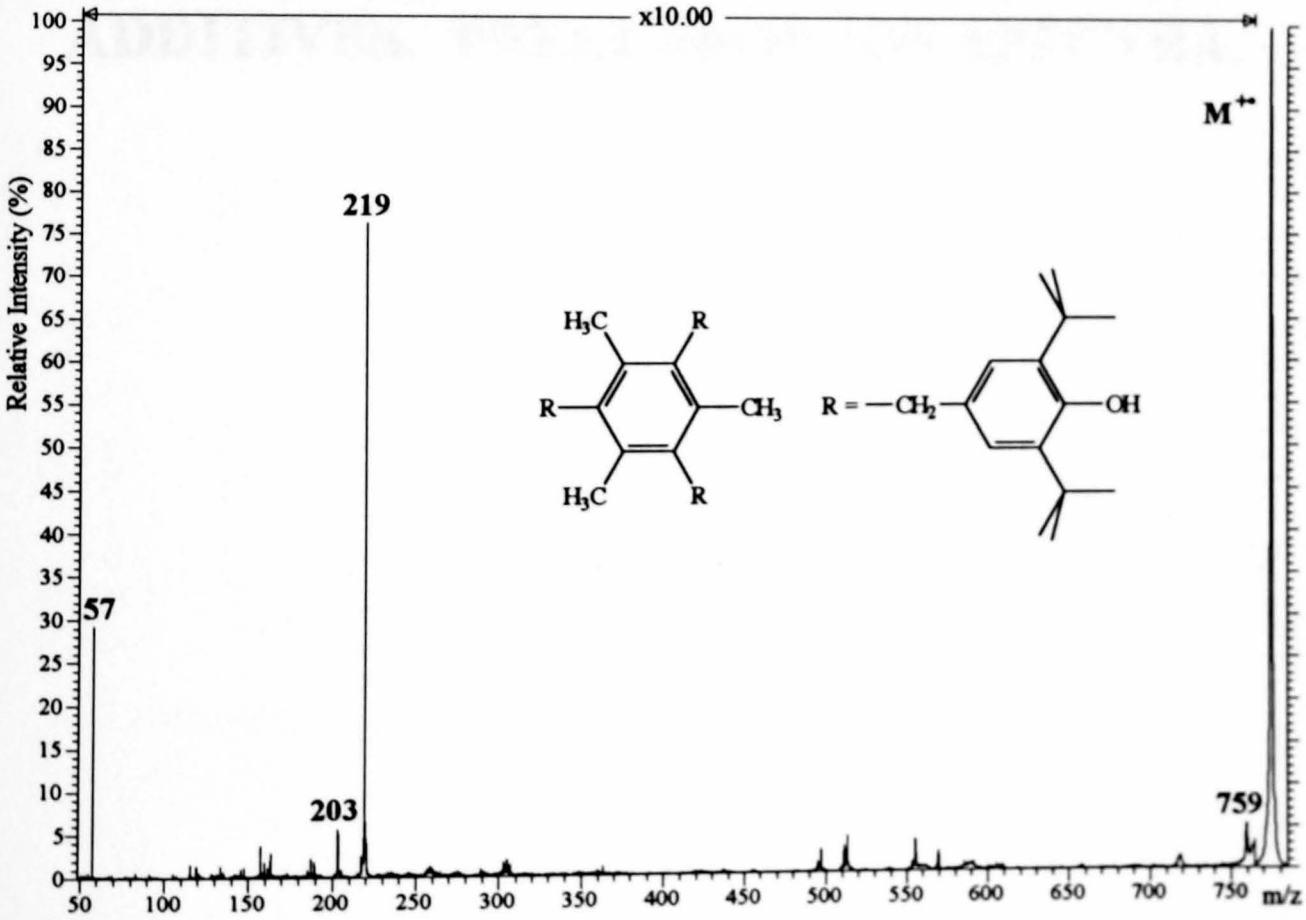

LSIMS-MS/MS Spectrum of Irganox 1330, $M^{+\bullet}$ m/z 774.3.

APPENDIX C.

ELECTROSPRAY-LOW ENERGY COLLISION INDUCED DISSOCIATION OF POLYMER ADDITIVES. PRECURSOR ION SPECTRA.

Precursor ion spectra of the fragment ions observed in the ESI-MS/MS spectra of polymer additives are shown below. The spectra were generated as described in Section 8.4.

Precursor Ion Spectra of Irganox 1010.

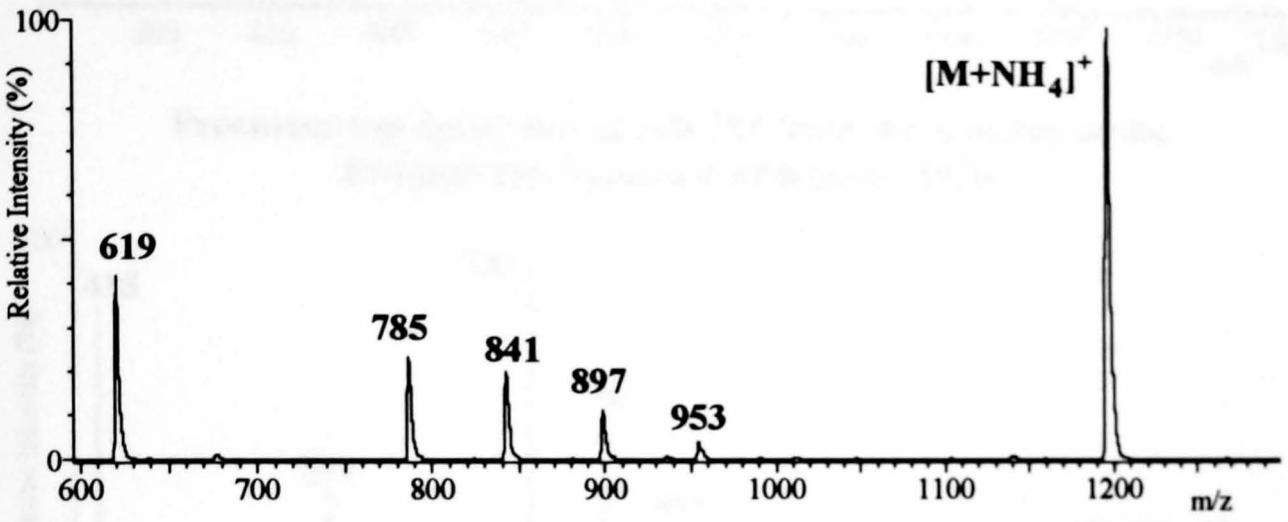

Precursor ion Spectrum of m/z 619 from the B Series in the Product Ion Spectrum of Irganox 1010.

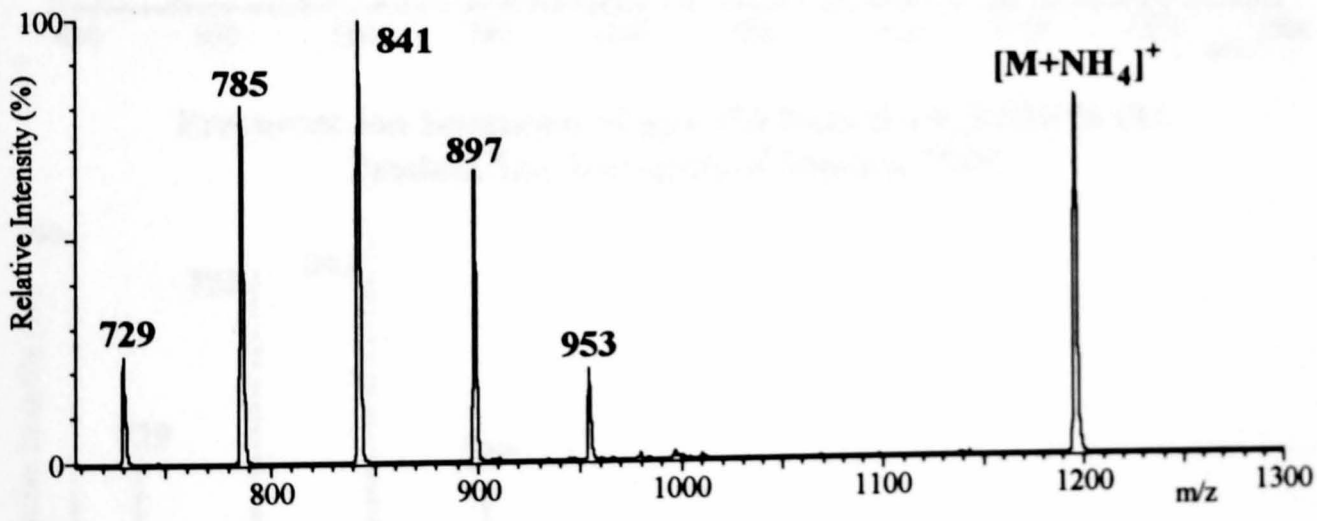

Precursor ion Spectrum of m/z 729 from the A Series in the Product Ion Spectrum of Irganox 1010.

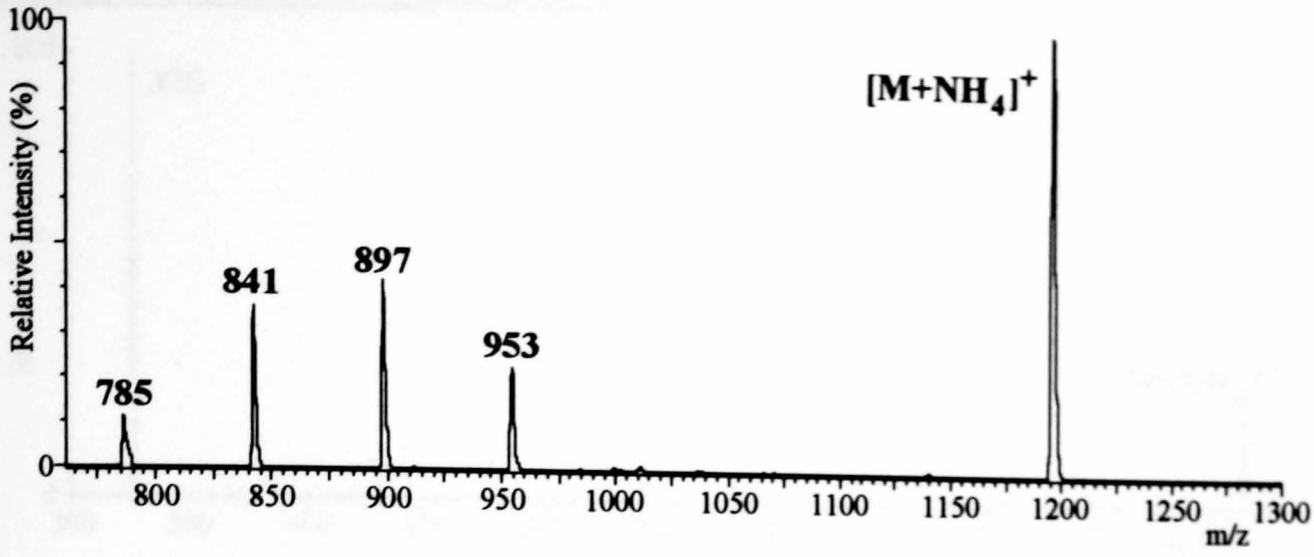

Precursor ion Spectrum of m/z 785 from the A Series in the Product Ion Spectrum of Irganox 1010.

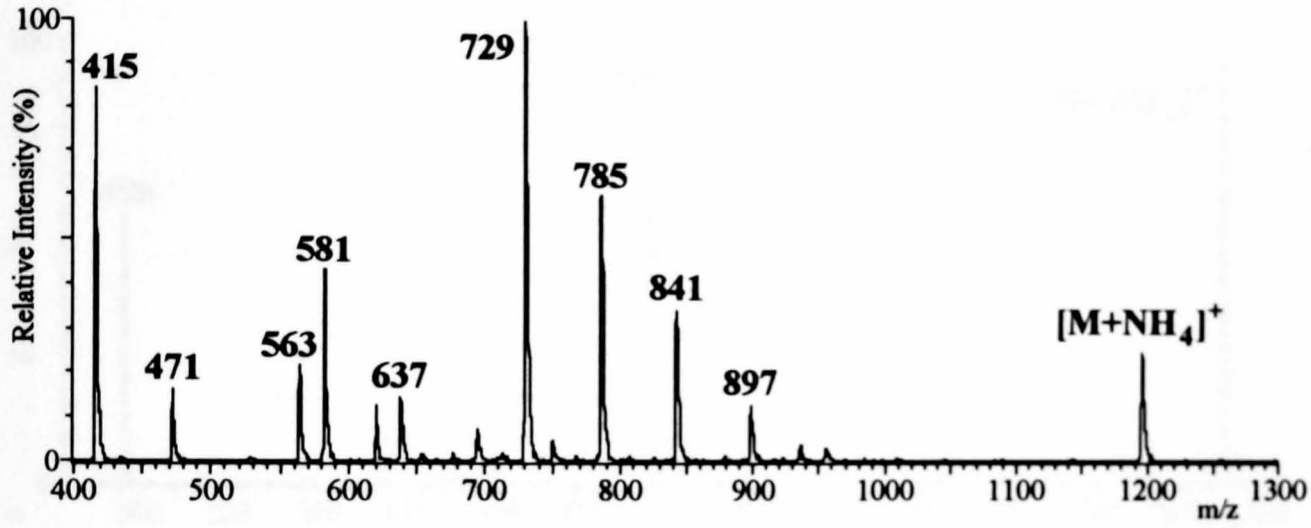

Precursor ion Spectrum of m/z 415 from the E Series in the Product Ion Spectrum of Irganox 1010.

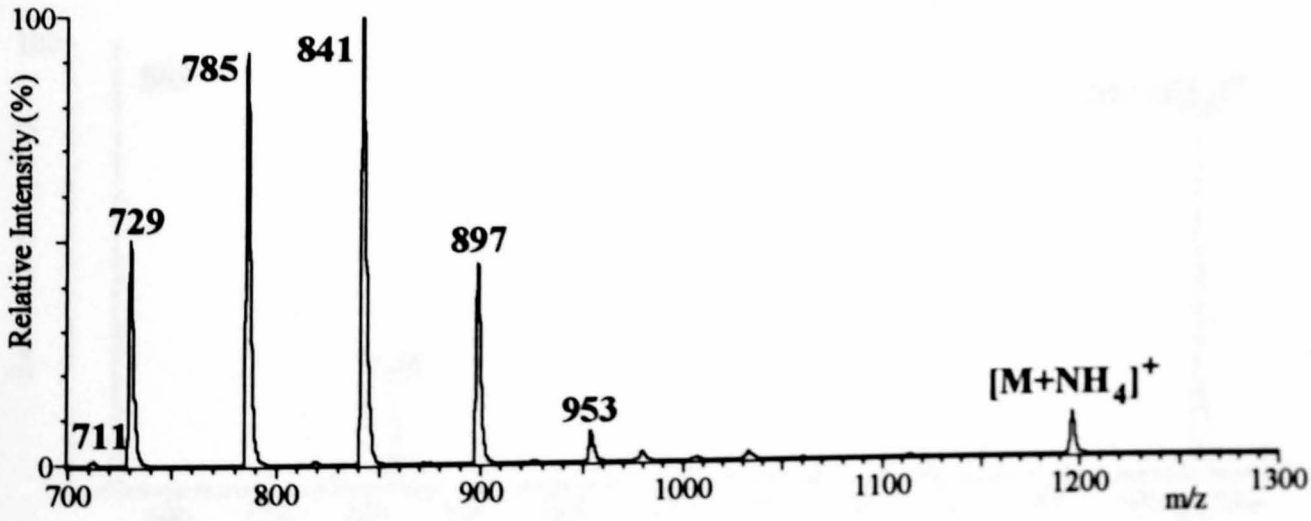

Precursor ion Spectrum of m/z 711 from the C Series in the Product Ion Spectrum of Irganox 1010.

Precursor Ion Spectra of Hostanox 03.

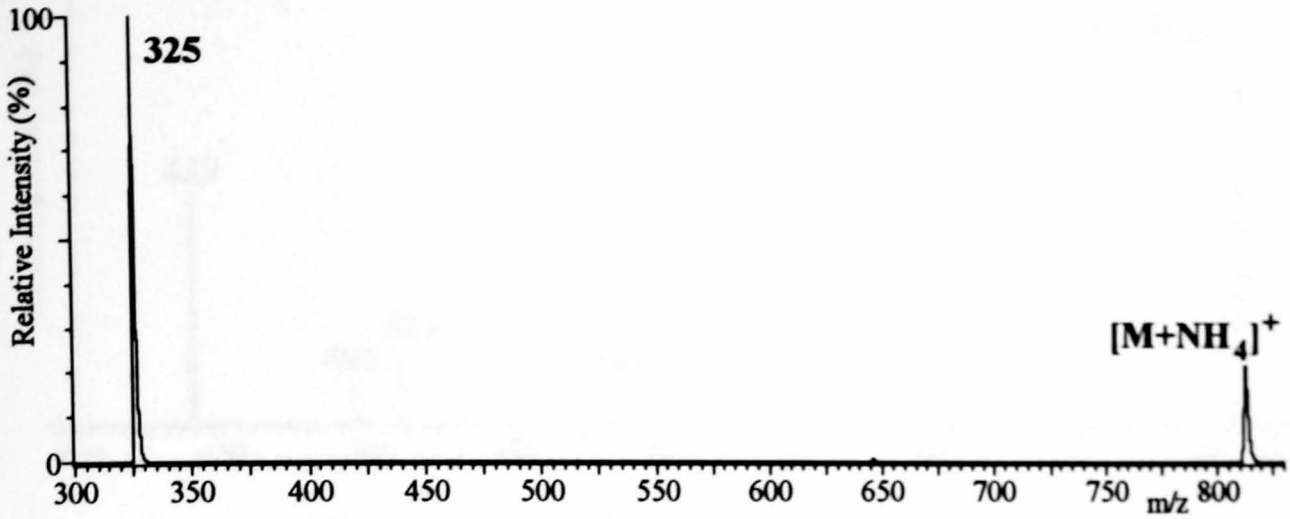

Precursor Ion Spectrum of m/z 325 from the Product Ion Spectrum of Hostanox 03.

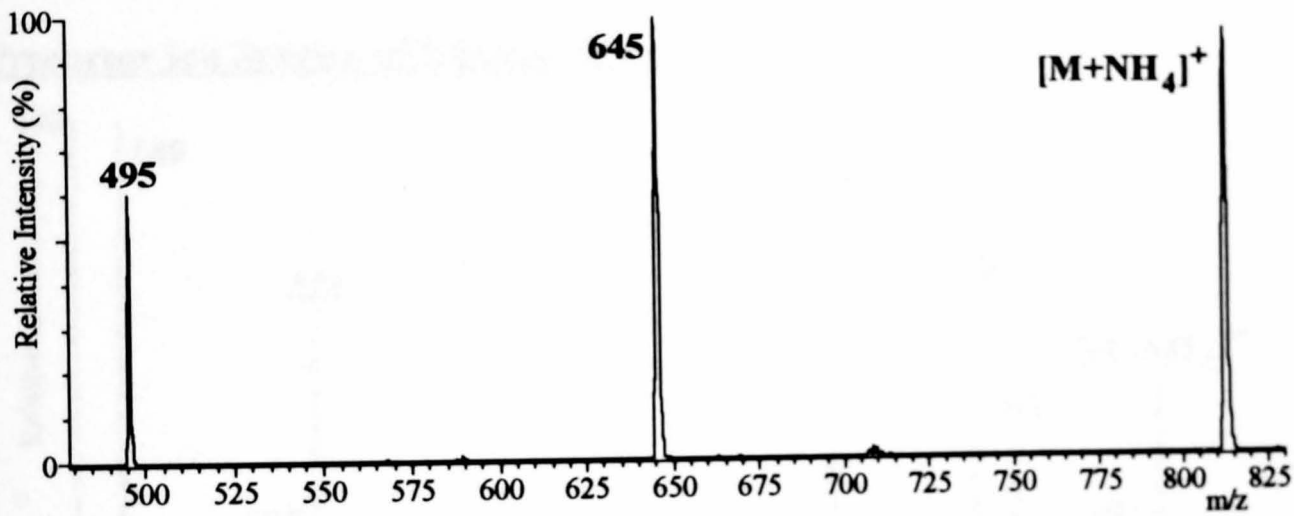

Precursor Ion Spectrum of m/z 495 from the Product Ion Spectrum of Hostanox 03.

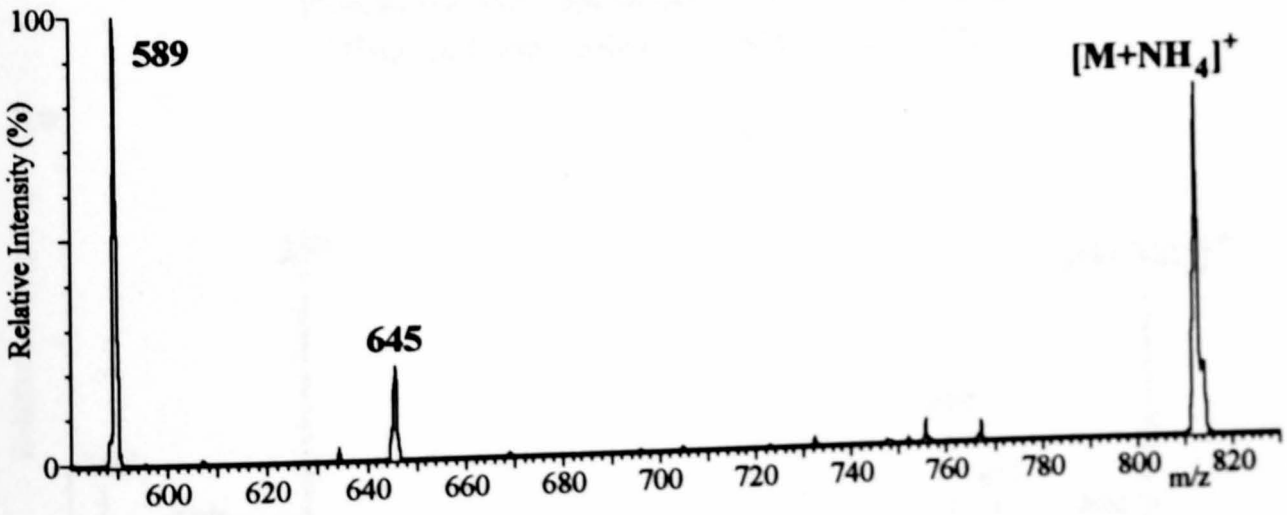

Precursor Ion Spectrum of m/z 589 from the Product Ion Spectrum of Hostanox 03.

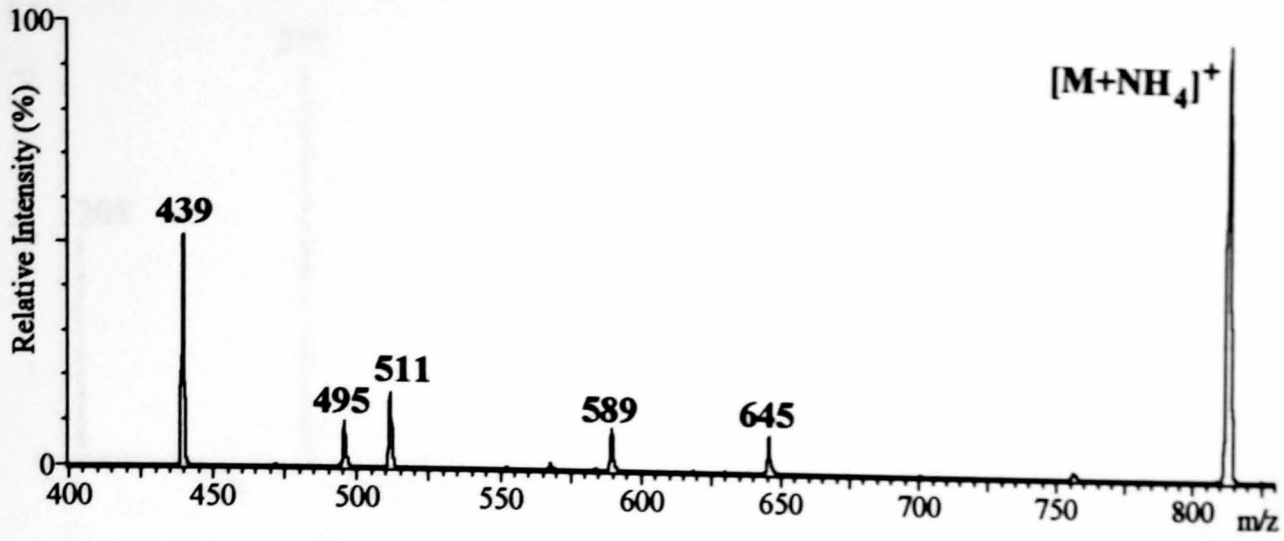

Precursor Ion Spectrum of m/z 439 from the Product Ion Spectrum of Hostanox 03.

Precursor Ion Spectra of Irganox 1076.

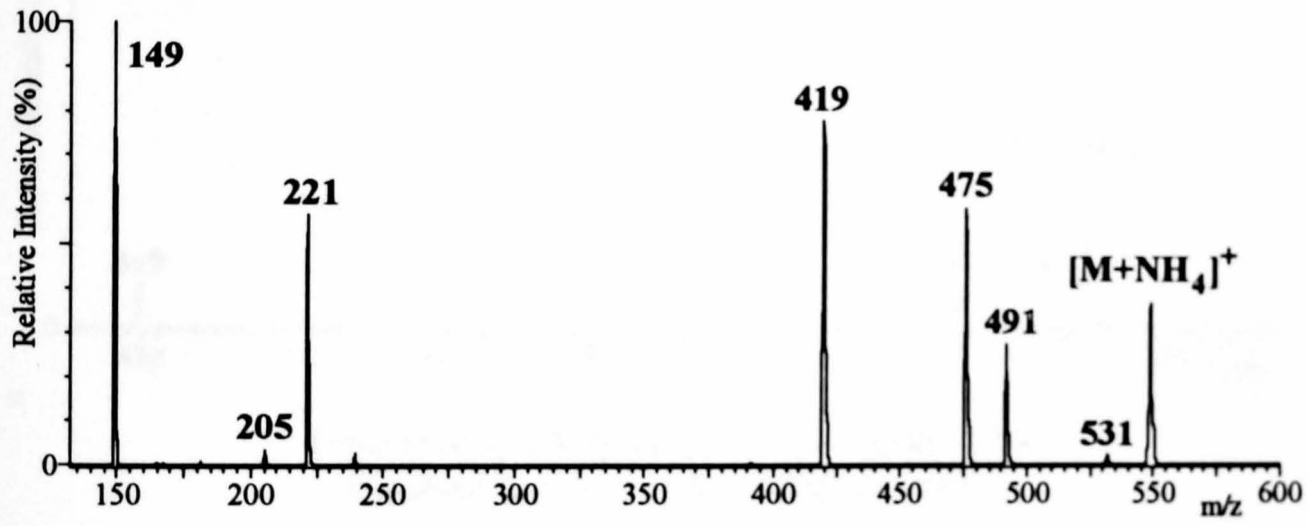

Precursor Ion Spectrum of m/z 149 from the Product Ion Spectrum of Irganox 1076.

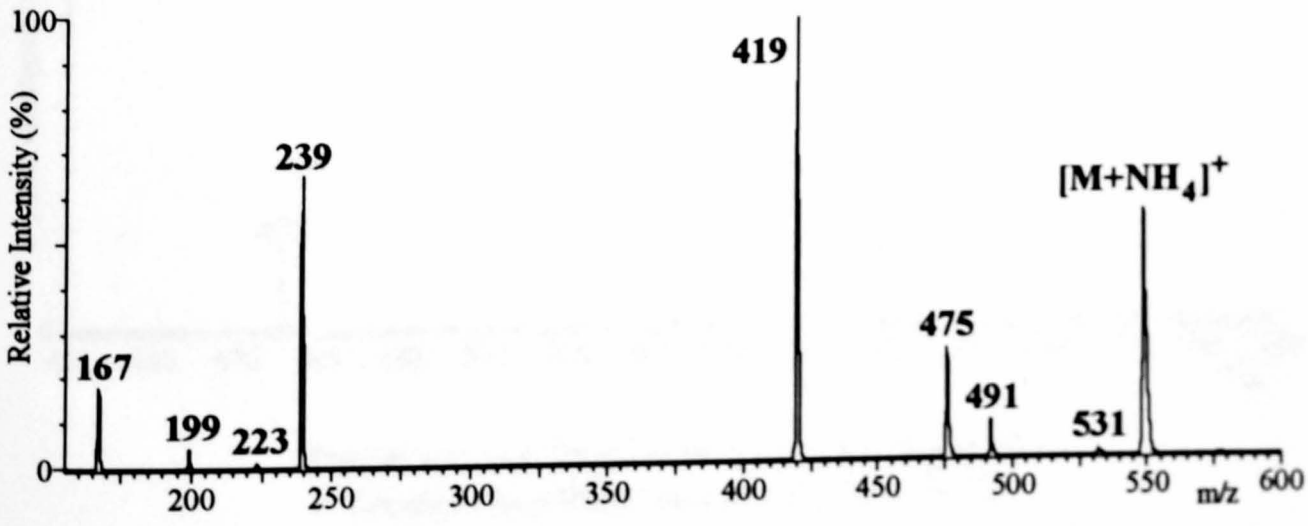

Precursor Ion Spectrum of m/z 167 from the Product Ion Spectrum of Irganox 1076.

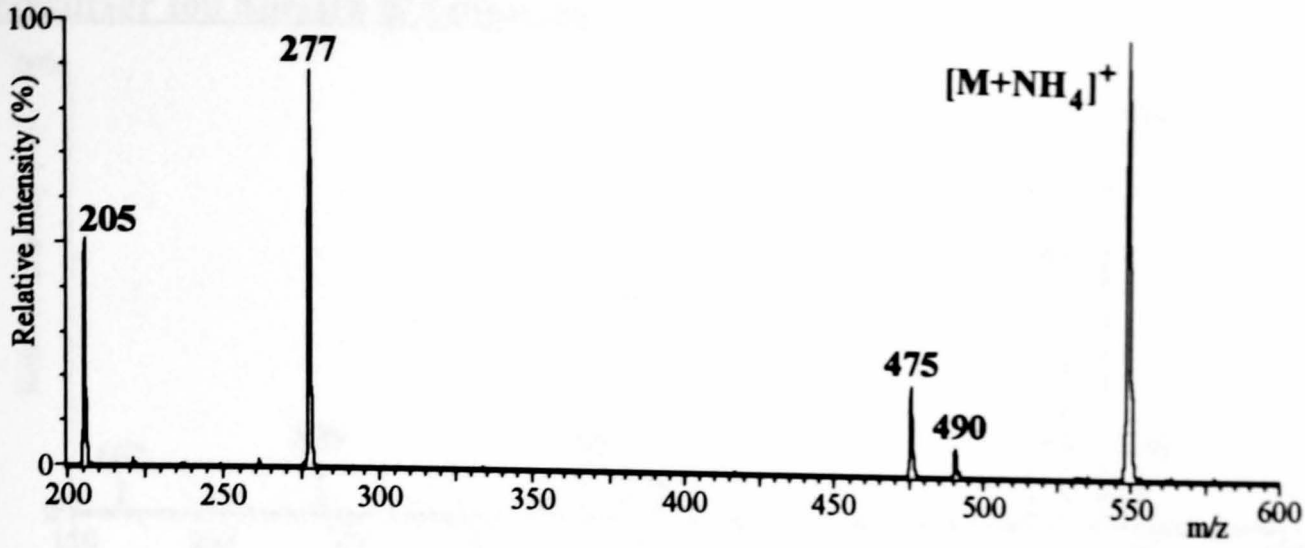

Precursor Ion Spectrum of m/z 205 from the Product Ion Spectrum of Irganox 1076.

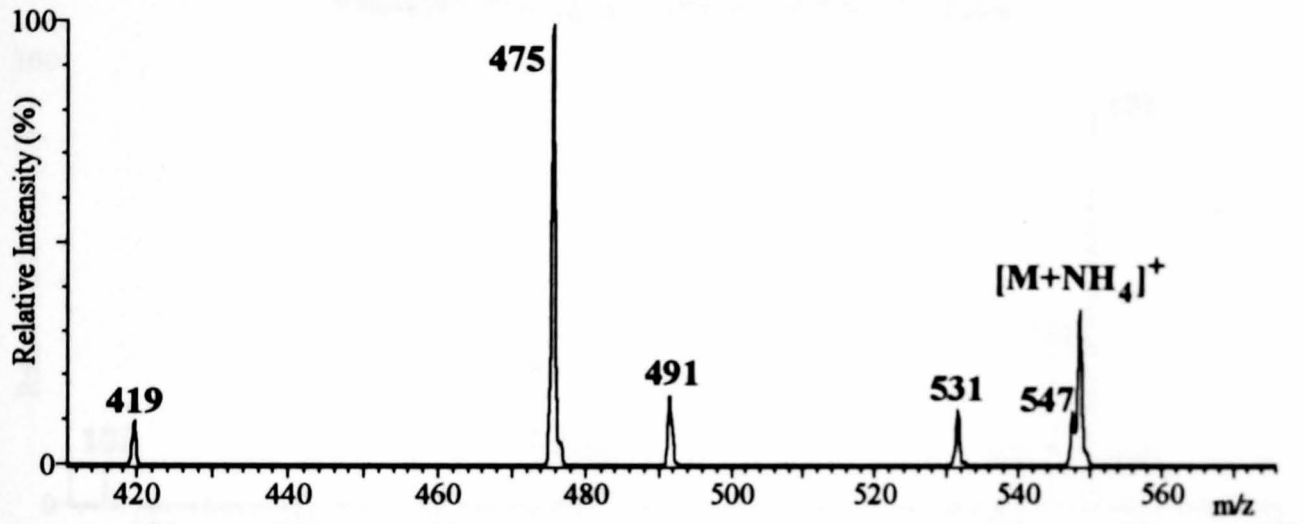

Precursor Ion Spectrum of m/z 419 from the Product Ion Spectrum of Irganox 1076.

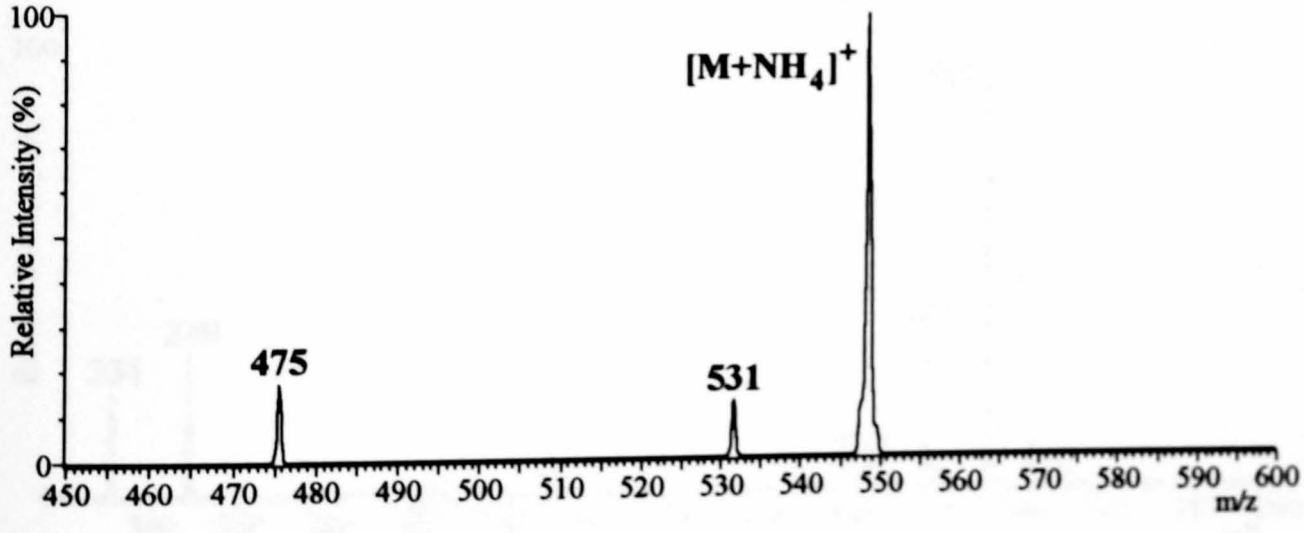

Precursor Ion Spectrum of m/z 475 from the Product Ion Spectrum of Irganox 1076.

Precursor Ion Spectra of Emkarate 3020.

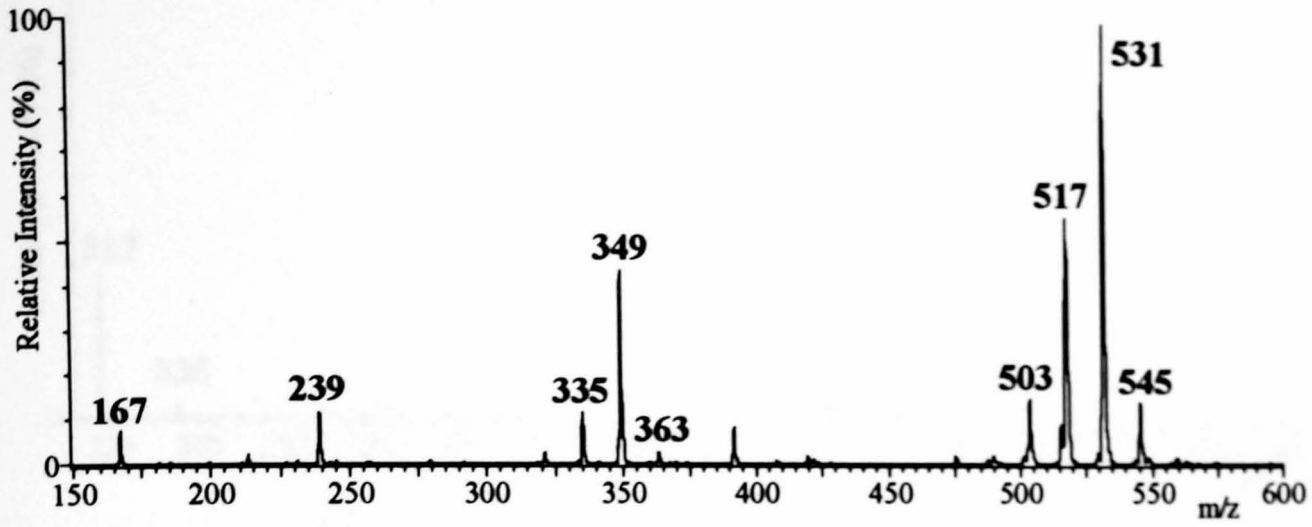

Precursor Ion Spectrum of m/z 167 from the Product Ion Spectrum of Emkarate 3020.

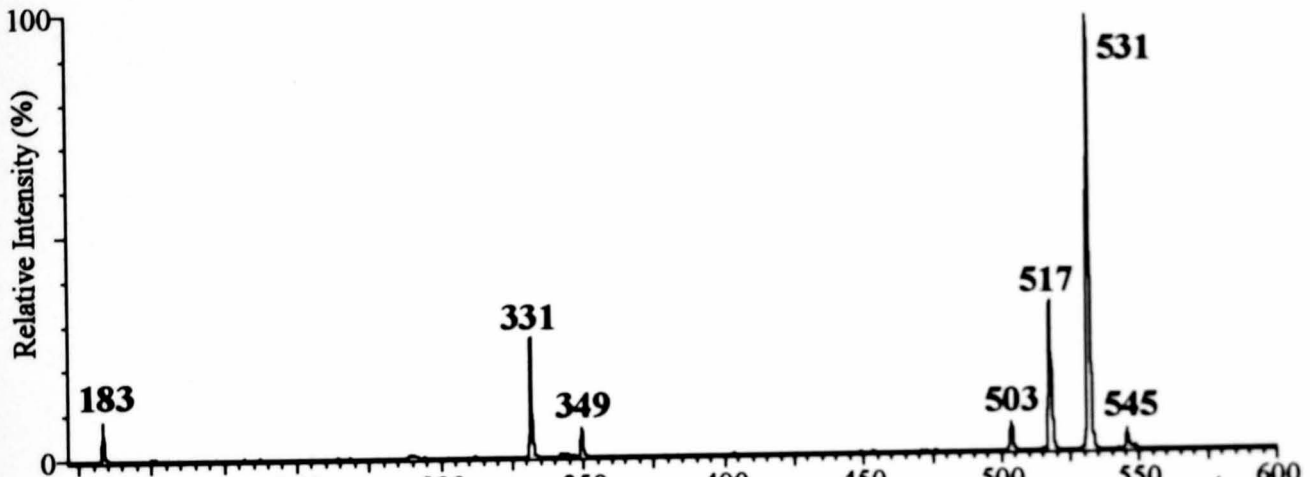

Precursor Ion Spectrum of m/z 183 from the Product Ion Spectrum of Emkarate 3020.

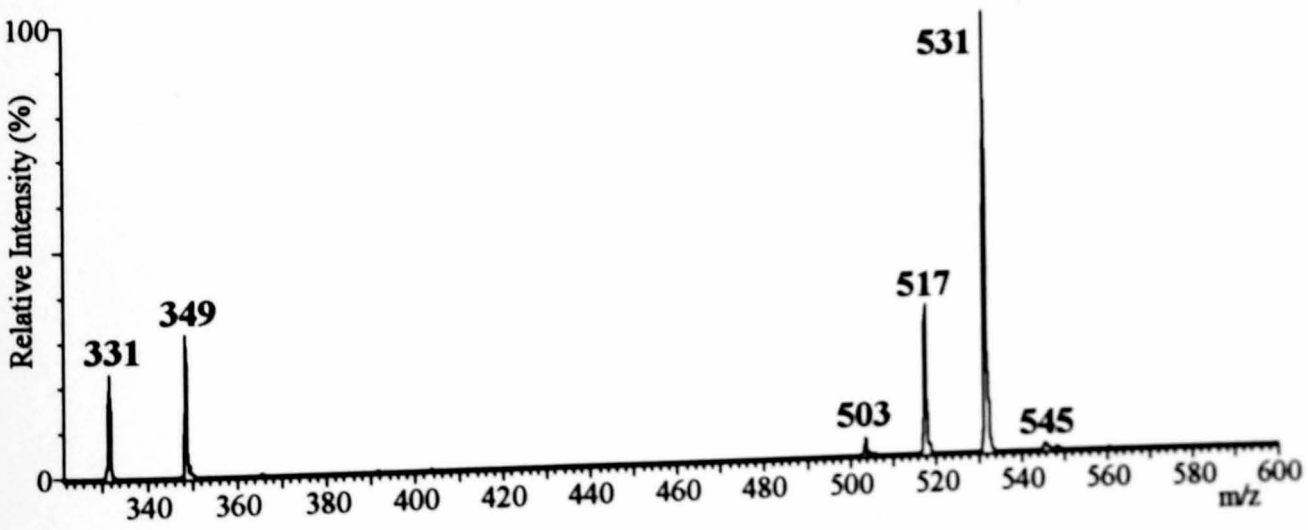

Precursor Ion Spectrum of m/z 331 from the Product Ion Spectrum of Emkarate 3020.

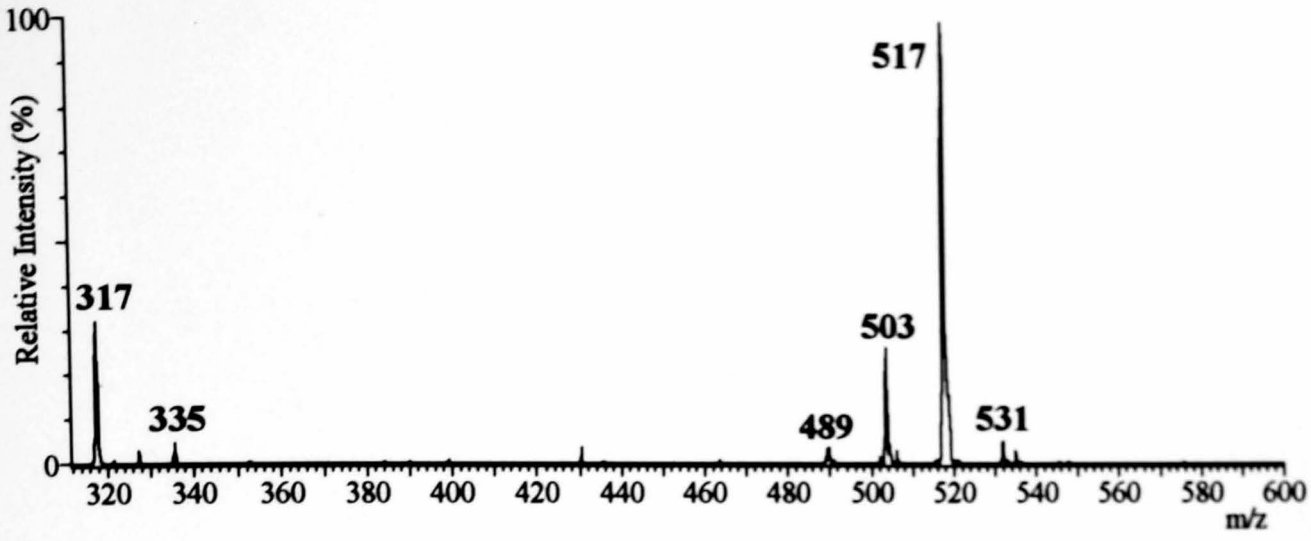

Precursor Ion Spectrum of m/z 317 from the Product Ion Spectrum of Emkarate 3020.